UNIVERSITA' DEGLI STUDI DI PADOVA

Sede Amministrativa: Università degli Studi di Padova

Centro Interdipartimentale di Studi e Attività Spaziali (CISAS)

SCUOLA DI DOTTORATO DI RICERCA IN: Scienze Tecnologie e Misure Spaziali
INDIRIZZO: Astronautica e Scienze da Satellite (ASS)
CICLO XXI

ANALISI DELLA POLVERE INTERPLANETARIA NELL'INTORNO DI MERCURIO E INTERAZIONE CON LA SUPERFICIE

INTERPLANETARY DUST ANALYSIS AROUND MERCURY AND THE INTERACTION WITH THE SURFACE

Direttore della Scuola: Ch.mo Prof. Cesare Barbieri
Supervisore: Ch.mo Prof. Giampiero Naletto
Co-supervisore: Dr. Gabriele Cremonese

Dottoranda: Patrizia Borin

2 Febbraio 2009

Contents

Summary

The research presented in this thesis concerns the determination of micrometeoritic flux on the Mercury surface.

The impact flux on Mercury is the consequence of several different physical processes providing bodies on planetary crossing orbits.

Such flux of material onto Mercury has several effect such as the space weathering and also a change in a planet exosphere.

The exosphere refers to the atmosphere where collisions among volatile species become negligible. In the case of Mercury, the exobase is represented by the surface of the planet. This means that the sources and sinks of the exosphere are strongly linked to the composition and structure of the surface. A fraction of volatiles released into the exosphere is thought to be produced by impact vaporization of meteoritic material [8, Cremonese et al., 2005] [52, Marchi et al., 2005].

Meteoritic flux on Mercury depends on the particle size, because meteoroids with different size have different dynamical evolution. Meteoritic sizes smaller than about 1 cm follow a dynamical evolution dominated by Poynting-Robertson drag. On the other hand, particles with sizes larger than 1 cm follow a completely different dynamical evolution. Most of large meteoroids arriving on the terrestrial planets come from two resonances located in the asteroids Main Belt, that is the resonance 3:1 and the resonance ν_6. The study of Mercury exosphere is then tightly correlated to the creation of dynamical model of particles evolution and then to a flux estimate of these bodies that, considering that Mercury will be the goal of the Bepi Colombo mission (2013), it will be an useful work for studies related to the mission.

To understand the dynamical evolution of dust particles, we begin this work making a survey of interplanetary dust and the different forces which this dust grains are subject.

The near-solar dust cloud is the central region of the meteoritic complex that evolves from the small bodies or our planetary system. Dust particles in the inner Solar System produce the solar F-corona and the zodiacal light. Yet, these astronomical phenomena reveal only a part of the dust cloud in the inner Solar System and especially do not yield sufficient information about the vicinity of the Sun, which is obscured by dust particles in the vicinity of the Earth. Further information is obtained from studies of the near-Earth environment, and subsequently, it has been possible to use data from the Ulysses (1990), Galileo (1989), IRAS (1983) and COBE (1989) missions.

Interplanetary dust particles are a component of the small bodies in the Solar System. Dust particles are released from comets and asteroids or are produced by fragmentation of larger cometary or asteroidal fragments. The major effects that determine the distribution of dust in interplanetary space are solar gravitation, the influence of magnetic fields, radiation pressure and solar wind pressure, including the Poynting-Robertson effect, mutual collisions, and the gravitational forces exerted by the planets.

The radiation pressure force deflects small particles directly outward and they may leave the Solar System after they are ejected from a comet or formed by collision, the exact condition depending on the initial orbital parameters. Particles for which solar gravity amounts to more than twice the radiation pressure may stay in bound orbits. The radiation pressure influences the orbital evolution of this latter component mainly through the Poynting-Robertson effect. The small deceleration that is induced by the anti-parallel component of velocity is denoted as the Poynting-Robertson effect. The deceleration of

particles by the Poynting-Robertson effect reduces the eccentricities and semimajor axes of their orbits. This leads to an increase of dust number density with decreasing solar distance. The Lorentz force acting on charged dust particles moving in the solar magnetic field moderately deflects the particles from their orbits. Depending on the local magnetic field direction the particles are subsequently pushed to either lower or higher latitudes. Also the gravity of the planets can deflect dust particles that closely encounter a planet in unbound and/or high inclination orbits. But the influence of these processes on the overall spatial distribution of the dust cloud is small [50, Mann et al., 2000].

As a result, the particles essentially form a rotationally symmetric cloud.

Inside this dust cloud we can distinguish two groups of particles: particles with size dimension greater than 1 cm, and particles with size dimension smaller than 1 cm. In this work we are interested only at the latest group.

In this work we adopt a statistical approach, based on a large number of simultaneous numerical integration, to explore the orbital evolution of dust particles originating from the Main Belt in order to obtain a statistical analysis, then to provide an estimate of the flux of particles hitting the Mercury's surface.

In order to determine the meteoritic flux at the heliocentric distance of Mercury we utilize the dynamical evolution model of dust particles of Marzari and Vanzani [54, Marzari and Vanzani, 1994] that numerically solves a $(N + 1) + M$ body problem (Sun + N planets + M body with zero mass) with the high-precision integrator RA15. The solar radiation pressure and Poynting-Robertson drag, together with the gravitational interactions of the planets, are taken as major perturbing forces affecting the orbital evolution of the dust particles. We will perform numerical simulations with different initial conditions for the dust particles, depending on the sources, with the aim of estimating the flux of dust on the surface of Mercury.

The adopted numerical method for solving the equations of motion is the RA15 version of the RADAU integrator by Everhart (1985). This numerical integrator is particularly accurate and suitable for modelling the orbital behaviour of dust particles because it uses a variable stepsize.

We have performed many simulations that considers particles with different size and different integration times.

The aim of these simulations is to study the dynamical evolution of dust particles with dimension smaller than 1 cm and to observe how many particles get Mercury surface and then determine the flux of particles hitting the planet.

To determine the flux at Mercury we have to calibrate our flux and to do this we need to know the number of particles in the Main Belt.

In order to estimate this number we have run the model for the Earth, assuming that the perturbations due to Mars are negligible, and we have compared our results with the observed terrestrial flux reported in literature. In particular we have considered, as reference values, the estimate of Love and Brownlee ([45, Love et al., 1993]).

After this, we can calibrate the flux given by our model and to obtain the flux on Mercury.

Sintesi

La ricerca presentata in questo lavoro di tesi riguarda la determinazione del flusso di micrometeoriti sulla superficie di Mercurio.

Il flusso di impattori su Mercurio, così come per gli altri pianeti del Sistema Solare, è conseguenza di alcuni processi fisici che portano corpi di differenti dimensioni ad attraversare le orbite planetarie e quindi ad impattare sul pianeta. Studi riguardanti la Terra hanno mostrato che gli oggetti che impattano sul nostro pianeta hanno dimensioni che si estendono per oltre otto ordini di grandezza, ovvero da dimensioni del micrometro fino a dimensioni di centinaia di metri. Allo stesso modo si pensa che questo possa valere per gli altri pianeti terrestri del Sistema Solare. Per quanto riguarda Mercurio, un aspetto di notevole interesse e studio è l'effetto che questo flusso di meteoroidi ha sull'esosfera del pianeta. Con il termine esosfera ci si riferisce a quella parte di atmosfera in cui le collisioni tra le particelle di differenti specie diventano trascurabili. Nel caso di Mercurio, l'esobase, il limite inferiore dell'esosfera al di sotto del quale le collisioni fra particelle iniziano ad essere rilevanti, risulta coincidere con la sua superficie. Questo significa che la composizione dell'esosfera è strettamente correlata alla composizione e struttura della superficie del pianeta. Le ipotesi riguardanti la formazione e composizione dell'esosfera di Mercurio si dividono essenzialmente in due gruppi [8, Cremonese et al., 2005] [52, Marchi et al., 2005]. Da un lato, si pensa che una parte di elementi volatili dell'esosfera di Mercurio sia prodotta dalla vaporizzazione di materiale in seguito ad impatto meteoritico; dall'altro si pensa che tutti gli elementi volatili presenti provengano solamente da impatti meteoritici. Sfortunatamente, il flusso meteoritico e le velocità di impatto sulla superficie di Mercurio sono molto difficili da determinare a causa di alcune incognite e variabili relative alla composizione della superficie e del flusso di meteoroidi. I flussi di meteoroidi che vengono utilizzati in letteratura per studi su Mercurio sono stati derivati da stime ricavate per la Terra. Questo significa che non si è in possesso di una buona statistica sul numero di impatti e sulla distribuzione delle velocità dei meteoroidi. In passato sono stati effettuati studi riguardo la determinazione dei flussi e degli impatti di meteoroidi da Cintala (1992).

Meteoroidi di differenti dimensioni seguono, differenti evoluzioni dinamiche. Corpi di dimensioni inferiori al centimetro hanno un'evoluzione dinamica dominata dall'effetto Poynting-Robertson, effetto causato dalla radiazione solare che agisce sull'energia rotazionale della particella accorciando il semiasse dell'orbita e portando quindi ad un moto a forma di spirale della particella che è destinata a cadere sul pianeta.

D'altra parte, particelle aventi dimensioni superiori al centimetro hanno un'evoluzione dinamica completamente differente. La maggior parte dei meteoroidi delle dimensioni suddette che raggiungono i pianeti terrestri provengono dalla fascia asteroidale posta tra Marte e Giove (la Main Belt) e sono caratterizzati da due importanti risonanze, ovvero la risonanza 3:1 e la risonanza ν_6. Lo studio dell'esosfera di Mercurio è quindi strettamente correlato alla creazione di un modello dinamico dell'evoluzione dei meteoroidi e quindi ad una stima del flusso di tali corpi che, considerando il fatto che Mercurio sarà l'obiettivo della missione Bepi Colombo (2013), sarà utile per gli studi di missione.

L'obiettivo di questo lavoro di ricerca è quindi quello di sviluppare un modello di evoluzione dinamica delle polveri di dimensioni inferiori a 1 centimetro e un modello che fornisca il numero di impatti che avvengono sulla superficie di Mercurio e le interazioni della polvere con la superficie del pianeta.

All'interno di questo modello si vuole analizzare la polvere dovuta alle cosiddette sungrazing comets, comete la cui orbita è radente il Sole, che potrebbero contribuire alla polvere che investe Mercurio.

Per poter affrontare un lavoro di questo tipo, è stato utile sviluppare uno studio riguardante la polvere interplanetaria e la dinamica che la governa, concentrando la nostra attenzione al Sistema Solare Interno.

La nube di polvere interplanetaria situata in prossimità del Sole è, infatti, la regione principale costituita da corpi meteoritici che, evolvendo in continuazione, creano una grande quantità di corpi di piccole dimensioni. Le particelle di polvere nel Sistema Solare Interno producono la cosiddetta corona F, in prossimità del Sole, e la nube zodiacale, anche se queste rappresentano solo una piccola parte della polvere interplanetaria. La maggior parte delle informazioni riguardo la polvere interplanetaria sono state ottenute, in un primo tempo, da studi effettuati in prossimità della Terra e, in seguito, si è potuto usufruire dei dati messi a disposizione dalle missioni Ulysses (1990), Galileo (1989), IRAS (1983) e COBE (1989).

Le particelle di polvere interplanetaria sono componenti di piccoli corpi del Sistema Solare originate da collisioni fra gli stessi o rilasciate da comete e asteroidi o derivanti da frammentazione di corpi maggiori.

I principali effetti che dominano la distribuzione e la dinamica della polvere interplanetaria sono la gravitazione solare, l'influenza di campi magnetici, la pressione di radiazione, la pressione del vento solare, il Poynting-Robetson drag, le collisione mutue e le forze gravitazionali esercitate dai pianeti.

La pressione di radiazione agisce sulle particelle di polvere deflettendone l'orbita e facendole espellere dal Sistema Solare, anche se si deve tenere in conto che sono di notevole importanza gli elementi orbitali iniziali.

Le particelle, invece, per cui la forza di gravità risulta essere doppia rispetto alla pressione di radiazione presentano orbite legate e rimangono nel Sistema Solare.

La pressione di radiazione influenza l'evoluzione orbitale delle particelle di polvere principalmente attraverso il Poynting-Robertson drag. La decelerazione indotta dalla componente anti-parallela della velocità viene denominata effetto Poynting-Robertson.

La decelerazione delle particelle causata dall'effetto Poynting-Robertson riduce l'eccentricità ed il semiasse maggiore dell'orbita delle particelle di polvere. Questo porta ad una crescita della densità della polvere con il diminuire della distanza dal Sole.

Per quanto riguarda la forza di Lorentz, questa agisce sulle particelle di polvere cariche che si muovono all'interno del campo magnetico solare, deflettendone l'orbita in modo moderato. L'azione di tale forza dipende dalla direzione del campo magnetico locale e ha come conseguenza la deflessione dell'orbita delle particelle di polvere a basse o alte latitudini.

Anche la gravità dovuta ai pianeti del Sistema Solare, seppur in piccola parte, può deflettere le orbite delle particelle di polvere che si trovano in prossimità di pianeti. Tali perturbazioni agiscono soprattutto sull'argomento di perielio e sul nodo ascendente su tempi scala che sono di molto superiori al periodo orbitale delle particelle di polvere [50, Mann et al., 2000].

Come risultato si ha quindi che le particelle di polvere si dispongono a formare una nube rotazionalmente simmetrica.

All'interno di questa nube di polvere dobbiamo distinguere essenzialmente due gruppi di particelle, quelle di dimensioni superiori al cm e quelle di dimensioni inferiori al cm dal momento che l'evoluzione dinamica di questi due tipi di particelle è completamente diversa.

Ogni corpo che si muove all'interno del Sistema Solare è soggetto al campo gravitazionale creato dal Sole a dagli altri corpi, ma è anche soggetto a forze di natura non gravitazionale.

Queste ultime, che derivano principalmente dal flusso di fotoni, protoni ed elettroni che costituiscono il vento solare, agiscono in particolar modo sui micrometeoroidi. I principali effeti dovuti a questo campo di radiazione sono la pressione di radiazione e l'effetto Poynting-Robertson.

Per quanto concerne l'effetto Poynting-Robertson possiamo riassuamerlo in poche parole dicendo che l'energia assorbita dalla particella viene continuamente reirradiata dalla particella stessa e, dal momento che si considerano particelle isoterme, nel sistema di riferimento della particella tale reirradiazione risulta essere isotropa e quindi non produce alcun tipo di forza. La reirradiazione si traduce in una perdita

di massa. Nel sistema di riferimento del Sole però, dove la particella possiede una certa velocità, la reirradiazione non è più da considerarsi isotropa, perchè le frequenze dei fotoni emissi nella direzione del moto risultano maggiori delle frequenze dei fotoni emessi nella direzione opposta per effetto Doppler. La particella quindi subisce una forza contro la direzione del moto che assume la forma [5, Burns et al., 1979]

$$m\dot{\mathbf{v}} = \frac{SA}{c} Q_{pr} \left[\left(1 - \frac{\dot{r}}{c} \right) \hat{\mathbf{S}} - \frac{\mathbf{v}}{c} \right] , \tag{1}$$

dove S è il flusso di energia, A è la sezione d'urto della particella, $\mathbf{v}$ è la velocità della particella rispetto al Sole, c è la velocità della luce, $\dot{r}$ è la velocità radiale e $\hat{\mathbf{S}}$ è il vettore unitario nella direzione del fascio incidente.

Q_{pr} rappresenta il coefficiente di pressione di radiazione il cui valore viene calcolato secondo la teoria di Mie che assume le particelle sferiche ed isotrope e prende in considerazione le costanti ottiche delle particelle di polvere, quindi la composizione e la forma, e lo spettro di energia solare. Oltre a questo coefficiente è utile introdurre il coefficiente β. A tale scopo scriviamo la forza gravitazionale del Sole esercitata su una particella sferica di raggio s e densità ϱ

$$F_g = \frac{4}{3} \pi s^3 \varrho \frac{GM}{r^2} , \tag{2}$$

dove G è la costante di gravitazione universale, e la forza della pressione di radiazione dovuta alla radiazione solare

$$F_r = \frac{SA}{c} Q_{pr} , \tag{3}$$

in cui si utilizza $S = \frac{L}{4\pi r^2}$ per il flusso ad una distanza r, con L luminosità solare.

Il coefficiente β viene definito come il rapporto di queste due forze

$$\beta = \frac{F_r}{F_g} = \frac{\frac{3L}{16\pi GMc}}{\frac{Q_{pr}}{\varrho s}} = 5.7 \cdot 10^{-5} \frac{Q_{pr}}{\varrho s} , \tag{4}$$

in cui ϱ e s sono espressi in unità cgs.

Dal momento che la forza di pressione di radiazione è diretta in senso contrario alla forza di gravità, la forza totale sarà attrattiva se vale la condizione $\beta < 1$ e viceversa nel caso in cui valga la relazione $\beta > 1$.

In questo lavoro di ricerca abbiamo adottato un approccio statistico, consistente di un ampio numero di simulazioni di integrazione numerica, al fine di indagare l'evoluzione orbitale di particelle di polvere provenienti dalla Main Belt e di ottenere analisi statistiche che riescano a fornire una stima del flusso di particelle che arrivano alla superficie di Mercurio.

Per determinare il flusso meteoritico alla distanza eliocentrica di Mercurio, abbiamo utilizzato il modello di evoluzione dinamica per particelle di polvere, sviluppato da Marzari e Vanzani [54, Marzari and Vanzani, 1994]. Tale modello risolve numericamente un problema di $(N + 1) + M$ corpi (Sole + N pianeti + M corpi) mediante l'utilizzo dell'integratore ad alta precisione RA15.

Le maggiori forze perturbatrici che vengono considerate nel modello sono l'effetto Poynting-Robertson, la pressione di radiazione solare e le interazioni gravitazionali dei pianeti, che agiscono sull'evoluzione orbitale della particella di polvere.

Il metodo numerico adottato per la risoluzione delle equazioni del moto è la versione RA15 dell'integratore RADAU di Everarth (1985). Questo integratore è particolarmente accurato per modelli di evoluzione orbitale di particelle di polvere.

Sono state effettuate numerose simulazioni che prendono in considerazione particelle di differenti dimensioni e tempi di integrazione diversi.

Lo scopo di queste simulazioni è quello di studiare l'evoluzione di particelle di dimensioni inferiori al cm e vedere quante particelle arrivano alla superficie di Mercurio per poi riuscire a determinare il flusso di particelle che arrivano sul pianeta.

Il flusso di agenti impattanti su un pianeta, misurato in numero di particelle di una data dimensione che impattano l'unità di area per l'unità di tempo, dipende essenzialmente da due fattori: la distribuzione delle velocità degli oggetti che impattano sul pianeta e la funzione densità spaziale (numero per unità di volume) delle particelle che arrivano sul pianeta.

Prendendo in considerazione l'articolo di Cintala [7, Cintala, 1992] si devono quindi considerare due fattori per calcolare il flusso e determinarlo mediante l'equazione

$$\Phi(v, \mu) = f(v)h(\mu)\,, \tag{5}$$

dove $f(v)$ è la funzione distribuzione velocità e $h(\mu)$ è una funzione che descrive la distribuzione in massa degli oggetti impattanti. L'equazione (5) sussiste con l'assunzione che la velocità e la distribuzione in massa siano indipendenti [7, Cintala, 1992].

Per confrontare il nostro lavoro con quello di Cintala si è preso in considerazione un set di 1000 particelle, con elementi orbitali randomici, provenienti dalla Main Belt. È stata studiata la loro evoluzione orbitale fino a quando questi micrometeoriti non si trovavano in prossimità di dieci volte la sfera di influenza di Mercurio. Ottenuto un output di tali particelle, si registra il numero di incontri tra particelle e Mercurio fino a che il grano di polvere non arriva alla sua minima distanza dal pianeta. Si calcola quindi il numero di particelle arrivate in prossimità del pianeta, N, attendendo un andamento proporzionale a R^2, distanza minima tra pianeta e particella di polvere, dal momento che la sezione d'urto è πR^2 [55, Marzari et al., 1996].

In questo lavoro non sono state prese in considerazione particelle con raggio di dimensioni inferiori a 1 μm perché l'effetto della pressione di radiazione solare è così intenso da portare i micrometeoriti all'esterno del Sistema Solare [5, Burns et al., 1979], [73, Sykes et al., 2004]. Nel calcolo del flusso abbiamo però preso, come limite inferiore, particelle di dimensione di 5 μm di raggio perché l'articolo utilizzato per la calibrazione del modello ha come limite inferiore tale dimensione [45, Love et al., 1993].

I dati ottenuti dalle simulazioni vanno poi calibrati. Per calibrare il modello è necessario conoscere il numero di particelle che si trova nella Main Belt. Dal momento che in letteratura non sono state trovate informazioni utili ai nostri scopi, si è deciso di applicare il modello alla Terra e confrontare quindi questi risultati con la vasta letteratura a disposizione per la Terra. In particolar modo si è deciso di considerare, come valori di riferimento, le stime riportate da Love and Brownlee ([45, Love et al., 1993]).

In questo modo, con opportune modifiche descritte nel capitolo 4, si è riusciti a calibrare il modello e a confrontarlo con i dati forniti da Cintala.

Introduction

The aim of this research work is to give an estimate of the flux of micrometeoroids on Mercury. Such flux of material onto Mercury has several effect such as the formation of craters and also a change in a planet exosphere.

The exosphere is the section of the atmosphere where collisions among volatile species become negligible. In the case of Mercury, the exobase, namely the limit under which the collisions start to be important, is represented by the surface of the planet. This means that the sources and sinks of the exosphere are strongly linked to the composition and structure of the surface. A fraction of volatiles released into the exosphere is thought to be produced by impact vaporization of meteoritic material [8, Cremonese et al., 2005] [52, Marchi et al., 2005].

Meteoritic flux on Mercury depends on the particle size, because meteoroids with different size have different dynamical evolution. Meteoritic sizes smaller than about 1 cm follow a dynamical evolution dominated by Poynting-Robertson drag. On the other hand, particles with sizes larger than 1 cm follow a completely different dynamical evolution.

To understand the dynamical evolution of dust particles, we begin this work making a survey of interplanetary dust and the different forces which the dust grains are affected.

In the first chapter we discuss about the interplanetary dust. We discuss about the major sources of dust population in the Inner Solar System like comets and asteroids, this latter mainly comes from the Main Belt. Moreover we discuss about the production and loss processes of dust in the Inner Solar System like, for the first, Poynting-Robertson drag, fragmentation into dust due to particle-particle collisions, and direct dust production from comets and, for the second, dust collisional fragmentation, sublimation, radiation pressure acceleration, sputtering and rotational bursting. These processes are very important because they release dust compounds in the interplanetary medium. Also long-period comets are a source of out-of-ecliptic particles.

In the second chapter we give information about the Yarkovsky effect that is an effect connected with radiation phenomena in a rotating particle and that consists in a recoil pressure excess of the radiation emitted by the evening hemisphere over the morning hemisphere. This effect interests only particles that have size dimensions larger than cm and it is important to understand that this effect do not interests particles with size dimensions smaller than 1 cm because this particles are isothermal and there is no a thermal gradient that is necessary for the Yarkovsky effect.

In the third chapter we discuss about the Poynting-Robertson effect that is the main force that acts on dust particles smaller than 1 cm. Bodies in interplanetary space are not only attracted to the Sun by gravity, but are also repelled from it by radiation pressure due to the momentum carried in solar photons. Moreover, the orbit of such particles are also modified by the velocity-dependent Poynting-Robertson effect.

In the fourth chapter we introduce the dynamical evolution model of dust particles of Marzari and Vanzani (1994) in order to determine the meteoritic flux at the heliocentric distance of Mercury. This model numerically solves a (N+1) + M body problem (Sun + N planets + M body with zero mass) with the high-precision integrator RA15 (Everhart 1985). The solar radiation pressure and Poynting-Robertson drag, together with the gravitational interactions of the planets, are taken as major perturbing forces

affecting the orbital evolution of the dust particles. We pay particularly attention to the solar wind and radiation forces along the line of the Mie theory. The adopted numerical method to solve the equations of motion is the RA15 version of the RADAU integrator by Everhart. This numerical integrator is particularly accurate and suitable for modelling the orbital behaviour of dust particles.

In the fifth chapter we discuss about comets and why we do not consider, at present, this source of dust in our work.

In the sixth chapter we compare our model with other model and results given by literature. We introduce the BepiColombo mission and we compare our results with the preliminary study of the mission.

This work is very important because, with this dynamical evolution model, we are going to study the dynamical evolution of dust particles that arrive on Mercury. This is very important because the latest works about the dust particles evolution are made by Cintala, who summarizes in his article [7, Cintala, 1992] works made by Sekanina and Southworth, Leinert, Zook and Morgan. It is important to point out that in the Cintala work, he extrapolates the flux on the Mercury surface from the flux of the Moon.

Our study is also very important to understand the composition of the exosphere of Mercury because is thought that a fraction of volatiles released into the exosphere is produced by impact vaporization of meteoritic material.

Chapter 1

Interplanetary Dust

The major sources of the dust population in the Inner Solar System are comets and asteroids, but the relative contributions of these sources are not quantified. The production processes inward from 1 AU are: Poynting-Robertson drag, fragmentation into dust due to particle-particle collisions, and direct dust production from comets. The loss processes are: dust collisional fragmentation, sublimation, radiation pressure acceleration, sputtering and rotational bursting. These loss processes as well as dust surface processes release dust compounds in the ambient interplanetary medium.

The dust densities are considerably lower above the solar poles but Lorentz forces can lift particles of sizes less than 5 μm to high latitudes and produce a random distribution of small grains that varies with the solar magnetic field. Also long-period comets are a source of out-of-ecliptic particles.

The near-solar dust cloud is the central region of the meteoritic complex that evolves from the small bodies of our planetary system. Dust particles in the inner solar system produce the solar F-corona and the zodiacal light. Yet, these astronomical phenomena reveal only a part of the dust cloud in the inner solar system and especially do not yield sufficient information about the vicinity of the Sun.

The most reliable data exists for dust near 1 AU. Observational results in combination with knowledge about the dust sources justify and constrain the extrapolation of the dust distribution from 1 AU inward. This is valid for dust near the ecliptic plane [51, Mann et al., 2004].

1.1 Observational Evidence of Dust

1.1.1 Zodiacal light

Scattering of sunlight and thermal emission of dust particles produce the observed brightness, called zodiacal light for night-time observations pointing away from the Sun, and called solar F-corona in the vicinity of the Sun [40, Leinert et al., 1998]. It is well established that zodiacal light observations describe predominantly particles in the 1 to 100 μm size interval, which covers the approximate mass interval from 10^{-11} to 10^{-5} g.

Based on observational results it is possible to conclude that most of the dust outward from 0.3 AU is distributed in a flat, rotationally symmetric cloud that is concentrated near the ecliptic plane. The number density increases with decreasing distance from the Sun, roughly proportional to r^{-1}, where r is the distance from the Sun.

The average polarization and geometric albedo, as well as the spectral variation of the albedo change with distance from the Sun and with latitude. Variations of these derived average properties may stem from several effects: changes of single-particle properties, changes of the overall dust cloud composition, and changes of the size distribution [51, Mann, 2004].

1.1.2 Solar F-corona

The solar corona results from a smooth continuation of the zodiacal light brightness to small elongations of the line of sight. But the signal from the K-corona produced by Thomson scattering of electrons near the Sun has to be subtracted in order to derive the F-corona brightness [40, Leinert et al., 1998]. Moreover, the observations are hampered by the presence of coronal and atmospheric stray light and therefore F-corona observations are preferably made in the near infrared and during solar eclipses or with coronagraphs from space.

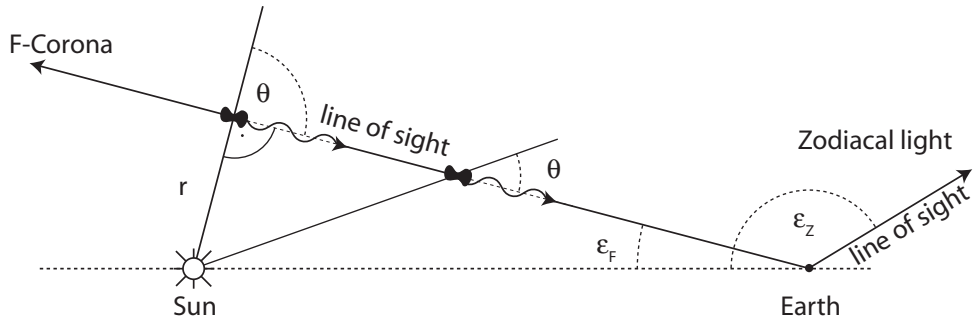

Figure 1.1: Geometry of zodiacal light and F-corona observations. Both phenomena are caused by the same physical effect: scattering of light and thermal emission from dust distributed along the line of sight (LOS), but are observed at different elongations, ϵ, of the LOS. In the figure r denotes the minimum distance from the Sun that is seen along the LOS with elongation ϵ. A sketch of the scattering pattern, i.e., intensity I of scattered light as function of scattering angle θ, is given in the upper part of the figure: dust particles close to the Earth contribute to the LOS brightness with enhanced scattering at small angles θ. Dust particles near Earth efficiently scatter the sunlight under small scattering angles toward the observer and therefore have a large contribution to the integrated LOS brightness. Note that in contrast to the depicted pattern for scattered light, thermal emission is isotropic, i.e., constant over θ. From Mann et al., "Dust Near the Sun "(2004).

The brightness that stems from dust near the Earth is scattered at small angles to reach the observer, while dust near the Sun is scattered at angles around 90° (see Figure 1.1). For particles in the $1-100\ \mu m$ size range the scattering is very efficient at small angle while light is less efficiently scattered at larger angles. It means that dust components near the observer yield a larger contribution to the F-corona than to zodiacal-light observations. This influence of dust near the observer makes observations in the near infrared more favorable because thermal emission from near-solar dust may contribute to the brightness.

The superposition of scattered light and thermal emission components can lead to a feature in the coronal brightness at the point where the line of sight crosses the dust-free zone. Due to this superposition, the appearance of the F-coronal brightness may depend on the material properties of dust. The appearance of an infrared feature is expected for a coronal brightness that consists to a significant amount of thermal emission, while the scattered light components tend to occult this features [63, Peterson, 1963] [46, Mann, 1992] [32, Kimura et al., 1998].

The F-corona polarization in the visible is close to zero indicating the predominance of forward-scattered light and possibly also a change of the polarization and geometric albedo with distance from the Sun.

The size range of observed particles may change in the F-corona compared to the zodiacal light here with causing a change of the average optical properties, but still the majority of observed particles are expected to have sizes larger than 1 μm, i.e., about 10^{-11} g [51, Mann et al., 2004].

1.1.3 Dust at high latitudes

It is well established that outward from about 0.5 AU the dust cloud is concentrated primarily in the ecliptic. Dust particles from long-period comets will form a spherical distribution with orbital inclinations distributed isotropically. This spherical component has half of its dust in retrograde orbits. The observed

distribution of sporadic meteors near Earth includes a small but noticeable component at high latitude and in retrograde orbits that can be described with isotropically distributed orbital inclinations. Also some models interpreting the visible zodiacal light assume an isotropic background component of dust, i.e., a spherical distribution of dust with orbital inclinations distributed isotropically [51, Mann et al., 2004].

1.2 Dust sources and orbital evolution

Interplanetary dust is a component of the small bodies in the solar system. The small bodies being closely related through mutual collisions and orbital dynamics, dust particles are the end product of what is ascribed as the "evolution of the meteoritic complex ". Dust particles are released from comets and asteroids or are produced by fragmentation of larger cometary or asteroidal fragments. Other components are Kuiper belt dust and interstellar dust. The contribution of interstellar dust inside 1 AU is smaller than in the outer Solar System [21, Grün et al., 1994].

We now restrict our discussion to the evolution of the dust cloud that is produced from comets and asteroids. Like meteoroids, the produced dust particles are initially in orbits with inclinations similar to those of their parent bodies. Parent body asteroids are in orbits with inclinations $i < 30°$ and eccentricities $e < 0.1$. Short period comets are in orbits with inclinations $i < 40°$ and eccentricities $e < 0.4$, long period comets have inclinations ranging from 0 to 180° with $N(i)di \propto \sin(i)di$ where $N(i)$ denotes the number of orbits between i and $i + di$ (i.e., spherical distribution in number density).

The major effects that determine the distribution of dust in interplanetary space are solar gravitation, the influence of magnetic fields, solar-radiation pressure and solar-wind pressure, including Poynting-Robertson effect and pseudo Poynting-Robertson effect, mutual collisions and the gravitational forces exerted by the planets. The radiation pressure force deflects small particles directly outward and they may leave the Solar System after they are ejected from a comet or formed by collision, the exact condition depending on the initial orbital parameters. Particles for which solar gravity amounts to more than twice the radiation pressure may stay in bound orbits. They form the main content of interplanetary dust cloud.

The radiation pressure influences the orbital evolution of this latter component mainly through the Poynting-Robertson effect. The momentum transfer caused by radiation falling onto a moving particle includes, when seen in the reference frame of the Sun, a small component anti-parallel to the particle's velocity that stems from the Lorentz transformation of radiation pressure force in the frame of the particle. This is the case for particles that move in orbital motion around the Sun and are exposed to the photon flux that is direct radially outward. The small deceleration that is induced by the anti-parallel component is denoted as the Poynting-Robertson effect. Thus a drift toward the Sun is superimposed on the motion in keplerian orbits and, just as collision do, limits the lifetime of the dust particles.

In addition to radiation pressure, bombardment with solar wind particles transfers momentum to the dust particles. The tangential component of this drag force gives rise to the so-called pseudo or plasma Poynting-Robertson effect. The plasma Poynting-Robertson effect varies with the plasma parameters and therefore depends on the latitude and on the solar activity [60, Mukai and Yamamoto, 1982].

Although the Poynting-Robertson effect may vary strongly with the size, composition, and structure of particles, the radial drift of the particles that it causes is small compared to the orbital velocities.

The deceleration of particles by the Poynting-Robertson effect reduces the eccentricities and semimajor axes of their orbits. This leads to an increase of dust number density with decreasing solar distance.

The Lorentz force acting on charged dust particles moving in the solar magnetic field moderately deflects the particles from their orbits. Depending on the local magnetic field direction, the particles are subsequently pushed to either lower or higher latitudes, which broadens the range of inclinations of the orbits but still the orbital inclinations are similar to those that are induced by the parent bodies. Also the gravity of the planets can deflect dust particles that closely encounter a planet in unbound and/or

high inclination orbits. But the influence of these processes on the overall spatial distribution of the dust cloud is small. While the inclinations of the majority of orbits are less affected, orbital perturbations by planets modify the arguments of the perihelia and the ascending nodes over time spans that are long compared to the orbital period. As a result, the particles essentially form a rotationally symmetric cloud [51, Mann et al., 2004].

1.3 Dust dynamics near the Sun

Although the overall distribution of dust in the Solar System seems stable on short time scales, the dust dynamics becomes complex in the vicinity of the Sun. Lorentz and radiation pressure forces increase since the solar magnetic field and the solar radiation increase and since dust particle may attain a higher electric surface charge. Particles that are only moderately deflected at large distances experience a significant change in their orbital inclination, even if the increase of surface charge is not taken into account. If the influence of the Lorentz force becomes even stronger, then particles can be deflected into randomly oriented orbits. The dust dynamics are also influenced by transient events, like the increasing solar wind drag during coronal mass ejection.

The calculations by Mann et al. [50, Mann et al., 2000] describe the dynamics of charged dust particles under solar magnetic field parameters that are derived from observations, the dust surface charge was estimated based on the influence of the solar wind and the solar photon flux. The derived distributions in latitude for small dust particles near the Sun is shown in Figure 1.2. Assuming an initial distribution with latitudes $\pm 30^\circ$, dust particles of size 25 μm will be scattered to latitudes $\pm 50^\circ$ at 10 $R_\odot$. Particles in the size range 0.52 μm show the strongest variation with the solar magnetic field. They reach latitudes of $\leq \pm 70^\circ$ for weak magnetic field and as high as $\pm 90^\circ$ for strong magnetic field.

Smaller silicate particles are almost randomly distributed at all phases of the solar cycle. Small carbon dust particles are ejected before their orbits can be randomized. Dust particles beyond 10 μm in size are only weakly influenced by the solar cycle magnetic field variations. In addition to the Lorentz force, radiation pressure becomes more important close to the Sun. The β-ratio, the ratio of radiation pressure force to solar gravitational force, increases when the sizes of particles are diminished either by sublimation or by collisional destruction. Radiation pressure can also lead to the formation of β-meteoroids that are ejected from the corona into hyperbolic orbits and leave the near-sun environment. The interplay of sublimation and increasing β-ratio for the diminished size of dust particles can lead to the formation of dust rings [51, Mann et al., 2004].

The near vicinity of the Sun is also the region where interactions of dust particles with the ambient interplanetary medium become particularly important. The principal effect of dust particles on the interplanetary medium and solar wind is to add neutral and ionized atoms to the environment. The neutral atoms are usually quickly ionized by solar UV, at which point they are picked up by the interplanetary magnetic field and carried outward with the solar wind as a distinct component of the solar wind called pick-up ions. While most of the pick-up ions are produced by ionization of neutral interstellar gas that penetrates the Solar System, dust particle interactions with the solar wind provide a second source that contributes a different mix of elements to the pick-up ion population.

The most direct mechanism by which dust particles can contribute to the pick-up ion population is by sublimation. Through sublimation neutral molecules and ions are released into the ambient interplanetary medium where most are quickly photo-ionized by the solar UV radiation and become pick-up ions.

Dust particles may also recycle solar wind particles into pick-up ions by adsorpition and desorption.

All pick-up ions, whether of interstellar or inner source origin, are identified by their distinct velocity distribution relative to the local solar wind speed as well as by their single charge state as opposed to highly charged solar wind ions [51, Mann et al., 2004].

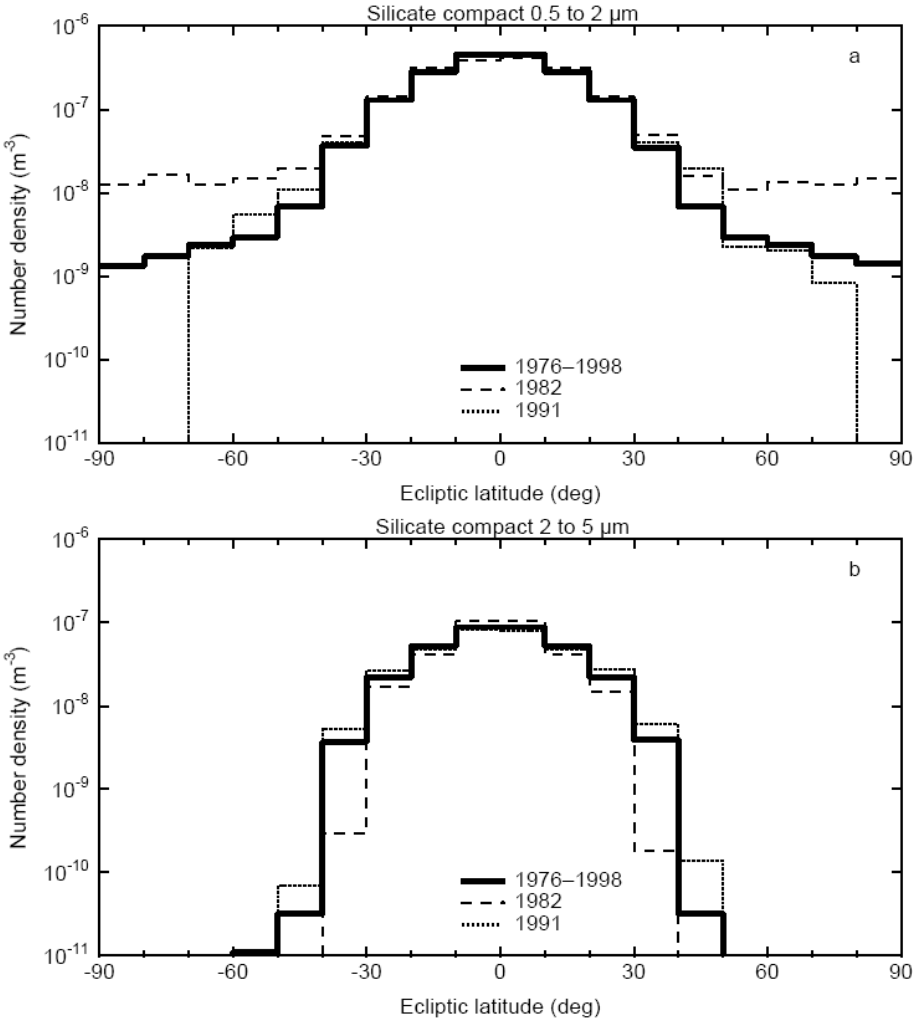

Figure 1.2: The variation of dust number density with latitude due to Lorentz force perturbations for compact silicate particles with an initial distribution $\pm 30°$. The solid line denotes an average profile for the entire solar cycle, the dashed line shows the profile for a strong magnetic field (1982) and the dotted line the profile for a weak magnetic field (1991). The upper figure shows particles with sizes 0.52 μm. The lower figure shows number densities for particles with sizes 25 μm. From Mann et al., "Dust Near the Sun "(2004).

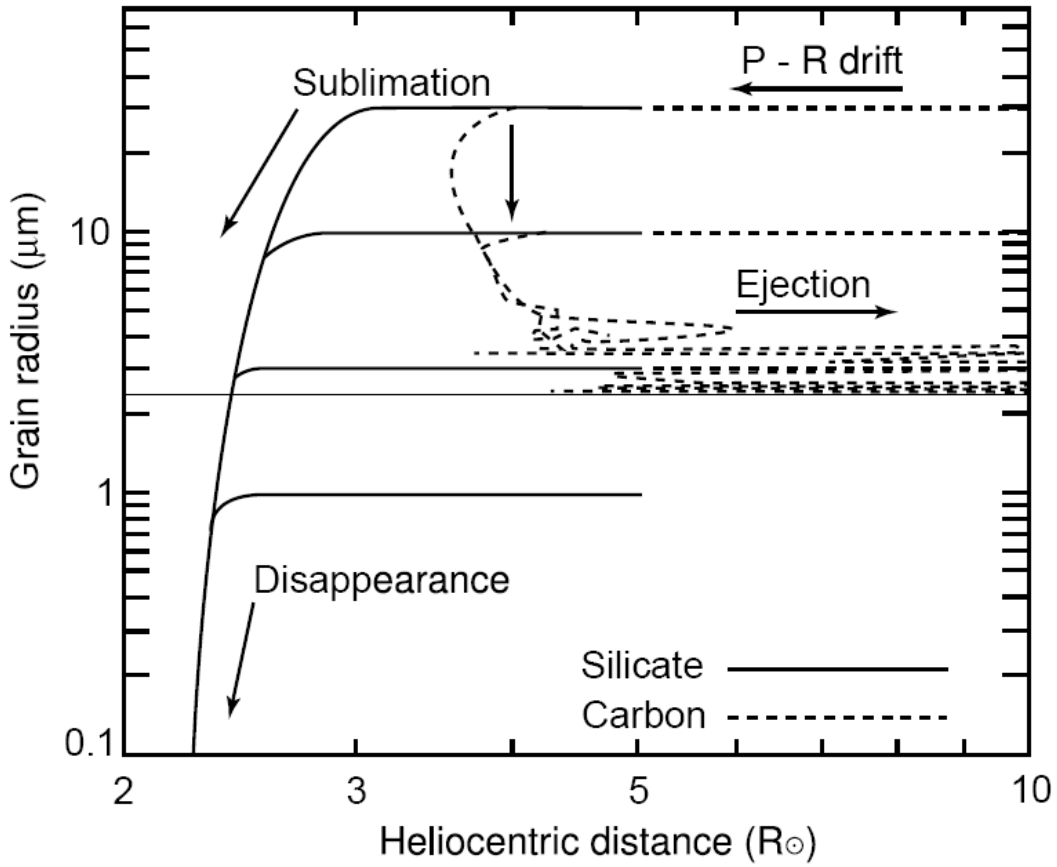

Figure 1.3: Dust ring formation depicted with the evolution of particle size vs. distance from the Sun for carbon particles (dashed lines) and silicate particles (thick solid lines). The change in distance from the Sun is caused by direct radiation pressure and Poynting-Robertson drift, respectively. While silicate particles disappear due to the sublimation, carbon particles are exposed to higher radiation pressure force compared to solar gravity once their size is reduced by sublimation. As a result they are pushed to larger distances and the sublimation rate decreases again until the Poynting-Robertson effect brings them inward to the sublimation zone again. The exact slope of this size-distance curve depends on the exact initial conditions but this interplay of radiation pressure and sublimation leads to an enhancement of dust number density at the sublimation zone. The thin horizontal line shows the size limit of carbon particles that are rejected by radiation pressure and cannot reach the vicinity of the Sun. From Mann et al., "Dust Near the Sun "(2004).

1.4 Mechanisms of Dust Destruction

1.4.1 Dust destruction at distances between 0.1 and 1 AU from the Sun

In-situ measurements at 1 AU and beyond indicate collisional destruction of dust in the inner Solar System. The dust experiment aboard Ulysses detected β-meteoroids, dust particles of sizes below 1 μm moving away from the Sun in hyperbolic orbits that are presumably collision fragments of larger particles [77, Wehry and Mann, 1999]. The analysis of radar head echoes produced by particles of sizes greater than 100 μm, on the other hand, shows an overabundance of ingoing particles compared to outgoing particles for orbits with small perihelia, which possibly indicates the collisional destruction of these particles in the inner Solar System. Collisional evolution causes a narrowing of the mass spectrum, i.e., the number of particles with masses $m > 10^{-6}$ g is strongly reduced. Small fragments may be removed by radiation pressure, which causes a reduction of particles in the 10^{-14} to 10^{-12} g interval. The location and the width of this gap depend on assumptions on the ratio of radiation pressure force to gravitational force [29, Ishimoto, 2000] [51, Mann et al., 2004].

1.4.2 Dust destruction at distances within 0.1 AU around the Sun

Russell (1929) was the first to estimate the drift of particles toward the Sun as a result of the Poynting-Robertson effect and to predict the presence of a dust free zone caused by sublimation of the dust particles near the Sun. Aside from sublimation, erosion through sputtering by solar wind particles [59, Mukai and Schwehm, 1981], and rotational bursting of grains are expected to destroy dust particles inward of 20 $R_\odot$ (approximately 0.1 AU) around the Sun.

Mie calculations for spherical dust particles have shown that particles with the absorption and scattering properties of FeO - poor obsidian, depending on their size, can exist very close to the Sun (up to 2 $R_\odot$) [36, Lamy, 1974].

Carbonaceous grains such as graphite and glassy carbon sublimate near 4 $R_\odot$. Model calculations for porous dust particles [47, Mann et al., 1994] have shown that depending on the amount of absorbing material versus silicate material (based on the optical properties of FeO - poor obsidian for the silicate) they can reach as close as 23 $R_\odot$ from the Sun. Pyroxene and olivine are the dominant forms of silicate minerals in interplanetary dust particles collected in the stratosphere of the Earth. Therefore numerical estimates of the dust sublimation in sungrazing comets were based on these materials. They show that pyroxene grains sublimate at 46 $R_\odot$ and olivine grains at 1013 $R_\odot$. The dust particles are also heated by solar wind sputtering. This process was shown to increase compared to heating by solar radiation with decreasing size of grains, but even for small grains it is small compared to the influence of solar radiation.

The disappearance of dust happens gradually with heliocentric distance, depending on the size and material composition of the dust particles and that the dust free zone is possibly not observed since it is in a region of the corona where the K-corona signal exceeds the F-corona signal.

In conclusion, inward from 10 $R_\odot$, dust destruction varies with size and material composition and may even vary with time, while the size distribution gradually varies between 0.1 and 1 AU. It is not clear whether the production or the destruction of dust is the predominant mechanism between 0.1 and 1 AU [51, Mann et al., 2004].

1.5 Dust production from comets

There are no direct measurements to estimate the dust sources inward from 1 AU but remote sensing observations point to the possibility of dust production from comets. While the production of centimeter sized and larger fragments was shown by infrared observations of cometary dust trails, optical observations of a cometary dust trail suggest that it consists of very dark (geometric albedo < 0.01) fragments of sizes

Material	**Sphere**	**Fluffy**	**Ref.**
Graphite	$\leq 5\ R_\odot$	$\leq 2\ R_\odot$	2, 3, 6, 8, 9
Glassy carbon	$4\ R_\odot$	$3-4\ R_\odot$	10, 11
Magnetite	$10-40\ R_\odot$	–	7
Iron	$11-24.3\ R_\odot$	–	4, 5
Water ice	$1-2.8\ AU$	–	2, 5, 7
FeO-poor obsidian	$1.9-7\ R_\odot$	$2.5-3\ R_\odot$	4, 6, 7, 8, 9, 10, 11
FeO-rich obsidian	$2.9-6\ R_\odot$	–	6, 9
Andesite	$9-10.5\ R_\odot$	–	3, 4, 5
Basalt	$6\ R_\odot$	–	9
Quartz	$1.5-4\ R_\odot$	–	1, 2, 5
Astronomical silicate	$14\ R_\odot$	–	9
Crystalline Mg-rich olivine	$10\ R_\odot$	$9.5-11\ R_\odot$	12
Amorphous Mg-rich olivine	$13.5-15.5\ R_\odot$	$12-15\ R_\odot$	12
Crystalline Mg-rich pyroxene	$5\ R_\odot$	$5\ R_\odot$	12
Amorphous Mg-rich piroxene	$5.5-6.5\ R_\odot$	$5-6.5\ R_\odot$	12

Table 1.1: The zone of sublimation calculated for different materials. References: (1) Over(1958); (2) Mukai and Mukai (1973); (3) Mukai et al. (1974); (4) Lamy (1974a); (5) Lamy (1974b); (6) Mukai and Yamamoto (1979); (7) Mukai and Schwehm (1981); (8) Mann et al. (1994); (9) Shestakova and Tambovtseva (1995); (10) Kimura et al. (1997); (11) Krivov et al. (1998); (12) Kimura et al. (2002). From Mann, I. et al., "Dust Near the Sun "(2004).

of a few centimeters [28, Ishiguro et al., 2002]. Due to their low albedo and low number density these fragments are not easily detected at visible wavelengths, but brightness observations in the inner Solar System were mainly made at visible wavelengths. At this point, it is not clear how large the contribution of these cometary fragments to the inner Solar System dust cloud could be. The dust fluxes that were measured from Helios show that the dust production cannot be significantly larger than the collisional losses between 0.3 and 1 AU [15, Fechtig, 1982]. Also brightness data indicate that the production most likely does not strongly exceed the dust destruction due to collisional fragmentation [51, Mann et al., 2004].

A contribution of dust production near the Sun, inside 0.1 AU, is the appearance of sungrazing comets.

The dust supply from a comet can be comparable to the dust densities in the solar environment, but, due to the fact that the coronal brightness stems to a large amount from dust components near the Earth rather than near the Sun, this does not necessarily cause an observable variation of the coronal brightness [50, Mann et al., 2000]. The sungrazing comets that are frequently observed with SOHO/LASCO neither cause a variation of the corona brightness nor do they provide a significant dust source.

The brightness distributions of the Kreutz comets detected with SOHO/LASCO indicate an increasing number of comets with decreasing size and the size distribution of nuclei is probably described with a power law.

The Kreutz group sungrazing comets have perihelion distances q in a range $0.004 < q < 0.01\ AU$, eccentricities $e \approx 1$ and inclinations $128 < i < 145°$. For an estimate of the dust supply, Mann et al. assume a spherical comet of 20 m radius is fragmented into 10 μm spherical particles and distributed in a sphere of 10 $R_\odot$ radius. An estimated number density of $10^{-17}\ cm^{-3}$ is found, which is below typical densities of $10^{-14}\ cm^{-3}$ for particles of this size range. Mann et al. assumed this large size of dust grains, since for size distributions that are similar to that in the interplanetary dust cloud, the majority of mass would be contained in fragments of this size. But analysis of the dust tails of sungrazing comets shows that the sungrazers emit small particles of sizes $a = 0.1\ \mu m$ and that the dust in the sungrazing comets has a narrow size distribution [67, Sekanina, 2000].

The dust that is produced by sungrazers will quickly leave the solar corona. The Kreutz comets are in highly elliptic or hyperbolic orbits, their speed is approximately 230 $\frac{km}{s}$ at 7 $R_\odot$ and can be described as bodies with initial speeds of zero at infinity that fall into the Sun. Dust grains released

from the sungrazers are in similar orbits. Sungrazing comets of the Kreutz group form two sub groups based on different perihelion distances and ascending nodes [53, Marsden, 1967]. From SOHO/LASCO observations, a further comet group with currently 33 members (Meyer group) and two groups with 14 members each (Marsden group, Kracht group) were identified in near-Sun orbits. The perihelion distances and inclinations of the three groups are 0.036 AU and 72.4°, 0.047 AU and 27.4°, and 0.047 AU and 13.6°, respectively, where each value is the mean weighted by the total observational time. The size of these comets is likely to be similar to the Kreutz family fragments SOHO sees, but because of the larger perihelion distances, the smallest members of the groups are probably not detected.

The dust supply from the frequently observed sungrazing comets is negligible. The dust supply from larger comets near the Sun can produce dust density enhancements that are comparable to the dust densities in the solar environment [51, Mann et al., 2004].

Chapter 2

Forces on big particles in the Solar System

A specific effect connected with radiation phenomena in a rotating particle consists in a recoil pressure excess of the radiation emitted by the evening hemisphere over the morning hemisphere. The temperature pattern is skewed by the particle's rotation in concert with thermal lags; this can be viewed as an evening hemisphere that on the average is slightly warmer than the morning hemisphere, just as on planets. The warmer evening hemisphere radiates more energy, and hence momentum, than the cooler morning hemisphere. The reaction force due to the absorbed and reemitted radiation is found by integrating over the entire surface; in general the reaction force will have a transverse component analogous to the nongravitational forces which perturb cometary orbits (but, of course, the latter forces are produced by outgassing of volatiles rather than by emitting radiation). Figure 2.1 depicts the essentials of this effect. One can anticipate that the force may involve the particle's rotation rate, thermal properties and dimensions, as well as the solar distance [5, Burns et al., 1979] [62, Öpik et al., 1951] [64, Peterson, 1976].

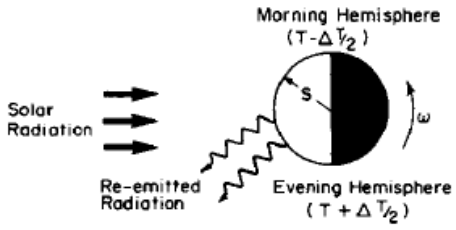

Figure 2.1: The Yarkovsky effect. The evening hemisphere radiates extra energy and momentum because it is hotter than the morning hemisphere. For prograde rotation as shown, the particle is thrust forward the momentum carried away in the reemitted radiation. From Burns. et al., "Radiation Forces on Small Particles in the Solar System "(1979).

The computation of the force will require a knowledge of the surface temperature on a rotating atmosphereless sphere of radius s having thermal diffusivity $\kappa = \frac{K}{\varrho C}$, where ϱ is the mass density, K is thermal conductivity, and C is specific heat. It is useful to distinguish particles that are rotating rapidly from those spinning slowly, because the thermal distributions, both in the interior and on the surface, in the two cases are qualitatively different.

The surface temperature of an element in sunlight is determined by a balance of the absorbed solar energy with the surface reemission plus that conducted to the interior.

A schematic diagram of the surface temperatures for the fast and slow cases is given in figure 2.2.

Starting on the left of the figure, at noon the temperature is at its peak and slowly decreases as

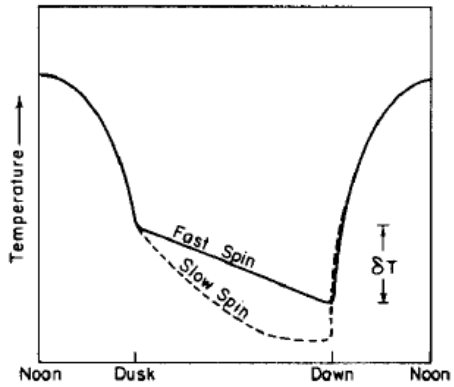

Figure 2.2: Sketch of the surface temperature on a rotating body. The fast rotation case is the solid line while the slow rotation case is the dotted curve. From Burns. et al., "Radiation Forces on Small Particles in the Solar System "(1979).

the solar elevation drops, since in this region the surface layers are in equilibrium with the solar flux. Beginning at dusk the surface cools by radiation so that the interior conducts its warmer heat there. At fast spins the temperature decay at night is essentially linear, the achieved δT being proportional to rotation period P. However, if the object rotates slowly enough, interior temperatures drop to the point where heat can be efficiently conducted through from the front; this causes the curve for slow spin to start to turn up near down. It would be symmetric for a nonrotating particle. Thus the maximum asymmetry on the night side will occur at spins near the transition between the slow and the fast rotation cases. Once dawn is reached, T grows quickly as equilibrium with the incoming radiation is sought. The morning surface temperature on rapidly spinning particles is cooler than with slow ones because in the fast case the temperature is not yet in equilibrium and appreciable heat is still being carried toward the center.

When an object falls into the rapid rotation class, its temperature fluctuations, as it turns in the sunlight, are restricted to surface layers, while in the slow spin case they penetrate deeply the particle's interior [5, Burns et al., 1979].

We take the size dividing these cases to be $s = h$ where h is the characteristic thickness traversed by a thermal pulse during half the rotation period $\frac{P}{2} = \frac{\pi}{\omega}$. To estimate h, we make use of the Green's function, which is the solution to a partial differential equation where a delta function is the source term. For the heat equation, the Green's function for the temperature T exhibits the characteristic manner in which T decays with time t and distance L. Since the Green's function contains the term $e^{\frac{-L^2}{\kappa t}}$, the interior temperature is damped to e^{-1} the surface value at an approximate depth L of $2(\kappa t)^{\frac{1}{2}}$.

Thus when considering the temperature fluctuations on a rotating particle, we are dealing only with a surface effect if the particle has a radius larger than the characteristic penetration depth of a thermal wave, i.e., if $s > (2\kappa P)^{\frac{1}{2}}$.

Typical values for the material parameters of most silicates that form the surface layers of the Earth are $C = 10^7\ ergs\ K^{-1}\ g^{-1}$, $\varrho = 2.5\ g\ cm^{-3}$, $K = 3.5 \cdot 10^5\ ergs\ K^{-1}\ cm^{-1}\ sec^{-1}$. Then for stony bodies the criterion distinguishing surficial from total heating is

$$h \geq 0.2 P^{\frac{1}{2}}\ cm\,, \tag{2.1}$$

with P in seconds. For metal-rich objects, we choose $C = 5 \cdot 10^6\ ergs\ K^{-l}\ g^{-1}$, $\varrho = 8.0\ g\ cm^{-3}$, $K = 4 \cdot 10^6\ ergs\ K^{-l}\ cm^{-1}\ sec^{-1}$, in which case the criterion reads

$$h \geq 0.5 P^{\frac{1}{2}}\ cm\,. \tag{2.2}$$

If we take P to be the rotation period of the smallest observed asteroids ($d \geq 1\ km$), all of which have periods in excess of several hours. We expect interplanetary boulders to spin even faster than asteroids

owing to the increased importance of collisions for smaller objects. If the surface layers of the particles are not solid but instead are rather porous or textured, as for a regolith, the right-hand sides of (2.1) and (2.2) are significant overestimates of the critical size [5, Burns et al., 1979].

2.1 Temperatures changes on rapidly rotating bodies

When the thermal effect is confined to the surface layers (i.e., $h < s$), the temperature change during a rotation may be estimated by equating the energy received with that stored in the volume contained in a thermal penetration depth h. During a complete rotation the energy striking an equatorial strip of unit height is $2sSP$. Thus for surface material with albedo δ the energy absorbed per rotation period by a unit area surface element on the equator is $(1-\delta)\frac{SP}{\pi}$. The internal energy which is added to the thermal penetration layer during a temperature rise of ΔT is $\varrho hC\Delta T \approx 2\Delta T(\frac{\pi K\varrho C}{\omega})^{\frac{1}{2}}$. Equating these, the typical temperature fluctuation within the thermal penetration depth for a rapidly rotating object is [5, Burns et al., 1979]

$$\Delta T \approx (1-\delta)\gamma S\left(\frac{P}{2\pi}\right)^{\frac{1}{2}}, \tag{2.3}$$

where the inverse thermal inertia γ is $(K\rho C)^{-\frac{1}{2}}$. Using the values for the parameters given previously, the temperature difference felt over the surface of a rapidly spinning stony body would be

$$\Delta T \approx \frac{1}{5}\frac{P^{\frac{1}{2}}}{R^2}, \tag{2.4}$$

and for iron,

$$\Delta T \approx \frac{1}{25}\frac{P^{\frac{1}{2}}}{R^2}. \tag{2.5}$$

2.2 Yarkovsky force for rapid rotation case

The Yarkovsky force results from the fact that the dusk-to-midnight portion radiates more than the midnight-to-dawn side while the dawn-to-noon area absorbs more radiation than does afternoon side. We idealize the actual temperature distribution by considering the entire evening hemisphere to be at a temperature $T + \Delta T/2$ whereas the morning hemisphere is at $T - \Delta T/2$, where ΔT is given by (2.3). For the force consider a surface element dA at temperature T, radiating isotropically into one hemisphere with intensity I. The outward energy flux is $\int I\cos\nu d\chi = \pi I = \sigma T^4$, where ν is the angle with respect to the surface normal, χ is solid angle, and σ is the Stefan-Boltzmann constant; we assume the surface emissivity $\epsilon(\lambda) \approx 1$. Then the radiation reaction upon the element, normal to its surface, is [5, Burns et al., 1979]

$$dF = \int (I\cos\nu)(\cos\nu dA)\frac{d\chi}{c} = \frac{2}{3}\sigma T^4\frac{dA}{c}. \tag{2.6}$$

For a spherical particle of radius s having the assumed surface temperature with $\frac{\Delta T}{T} \ll 1$, the transverse reaction force in the orbit plane, that is the Yarkovsky force, resulting from the excess emission on the evening side is computed to be

$$F_Y = \frac{8}{3}\pi s^2\frac{\sigma T^4}{c}\frac{\Delta T}{T}\cos\zeta, \tag{2.7}$$

ζ is the particle's obliquity, the angle between its rotation axis and orbit pole. Note that this perturbation force can be either positive or negative, depending on whether the particle rotates prograde ($0 < \zeta < \frac{\pi}{2}$) or retrograde ($\frac{\pi}{2} < \zeta < \pi$), respectively. If the rotation is retrograde, the particle's leading hemisphere has a larger force on it than the trailing side and so the Yarkovsky force then adds to the Poynting-Robertson drag, causing a faster inward spiral. However, for prograde rotation the Yarkovsky force , opposes the Poynting-Robertson force and, if large enough, can actually produce outward spiraling [5, Burns et al., 1979].

2.3 Yarkovsky force for slowly rotating bodies

In the slow rotation case the temperature on the night side at the start drops linearly with time. In this region equation (2.3) will represent ΔT if the rotation period P is replaced by the thermal penetration time $\tau = \frac{s^2}{2\kappa}$ from $s > (2\kappa P)^{\frac{1}{2}}$; this decreases the effect over what it would be if the fast spin condition were still satisfied. The Yarkovsky force is further reduced due to the shifted location of the asymmetry in the reradiation and the absorption; as slower and slower rotations are considered, the radiation and absorption patterns become more and more symmetrical with respect to the direction along which the radiation arrives [5, Burns et al., 1979].

After this discussion, it is important to note that the Yarkovsky force depends upon the body's composition, such that the maximum perturbation on a stony object is five times that on an iron. Thus the orbital evolution timescales may differ for stony and iron object.

Chapter 3

Radiation forces on small particles in the Solar System

In general, the motion of small particles in space over short times is dominated by the gravitational force of the Sun. Over long times, the dynamical evolution of such bodies is commonly produced by non gravitational forces because these change a body's total mechanical energy and angular momentum.

Radiation pressure and Poynting-Robertson drag in the Solar System are significant only for particles with size range 10^{-2} e 10^{-8} m.

Afterwards we provide a derivation of the radiation pressure and Poynting-Robertson drag felt by a perfectly absorbing particle, and after with a scattering particle [5, Burns et al., 1979].

3.1 Radiation pressure and Poynting-Robertson drag

3.1.1 Perfectly absorbing particles

The force on a perfectly absorbing particle due to solar radiation can be viewed as composed of two parts:

- radiation pressure;
- mass-loading drag.

The total amount of energy intercepted per second from a radiation beam of integrated flux density S ($ergs\ cm^{-2}s^{-1}$) by a stationary, perfectly absorbing particle of geometrical cross section A is SA. If the particle is moving relative to the Sun with velocity $\mathbf{v}$, we replace S by [5, Burns et al., 1979]

$$S' = S\left(1 - \frac{\dot{r}}{c}\right), \tag{3.1}$$

where $\dot{r} = \mathbf{v} \cdot \hat{\mathbf{S}}$ is the radial velocity, $\hat{\mathbf{S}}$ is a unit vector in the direction of the incident beam, and c is the speed of the light. The factor in parentheses is due to the Doppler effect, which alters the incident energy flux by shifting the received wavelengths.

The momentum removed per second from incident beam as seen by the particle is $\frac{S'A}{c}\hat{\mathbf{S}}$.

The absorbed energy flux $S'A$ is continuously reradiated from the particle. Since the reradiation is nearly isotropic, because small particles are effectively isothermal, there is no net force exerted thereby on the particle in its own frame.

However, the reradiation is equivalent to a mass loss rate of $\frac{S'A}{c^2}$ from the moving particle, which has velocity $\mathbf{v}$ as seen from the inertial frame of the Sun, and, as measured in the solar frame, this gives rise

to a momentum flux from the particle of $-\frac{S'A}{c^2}\mathbf{v}$. Since the particle is losing momentum while its mass is in fact always conserved, the particle is decelerated and so it suffers a dynamical drag.

The net force on the particle is then the sum of the forces due to the impulse exerted by the incident beam and the momentum density loss from the moving particle or for a particle of mass m

$$m\dot{\mathbf{v}} = \left(\frac{S'A}{c}\right)\hat{\mathbf{S}} - \left(\frac{S'A}{c^2}\right)\mathbf{v} \cong \left(\frac{S'A}{c}\right)\left[\left(1-\frac{\dot{r}}{c}\right)\hat{\mathbf{S}} - \frac{\mathbf{v}}{c}\right] . \tag{3.2}$$

This expression is the Robertson equation [5, Burns et al., 1979].

3.1.2 Scattering particles

A small spherical particle of geometrical cross section A will scatter an amount of light equivalent to that incident on an area AQ_{sca}, and absorb that incident on AQ_{abs}, where Q_{sca} and Q_{abs} are defined as the scattering and absorption coefficients, respectively. They correspond to the fractional amounts of energy scattered and absorbed. For a given particle, Q_{sca} and Q_{abs} depend on wavelength.

The scattering diagram resulting from unpolarized light incident on a spherical particle has rotational symmetry about the radial direction $\hat{\mathbf{S}}$. The intensity of the scattered light thus depends only on the angle α it makes with the incident beam direction (where $\alpha = 0$ corresponds to forward-scattering). The energy scattered into the incremental solid angle annulus $d\chi = 2\pi \sin\alpha d\alpha$ in the direction α is proportional to $f(\alpha)d\chi$, where $f(\alpha)$ is the phase function of the scattering particle, normalized so that $f(\alpha)d\chi$ integrated over all directions is unity. Then the net energy flux anisotropically scattered per second into the forward direction is $S'AQ_{sca}\langle\cos\alpha\rangle\hat{\mathbf{S}}$, where the anisotropy parameter is [5, Burns et al., 1979]

$$\langle\cos\alpha\rangle = \int_{4\pi} f(\alpha)\cos\alpha d\chi\,. \tag{3.3}$$

When the scattering on the average is in the direction of the beam, $\langle\cos\alpha\rangle$ is a positive number whereas it is negative for reflected radiation. The radiation pressure coefficient,

$$Q_{pr} = Q_{abs} + Q_{sca}(1 - \langle\cos\alpha\rangle)\,, \tag{3.4}$$

will appear in the expressions for the forces felt by particles having general optical properties. For a stationary particle (at least) this factor multiplies the incident momentum flux to transform it into the radiation pressure force. In perfect forward-scattering, $Q_{pr} = Q_{abs}$; with isotropic scattering, $Q_{pr} = Q_{abs} + Q_{sca}$; while for perfect back-scattering, $Q_{pr} = Q_{abs} + 2Q_{sca}$.

At the top of Figure (3.3) we consider particle of mass m, moving with velocity $\mathbf{v}$, is struck by a beam of projectiles, M per second, which travel relative to the stationary frame with velocity c.

In the middle panel of Figure (3.3), the same scene is viewed one second after the first projectile in the stream strikes m. In the meantime $M' = M(1 - \frac{v\cos\xi}{c})$ mass has collided with m. A fraction fM' of this mass has been absorbed but it is continuously remitted (or, equivalently, isotropically scattered) so as to keep the particle's mass m constant. The remaining mass gM' which strikes the particle leaves it with the same relative vector velocity with which it arrived. This mean that, if forward-scattered, gM' passes directly through m while, if back-scattered, it undergoes perfect reflection.

$\Delta\mathbf{V}$ per second in the direction of the beam's original momentum is the acceleration due to the radiation pressure whereas $\Delta\mathbf{v}$ per second along particle's velocity vector is the deceleration due to mass loading. Conservation of linear momentum in the x and y directions will provide $\Delta\mathbf{V}$ and $\Delta\mathbf{v}$ [5, Burns et al., 1979].

Equating the momentum in the y direction before and after the interaction, we have

$$mv\sin\xi = (m + fM')(v + \Delta v)\sin\xi + gM'[\mp v\sin\xi + v\sin\xi]\,, \tag{3.5}$$

where the top sign corresponds to forward-scattering and the bottom sign to back-scattering. The first part of the bracketed term is then the vertical velocity of the scattered beam as measured relative to the

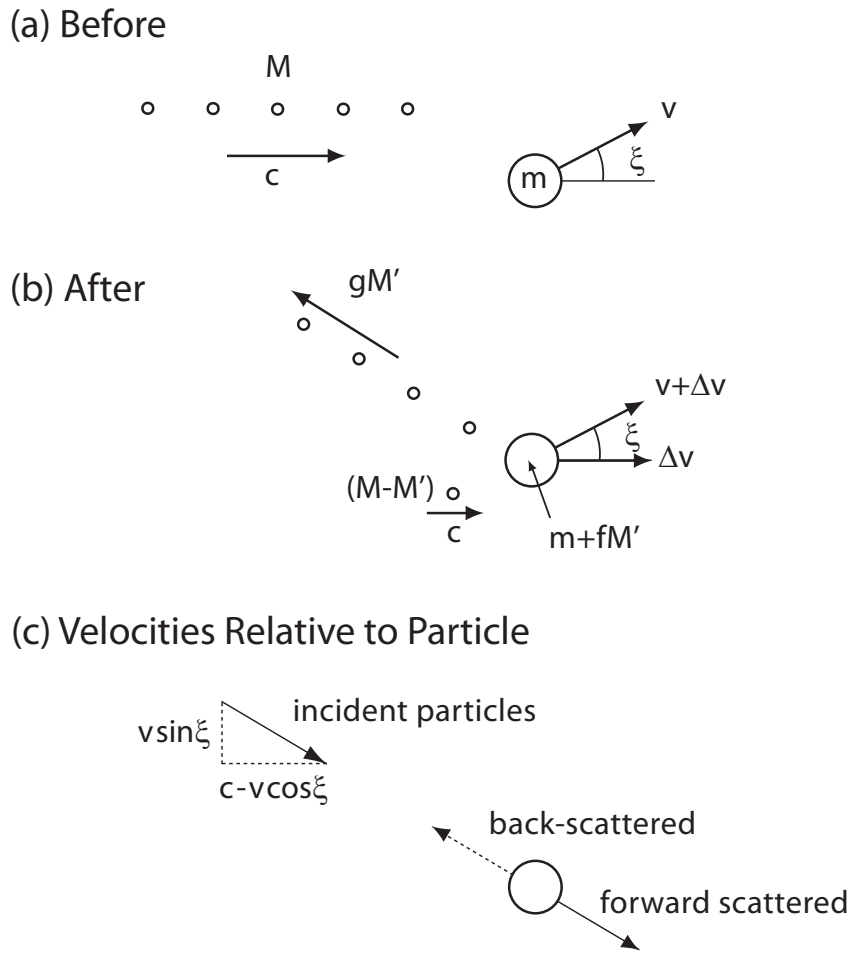

Figure 3.1: A nonrelativistic model to demonstrate radiation pressure and Poynting-Robertson drag. (a) The top diagram shows a beam of projectiles on its way to strike a particle. (b) A fraction fM' of the projectiles has been absorbed and then isotropically reemitted (or isotropically scattered). The remainder gM' is either forward-scattered or back-scattered; here it is shown back-scattered. (c) The interaction as viewed from the particle where only the incident and the scattered radiation are seen. From Burns et al., "Radiation Forces on Small Particles in the Solar System"(1979).

particle; in magnitude, it is the y component of the received velocity according to the particle [5, Burns et al., 1979].

Realizing that $f + g = 1$ and assuming that $\Delta v << v$ and $\Delta v << c$ and that $M << m$, we have that

$$\Delta v = -(1 \mp g)\frac{M'v}{m}\,. \tag{3.6}$$

This slowing of the particle along its path is caused by a mass-loading drag.

We can now determine ΔV in the same way from conservation of the momentum in the x direction

$$Mc + mv\cos\xi = (m + fM')[(v + \Delta v)\cos\xi + \Delta V] + gM'[\pm(c - v\cos\xi) + v\cos\xi](M - M')c\,. \tag{3.7}$$

Using the same approximations as for the drag case and substituting for Δv, we have

$$\Delta V = (1 \mp g)\frac{M'c}{m}\,, \tag{3.8}$$

this is produced by the momentum in the beam. It is the radiation pressure in the case where the impacting beam is composed of photons.

The total effect of the projectile beam can be found by vectorially adding the two velocity changes

$$\Delta V + \Delta v = (1 \mp g)\frac{M'}{m}(c\hat{\mathbf{S}} - \mathbf{v})\,. \tag{3.9}$$

The transference of this result from colliding material objects to the case when radiation instead strikes a particle is direct, since we can associate $\mp g$ with $-Q_{sca}\langle\cos\alpha\rangle$ and $f + g = 1$ with $Q_{abs} + Q_{sca}$; we note however that, owing to diffraction, $Q_{abs} + Q_{sca}$ need not be unity for microscopic particles. Any directly transmitted radiation is the same as scattered radiation with $\langle\cos\alpha\rangle = 1$. Therefore from equation (3.4) we have that

$$\mathbf{F}_{rad} = m\dot{\mathbf{v}} = Q_{pr}M'(\mathbf{c} - \mathbf{v})\,, \tag{3.10}$$

where M' is the mass of the photons which strike the particle or $\frac{S'A}{c^2}$. In the above form, the radiation force can be viewed as a drag force caused by the relative velocity, $\mathbf{c} - \mathbf{v}$, of the particle through a beam of photons. Finally, to terms of order $\frac{v}{c}$, we can write the net force on the particle as

$$m\dot{\mathbf{v}} \cong \frac{SA}{c}Q_{pr}\left[\left(1 - \frac{\dot{r}}{c}\right)\hat{\mathbf{S}} - \frac{\mathbf{v}}{c}\right]\,. \tag{3.11}$$

For heliocentric particles with $\mathbf{v} = \dot{r}\hat{\mathbf{r}} + r\dot{\vartheta}\hat{\vartheta}$, where $\hat{\mathbf{r}} = \hat{\mathbf{S}}$ is the orbital radius unit vector and $\hat{\vartheta}$ is normal to $\hat{r}$ in the orbit plane, we can also write the radiation force as

$$m\dot{\mathbf{v}} \cong \frac{SA}{c}Q_{pr}\left[\left(1 - 2\frac{\dot{r}}{c}\right)\hat{\mathbf{r}} - \frac{r\dot{\vartheta}}{c}\hat{\vartheta}\right]\,. \tag{3.12}$$

Perfect transmission occurs when $Q_{pr} = 0$. Complete absorption, the case considered by Robertson (1937), has $Q_{pr} = Q_{abs} = 1$. An isotropically scattering particle, such as a perfect reflector, has $Q_{pr} = Q_{abs} + Q_{sca}$. A particle which perfectly backscatters undergoes twice the drag of a totally absorbing or a perfectly reflecting particle. This happens because electromagnetic momentum is carried by the back-scattered beam in the direction of the particle's motion since its component in that direction is due to the angle $\frac{2v}{c}$ of reflection; this momentum is withdrawn from the particle's motion. A stationary particle feels a radiation pressure without a Doppler shift and, of course, has no Poynting-Robertson drag [5, Burns et al., 1979].

3.2 Expressions of radiation forces using special relativity transformations

In the previous section the forces derived presume the particle's mass to be constant; it remains the same even though the body is continually radiating energy (and therefore mass) because the body absorbs just as much energy. If we consider a particle that is not in thermal equilibrium and which is radiating into free space, its mass decreases. The loss of mass occurs at precisely the correct rate so that, considering momentum loss, the particle velocity stays constant, permitting the principle of relativity to be satisfied.

For any particle in thermal equilibrium, the energy radiated away carries with it mass and linear momentum in exactly the ratio needed to conserve the particle's linear momentum density (i.e., velocity). On the other hand, the absorbed radiation brings in only mass and not a concomitant increase in transverse momentum. This added mass burdens the particle so that it slows down.

The Poynting-Robertson drag takes place because the momentum in the incoming and outgoing radiation equilibrium is not the same: any body in thermal equilibrium will suffer a decelerating drag [5, Burns et al., 1979].

To find the forces experienced by a particle of constant mass moving through a beam of radiation, we use the principle of conservation of total linear momentum, including electromagnetic in addition to mechanical momentum. We can calculate the electromagnetic momentum added per unit time to the beam; this must be equal the mechanical momentum lost per unit time by the particle.

The following transformation law for the four-vector of momentum-energy is used:

$$\begin{aligned} p_x &= p_{x'} \\ p_y &= p_{y'} \\ p_z &= \gamma \left[p_{z'} + \frac{v}{c} \frac{E'}{c} \right] \\ p_4 &= i\frac{E}{c} = i\gamma \frac{E' + v p_{z'}}{c} , \end{aligned} \tag{3.13}$$

where $\gamma = (1 - \frac{v^2}{c^2})^{-\frac{1}{2}}$ and $i = \sqrt{-1}$. The primed quantities are measured in a frame of reference which moves with a velocity v along the positive z axis.

Since the particle velocities relative to the Sun are small in comparison to the speed of light c, we will consider two separate cases:

- the particle moving with a purely transverse velocity v relative to the beam;
- the particle moving with a purely radial motion u

and then add the results from them together [5, Burns et al., 1979].

3.2.1 Transverse motion

The case of a purely transverse motion corresponds to a particle on a perfectly circular orbit, ignoring the centrifugal acceleration.

The figure 3.2 shows the solar frame centered on the Sun and the other frame attached to the particle which moves with uniform velocity v in the tangential direction z.

As seen by solar observer when a radiation beam of energy flux E_i strikes the particle, the incoming four-vector of momentum-energy flux contained in it is

$$\mathbf{p}_i = \left(p_x, p_y, p_z, i\frac{E}{c} \right) = \left(-\frac{E_i}{c}, 0, 0, i\frac{E_i}{c} \right) , \tag{3.14}$$

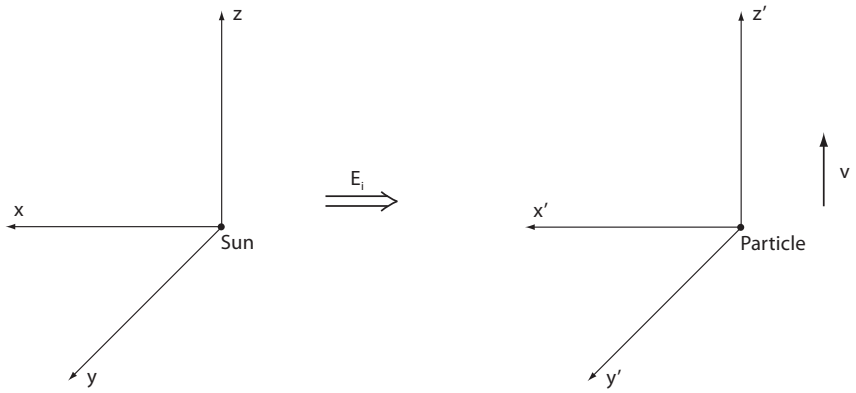

Figure 3.2: The frame of reference attached to the particle moves with transverse velocity **v** in the z (z') direction relative to the frame of reference attached to the Sun. E_i is the energy per second striking the particle as seen by an observer on the Sun. From Burns et al., "Radiation Forces on Small Particles in the Solar System"(1979).

where the first three components of the row vector are the x, y, z momentum fluxes while the fourth is the energy flux in momentum units. According to an observer on the particle, this vector is

$$\mathbf{p}_i' = \left(p_{x'}, p_{y'}, p_{z'}, i\frac{E'}{c}\right) = \left(-\frac{E_i}{c}, 0, -\gamma E_i \frac{v}{c^2}, i\gamma\frac{E_i}{c}\right) , \tag{3.15}$$

by a direct application of the transformation law (3.13). We note that the beam's trajectory makes an angle with respect to the x axis of $\psi = \tan^{-1}(\frac{p_z}{p_x}) = \frac{\gamma v}{c}$ as seen by the particle.

This then is the radiation which strikes the particle. some is scattered, some is absorbed to be immediately reemitted isotropically, and the rest passes directly through [5, Burns et al., 1979].

The outgoing radiation leaving the vicinity of the particle has a four-vector momentum flux of

$$\mathbf{p}_0' = \left(-\frac{E_i}{c}(1-Q_{pr}), 0, -\gamma\frac{E_i v}{c^2}(1-Q_{pr}), i\gamma\frac{E_i}{c}\right) , \tag{3.16}$$

as seen by an observer in the particle's frame of reference. Equation (3.13) permits this to be transformed at once to the outgoing momentum flux as seen in the solar frame,

$$\mathbf{p}_0 = \left(-\frac{E_i}{c}(1-Q_{pr}), 0, \gamma^2 E_i \frac{v}{c^2}Q_{pr}, i(1+\gamma^2 Q_{pr}\frac{v^2}{c^2})\frac{E_i}{c}\right) . \tag{3.17}$$

Equations (3.14) and (3.17) express the interaction of the radiation beam with the particle as seen from a specific frame of reference. Since the system is isolated, any change in the electromagnetic momentum flux must be directly associated with a change of opposite sign in the particle's mechanical momentum flux. But the change per unit time in the linear mechanical momentum of the particle is equal to a force. The force felt by a transversely moving particle, then, is minus the four-vector momentum loss per unit time from the beam, or

$$\mathbf{F}_v = -\Delta\mathbf{p} = \mathbf{p}_i - \mathbf{p}_0 = \left[-Q_{pr}\frac{E_i}{c}, 0, -Q_{pr}\frac{E_i}{c}\gamma^2\frac{v}{c}, -iQ_{pr}E_i\gamma^2\frac{v^2}{c^3}\right] , \tag{3.18}$$

in which $E_i = SA$.

The x term, since it is radial, is the radiation pressure force while the z term is the tangential Poynting-Robertson drag. Although it might appear that energy is not conserved because of the beam's energy gain expressed by minus the fourth component of (3.18), this added energy is lost from the particle's kinetic energy: $\Delta E_{beam} = \mathbf{F}\cdot\mathbf{v} = F_z v$ [5, Burns et al., 1979].

3.2.2 Parallel motion

We now consider the particle to be moving with velocity u in the direction of the radiation beam. The same approach used for the transverse motion. The four-vectors of momentum energy flux are

$$\mathbf{p}_i = \left[0, 0, \frac{E_i}{c}, i\frac{E_i}{c}\right], \tag{3.19}$$

$$\mathbf{p}'_i = \left\{0, 0, \frac{E_i}{c}\left[\left(1-\frac{u}{c}\right)\left(1+\frac{u}{c}\right)\right]^{\frac{1}{2}}, i\frac{E_i}{c}\left[\left(1-\frac{u}{c}\right)\left(1+\frac{u}{c}\right)\right]^{\frac{1}{2}}\right\}, \tag{3.20}$$

and the outgoing four-vectors of momentum-energy flux are

$$\mathbf{p}'_0 = \left\{0, 0, \frac{E_i}{c}(1-Q_{pr})\left[\frac{\sqrt{1-\frac{u}{c}}}{\sqrt{1+\frac{u}{c}}}\right], i\frac{E_i}{c}\left[\frac{\sqrt{1-\frac{u}{c}}}{\sqrt{1+\frac{u}{c}}}\right]\right\}, \tag{3.21}$$

$$\mathbf{p}_0 = \left\{0, 0, \frac{E_i}{c}\left[\frac{1-Q_{pr}}{1+\frac{u}{c}}\right], i\frac{E_i}{c}\left[\frac{1-Q_{pr}u}{c\left(1+\frac{u}{c}\right)}\right]\right\}. \tag{3.22}$$

The force experienced by a particle moving in the direction of the radiation beam is minus the four-vector momentum-energy flux loss from the beam

$$\mathbf{F}_u = -\Delta\mathbf{p} = \left[0, 0, \frac{E_i}{c}\frac{Q_{pr}}{1+\frac{u}{c}}, i\frac{E_i}{c}Q_{pr}\frac{u}{c}\frac{1}{1+\frac{u}{c}}\right]. \tag{3.23}$$

The z term now includes a change in the radiation pressure force because of the motion. Once again the fourth term $-\Delta E_{beam} = \mathbf{F}\cdot\mathbf{u} = F_z u$ and so total energy is conserved.

For $u \ll c$, the denominator of (3.18) can be accurately expanded to give

$$F_u = \left[0, 0, \frac{SA}{c}Q_{pr}\left(1-2\frac{u}{c}\right), i\frac{SA}{c}Q_{pr}\frac{u}{c}\left(1-2\frac{u}{c}\right)\right]. \tag{3.24}$$

The z component of (3.24) is the radiation pressure force as modified by a double Doppler shift.

Using $\dot{r} = u$ and $r\dot{\vartheta} = v$, the final equation of motion is [5, Burns et al., 1979]

$$\dot{\mathbf{v}} = \frac{SA}{mc}Q_{pr}\left[\left(1-2\frac{\dot{r}}{c}\right)\hat{\mathbf{r}} - \frac{r\dot{\vartheta}}{c}\hat{\vartheta}\right]. \tag{3.25}$$

3.3 Evaluation of radiation pressure efficiency factors

3.3.1 The Q_{pr} coefficient

All that remains in order to find the radiation pressure and Poynting-Robertson drag forces actually experienced by small particles in interplanetary space is to evaluate the coefficient Q_{pr}. For this calculation, the particles are assumed to be spheres. While this is obviously done for reasons of computational simplicity, it has some observational justification. The shapes of lunar microcraters, and those found on returned spacecraft detectors, are often nearly circular, which means that the impacting particles are approximately spherical. More often these interplanetary particles are irregular agglomerates built out of approximately spheroidal submicron elements. The structures are quite compact, with empty space comprising much less than half the volume, and typically have densities of 2 to 2.5 $\frac{g}{cm^3}$; this is in fair agreement with the derived density of 2 to 4 $\frac{g}{cm^3}$ for the impacting bodies that cause the lunar microcraters but is in contradiction to the traditional view of "fluffy"meteroroids [5, Burns et al., 1979].

3.3.2 Definition of β

The gravitational attraction of the Sun (mass M at distance r) upon a spherical particle of radius s and density ϱ is

$$F_g = \frac{4}{3}\pi s^3 \varrho \frac{GM}{r^2}\,, \tag{3.26}$$

where G is the gravitational constant. The radiation pressure force due to solar radiation, as given in (3.11), is

$$F_r = \frac{SA}{c} Q_{pr}\,, \tag{3.27}$$

using $S = \frac{L}{4\pi r^2}$ for the radiation flux density at distance r, and L is the solar luminosity. We then compare the radiation force to the gravitational force, defining their ratio by the parameter

$$\beta \equiv \frac{F_r}{F_g} = \frac{3L}{16\pi GMc}\frac{Q_{pr}}{\varrho s} = 5.7 \cdot 10^{-5}\frac{Q_{pr}}{\varrho s}\,, \tag{3.28}$$

where Q_{pr} is averaged over the solar spectrum, and ϱ and s are in cgs units.

We have assumed that the Sun is a point source of radiation; for coronal particles this is not a good approximation and instead the solid angle Ω subtended by the Sun should be taken as $\frac{\Omega}{2\pi} = 1 - [1 - (R_\odot/r)^2]^{\frac{1}{2}}$ and, to be even more correct, the radiation pressure and Poynting- Robertson forces can be rederived.

We see that the force ratio is independent of the distance from the Sun and thus the orbits remain conic sections even with the addition of radiation pressure. We note that $\frac{\beta}{Q_{pr}}$ is of order unity for particle radii of order 0.5 μm, or near where most of the solar energy is contained. Therefore, the important interactions begin to occur when the particle is roughly the same size as a characteristic wavelength of the incident solar spectrum. Unhappily, geometrical optics is therefore not valid in the region where the force becomes significant. The more general Mie calculation must be substituted for sizes smaller than about a micron [5, Burns et al., 1979].

A small fragment particle which is generated at distance r by the collision between a larger parent meteoroid and another meteoroid will move on an unbound trajectory if

$$(1-\beta)U + E_{kin} \geq 0\,, \tag{3.29}$$

where $U = -\gamma\frac{M}{r}$ is the specific potential energy in the solar gravitational field (γ is the gravitational constant and M is the solar mass) and $E_{kin} = \frac{1}{2}mv^2$ is the specific kinetic energy of the fragment particle and v is the heliocentric velocity. For example, a fragment particle with radiation pressure constant $\beta > 0$ which has been released at heliocentric distance r from a larger parent particle ($\beta_p \sim 0$) will not be bound to the Solar System when

$$\beta \geq \frac{r}{2a_p}\,, \tag{3.30}$$

where a_p is the semimajor axis of the parent particle. it is to note that we have assumed that the specific kinetic energies of the parent and the fragment are the same; $E_{kin} = \gamma M(\frac{1}{r} - \frac{1}{2a_p})$. If the collision occurs at the perihelion distance of the parent's orbit $r = a_p(1-e_p)$, we then obtain the minimum β for unbound orbits

$$\beta \geq \frac{1}{2}(1 - e_p)\,. \tag{3.31}$$

Since the eccentricities of the parent particles can be significant, many fragments will get on hyperbolic trajectories. Particles of masses $m \leq 10^{-10}$ g which are made from materials like olivine, basalt, magnetite, graphite, or iron will have β values in excess of 0.1. Maximum β values (≥ 0.5) are reached for particles of masses 10^{-15} to 10^{-12} g. Almost all fragments in this size range will be injected into hyperbolic orbits and become β meteoroids [20, Grün et al., 1985].

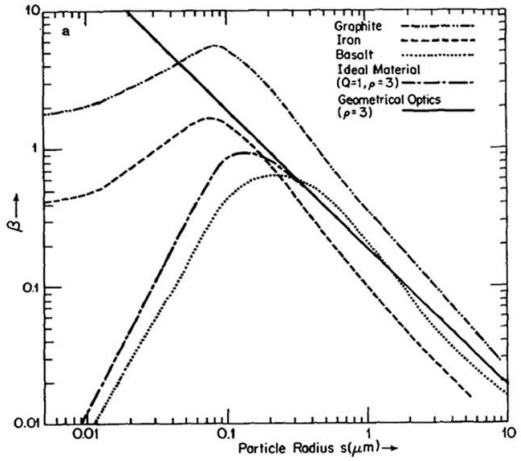

Figure 3.3: A log-log plot of the relative radiation pressure force $\beta = \frac{F_r}{F_g}$ as a function of particle size for three cosmically significant materials and two comparison standards. It is important to note that the application of geometric optic give a wrong result for an ideal material (continuous line) and a correct result with application of the Mie theory for the same material (dot-dashed line). From Burns et al., "Radiation Forces on Small Particles in the Solar System"(1979).

3.4 Dynamical effects of radiation pressure

3.4.1 Abrupt orbital changes; escape from the Solar System

Since the radiation pressure force is a radially-directed, inverse-square force like gravity, it alone does little to complicate the orbital dynamics of dust particles so long as its coefficient remains constant. With the introduction of radiation pressure, a particle's motion is now controlled by the net force, so that, ignoring the small Poynting- Robertson drag

$$\ddot{r} = -(1-\beta)\mu\frac{\hat{S}}{r^2}\,, \tag{3.32}$$

where β is the ratio of radiation repulsion to gravitational attraction and $\mu = GM$. Since the force remains radial, the orbits are still conic sections. If $\beta < 1$, the net force is attractive and so elliptic, parabolic, and hyperbolic orbits are permitted, depending on the orbital energy. If $\beta > 1$, only hyperbolic orbits occur as in the case of electron-electron collisions [5, Burns et al., 1979].

All that is necessary for ejection from the Solar System is for a particle's specific orbital energy

$$\frac{E}{m} = \frac{v^2}{2} - \frac{\mu}{r} \equiv -\frac{\mu}{2a}\,, \tag{3.33}$$

to become positive; v is the particle velocity at heliocentric distance r and a is the semimajor axis of the elliptical orbit. For particles unaffected by radiation, the orbital semimajor axis a is constant because E is conserved in a r^{-2} field. However, consider a small particle which is suddenly released from a much larger parent body: radiation pressure immediately comes into play and the particle's β undergoes an abrupt change from essentially zero (that of the parent body) to some finite value. Equation (3.33) still holds except that μ is replaced by a new value

$$\mu' = \mu(1-\beta) \tag{3.34}$$

if β is sufficiently large, E will be positive.

To illustrate the size of particles for which ejection becomes possible, consider a particle to be released at perihelion, where $r_p = a(1-e)$ and $v_p^2 = (\frac{\mu}{a})(\frac{1+e}{1-e})$ for an orbit of eccentricity e. Ejection then occurs

for $E \geq 0$, so that, from previuos equations, particles for which

$$\beta_p \geq \frac{1-e}{2}\,, \tag{3.35}$$

are placed on hyperbolic trajectories; the corresponding limit for aphelion ejection is $\beta_a \geq \frac{1+e}{2}$ [5, Burns et al., 1979].

Even particles on circular orbits ($e = 0$) should have $\beta = \frac{1}{2}$ for ejection. This is understandable qualitatively since the particle's velocity at the instant of release is governed by its motion before release, that is, by the motion of the large particle that experiences essentially no radiation force; after release the particle's motion is controlled by the forces it then feels. If the particle is of the proper size, following release it may be moving too fast to be bound by the new potential field (i.e., μ'). Hence such particles are placed on hyperbolic orbits even though their $\beta < 1$.

Any small particle produced close to a star can be accelerated to enormous radial velocities if it does not burn up first. Using conservation of energy, we find that a particle introduced at distance r_0 with the initial velocity v_0 will have acquired, by the time it reaches a distance $\gg r_0$, a terminal velocity v_∞ given by

$$v_\infty^2 = v_0^2 + 2\mu\frac{\beta-1}{r_0}\,. \tag{3.36}$$

Thus a particle released from a long-period Sun-grazing comet at perihelion distance R_0 (measured in solar radii) will have a terminal velocity

$$v_\infty = v_{esc}\left(\frac{\beta}{R_0}\right)^{1/2}\,, \tag{3.37}$$

where $v_{esc} = 617\ \frac{km}{s}$ is the usual escape velocity from the surface of the Sun.

Thus a hypothetical particle formed in a stellar atmosphere at R_0 stellar radii from the center will have a terminal velocity, neglecting drag forces, of

$$v_\infty = v_{esc}\left(\frac{\beta-1}{R_0}\right)^{1/2}\,, \tag{3.38}$$

where v_{esc} is now the escape velocity from the surface of the particular star.

Numerous particles on hyperbolic orbits, called β meteoroids appear to exist in interplanetary space. Doppler shifts of the zodiacal light spectrum have been taken to show many scattering particles have orbital velocities greater than the local escape velocity. Further evidence for hyperbolic particles is the hint in the lunar micro-crater data for two species of dust at very small particle sizes: one class might be hyperbolic particles while the other would be the usual interplanetary dust. The hyperbolic trajectories of those β meteoroids, streaming out from the Sun's vicinity, which manage to impact the lunar surface must be confined more closely to the ecliptic plane [5, Burns et al., 1979].

3.4.2 Continuous orbital changes: gradual modification of radiation pressure

The orbital energy of a small particle can be abruptly changed when it is detached from the parent body which was shielded from the effects of radiation pressure. In such cases the particle departs along a simple conic section (perhaps a hyperbola), smoothly patched to that of its parent body. A particle with β changing continuously will follow a more elaborate trajectory. This occurs most readily for particles sufficiently near the Sun to undergo gradual mass loss due to sputtering and/or sublimation. One can write the orbital semimajor axis a and eccentricity e as functions of the orbital velocity $v = (\dot{r}^2 + H^2 r^{-2})^{1/2}$ and specific angular momentum $H = r^2\dot{\vartheta}$, which are themselves functions of the particle position (r, ϑ):

$$a = \frac{r}{2 - \frac{rv^2}{\mu}} \tag{3.39}$$

$$e = \left(1 - \frac{H^2}{\mu a}\right)^{1/2}\,. \tag{3.40}$$

In the typical orbital problem, $\mu = GM$ is the coefficient of the r^{-2} force but, once radiation pressure is included, it becomes $\mu' = GM(1-\beta)$. Increasing the radiation pressure decreases μ' and thus the size of the orbit increases; it is as if the dust were attracted by a continuously less massive Sun. The above expressions are convenient for considering cases in which μ' is not constant, such as can occur when the particle's size changes because of sputtering and/or sublimation/condensation or when the stellar luminosity varies.

Differentiation of (3.39) with position and velocity constant yields

$$\frac{da}{a} = -a\left(\frac{v}{\mu'}\right)^2 d\mu' \,, \tag{3.41}$$

and

$$\frac{de}{e} = \left[\frac{\left(\frac{H}{\mu' e}\right)^2}{a}\right]\left(1-\frac{a}{r}\right) d\mu' \,. \tag{3.42}$$

From (3.34) and (3.41), it is possible to see that the orbital size always increases with increasing radiation pressure (i.e., for $d\mu' < 0$) and decreases as μ' becomes smaller. Similarly, the term $(1 - a/r)$ in (3.42) is negative near pericenter and therefore an increase in radiation pressure at that position causes a more eccentric orbit. To compute the trajectory of a particle that is losing mass by sublimation requires a calculation of the sublimation rate, which is a strong function of the particle's temperature and surface properties, and involves the complex problem of sputtering [5, Burns et al., 1979].

3.4.3 Continuous orbital changes: effects of perturbing forces

We know that an inverse-square radial force field, like that of the gravity field of a spherical mass, produces orbits that are conic sections. Any small deviation from this ideal field, however, means that the orbits approximate, but differ slightly from, conic sections. To describe the manner in which the orbit is modified, we use the perturbation equations of celestial mechanics, which show the variation of the orbital elements with time under the action of a small perturbing force dF above and beyond the gravity force. If a particle in an elliptical orbit is affected by this perturbation, the particle's orbit is no longer elliptical. This is the (elliptical) path that the particle would follow if dF suddenly vanished, say at $t = t_l$, and the particle continued along its way with $r(t_1)$ and $v(t_1)$ as initial conditions. The orbital elements specifying the osculating orbit are the osculating elements; governed by the perturbation equations of celestial mechanics, these changes slowly owing to dF and represent a gradually evolving orbit. Burns (1976) has derived the perturbation equations in terms of the disturbing force components by differentiating expressions for the orbital elements written in terms of the orbital energy and angular momentum per unit mass and then substituting for the manner in which the energy and angular momentum change with time under the action of the perturbation. He found that the changes in the orbital elements of interest are

$$\frac{da}{dt} = -\frac{a\dot{E}}{E} = 2\left(\frac{a^2}{mH}\right)\left[F_R e \sin f + F_T(1 + e\cos f)\right], \tag{3.43}$$

$$\frac{de}{dt} = (e^2-1)\frac{\left(\frac{2\dot{H}}{H} + \frac{\dot{E}}{E}\right)}{2e} = \left(\frac{H}{m\mu}\right)\left[F_R \sin f + F_T(\cos f + \cos\psi)\right], \tag{3.44}$$

$$\frac{di}{dt} = \left(\frac{\dot{H}}{H} - \frac{\dot{H}_z}{H_z}\right)\left[\left(\frac{H}{H_z}\right)^2 - 1\right]^{-\frac{1}{2}} = \frac{r}{mH} F_N \cos\vartheta \,, \tag{3.45}$$

$$\frac{d\omega}{dt} + \cos i \frac{d\Omega}{dt} = \left(\frac{H}{m\mu e}\right)\left[-F_R \cos f + \frac{F_T \sin f(2 + e\cos f)}{1 + e\cos f}\right], \tag{3.46}$$

where $E = -\frac{\mu m}{2a}$ is the orbital energy; (F_R, F_T, F_N) are the radial, transverse and normal components of the perturbing force; $H = [a\mu(1-e^2)]^{1/2}$ is the angular momentum per unit mass and H_z is its component perpendicular to the reference plane (the plane above which i is measured); f is the particle's true anomaly; ψ its eccentric anomaly, $\cos\psi = \frac{e+\cos f}{1+e\cos f}$; $\vartheta = \omega + f$ is the orbital longitude of the particle and, finally, Ω is the longitude of node [5, Burns et al., 1979].

3.5 Dynamical consequences of Poynting-Robertson drag

3.5.1 Heliocentric orbits

Considering equation (3.11), it is possible to note that the Poynting- Robertson force works in the opposite direction of the particle velocity. This takes both energy and angular momentum from the particle orbit, decreasing both the orbital semimajor axis and the eccentricity. To compute the consequences of these changes we return to the perturbation equations of celestial mechanics; the perturbation forces per unit mass for our problem are given by (3.12). The radial and transverse parts of the Poynting-Robertson acceleration are [5, Burns et al., 1979]

$$F_R = -2\frac{SAQ_{pr}}{mc^2}\dot{r} \tag{3.47}$$

$$F_T = -\frac{SAQ_{pr}}{mc^2}r\dot{\vartheta}\,, \tag{3.48}$$

where $S = S_0(r_0/r)^2$ is the solar flux at distance r from the Sun. There is no normal force component, demonstrating immediately by (3.45) that there is no change in the orbital inclination for a heliocentric particle under the action of radiation pressure and Poynting-Robertson drag. The secular changes in a and e can be found by substituting F_R and F_T into (3.43) and (3.44) and time averaging the resulting expressions for $\dot{a}$ and $\dot{e}$ using

$$\dot{r} = \left[\frac{\mu}{a(1-e^2)^{\frac{1}{2}}}\right]^{\frac{1}{2}} e\sin f\,, \tag{3.49}$$

and

$$r\dot{\vartheta} = \left[\frac{\mu}{a(1-e^2)^{\frac{1}{2}}}\right]^{\frac{1}{2}} (1+e\cos f)\,. \tag{3.50}$$

This procedure then yields

$$\langle\frac{da}{dt}\rangle = -\frac{\eta}{a}Q_{pr}\frac{2+3e^2}{(1-e^2)^{\frac{3}{2}}}\,, \tag{3.51}$$

$$\langle\frac{de}{dt}\rangle = -\frac{5}{2}\frac{\eta}{a^2}Q_{pr}\frac{e}{(1-e^2)^{\frac{1}{2}}}\,, \tag{3.52}$$

where $\eta = \frac{S_0 r_0^2 A}{mc^2} = \frac{2.53\cdot 10^{11}}{\rho s}$ for spherical particles, with ρ and s in cgs units. Because the perturbing forces lie in the orbit plane, the only other secular variation of an orbital element is the advance of perihelion whose change, even accounting for relativistic effects, is much slower than the variations of a or e.

The characteristic orbital decay time with $e = 0$ is easily found by integrating (3.51):

$$t_{P-R} = \frac{a^2}{4\eta Q_{pr}} = 7.0\cdot 10^6\frac{s\varrho R^2}{Q_{pr}} = 400\frac{R^2}{\beta}years\,, \tag{3.53}$$

where R is a measured in AU.

It is readily shown that $\frac{a^2}{\eta}$ is the time it takes for a particle at a to be struck by its own equivalent mass in solar radiation; that the collapse time is of the same order as, but smaller than this, is understandable that the Poynting-Robertson drag results from the absorption of mass but not momentum. The

integration of da and de for finite e is not simple but can be accomplished in closed form; their results, when divided by Q_{pr}, produce characteristic Poynting-Robertson lifetimes for very small particles that become long, contradicating classical. However, the inclusion of solar wind drag will considerably shorten these times, since the drag due to the particulate radiation dominates that produced by electromagnetic radiation at particle sizes less than about a tenth of a micron [5, Burns et al., 1979].

3.5.2 Planetocentric orbits

Any calculation of the effects of the Poynting-Robertson force on the orbit of a circumplanetary particle has to account for the fact that $\hat{S}$ does not in general lies in the orbit plane. In terms of the vectors $\mathbf{a} = a\hat{\mathbf{a}}$ and $\mathbf{b} = a(1-e^2)^{1/2}\hat{\mathbf{b}}$, it is readily shown that $r = \mathbf{a}(\cos\psi - e) + \mathbf{b}\sin\psi$ and

$$\dot{\mathbf{r}} = \dot{\psi}(-\mathbf{a}\sin\psi + \mathbf{b}\cos\psi)\,. \tag{3.54}$$

The Poynting-Robertson force may be written

$$\mathbf{F}_{P-R} = -\frac{SA}{c^2}Q_{pr}[(\hat{\mathbf{r}}\cdot\hat{\mathbf{S}})\hat{\mathbf{S}} + \dot{\mathbf{r}}]\,. \tag{3.55}$$

Then the rate of change of a circumplanetary particle's orbital energy is [5, Burns et al., 1979]

$$\begin{aligned}\dot{E} &= \mathbf{F}_{P-R}\cdot\dot{\mathbf{r}} = -\frac{SA}{c^2}Q_{pr}[(\hat{\mathbf{r}}\cdot\hat{\mathbf{S}})^2 + \dot{\mathbf{r}}\cdot\dot{\mathbf{r}}] \qquad (3.56)\\ &= -\frac{SA}{c^2}Q_{pr}\dot{\psi}^2[(\hat{\mathbf{a}}\cdot\hat{\mathbf{S}})^2\sin^2\psi + (\hat{\mathbf{b}}\cdot\hat{\mathbf{S}})^2\cos^2\psi\\ &- 2(\hat{\mathbf{a}}\cdot\hat{\mathbf{S}})(\hat{\mathbf{b}}\cdot\hat{\mathbf{S}})\sin\psi\cos\psi + a^2(1-e^2\cos^2\psi)]\,.\end{aligned}$$

This must now be time averaged over the particle's orbital motion (ψ), its advance of pericenter (ω), and the (assumed circular) orbital motion of its parent planet (Ω'). The averaging integrations of $\dot{E}$ can be performed in any order, but to obtain all expressions in closed form it is convenient to take ω and Ω' first. Finally we obtain

$$\langle\dot{E}\rangle = -\frac{SA\mu}{4ac^2}Q_{pr}(5+\cos^2 i)\,, \tag{3.57}$$

From (3.43), $\langle\dot{a}\rangle = 2a^2\frac{\langle\dot{E}\rangle}{\mu m}$, where m is the particle's mass, so we have

$$\langle\dot{a}a\rangle = -\frac{3}{8}\frac{S_0}{R^2c^2}\frac{Q_{pr}}{\varrho s}(5+\cos^2 i)\,, \tag{3.58}$$

where $S_0 = 1.36\cdot 10^6\ ergs\cdot cm^{-2}\cdot s^{-1}$ is the solar constant and R is the heliocentric distance in AU. Integrating (3.58), it is possible to write the exponential decay time for circumplanetary particles with $i = 0$ as

$$\tau_{P-R} = 9.3\cdot 10^6\frac{R^2\varrho s}{Q_{pr}}\ years\,, \tag{3.59}$$

with ρ and s in cgs units.

This ratio for planetocentric orbit collapse is essentially the same as (3.53), that for heliocentric orbit collapse; fundamentally this results because the Poynting-Robertson drag is due to the reradiation of the absorbed energy, which is nearly the same regardless of whether the planet or the Sun is being orbited. The small difference in the coefficients is principally due to one being a characteristic decay time while the other is the integrated collapse time. Even though this collapse time can be short, the loss of highly perturbed circumplanetary particles more commonly happens due to the eccentricity variations induced by radiation pressure forces.

By a procedure similar to the above, we can examine the effect on the eccentricity of a circumplanetary particle due to the Poynting-Robertson force. The torque on the particle's orbit due to $\mathbf{F}_{P-R}$ is $m\dot{\mathbf{H}} =$

$\mathbf{r} \times \mathbf{F}_{P-R}$. Expressing this in terms of the **a** and **b** vectors and integrating over ψ, ω, and Ω', as before, we find that $\frac{\dot{H}}{H} = \frac{\dot{a}}{2a}$. Expressing $\dot{e}$ in terms of $\dot{H}$ and $\dot{a}$ from (3.43) and (3.44), we find that $\langle \dot{e} \rangle = 0$.

The orbital inclination can be shown to exhibit an oscillation with the orbital period of the planet [5, Burns et al., 1979].

Chapter 4

Dynamical model of dust flux on Mercury

Dust particles undergo a complex dynamical evolution which significantly differs from the simple classical monotonic decrease of the orbital semimajor axis and eccentricity as due to Poynting-Robertson drag and solar wind drag alone.

Gustafson and Misconi (1983, 1986) have shown that planetary perturbations significantly affect the long-term orbital evolution of dust particles. They found monotonic changes in semimajor axis, eccentricity, inclination and line of nodes, caused by gravitational influence from the planets. Moreover their calculations show that dust particles can temporary interrupt their slow spiralling in toward the Sun and become trapped into orbital resonances with a planet. Grains can be remained trapped in orbits resonant with massive perturbing bodies after being gradually driven there by drag forces [54, Marzari and Vanzani, 1994].

4.1 Solar radiation and wind forces

The solar radiation and solar wind forces, together with the gravitational interactions with the planets, are major perturbing forces affecting the orbital evolution of the dust particles with size in the range $10^{-4} - 1\ cm$. The dominant perturbing forces, in particular the resistive forces due to solar radiation and wind bombardment, need a careful consideration in view of an accurate study of the long-term dynamics of interplanetary dust.

Solar wind forces were not accurately modeled in interplanetary dust dynamics studies which combined non-gravitational with gravitational perturbing force effects. In modeling these forces major problems arise from difficulties in the determination of average physical parameters for the solar wind, which is intrinsically highly structured in space and variable in time and from complications due to complex phenomena caused by the interaction of solar wind particles with interplanetary dust grains.

Lorentz forces, resulting from the interaction of charged dust grains with the interplanetary magnetic field, are regarded negligible in the size range we consider, for which the charge-to-mass ratio is expected to be sufficiently small.

Collisions between dust grains, which may drastically alter the dynamical evolution, or even put end to the individual evolutionary history of colliding bodies, become important for sizes larger than 100 μm.

In terms of characteristics timescales, grains in the size range 10-100 μm have a radiation and corpuscular drag timescales (the typical orbital decay time under the combined drag forces) quite shorter than both the Lorentz-effect timescale and the collisional lifetime.

Mass loss mechanisms (sublimation and sputtering) could be properly taken into account introducing the relevant mass loss rates in the equation of the motion. The problem becomes complicated especially

with regard to the complex effects of sputtering [54, Marzari and Vanzani, 1994].

We take the non-gravitational term in the dust-grain equation of motion as given by

$$\mathbf{F}_{ngr} = \mathbf{F}_{rad} + \mathbf{F}_{wnd}\,, \tag{4.1}$$

with

$$\mathbf{F}_{rad} = \frac{S}{c}\left(1 - \frac{\dot{r}}{c}\right) AQ_{pr}\hat{\mathbf{p}} = f_r\hat{\mathbf{p}}\,, \tag{4.2}$$

the resistive force on the dust grain due to its interaction with the solar radiation

$$\mathbf{F}_{wnd} = \sum_j \left(\frac{\eta_j u^2}{2}\right) AC_{D,j}\hat{\mathbf{u}} = f_w\hat{\mathbf{u}}\,, \tag{4.3}$$

the corpuscular counterpart of $\mathbf{F}_{rad}$, i.e. the resistive force caused by solar wind bombardment, and with a self-explanatory notation for f_r and f_w. In equations (4.2) and (4.3) $\hat{\mathbf{p}} = \frac{\mathbf{c}-\mathbf{v}}{c}$, where $\mathbf{c}$ is the velocity of the light and $\mathbf{v}$ is the orbital velocity of the dust particle; $\hat{\mathbf{u}} = \frac{\mathbf{u}}{u}$ with $\mathbf{u} = \mathbf{w} - \mathbf{v}$ and w the solar wind bulk velocity. $S = \frac{L_\odot}{4\pi r^2}$ is the solar radiation flux density at heliocentric distance r, with $L_\odot$ the solar luminosity; $\eta_j = n_j m_j$ the spatial mass density of the corpuscular component j of the solar wind, having mass m_j and number density n_j; A is the grain's geometrical cross section; Q_{pr} the dimensionless radiation-pressure coefficient averaged over the solar spectrum; $C_{D,j}$ is the partial corpuscular counterpart, i.e. the dimensionless drag coefficient due to the j-component of the wind flow.

The standard computation of Q_{pr} is based on the Mie theory with detailed considerations of the optical constants of the grain material and of the solar energy spectrum.

The radial and transverse components of $\mathbf{F}_{rad}$ and $\mathbf{F}_{wnd}$ can be separated as follows:

$$\mathbf{F}_{rad} = \frac{SAQ_{pr}}{c}\left[\left(1 - 2\frac{\dot{r}}{c}\right)\hat{\mathbf{r}} - \left(r\frac{\dot{\vartheta}}{c}\right)\hat{\vartheta}\right]\,, \tag{4.4}$$

and

$$\mathbf{F}_{wnd} = \sum_j \left(\frac{\eta_j u w}{2}\right) AC_{D,j}\left[\left(\cos\varphi - \frac{\dot{r}}{w}\right)\hat{\mathbf{r}} + \left(\mp\sin\varphi - r\frac{\dot{\vartheta}}{w}\right)\hat{\vartheta}\right]\,. \tag{4.5}$$

Here $\hat{\vartheta}$ is the unit vector normal to $\mathbf{r}$ in the orbital plane (positive in the direction of the grain's motion), $\varphi = \arccos(\frac{\mathbf{w}\cdot\hat{\mathbf{r}}}{w})$ is the angle that average solar wind direction forms with the grain's velocity.

In equation (4.5) the upper sign $(-)$ applies to grains in prograde orbits, the lower $(+)$ sign to grains in retrograde orbits. The contribution to $\mathbf{F}_{wnd}$ from the transverse component $\mp w\sin\varphi$ of the solar wind velocity arises because the wind does not quite flow radially from the Sun ($\varphi \simeq 1.5°$ as average value). For the most common case of prograde orbits it leads to a larger resistive force [54, Marzari and Vanzani, 1994].

The efficiency of the radiation and corpuscular resistive forces can be expressed by defining their ratio to the solar gravity by parameters

$$\beta_r = \frac{f_r}{f_g}\frac{c}{c-\dot{r}} = \frac{\frac{SAQ_{pr}}{c}}{\frac{GM_\odot m}{r^2}}\,, \tag{4.6}$$

$$\beta_w = \frac{f_w}{f_g}\frac{w}{|\mathbf{w}-\mathbf{v}|} = \frac{\frac{f_{w0}\psi}{\kappa}}{\frac{GM_\odot m}{r^2}}\,. \tag{4.7}$$

In equation (4.7), $\kappa = \frac{u}{w}$ and $\psi = \frac{f_w}{f_{w0}}$, with f_{w0} obtained from f_w in the limit of neglecting the velocity dispersion of wind particles and omitting the contribution to $\mathbf{F}_{wnd}$ arising from the momentum carried away by the sputtered molecules [54, Marzari and Vanzani, 1994].

The inverse-square heliocentric-distance behaviour of S and η_j, i.e. $S = S_0(\frac{r_0}{r})^2$ and $\eta_j = \eta_{j,0}(\frac{r_0}{r})^2(\frac{w_0}{w})^2$ makes β_r and β_w independent from r. Taking the reference distance r_0 equal to 1 AU and assuming a spherical shape with radius s for the grain, one gets from equations (4.6) and (4.7)

$$\beta_r = \frac{3S_0 r_0^2}{4GM_\odot c}\frac{Q_{pr}}{\varrho s} = 5.74 \cdot 10^{-5}\frac{Q_{pr}}{(\varrho s)_{cgs}}\,, \tag{4.8}$$

and

$$\beta_w = \frac{3(\eta_{p,0}+\eta_{\alpha,0})r_0^2 w_0^2}{4GM_\odot}\frac{\psi\kappa}{\varrho s} \simeq 3.27 \cdot 10^{-8}\frac{\psi\kappa}{(\varrho s)_{cgs}} \tag{4.9}$$

where ϱ is the mass density of the grain, and $(\varrho s)_{cgs}$ denotes that ϱ and s are in cgs units.

The final expression in equations (4.8) and (4.9) follow from the average value $S \simeq 1.367{\cdot}10^6\ erg\ cm^{-2}\ s^{-1}$ for the solar constant, $w_0 \simeq 4 \cdot 10^7\ cm\ s^{-1}$ for w at 1 AU and $\eta_{p,0} + \eta_{\alpha,0} \simeq 1.2\eta_{p,0}$ as a consequence of $\frac{\eta_{\alpha,0}}{\eta_{p,0}} \simeq 0.05$.

The relative importance of the radiation and corpuscular forces can be estimated by introducing the parameter

$$\gamma = \frac{\beta_w}{\beta_r} \simeq 5.74 \cdot 10^{-4}\frac{\psi\kappa}{Q_{pr}}\,. \tag{4.10}$$

In terms of the parameters β_r and γ the sum of the radiation and solar resistive forces takes the form

$$\mathbf{F}_{ngr} = \beta_r f_g[(1+\gamma\cos\varphi)\hat{\mathbf{r}} \mp \gamma\sin\varphi\hat{\vartheta}] - \beta_r f_g\left[\left(2+\gamma\frac{c}{w}\right)\frac{\dot{r}}{c}\hat{\mathbf{r}} + \left(1+\gamma\frac{c}{w}\right)\frac{r\dot{\vartheta}}{c}\hat{\vartheta}\right]\,, \tag{4.11}$$

where the terms dependent and independent on dust grain's velocity appear separated. The first part in equation (4.11) is the sum of radiation pressure force $\beta_r f_g\hat{\mathbf{r}}$ with the corpuscular pressure force $\beta_w f_g\hat{\mathbf{w}} = f_w\frac{\mathbf{w}}{u}$ splitted into radial and transverse components. The latter part in equation (4.11) is the sum of the classical Poynting-Robertson drag with the solar wind drag or pseudo Poynting-Robertson drag $-\beta_w f_g\frac{\mathbf{v}}{w} = -f_w\frac{\mathbf{v}}{u}$ [54, Marzari and Vanzani, 1994].

4.2 Calculation of impact fluxes

The impact flux for a planet (measured in terms of the number of particles of a defined size impacting a unit area per unit time) is dependent on two specific factors: the distribution of velocities of the impacting objects and spatial density (number per unit volume) of those particles as they are encountered by the planet.

Taking into account the article of Cintala we have to consider two factors to determine the flux. A differential mass flux distribution, that describes the number of impacting particles between the masses of μ and $\mu + d\mu$ per unit area per unit time, where $d\mu$ is a differential mass increment. Similarly, a differential velocity flux distribution describes the impact flux in terms of impacts per unit area per unit time per differential velocity increment. Such differential distributions can be derived from measured cumulative fluxes by performing a regression to the observed data and taking the first derivative of the fit with respect to the variable of interest. For example, the differential flux $\Phi(v,\mu)$ can be written as

$$\Phi(v,\mu) = f(v)h(\mu)\,, \tag{4.12}$$

where $f(v)$ is the velocity distribution of the impactors and $h(\mu)$ is a function describing the mass distribution of impacting objects. Implicit in (4.12) is the assumption that the velocity and mass distributions are independent of each other [7, Cintala, 1992].

Meteoroid velocity distribution curves have been derived by Southworth and Sekanina (1973) from radar meteor observations and by Erickson (1968), Kessler (1969), and Dohnanyi (1966) from independent analyses of the photographic meteor observations.

The Southworth and Sekanina distribution is given by [66, Sekanina et al., 1973]

$$f_e(v_e) = 3.822 \cdot e^{-0.2468 v_e}\,, \tag{4.13}$$

with $11.1 \leq v_e \leq 72$, where v_e is the velocity (in km/sec) of entry of a meteoroid into the top of the atmosphere of the Earth, and $f_e(v_e)dv_e$ is the fraction of meteoroids entering with velocities between v_e and $v_e + dv_e$.

The distribution due to Erickson takes the form [14, Erickson, 1968]

$$f_e(v_e) = 0.1116\,, \tag{4.14}$$

with $11.1 \leq v_e \leq 16.3$

$$f_e(v_e) = 3.316 \cdot 10^5 v_e^{-5.34}\,, \tag{4.15}$$

with $16.3 \leq v_e \leq 55.0$

$$f_e(v_e) = 1.689 \cdot 10^{-4}\,, \tag{4.16}$$

with $55.0 \leq v_e \leq 72.2$.

The distribution due to Dohnanyi takes the form [13, Dohnanyi, 1966]

$$f_e(v_e) = 1.21 \cdot 10^{-3} v_e^{1.6}\,, \tag{4.17}$$

with $11.1 \leq v_e \leq 16.6$

$$f_e(v_e) = 1.948 \cdot 10^{-4} v_e^{-4.3}\,, \tag{4.18}$$

with $16.6 \leq v_e \leq 72.2$.

The distribution due to Morgan take into account that conservation of angular momentum and of particles requires that the flux of particles of a single velocity near a body with a non negligible gravitational field be increased over the flux at infinite distance from the body by the factor $(\frac{v_e}{v_1})^2$, where v_e is the particle velocity near the gravitating body (in our case, at the top of the Earth's atmosphere) and v_1 is the particle velocity at an effectively infinite distance from the body (in our case, at 1 AU but far from Earth) [57, Morgan et al., 1988]. The normalized differential flux at far distance from the Earth (but at 1 AU), $f_1(v_1)$, is therefore related to the normalized differential flux at the top of the Earth's atmosphere, $f_e(v_e)$, as follows:

$$f_1(v_1) = k_1 \left(\frac{v_1}{v_e}\right)^2 f_e(v_e) dv_e\,, \tag{4.19}$$

k_1 is the constant required to normalize f_1 (i.e., to cause the integral of f_1 over all values of v_1 to equal 1). Conservation of energy gives

$$v_e^2 = v_1^2 + v_{ee}^2\,, \tag{4.20}$$

where $v_{ee} = 11.1\ \frac{km}{s}$ is the gravitational escape velocity from the top of the Earth's atmosphere. Differentiating Eq. (4.20) gives

$$dv_e = \frac{v_1}{v_e} dv_1\,, \tag{4.21}$$

and using equation (4.19) and (4.21), one derives that

$$f_1(v_1) = k_1 \left(\frac{v_1}{v_e}\right)^3 f_e(v_e)\,. \tag{4.22}$$

The constant k_1 depends on the original velocity distribution, f_e, that is used. It measures the decrease in flux that should be observed as one moves far away from the Earth [57, Morgan et al., 1988].

To derive a plausible distribution in velocity with which meteoroids might impact on a body that is in circular orbit in the ecliptic plane at distance r from the Sun (in the absence of gravitational focusing), it is first assumed that the normalized distribution in $\frac{a}{r}$, e, and i that would be observed for meteoroids at

distance r AU from the Sun is exactly the same as the normalized a, e, and i distribution that is derived from observations 1 AU from the Sun. Here, a is the semimajor axis of the orbit of the meteoroid, e is the eccentricity, and i is the inclination to the ecliptic plane. The meteoroid velocities, v_r, relative to a body at distance r (in AU) from the Sun then scale to corresponding relative velocities at 1 AU as $r^{-0.5}$. Thus,

$$v_r = r^{-0.5} v_1 \,, \tag{4.23}$$

and

$$f_1(v_1)dv_1 = f_r(v_r)dv_r \,. \tag{4.24}$$

If therefore follows that

$$f_r(v_r) = r^{0.5} f_1(v_1) \,. \tag{4.25}$$

With an aphelion at 0.4667 AU and a perihelion at 0.3075 AU, Mercury's orbit is far from circular. Its orbital velocities at aphelion or perihelion are, respectively, slower or faster than are circular orbital velocities at the corresponding heliocentric distances. Morgan assume meteoroids will impact on Mercury with a distribution of velocities that depends only on r and is given by equation (4.25) plus a gravitational enhancement factor that is similar to that of equation (4.22). The orbit of Mercury is inclined by 7° to the plane of the ecliptic, which will result in some increase in the impact velocity over an orbit in the plane of the ecliptic; however, the effect is small and is not considered here. By combining equations (4.22) and (4.25) with the velocity of escape from the surface of Mercury ($v_{em} = 4.267\ \frac{km}{s}$), one obtains the velocity distribution of the meteoroids impacting the surface of Mercury at velocity v_m,

$$f_m(v_m) = k_2(r) r^2 \left(\frac{v_m}{v_1}\right)^3 f_1(v_1) \tag{4.26}$$

where

$$v_m = (v_r^2 + v_{em}^2)^{0.5} \,, \tag{4.27}$$

and $k_2(r)$ is adjusted at each radial distance so as to normalize $f_m(v_m)$. For simplicity the r dependence of f_m is suppressed in the notation [57, Morgan et al., 1988].

The distribution due to Cintala, take into account the work of Morgan and starting from equation (4.19). Cintala founded the velocity distribution for Mercury

$$f_M(v_M) = \kappa r^{0.2} \left[\frac{v_M}{\sqrt{r(v_M^2 - v_{Me}^2) + v_{Ee}^2}}\right]^3 e^{-\gamma\sqrt{r(v_M^2 - v_{Me}^2)+v_{Ee}^2}} \,, \tag{4.28}$$

where r is the mean distance of Mercury from the Sun, v_{Ee} is the escape velocity for the Earth at 100 km altitude, v_M is the impact velocity for Mercury and v_{Me} is the escape velocity at the surface of Mercury [7, Cintala, 1992].

4.3 A statistical study about dynamical evolution of dust particles

In this work we adopt a statistical approach, based on a large number of simultaneous numerical integrations, to explore the orbital evolution of dust particles originating from the Main Belt in order to obtain a statistical analysis, then to provide an estimate of the flux of particles hitting the Mercury's surface.

In order to determine the meteoritic flux at the heliocentric distance of Mercury we utilize the dynamical evolution model of dust particles of Marzari and Vanzani ([54, Marzari and Vanzani, 1994]) that numerically solves a $(N + 1) + M$ body problem (Sun + N planets + M body with zero mass) with the high-precision integrator RA15. The solar radiation pressure and Poynting-Robertson drag, together with

the gravitational interactions of the planets, are taken as major perturbing forces affecting the orbital evolution of the dust particles. We will perform numerical simulations with different initial conditions for the dust particles, depending on the sources, with the aim of estimating the flux of dust on the surface of Mercury.

The adopted numerical method for solving the equations of motion is the RA15 version of the RADAU integrator by Everarth (1985). This numerical integrator is particularly accurate and suitable for modelling the orbital behaviour of dust particles because it uses a variable stepsize.

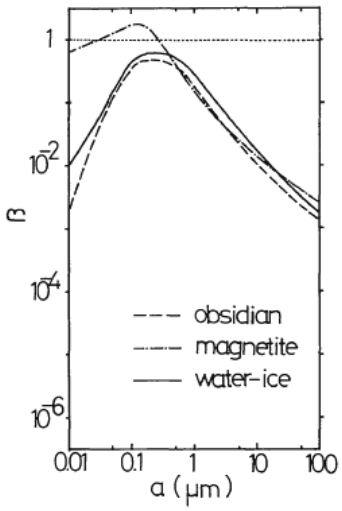

Figure 4.1: The figure shows the values of β as function of a (radius of dust particles), where Q_{pr} is computed based on the Mie theory under the detailed considerations of the optical constants of grain material and of the solar energy spectrum. From Mukay and Yamamoto, "Solar Wind Pressure on Interplanetary Dust"(1982).

We have considered a set of 1000 particles, with random orbital elements. In particularly we put some limitations in some orbital elements: semi-major axis, eccentricity and inclination. In fact, we take random semi-major axis in a range 2.1-3.3 AU, eccentricity in a range 0.0-0.4 and inclination in a range $0 - 20°$. We assume a density of 2.5 $g\ cm^{-3}$ that is a reasonable value for dust particles that come from the Main Belt. We consider a Q_{pr}, the dimensionless radiation-pressure coefficient averaged over the solar spectrum, of 0.53 considering the figure 4.1 [54, Marzari and Vanzani, 1994] [60, Mukai and Yamamoto, 1982]. We adopt a statistical approach to know the orbital evolution of dust and when these dust particles fall down in ten times the influence sphere of Mercury. In order to detect close encounters between dust particles and Mercury, the orbits of the dust particles and the planets were integrated numerically. At each time step, mutual distances among all particles that fall down in ten times the influence sphere of the planet are computed. A close encounter was calculated whenever the dust particles is in a ten time the sphere of influence. Once we obtain the list of particles, falling within ten times the influence sphere, we compute the cumulative number of close encounters N using a number of bins of equal width. We expect that N is proportional to R^2, minimum mutual distance between dust particles and Mercury, since the cross section for a close approach is just πR^2 [55, Marzari et al., 1996]. A least square fit to the data with the model function $f(R) = P_1 R^2$ is then performed.

We don't consider particles with radius smaller than 1 μm because, in general, solar radiation pressure reduces solar gravity sufficiently to drive fragments out of the solar system (they become beta meteoroids). Only meteoroids smaller than 0.1 mm rapidly drift by the Poynting-Robertson effect toward the Sun where they sublimate [5, Burns et al., 1979], [73, Sykes et al., 2004].

4.3.1 Particles of $5 \cdot 10^{-4}$ cm of radius

We consider 1000 particles with $5 \cdot 10^{-4}$ cm of radius. In the figures below we show the three-dimensional coordinates distribution (figure 4.2) the bi-dimensional coordinates distribution (figure 4.3), the histogram that represent the distance distribution of dust particles (figure 4.4), that is the minimum distance particle-Mercury in a ten times the radius of the sphere of influence of the planet, and velocity distribution of dust particles (figure 4.5). After this we show in the figures (4.6) and (4.7) the best fit that adapt to our data.

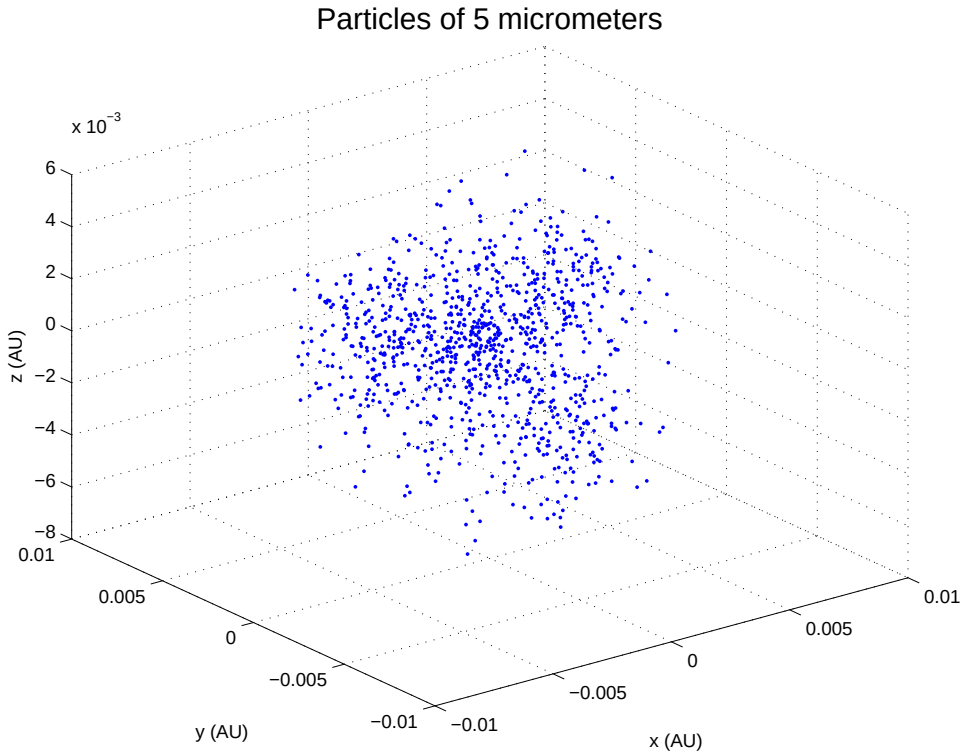

Figure 4.2: Coordinates distribution of particles of $5 \cdot 10^{-4}$ cm of radius.

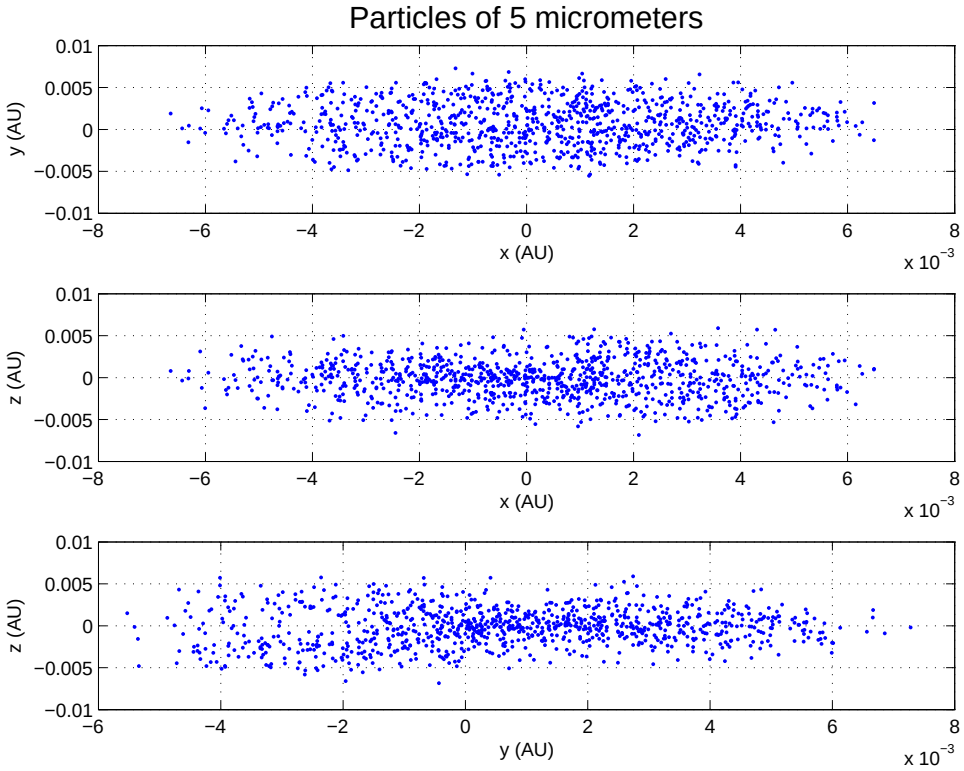

Figure 4.3: Coordinates distribution of particles of $5 \cdot 10^{-4}$ cm of radius.

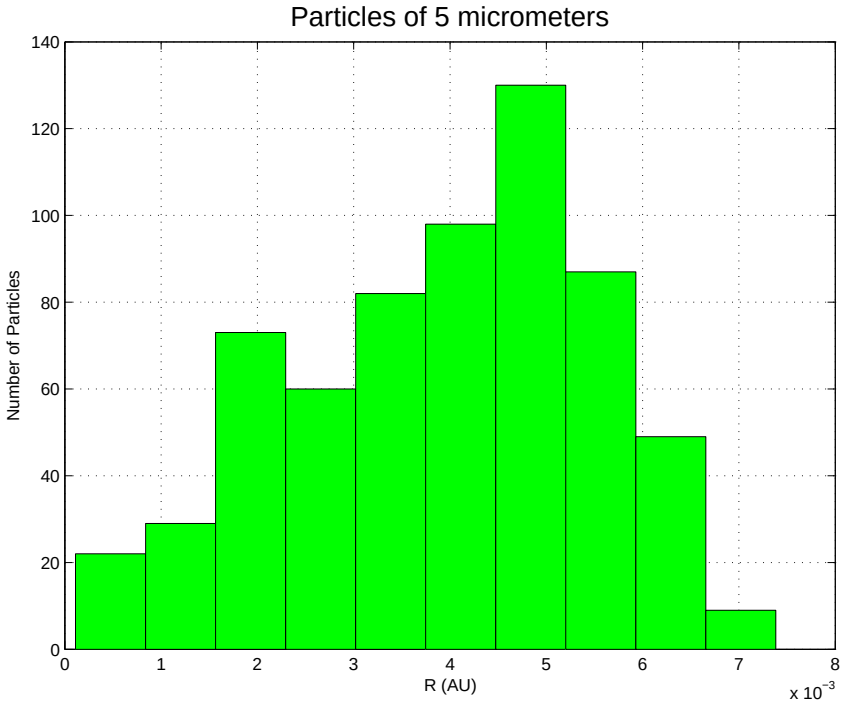

Figure 4.4: Distance distribution of particles of $5 \cdot 10^{-4}$ cm of radius.

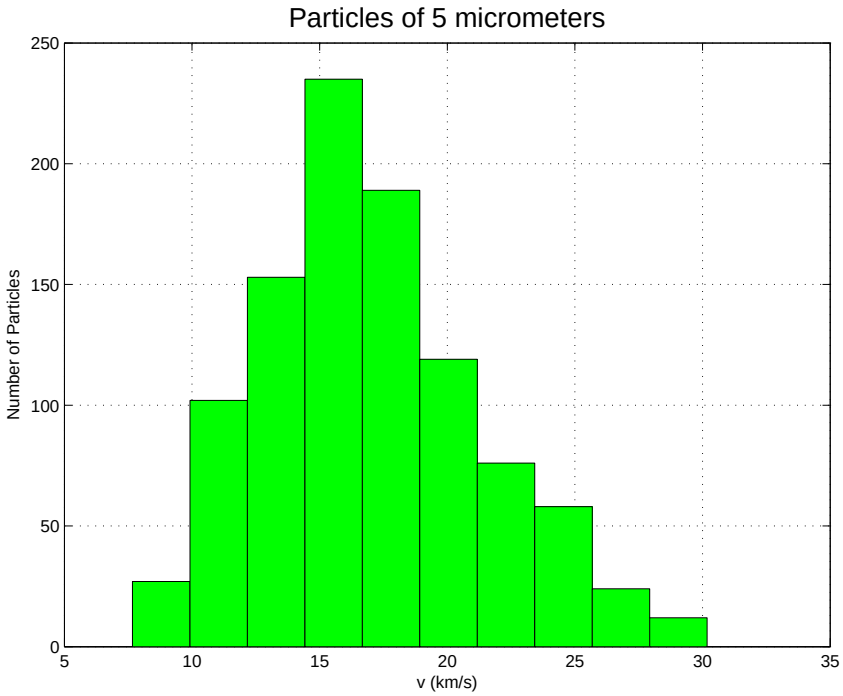

Figure 4.5: Velocity distribution of particles of $5 \cdot 10^{-4}$ cm od radius.

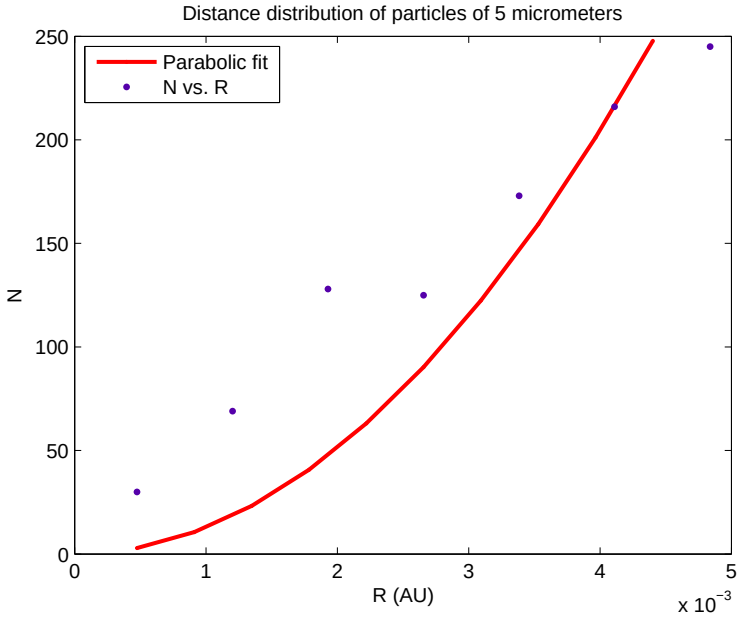

Figure 4.6: Quadratic distance distribution of particles of $5 \cdot 10^{-4}$ cm od radius.

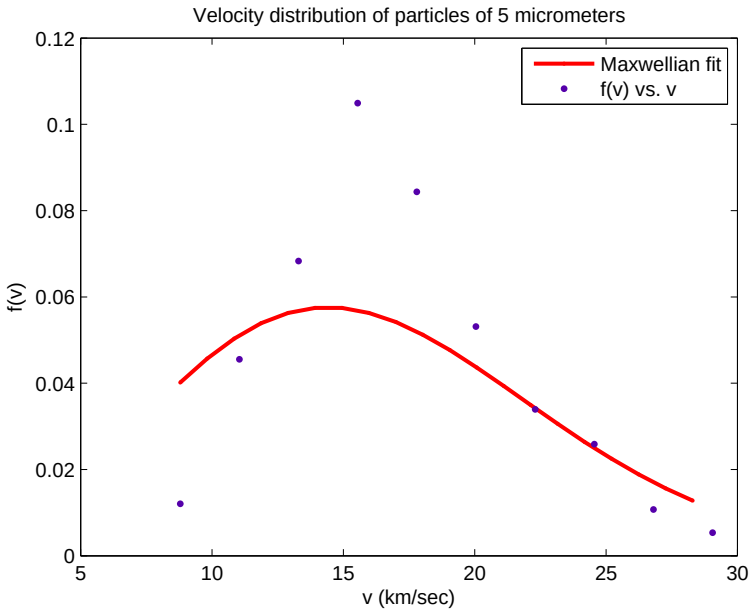

Figure 4.7: Gaussian velocity distribution of particles of $5 \cdot 10^{-4}$ cm od radius.

The best fit for the minimum distance distribution is a polynomial fit of degree 2

$$f(r) = p_1 r^2 \,. \tag{4.29}$$

The best fit for velocity distribution is a maxwellian expression

$$f(v) = \sqrt{\frac{2}{\pi}} a^{-\frac{3}{2}} v^2 \exp\left(-\frac{v^2}{2a}\right) \,. \tag{4.30}$$

After fitting data with a model, we evaluate the goodness of fit with three step:

1. residuals;
2. goodness of fit statistics;
3. confidence and prediction bounds.

The residuals and prediction bounds are graphical measures, while the goodness of fit statistics and confidence bounds are numerical measures.

Residuals

The residuals from a fitted model are defined as the differences between the response data and the fit to the response data at each predictor value $residual = data - fit$. We show in the figure (4.8) the residuals for the minimum distance distribution and in the figure (4.9) the residuals for the velocity distribution.

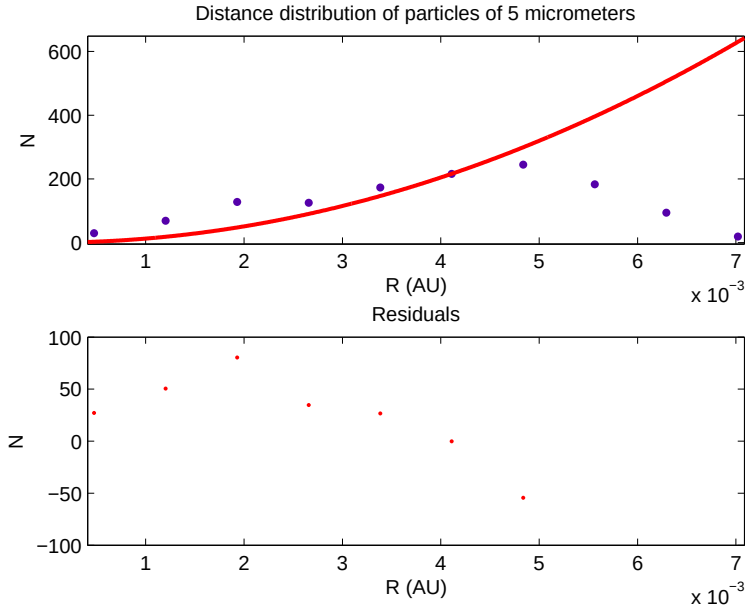

Figure 4.8: Residuals of distance distribution of particles with $5 \cdot 10^{-4}$ cm of radius.

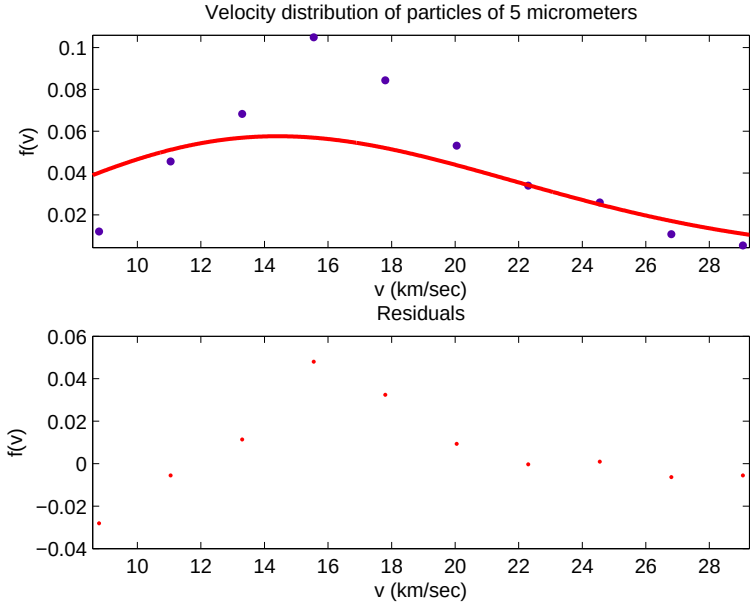

Figure 4.9: Residuals of velocity distribution of particles with $5 \cdot 10^{-4}$ cm of radius.

Goodness of fit statistics

After using graphical methods to evaluate the goodness of fit, we examine the goodness of fit statistics by means of

- sum of squares due to error (SSE);
- R-square;
- adjusted R-square;
- root mean squared error (RMSE).

For dust particles with $5 \cdot 10^{-4}$ cm of radius we report the value in the table (4.1) for the minimum distance distribution and in the table (4.2) for velocity distribution.

Goodness of fit	**Value**
SSE	1363
R-square	0.6242
Adjusted R-square	0.6242
RMSE	15.07

Table 4.1: Goodness of fit for minimum distance distribution of dust particles with $5 \cdot 10^{-4}$ cm of radius.

Goodness of fit	**Value**
SSE	0.004465
R-square	0.5564
Adjusted R-square	0.5564
RMSE	0.02227

Table 4.2: Goodness of fit for velocity distribution of dust particles with 10^{-4} cm of radius.

Confidence and prediction bounds

Confidence and prediction bounds define the lower and upper values of the associated interval, and define the width of the interval. The width of the interval indicates how uncertain there are about the fitted coefficients.

The bounds are defined with a level of certainty that it is possible to specify. The level of certainty is fixed at 95%. Below we report the confidence bound in table 4.3 for minimum distance distribution and in table 4.4 for velocity distribution. The predictions bounds are in figure (4.10) for minimum distance distribution and in figure (4.11) for velocity distribution.

Coefficients of fit	Coefficient values	Confidence bound at 95%
p_1	$1.279 \cdot 10^7$	$8.391 \cdot 10^6 - 1.718 \cdot 10^7$

Table 4.3: Goodness of fit for minimum distance distribution of dust particles with $5 \cdot 10^{-4}$ cm of radius.

Coefficients of fit	Coefficient values	Confidence bound at 95%
a	103.9	$52.52 - 155.3$

Table 4.4: Goodness of fit for velocity distribution of dust particles with $5 \cdot 10^{-4}$ cm of radius.

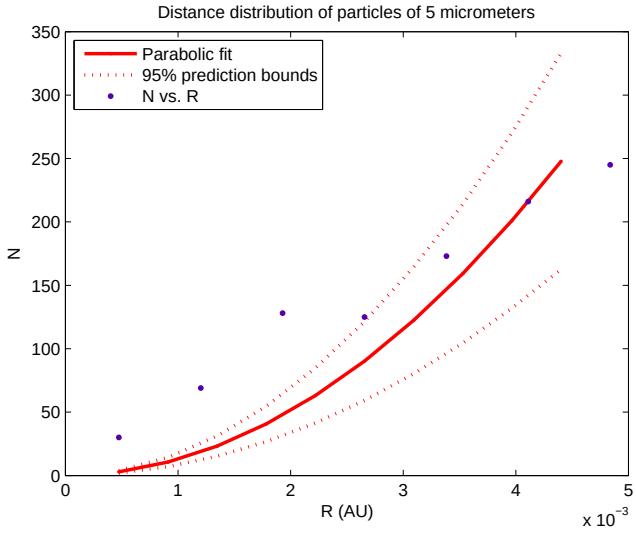

Figure 4.10: Bound of distance distribution of particles with $5 \cdot 10^{-4}$ cm of radius.

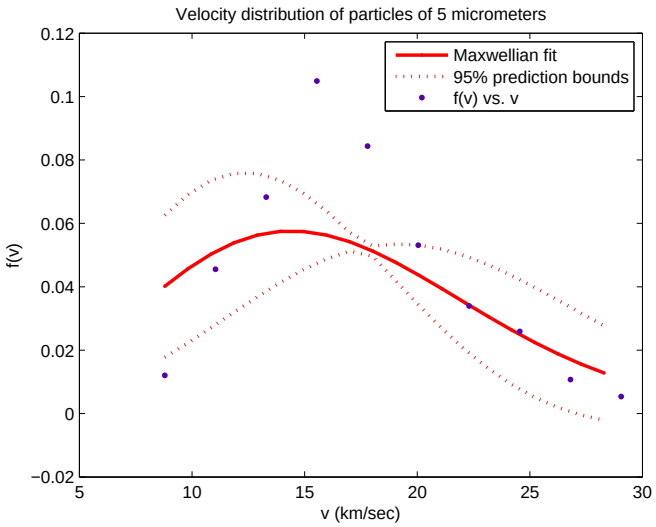

Figure 4.11: Bound of velocity distribution of particles with $5 \cdot 10^{-4}$ cm of radius.

4.3.2 Particles of 10^{-3} cm of radius

Here we consider 1000 particles with 10^{-3} cm of radius. In the figures below we show the three-dimensional coordinates distribution (figure 4.12) the bi-dimensional coordinates distribution (figure 4.13), the histogram that represent the distance distribution of dust particles (figure 4.14), that is the minimum distance particle-Mercury in a ten times the radius of the sphere of influence, and velocity distribution of dust particles (figure 4.15). After this we show in the figures (4.16) and (4.17) the best fit that adapt to our data.

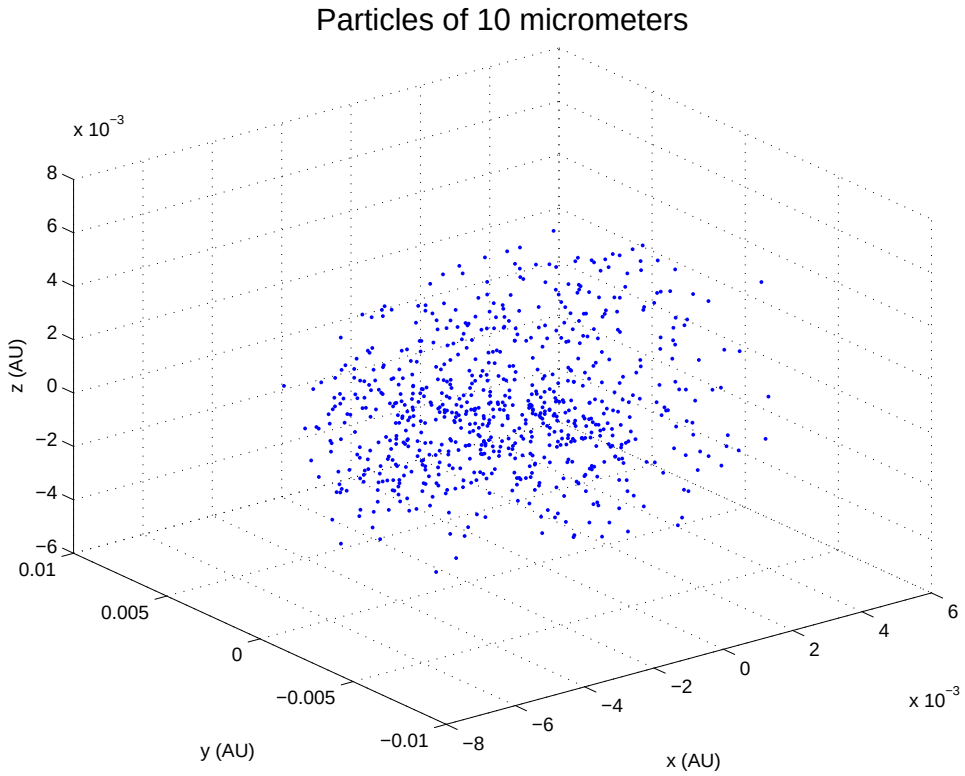

Figure 4.12: Coordinates distribution of particles of 10^{-3} cm of radius.

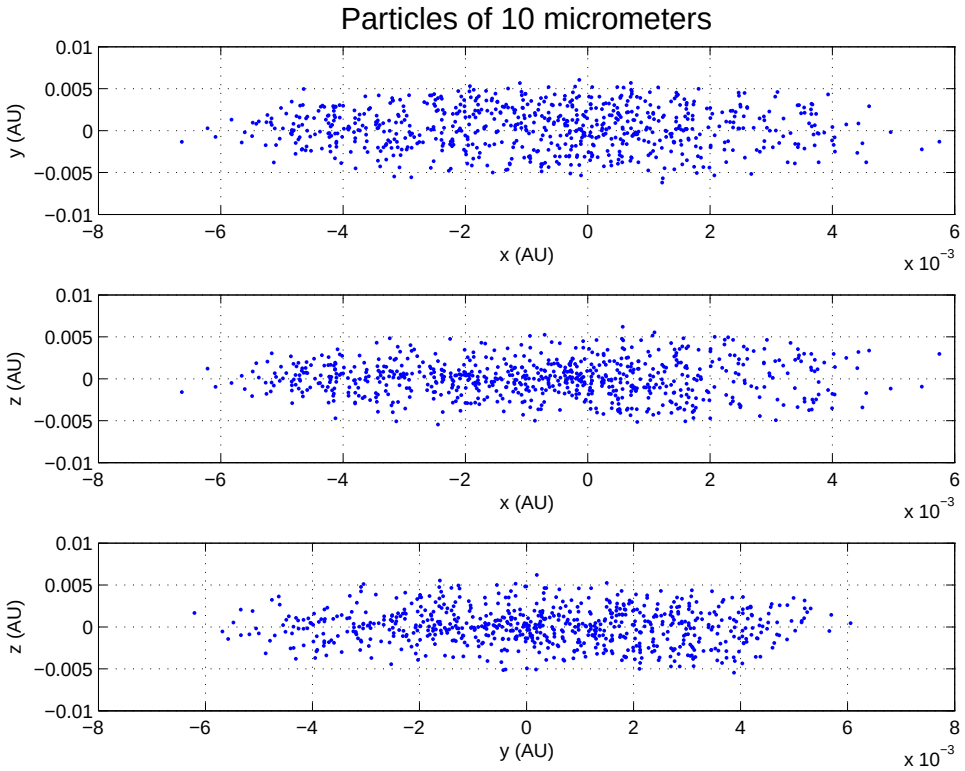

Figure 4.13: Coordinates distribution of particles of 10^{-3} cm of radius.

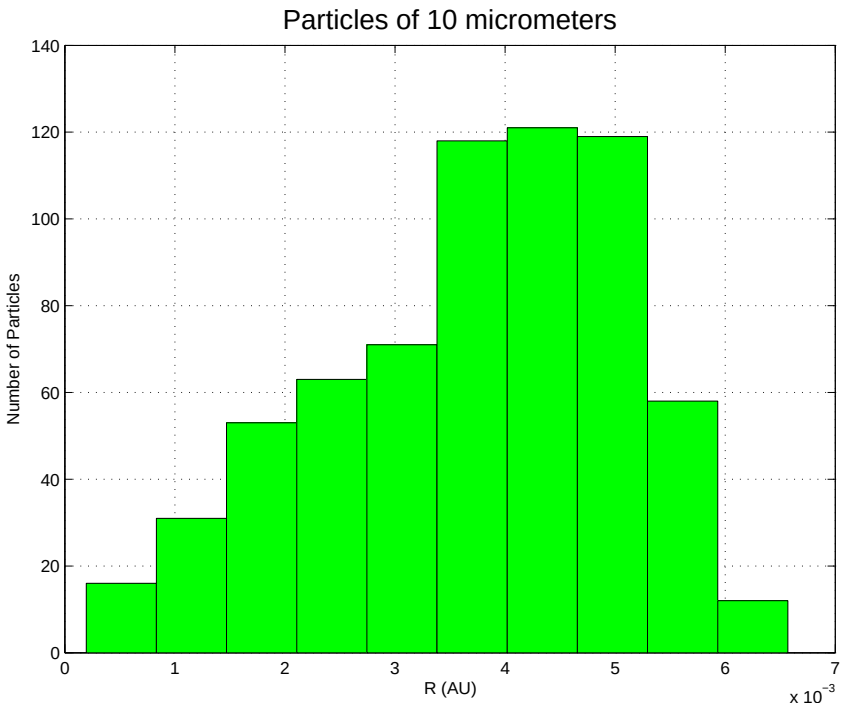

Figure 4.14: Distance distribution of particles of 10^{-3} cm of radius.

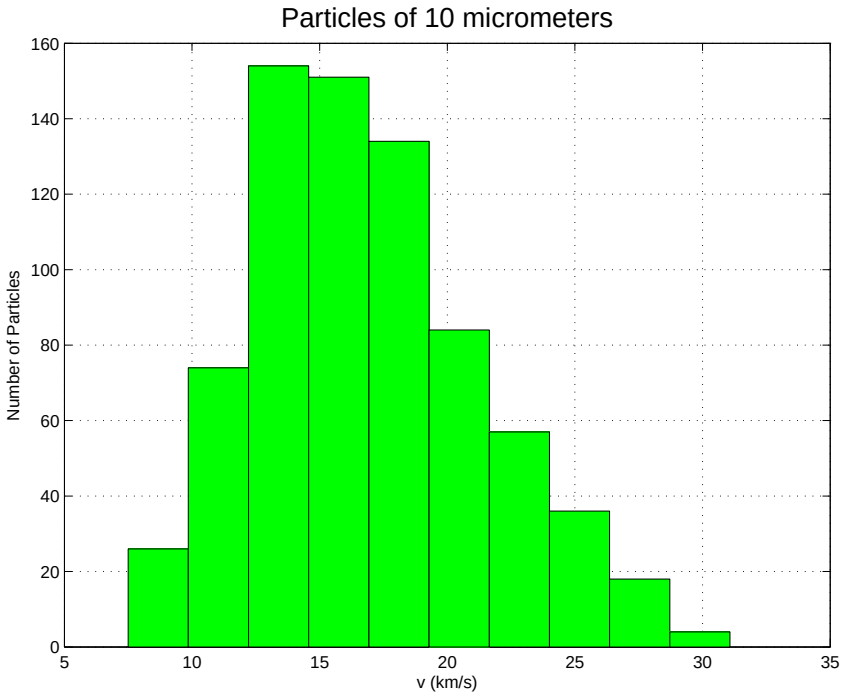

Figure 4.15: Velocity distribution of particles of 10^{-3} cm od radius.

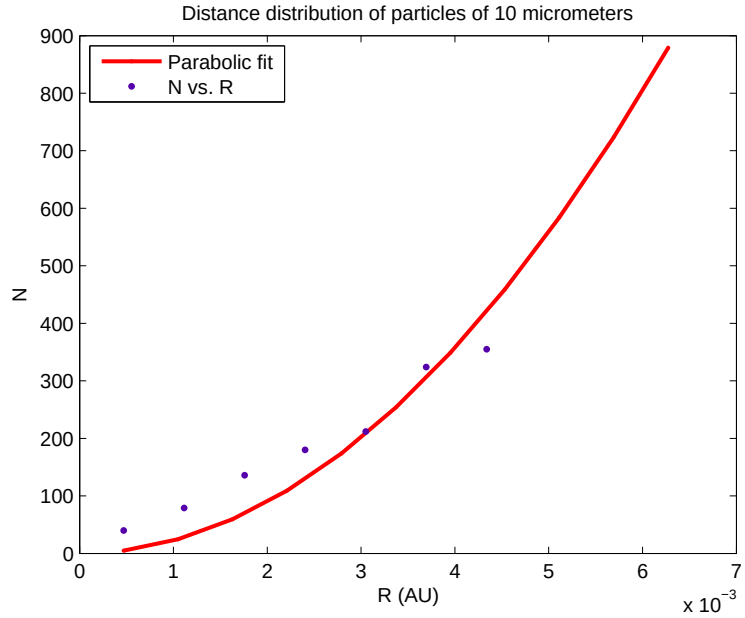

Figure 4.16: Quadratic distance distribution of particles of 10^{-3} cm od radius.

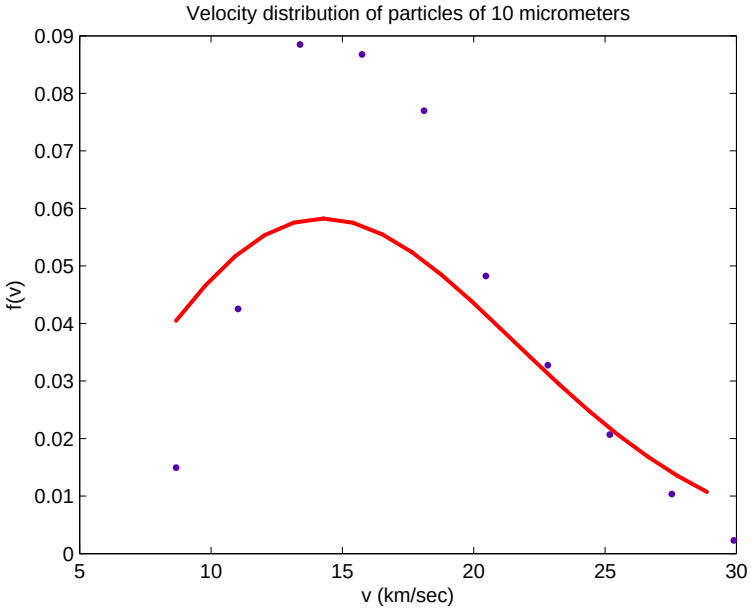

Figure 4.17: Gaussian velocity distribution of particles of 10^{-3} cm od radius.

The best fit for the minimum distance distribution is a polynomial fit of degree 2

$$f(r) = p_1 r^2 \,. \tag{4.31}$$

The best fit for velocity distribution is a maxwellian expression

$$f(v) = \sqrt{\frac{2}{\pi}} a^{-\frac{3}{2}} v^2 \exp\left(-\frac{v^2}{2a}\right) \,. \tag{4.32}$$

Residuals

We show in the figure (4.18) the residuals for the minimum distance distribution and in the figure (4.19) the residuals for the velocity distribution.

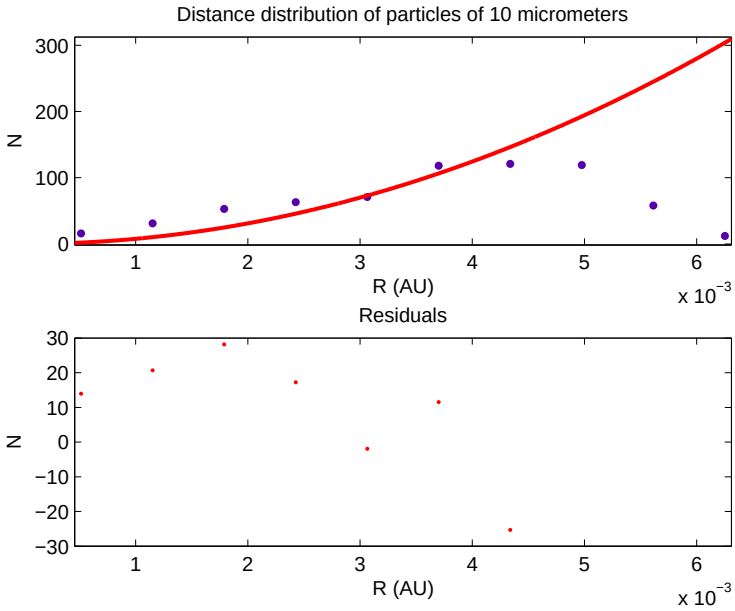

Figure 4.18: Residuals of distance distribution of particles with 10^{-3} *cm* of radius.

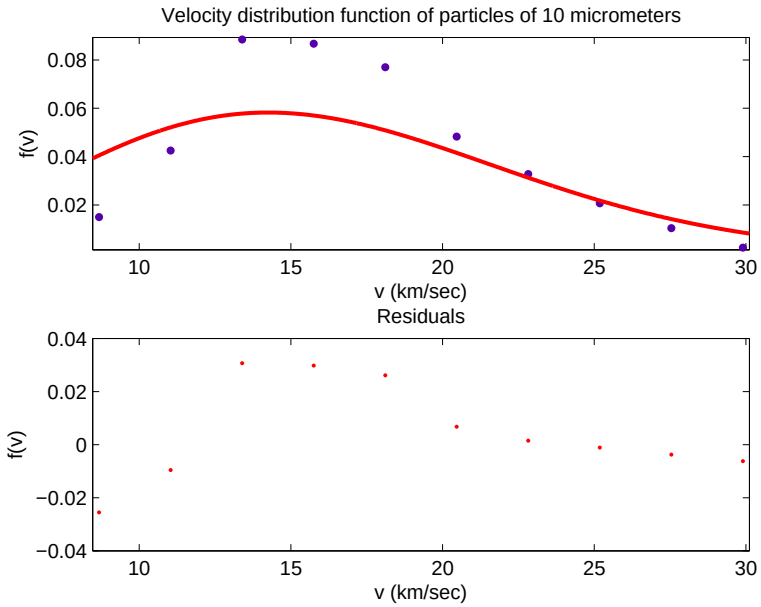

Figure 4.19: Residuals of velocity distribution of particles with 10^{-3} cm of radius.

Goodness of fit statistics

For dust particles with 10^{-3} cm of radius we report the value in the table (4.5) for the minimum distance distribution and in the table (4.6) for velocity distribution.

Goodness of fit	Value
SSE	342.7
R-square	0.7331
Adjusted R-square	0.7331
RMSE	7.558

Table 4.5: Goodness of fit for minimum distance distribution of dust particles with 10^{-3} cm of radius.

Goodness of fit	Value
SSE	0.003355
R-square	0.6384
Adjusted R-square	0.6384
RMSE	0.01931

Table 4.6: Goodness of fit for velocity distribution of dust particles with 10^{-3} cm of radius.

Confidence and prediction bounds

The bounds are defined with a level of certainty that it is possible to specify. The level of certainty is fixed at 95%. Below we report the confidence bound in table 4.7 for minimum distance distribution and in table 4.8 for velocity distribution. The predictions bounds are in figure (4.20) for minimum distance distribution and in figure (4.21) for velocity distribution.

Coefficients of fit	**Coefficient values**	**Confidence bound at 95%**
p_1	$7.774 \cdot 10^6$	$5.498 \cdot 10^6 - 1.005 \cdot 10^7$

Table 4.7: Goodness of fit for minimum distance distribution of dust particles with 10^{-3} cm of radius.

Coefficients of fit	**Coefficient values**	**Confidence bound at 95%**
a	101.6	$58.01 - 145.2$

Table 4.8: Goodness of fit for velocity distribution of dust particles with 10^{-3} cm of radius.

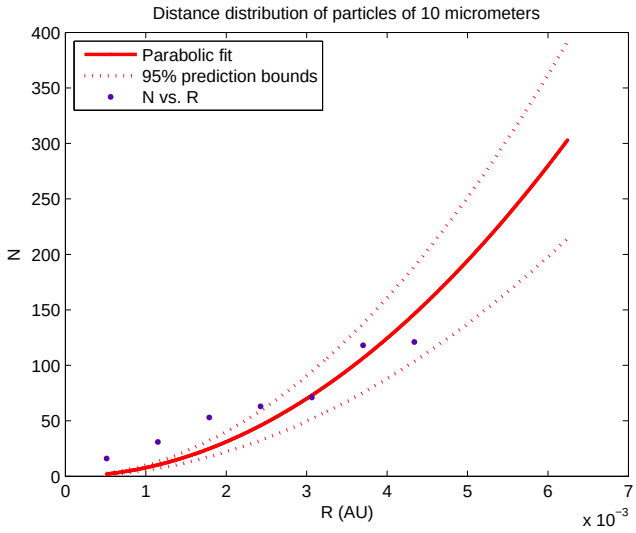

Figure 4.20: Bound of distance distribution of particles with 10^{-3} cm of radius.

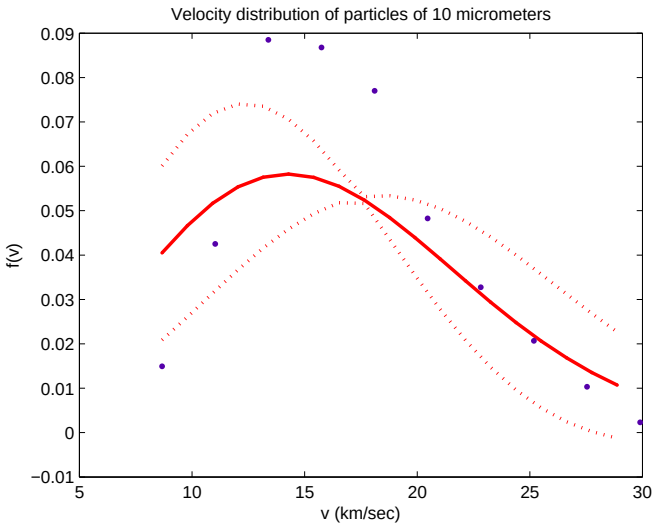

Figure 4.21: Bound of velocity distribution of particles with 10^{-3} cm of radius.

4.3.3 Particles of $2 \cdot 10^{-3}$ cm of radius

Here we consider 1000 particles with $2 \cdot 10^{-3}$ cm of radius. In the figures below we show the three-dimensional coordinates distribution (figure 4.22) the bi-dimensional coordinates distribution (figure 4.23), the histogram that represent the distance distribution of dust particles (figure 4.24), that is the minimum distance particle-Mercury in a ten times the radius of the sphere of influence, and velocity distribution of dust particles (figure 4.25). After this we show in the figures (4.26) and (4.27) the best fit that adapt to our data.

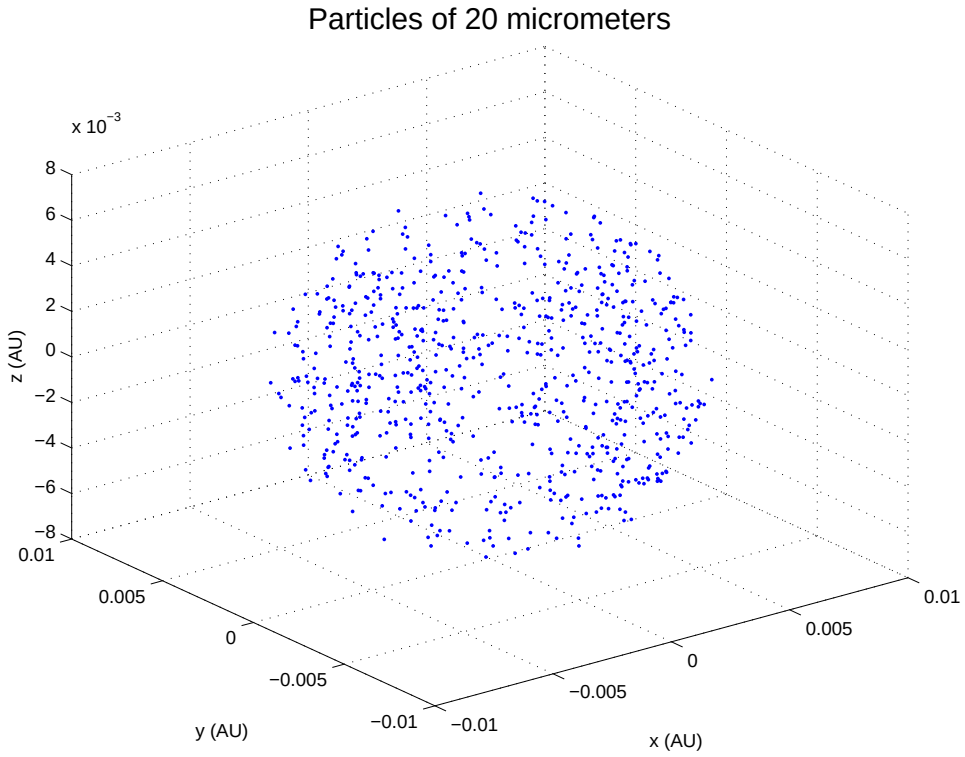

Figure 4.22: Coordinates distribution of particles of $2 \cdot 10^{-3}$ cm of radius.

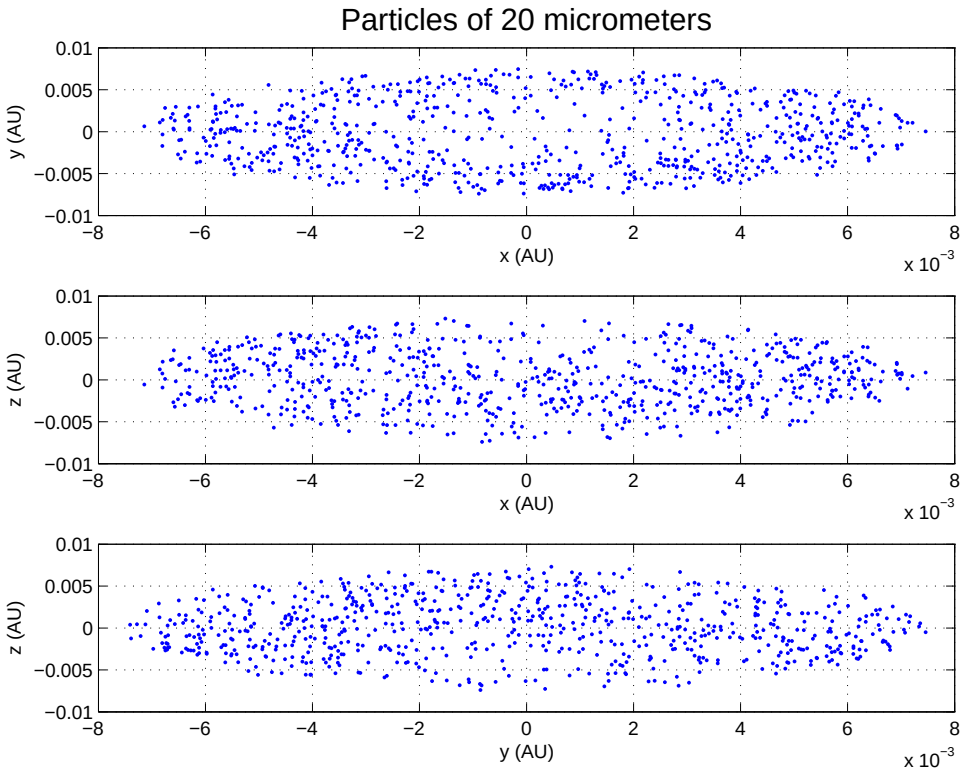

Figure 4.23: Coordinates distribution of particles of $2 \cdot 10^{-3}$ cm of radius.

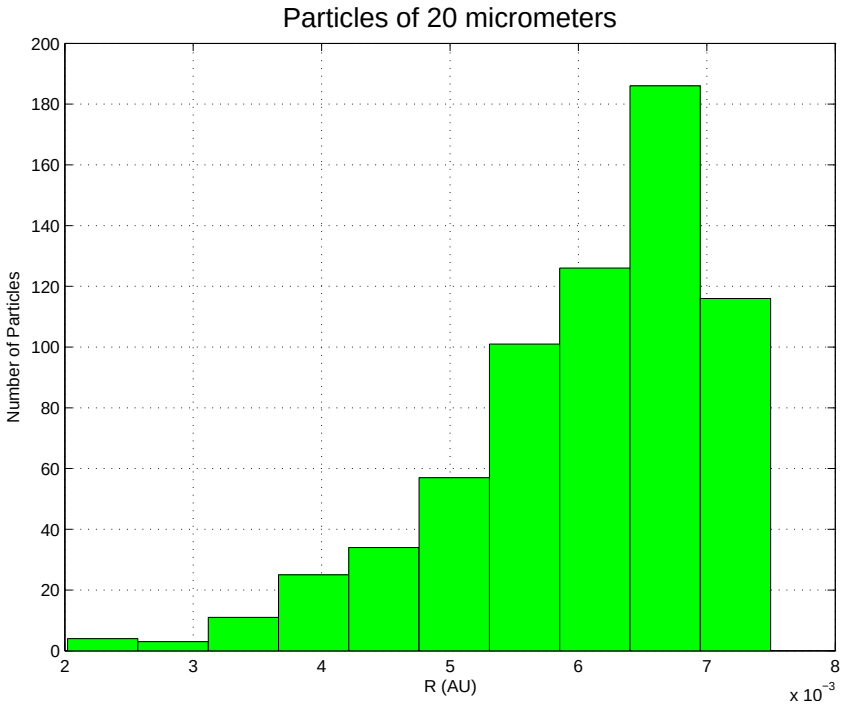

Figure 4.24: Distance distribution of particles of $2 \cdot 10^{-3}$ cm of radius.

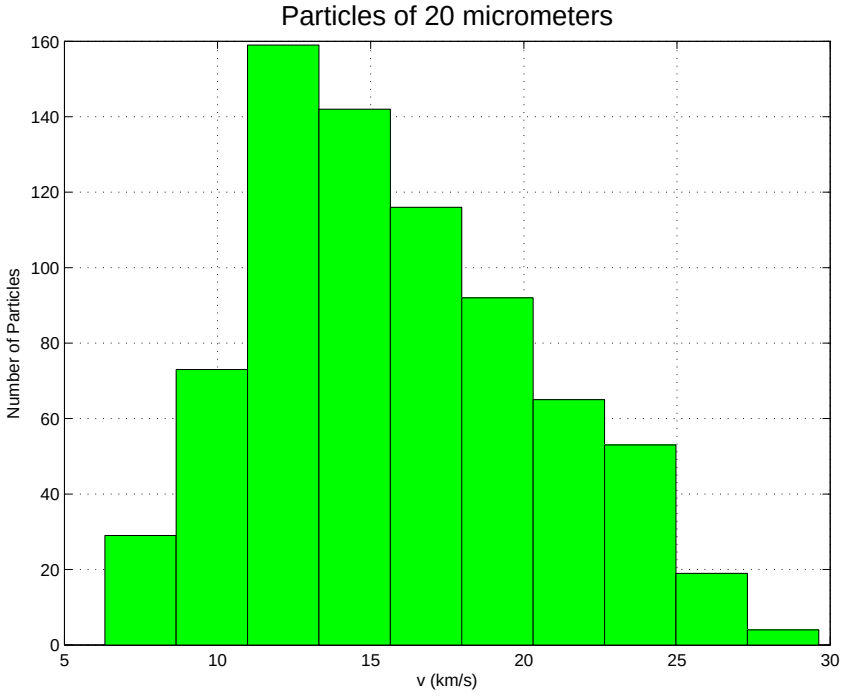

Figure 4.25: Velocity distribution of particles of $2 \cdot 10^{-3}$ cm od radius.

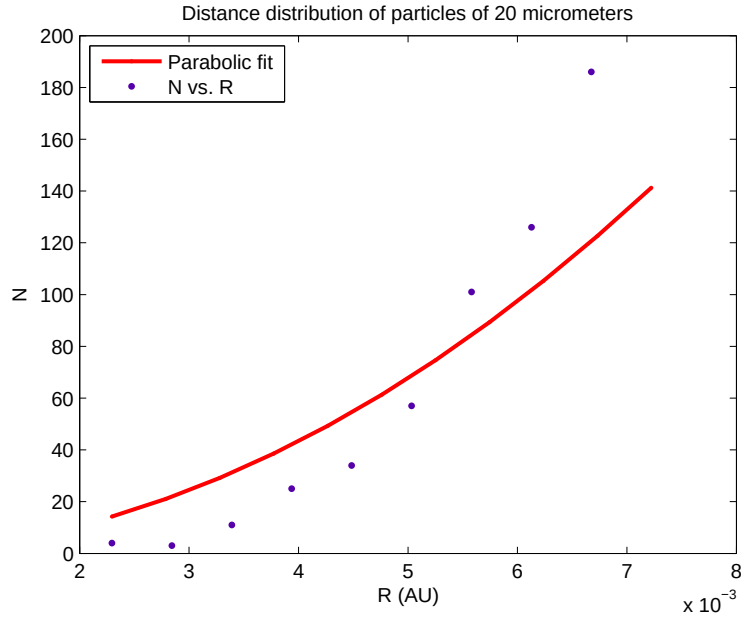

Figure 4.26: Quadratic distance distribution of particles of $2 \cdot 10^{-3}$ cm od radius.

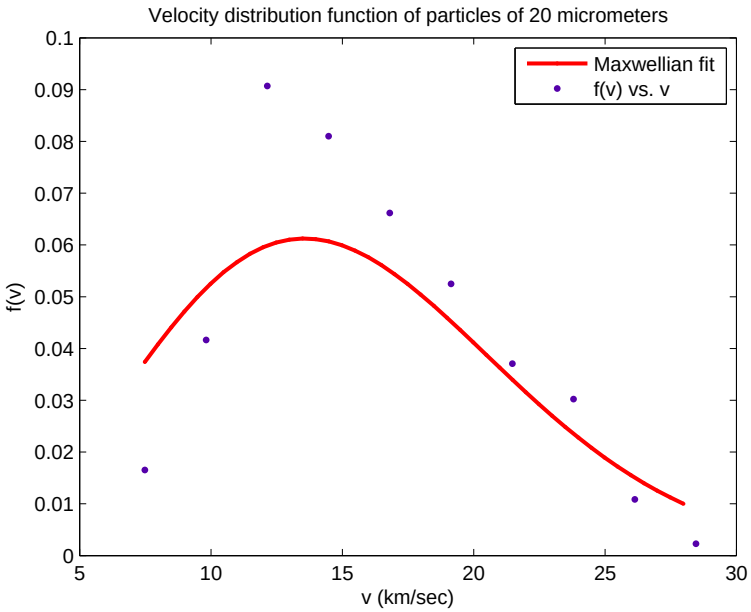

Figure 4.27: Gaussian velocity distribution of particles of $2 \cdot 10^{-3}$ cm od radius.

The best fit for the minimum distance distribution is a polynomial fit of degree 2

$$f(r) = p_1 r^2 \,. \tag{4.33}$$

The best fit for velocity distribution is a maxwellian expression

$$f(v) = \sqrt{\frac{2}{\pi}} a^{-\frac{3}{2}} v^2 \exp\left(-\frac{v^2}{2a}\right) \,. \tag{4.34}$$

Residuals

We show in the figure (4.28) the residuals for the minimum distance distribution and in the figure (4.29) the residuals for the velocity distribution.

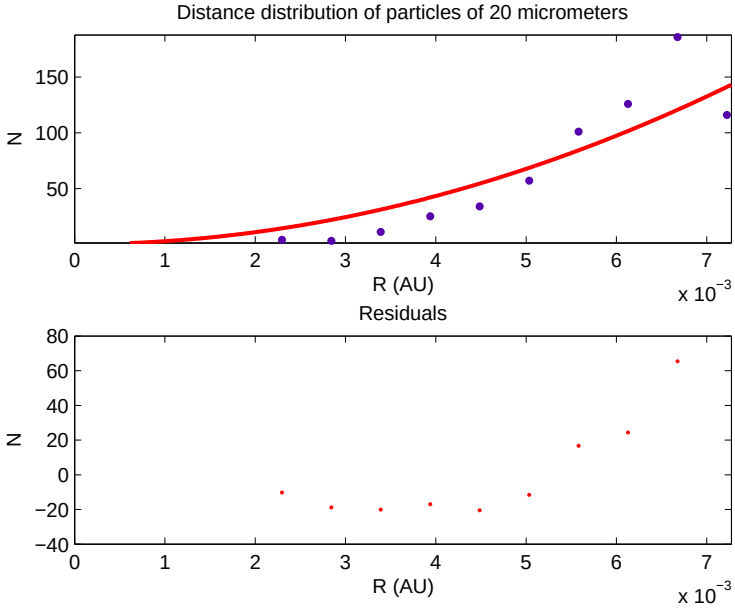

Figure 4.28: Residuals of distance distribution of particles with $2 \cdot 10^{-3}$ *cm* of radius.

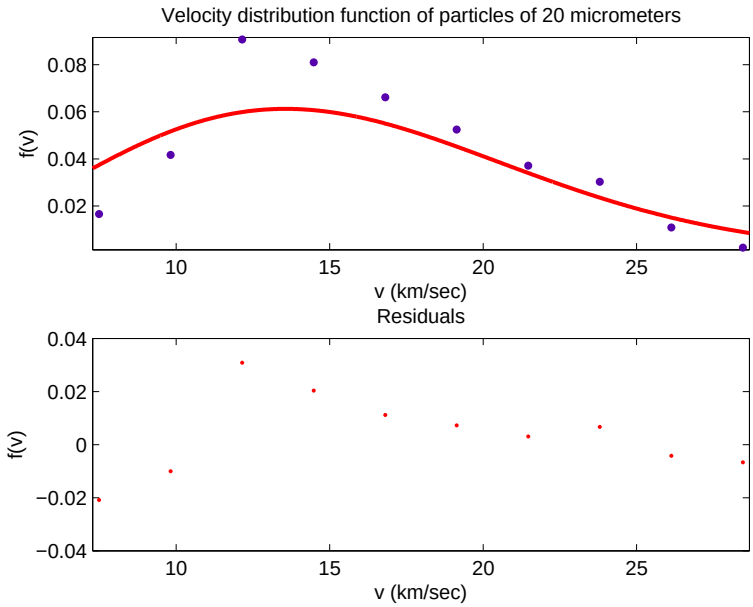

Figure 4.29: Residuals of velocity distribution of particles with $2 \cdot 10^{-3}$ cm of radius.

Goodness of fit statistics

For dust particles with $2 \cdot 10^{-3}$ cm of radius we report the value in the table (4.9) for the minimum distance distribution and in the table (4.10) for velocity distribution.

Goodness of fit	Value
SSE	921.7
R-square	0.7736
Adjusted R-square	0.7736
RMSE	10.73

Table 4.9: Goodness of fit for minimum distance distribution of dust particles with $2 \cdot 10^{-3}$ cm of radius.

Goodness of fit	Value
SSE	0.002193
R-square	0.7238
Adjusted R-square	0.7238
RMSE	0.01561

Table 4.10: Goodness of fit for velocity distribution of dust particles with $2 \cdot 10^{-3}$ cm of radius.

Confidence and prediction bounds

The bounds are defined with a level of certainty that it is possible to specify. The level of certainty is fixed at 95%. Below we report the confidence bound in table 4.11 for minimum distance distribution and in table 4.12 for velocity distribution. The predictions bounds are in figure (4.30) for minimum distance distribution and in figure (4.31) for velocity distribution.

Coefficients of fit	Coefficient values	Confidence bound at 95%
p_1	$2.707 \cdot 10^6$	$1.744 \cdot 10^6 - 3.669 \cdot 10^6$

Table 4.11: Goodness of fit for minimum distance distribution of dust particles with $2 \cdot 10^{-3}$ cm of radius.

Coefficients of fit	Coefficient values	Confidence bound at 95%
a	91.91	$61.78 - 122$

Table 4.12: Goodness of fit for velocity distribution of dust particles with $2 \cdot 10^{-3}$ cm of radius.

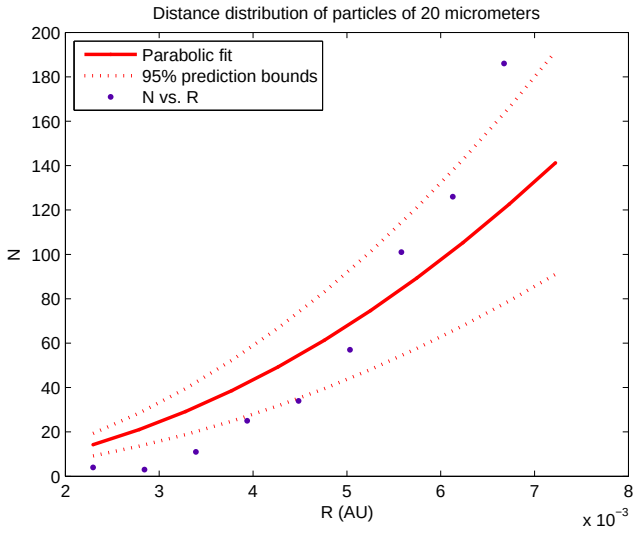

Figure 4.30: Bound of distance distribution of particles with $2 \cdot 10^{-3}$ cm of radius.

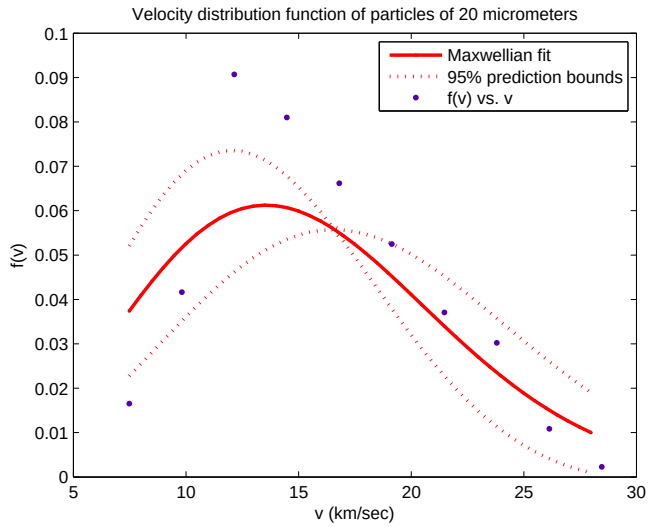

Figure 4.31: Bound of velocity distribution of particles with $2 \cdot 10^{-3}$ cm of radius.

4.3.4 Particles of $3 \cdot 10^{-3}$ cm of radius

Here we consider 1000 particles with $3 \cdot 10^{-3}$ cm of radius. In the figures below we show the three-dimensional coordinates distribution (figure 4.32) the bi-dimensional coordinates distribution (figure 4.33), the histogram that represent the distance distribution of dust particles (figure 4.34), that is the minimum distance particle-Mercury in a ten times the radius of the sphere of influence, and velocity distribution of dust particles (figure 4.35). After this we show in the figures (4.36) and (4.37) the best fit that adapt to our data.

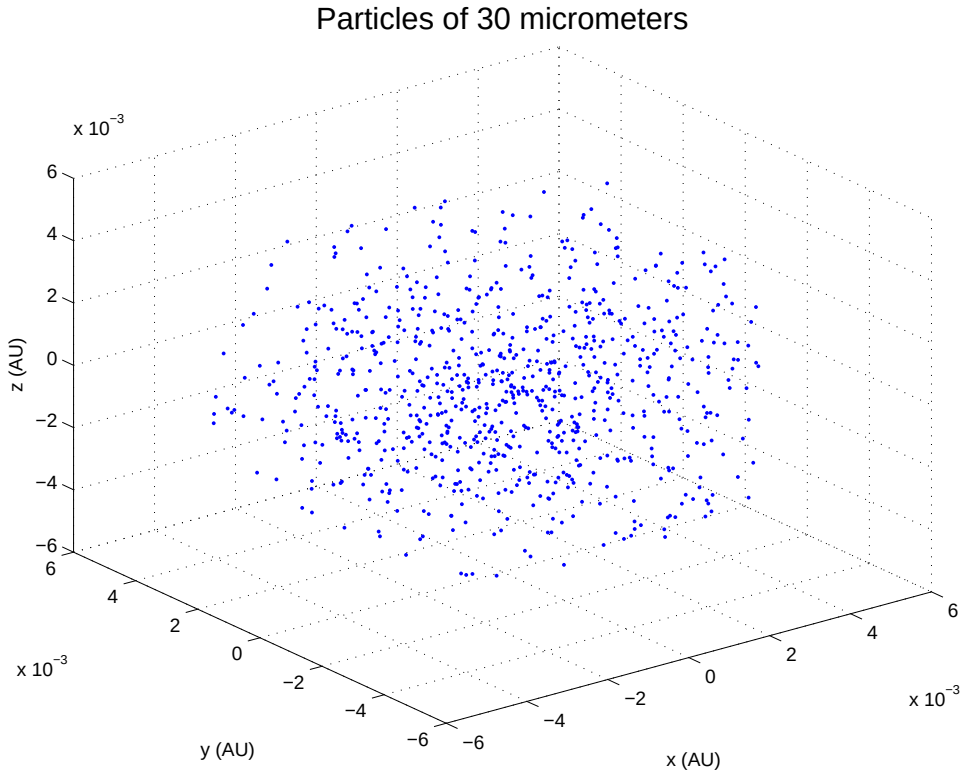

Figure 4.32: Coordinates distribution of particles of $3 \cdot 10^{-3}$ cm of radius.

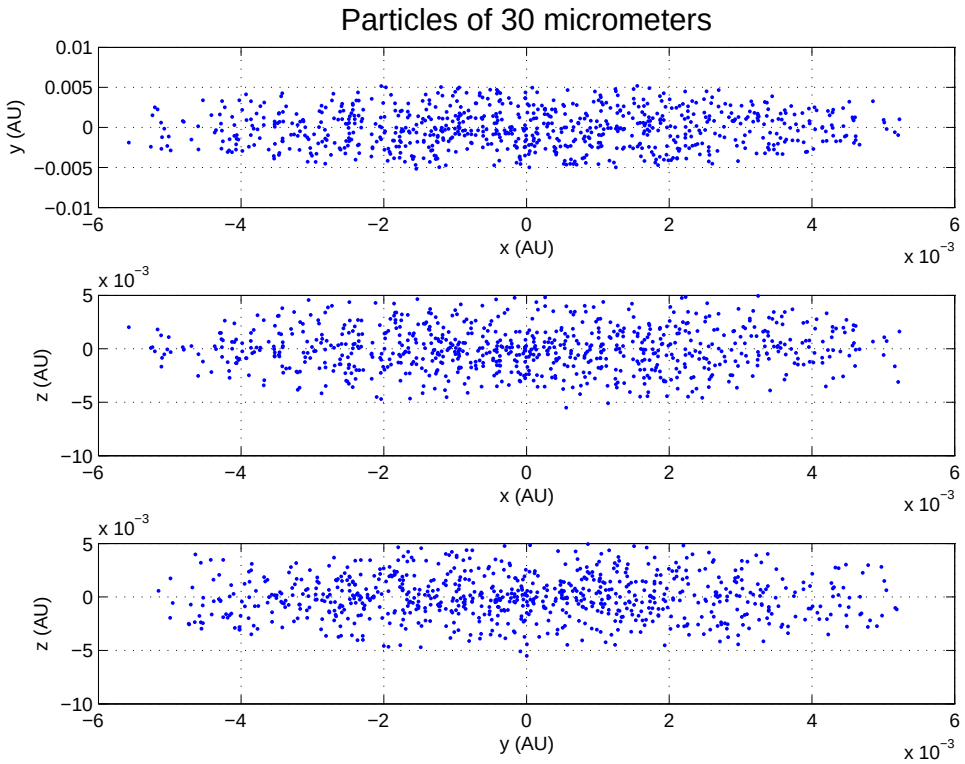

Figure 4.33: Coordinates distribution of particles of $3 \cdot 10^{-3}$ cm of radius.

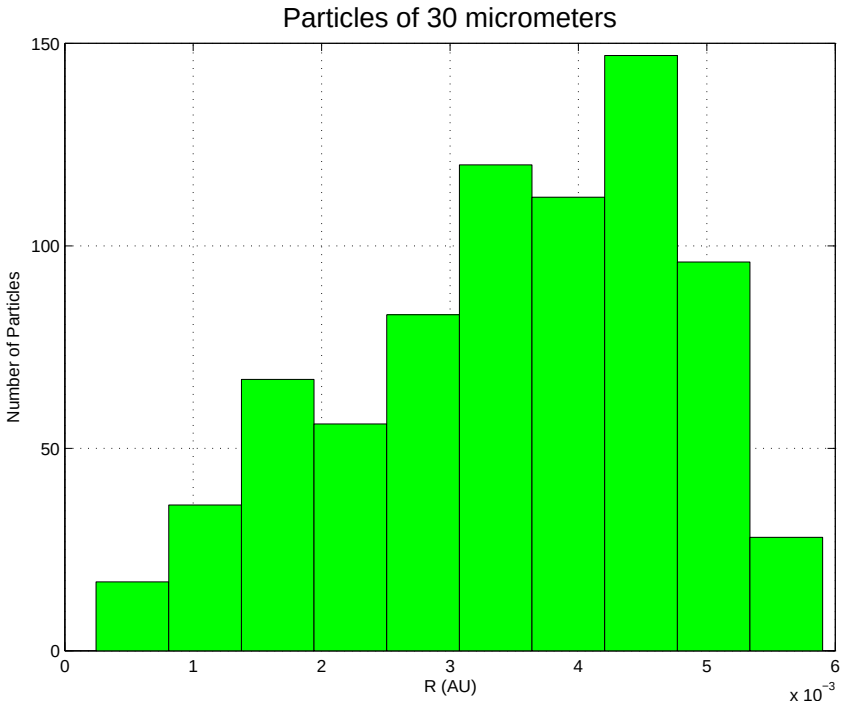

Figure 4.34: Distance distribution of particles of $3 \cdot 10^{-3}$ cm of radius.

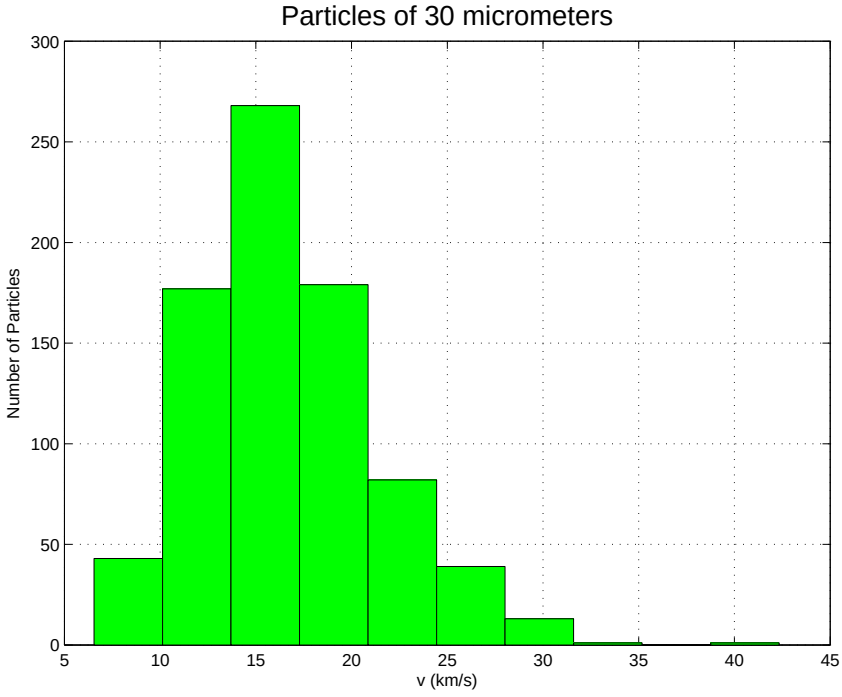

Figure 4.35: Velocity distribution of particles of $3 \cdot 10^{-3}$ cm od radius.

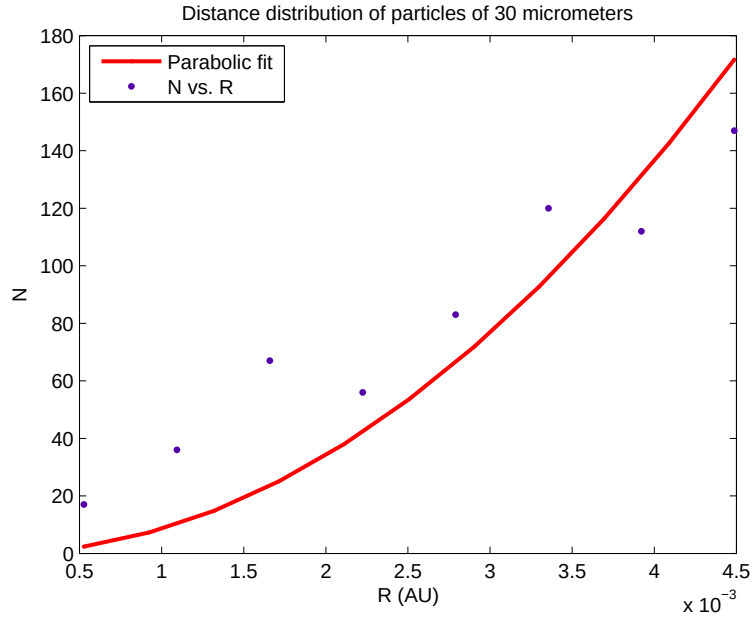

Figure 4.36: Quadratic distance distribution of particles of $3 \cdot 10^{-3}$ cm od radius.

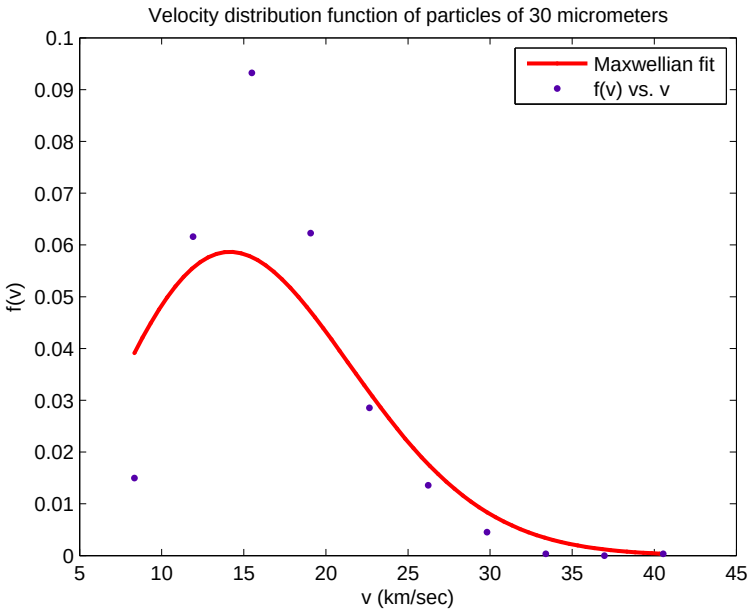

Figure 4.37: Gaussian velocity distribution of particles of $3 \cdot 10^{-3}$ cm od radius.

The best fit for the minimum distance distribution is a polynomial fit of degree 2

$$f(r) = p_1 r^2 \,. \tag{4.35}$$

The best fit for velocity distribution is a maxwellian expression

$$f(v) = \sqrt{\frac{2}{\pi}} a^{-\frac{3}{2}} v^2 \exp\left(-\frac{v^2}{2a}\right) \,. \tag{4.36}$$

Residuals

We show in the figure (4.38) the residuals for the minimum distance distribution and in the figure (4.39) the residuals for the velocity distribution.

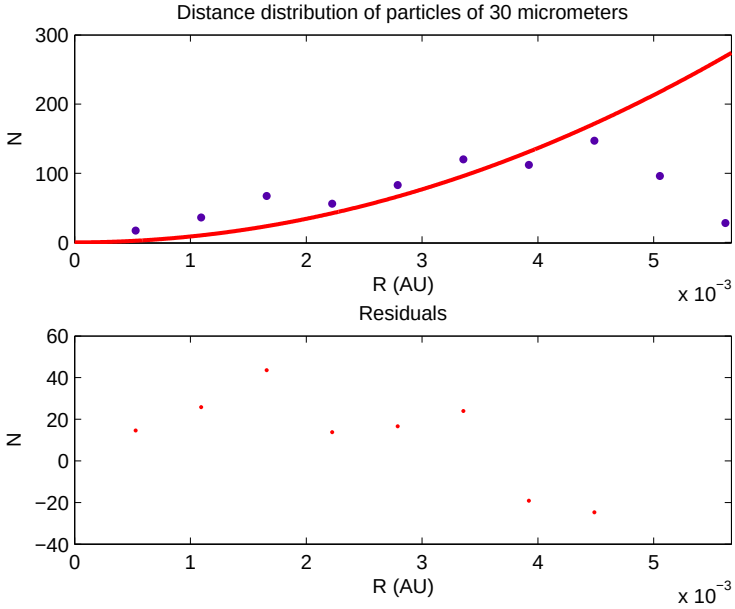

Figure 4.38: Residuals of distance distribution of particles with $3 \cdot 10^{-3}$ *cm* of radius.

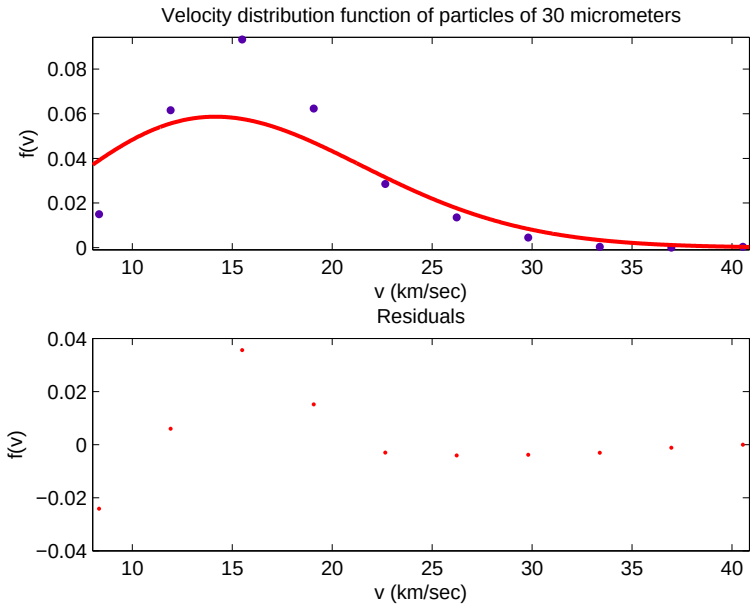

Figure 4.39: Residuals of velocity distribution of particles with $3 \cdot 10^{-3}$ cm of radius.

Goodness of fit statistics

For dust particles with $3 \cdot 10^{-3}$ cm of radius we report the value in the table (4.13) for the minimum distance distribution and in the table (4.14) for velocity distribution.

Goodness of fit	Value
SSE	588.1
R-square	0.6705
Adjusted R-square	0.6705
RMSE	9.166

Table 4.13: Goodness of fit for minimum distance distribution of dust particles with $3 \cdot 10^{-3}$ cm of radius.

Goodness of fit	Value
SSE	0.002167
R-square	0.779
Adjusted R-square	0.779
RMSE	0.01552

Table 4.14: Goodness of fit for velocity distribution of dust particles with $3 \cdot 10^{-3}$ cm of radius.

Confidence and prediction bounds

The bounds are defined with a level of certainty that it is possible to specify. The level of certainty is fixed at 95%. Below we report the confidence bound in table 4.15 for minimum distance distribution and in table 4.16 for velocity distribution. The predictions bounds are in figure (4.40) for minimum distance distribution and in figure (4.41) for velocity distribution.

Coefficients of fit	**Coefficient values**	**Confidence bound at 95%**
p_1	$8.526 \cdot 10^6$	$6.079 \cdot 10^6 - 1.097 \cdot 10^7$

Table 4.15: Goodness of fit for minimum distance distribution of dust particles with $3 \cdot 10^{-3}$ cm of radius.

Coefficients of fit	**Coefficient values**	**Confidence bound at 95%**
a	100.2	59.88 – 140.4

Table 4.16: Goodness of fit for velocity distribution of dust particles with $3 \cdot 10^{-3}$ cm of radius.

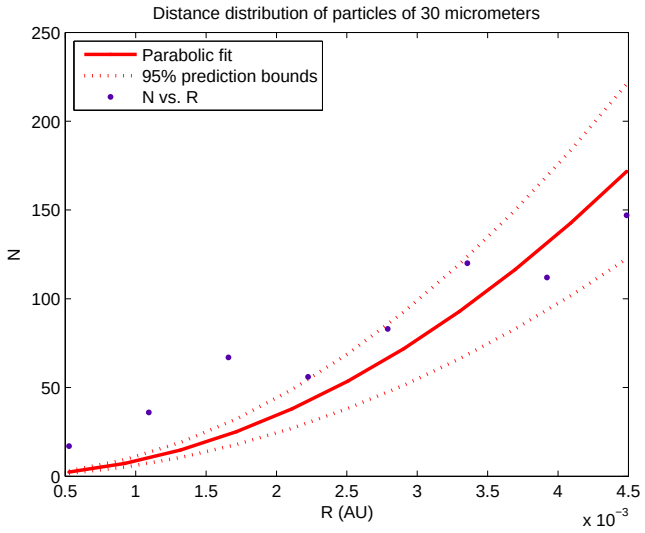

Figure 4.40: Bound of distance distribution of particles with $3 \cdot 10^{-3}$ cm of radius.

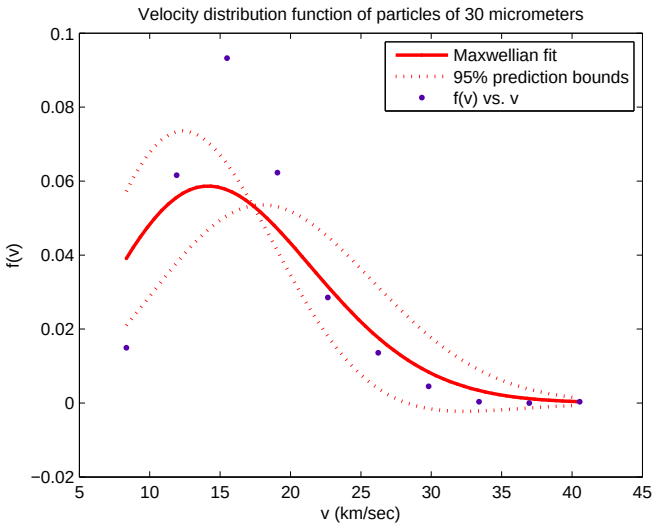

Figure 4.41: Bound of velocity distribution of particles with $3 \cdot 10^{-3}$ cm of radius.

4.3.5 Particles of $4 \cdot 10^{-3}$ cm of radius

Here we consider 1000 particles with $4 \cdot 10^{-3}$ cm of radius. In the figures below we show the three-dimensional coordinates distribution (figure 4.42) the bi-dimensional coordinates distribution (figure 4.43), the histogram that represent the distance distribution of dust particles (figure 4.44), that is the minimum distance particle-Mercury in a ten times the radius of the sphere of influence, and velocity distribution of dust particles (figure 4.45). After this we show in the figures (4.46) and (4.47) the best fit that adapt to our data.

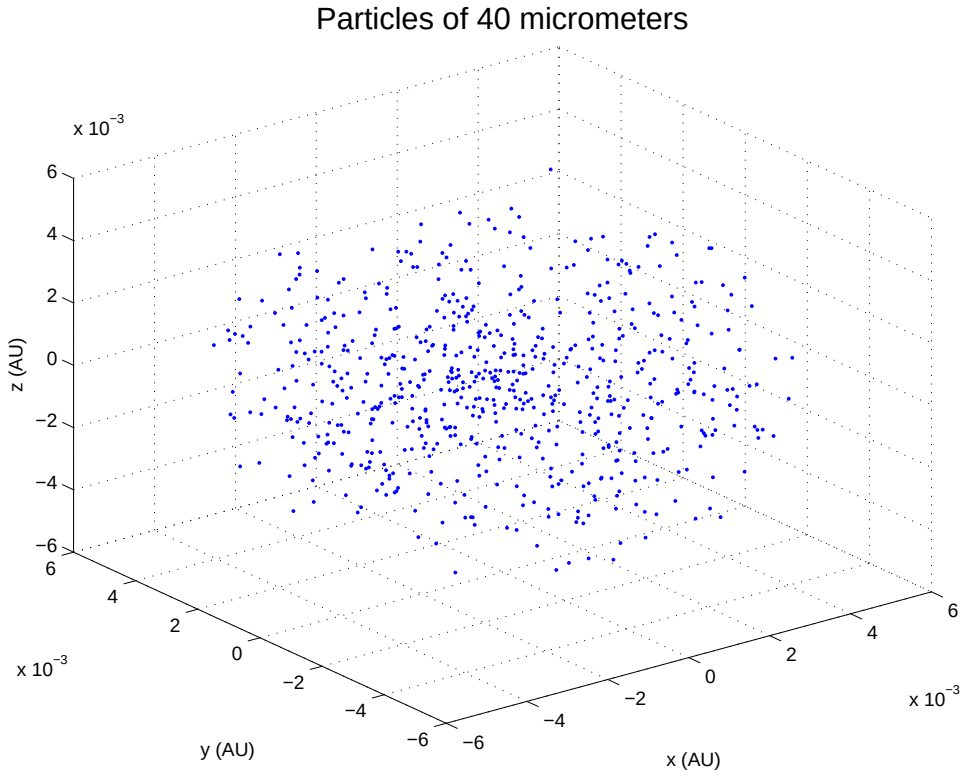

Figure 4.42: Coordinates distribution of particles of $4 \cdot 10^{-3}$ *cm* of radius.

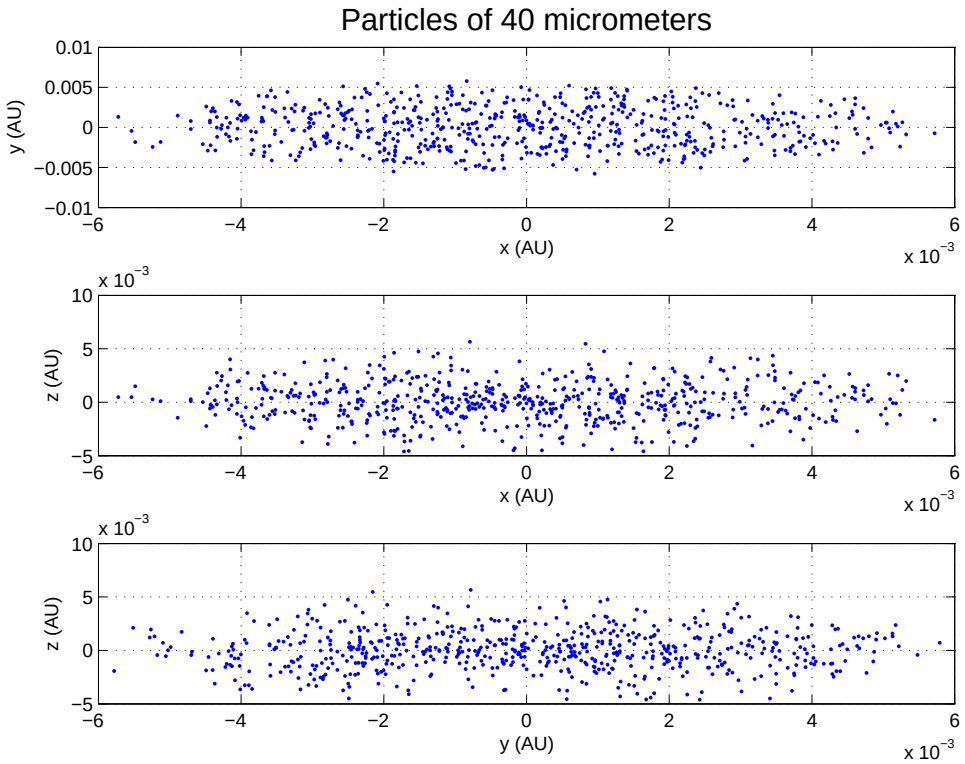

Figure 4.43: Coordinates distribution of particles of $4 \cdot 10^{-3}$ *cm* of radius.

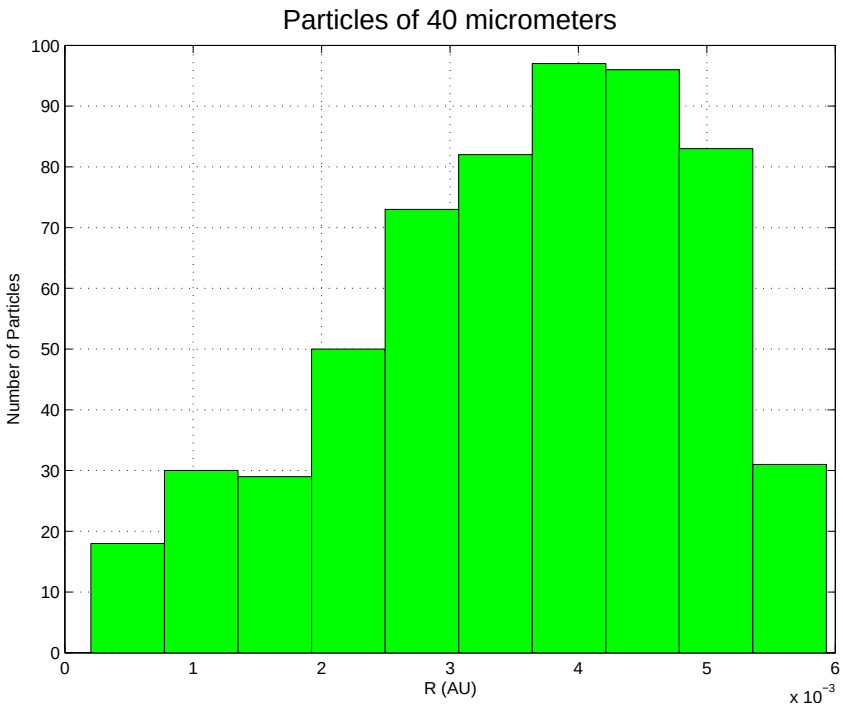

Figure 4.44: Distance distribution of particles of $4 \cdot 10^{-3}$ cm of radius.

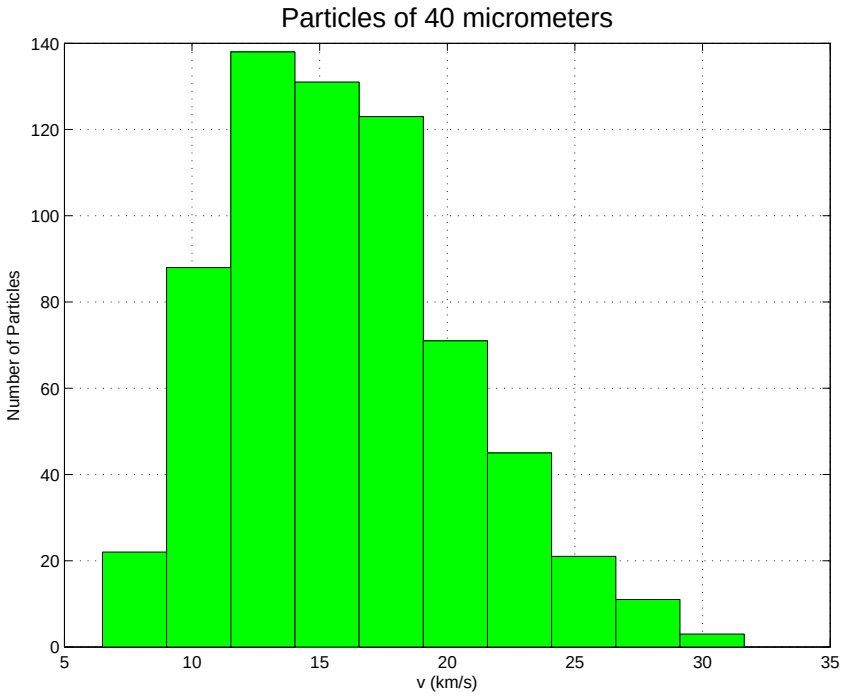

Figure 4.45: Velocity distribution of particles of $4 \cdot 10^{-3}$ cm od radius.

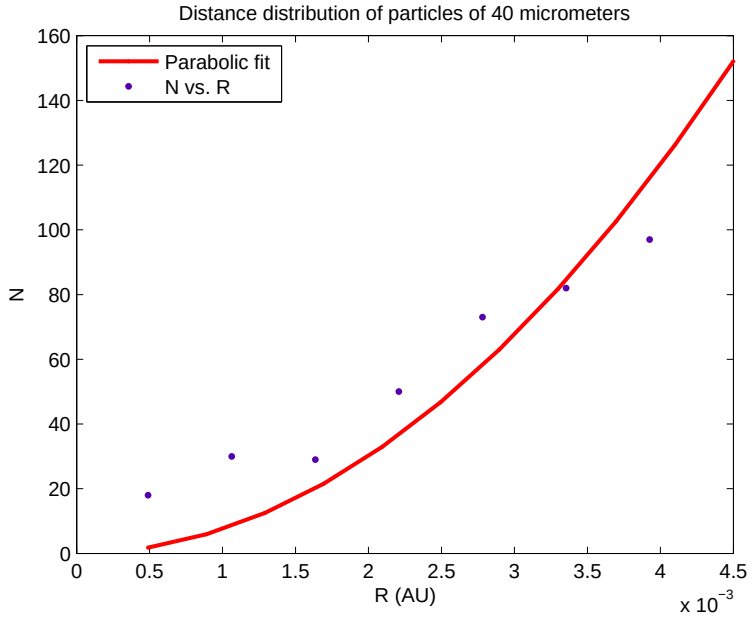

Figure 4.46: Quadratic distance distribution of particles of $4 \cdot 10^{-3}$ cm od radius.

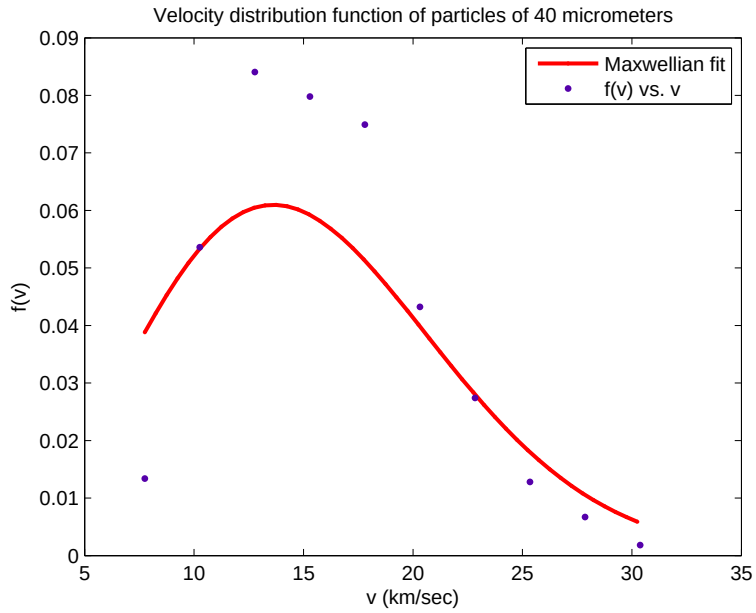

Figure 4.47: Gaussian velocity distribution of particles of $4 \cdot 10^{-3}$ cm od radius.

The best fit for the minimum distance distribution is a polynomial fit of degree 2

$$f(r) = p_1 r^2 \,. \tag{4.37}$$

The best fit for velocity distribution is a maxwellian expression

$$f(v) = \sqrt{\frac{2}{\pi}} a^{-\frac{3}{2}} v^2 \exp\left(-\frac{v^2}{2a}\right) \,. \tag{4.38}$$

Residuals

We show in the figure (4.38) the residuals for the minimum distance distribution and in the figure (4.39) the residuals for the velocity distribution.

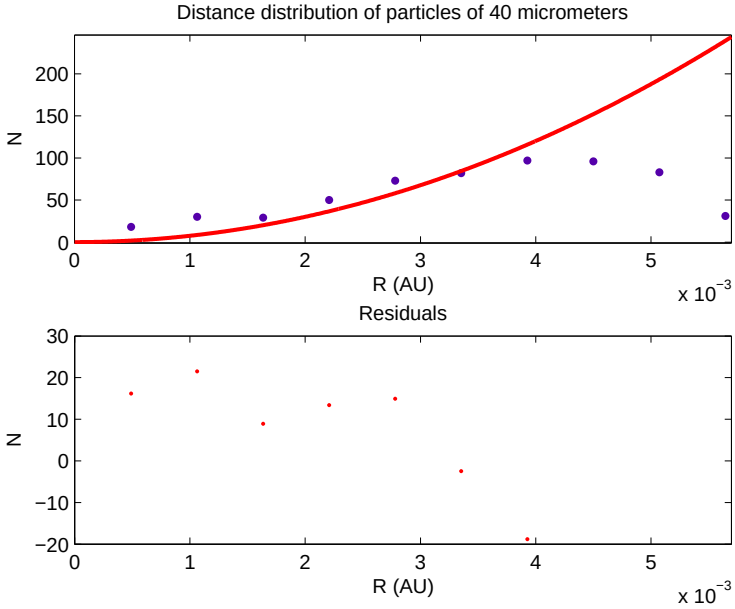

Figure 4.48: Residuals of distance distribution of particles with $4 \cdot 10^{-3}$ *cm* of radius.

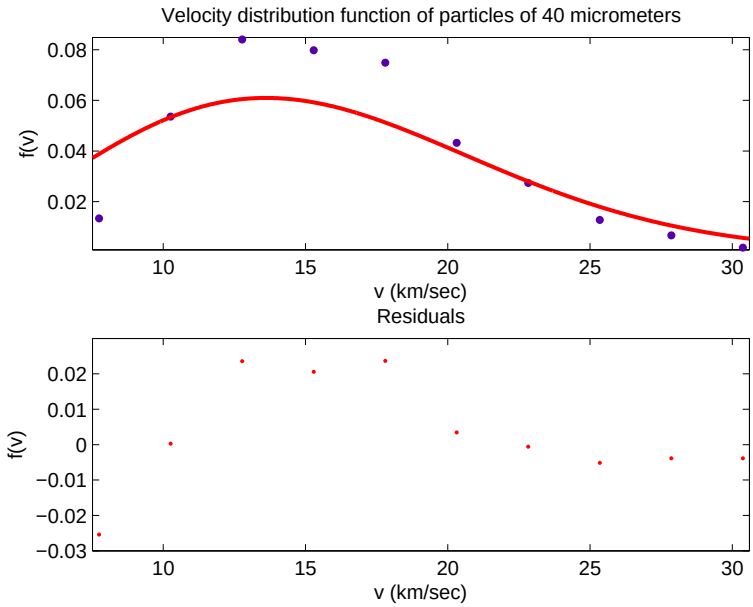

Figure 4.49: Residuals of velocity distribution of particles with $4 \cdot 10^{-3}$ cm of radius.

Goodness of fit statistics

For dust particles with $4 \cdot 10^{-3}$ cm of radius we report the value in the table (4.17) for the minimum distance distribution and in the table (4.18) for velocity distribution.

Goodness of fit	**Value**
SSE	249
R-square	0.6807
Adjusted R-square	0.6807
RMSE	6.443

Table 4.17: Goodness of fit for minimum distance distribution of dust particles with $4 \cdot 10^{-3}$ cm of radius.

Goodness of fit	**Value**
SSE	0.002251
R-square	0.7529
Adjusted R-square	0.7529
RMSE	0.01582

Table 4.18: Goodness of fit for velocity distribution of dust particles with $4 \cdot 10^{-3}$ cm of radius.

Confidence and prediction bounds

The bounds are defined with a level of certainty that it is possible to specify. The level of certainty is fixed at 95%. Below we report the confidence bound in table 4.19 for minimum distance distribution and in table 4.20 for velocity distribution. The predictions bounds are in figure (4.50) for minimum distance distribution and in figure (4.51) for velocity distribution.

Coefficients of fit	Coefficient values	Confidence bound at 95%
p_1	$7.51 \cdot 10^6$	$5.282 \cdot 10^6 - 9.738 \cdot 10^7$

Table 4.19: Goodness of fit for minimum distance distribution of dust particles with $4 \cdot 10^{-3}$ cm of radius.

Coefficients of fit	Coefficient values	Confidence bound at 95%
a	92.71	$60.94 - 124.5$

Table 4.20: Goodness of fit for velocity distribution of dust particles with $4 \cdot 10^{-3}$ cm of radius.

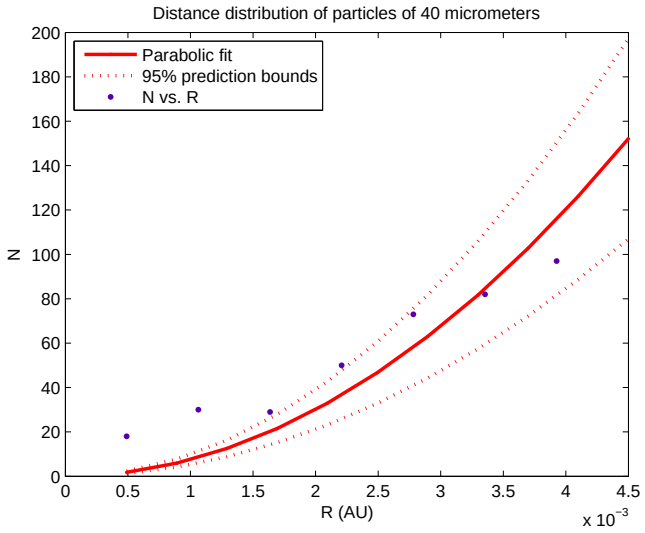

Figure 4.50: Bound of distance distribution of particles with $4 \cdot 10^{-3}$ cm of radius.

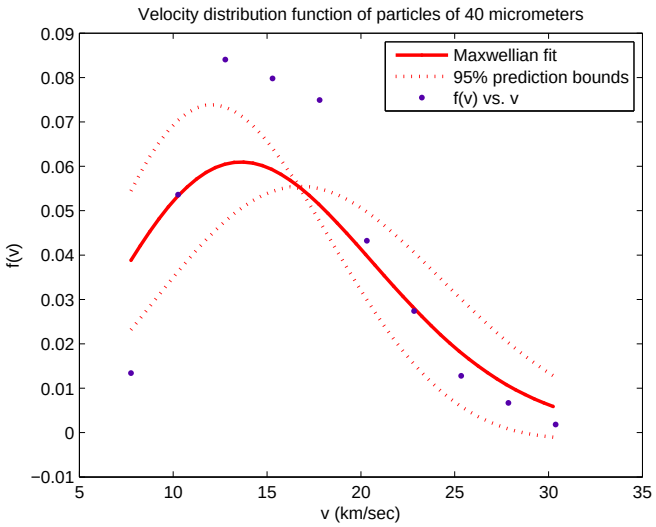

Figure 4.51: Bound of velocity distribution of particles with $4 \cdot 10^{-3}$ cm of radius.

4.3.6 Particles of $5 \cdot 10^{-3}$ cm of radius

Here we consider 1000 particles with $5 \cdot 10^{-3}$ cm of radius. In the figures below we show the three-dimensional coordinates distribution (figure 4.52) the bi-dimensional coordinates distribution (figure 4.53), the histogram that represent the distance distribution of dust particles (figure 4.54), that is the minimum distance particle-Mercury in a ten times the radius of the sphere of influence, and velocity distribution of dust particles (figure 4.55). After this we show in the figures (4.56) and (4.57) the best fit that adapt to our data.

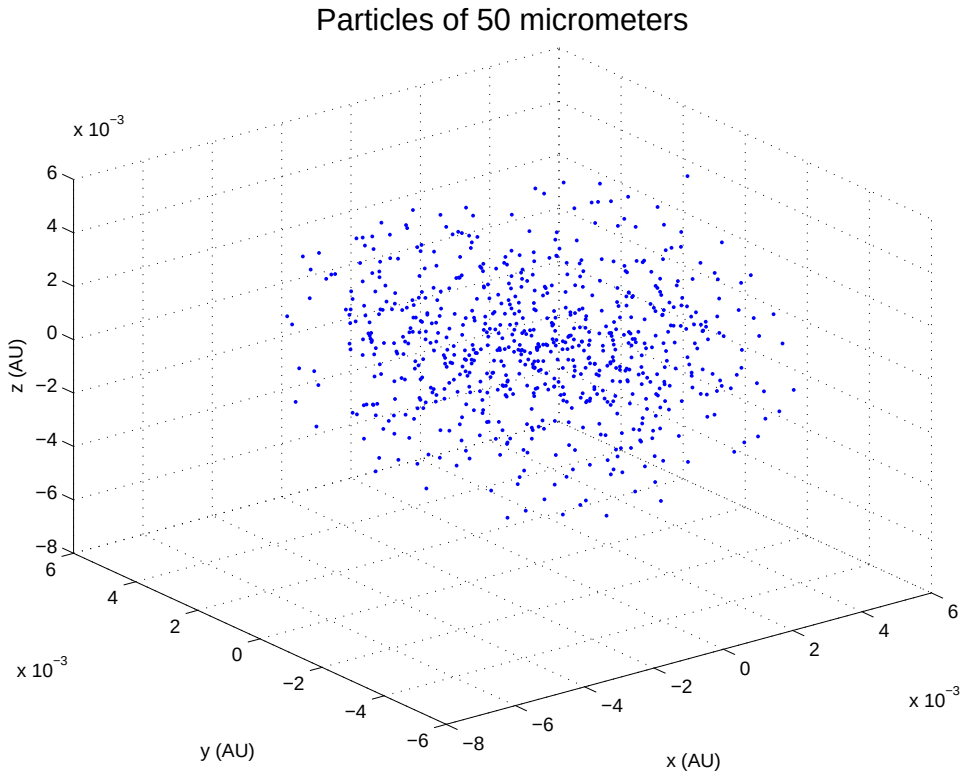

Figure 4.52: Coordinates distribution of particles of $5 \cdot 10^{-3}$ cm of radius.

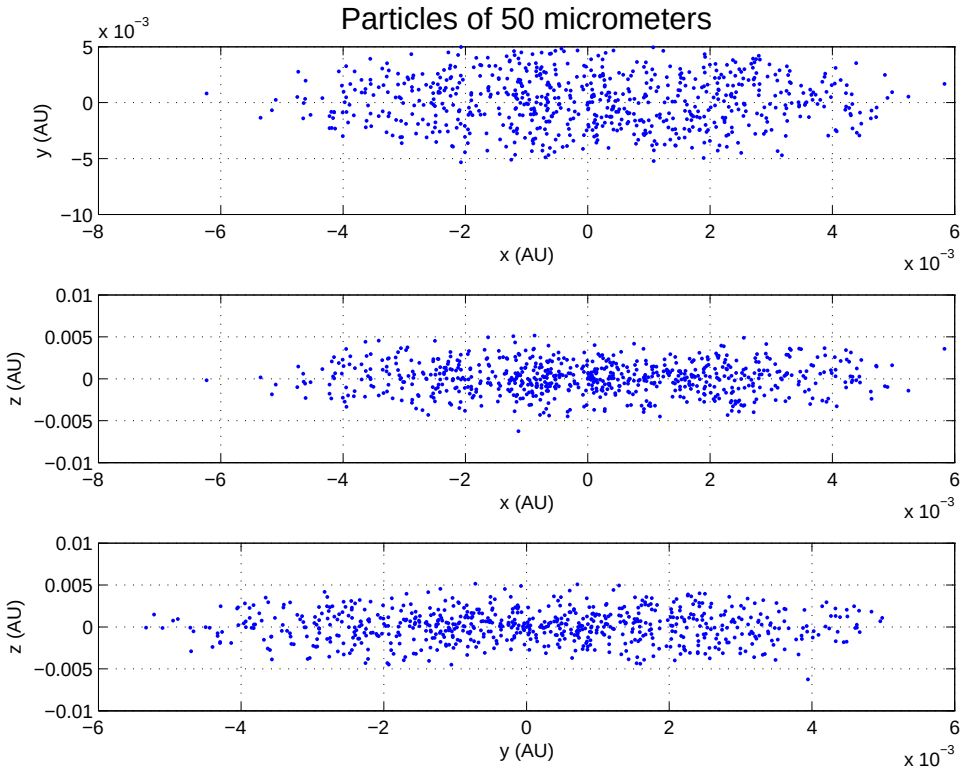

Figure 4.53: Coordinates distribution of particles of $5 \cdot 10^{-3}$ cm of radius.

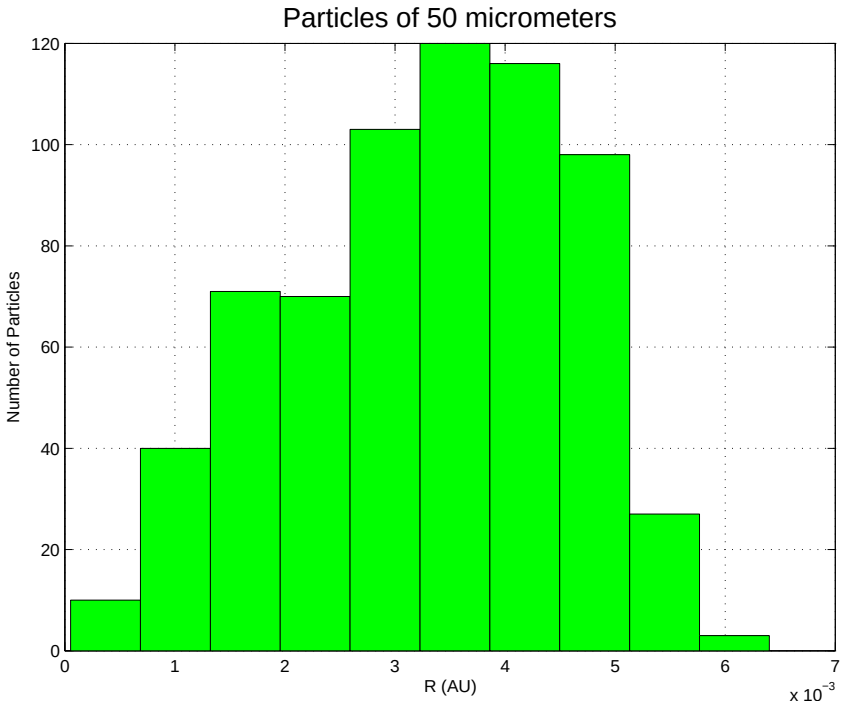

Figure 4.54: Distance distribution of particles of $5 \cdot 10^{-3}$ cm of radius.

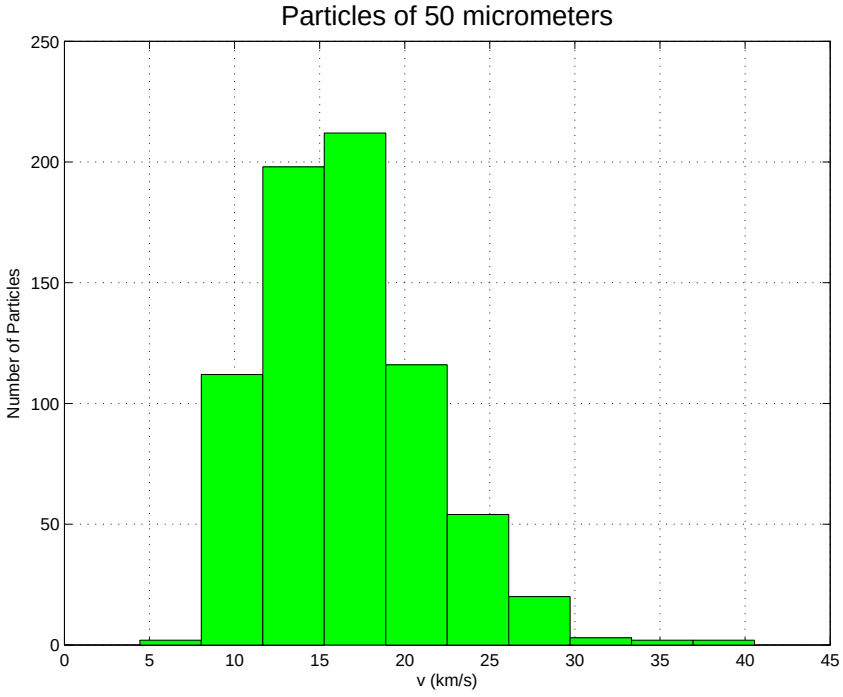

Figure 4.55: Velocity distribution of particles of $5 \cdot 10^{-3}$ cm od radius.

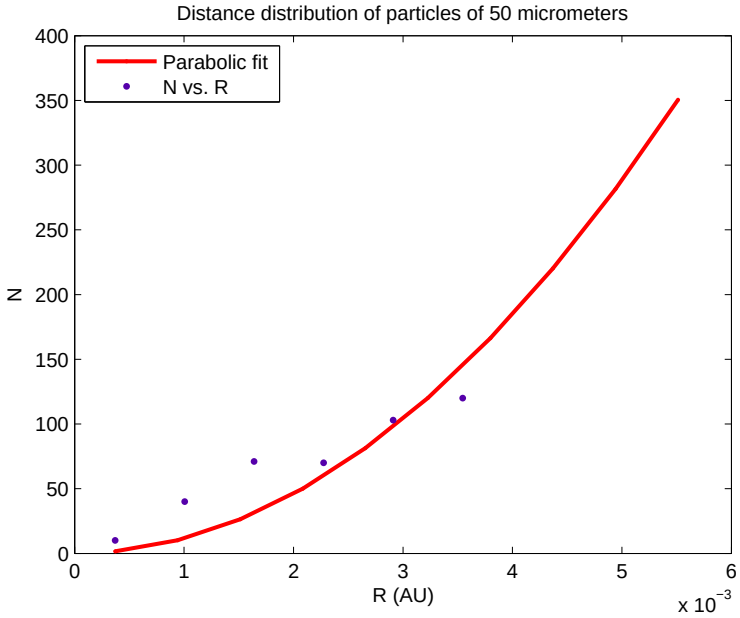

Figure 4.56: Quadratic distance distribution of particles of $5 \cdot 10^{-3}$ cm od radius.

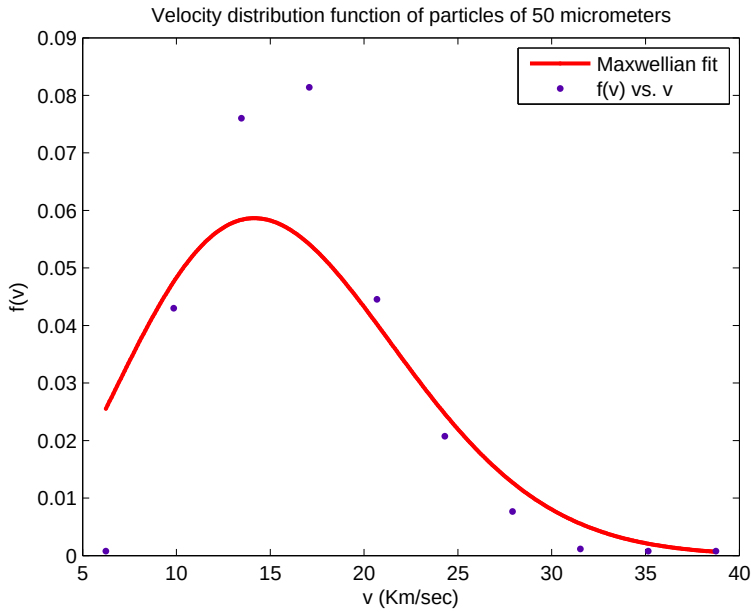

Figure 4.57: Gaussian velocity distribution of particles of $5 \cdot 10^{-3}$ cm od radius.

The best fit for the minimum distance distribution is a polynomial fit of degree 2

$$f(r) = p_1 r^2 \,. \tag{4.39}$$

The best fit for velocity distribution is a maxwellian expression

$$f(v) = \sqrt{\frac{2}{\pi}} a^{-\frac{3}{2}} v^2 \exp\left(-\frac{v^2}{2a}\right) \,. \tag{4.40}$$

Residuals

We show in the figure (4.58) the residuals for the minimum distance distribution and in the figure (4.59) the residuals for the velocity distribution.

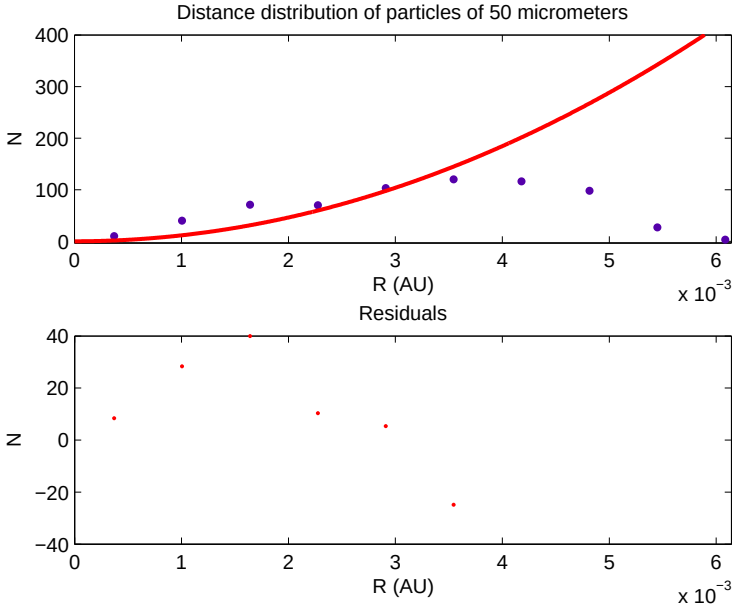

Figure 4.58: Residuals of distance distribution of particles with $5 \cdot 10^{-3}$ *cm* of radius.

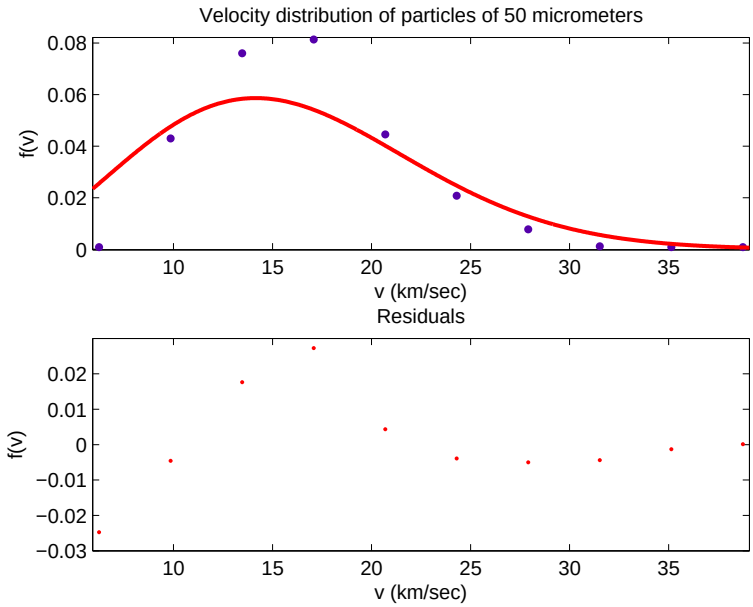

Figure 4.59: Residuals of velocity distribution of particles with $5 \cdot 10^{-3}$ cm of radius.

Goodness of fit statistics

For dust particles with $5 \cdot 10^{-3}$ cm of radius we report the value in the table (4.21) for the minimum distance distribution and in the table (4.22) for velocity distribution.

Goodness of fit	Value
SSE	411.4
R-square	0.6931
Adjusted R-square	0.6931
RMSE	9.071

Table 4.21: Goodness of fit for minimum distance distribution of dust particles with $5 \cdot 10^{-3}$ cm of radius.

Goodness of fit	Value
SSE	0.001769
R-square	0.8049
Adjusted R-square	0.8049
RMSE	0.01402

Table 4.22: Goodness of fit for velocity distribution of dust particles with $4 \cdot 10^{-3}$ cm of radius.

Confidence and prediction bounds

The bounds are defined with a level of certainty that it is possible to specify. The level of certainty is fixed at 95%. Below we report the confidence bound in table 4.19 for minimum distance distribution and in table 4.20 for velocity distribution. The predictions bounds are in figure (4.50) for minimum distance distribution and in figure (4.51) for velocity distribution.

Coefficients of fit	**Coefficient values**	**Confidence bound at 95%**
p_1	$1.153 \cdot 10^7$	$6.931 \cdot 10^6 - 1.613 \cdot 10^7$

Table 4.23: Goodness of fit for minimum distance distribution of dust particles with $5 \cdot 10^{-3}$ cm of radius.

Coefficients of fit	**Coefficient values**	**Confidence bound at 95%**
a	100.2	$64.62 - 135.7$

Table 4.24: Goodness of fit for velocity distribution of dust particles with $5 \cdot 10^{-3}$ cm of radius.

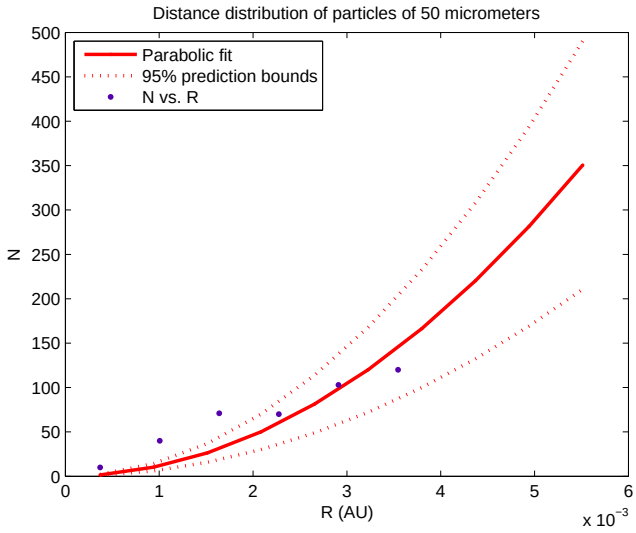

Figure 4.60: Bound of distance distribution of particles with $5 \cdot 10^{-3}$ cm of radius.

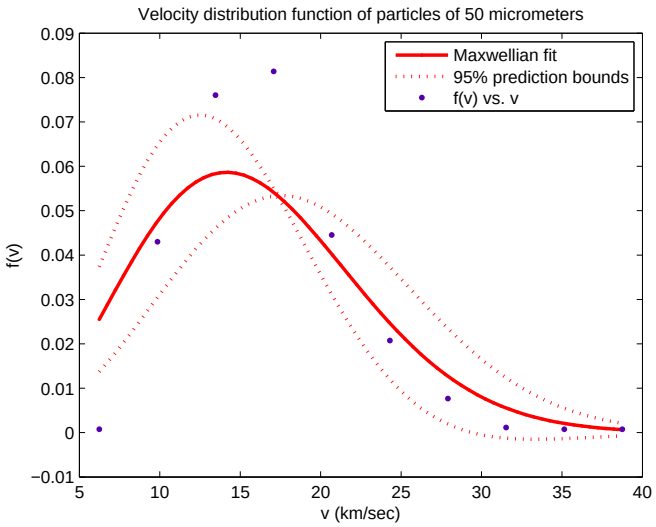

Figure 4.61: Bound of velocity distribution of particles with $5 \cdot 10^{-3}$ cm of radius.

4.3.7 Particles of $6 \cdot 10^{-3}$ cm of radius

Here we consider 1000 particles with $6 \cdot 10^{-3}$ cm of radius. In the figures below we show the three-dimensional coordinates distribution (figure 4.62) the bi-dimensional coordinates distribution (figure 4.63), the histogram that represent the distance distribution of dust particles (figure 4.64), that is the minimum distance particle-Mercury in a ten times the radius of the sphere of influence, and velocity distribution of dust particles (figure 4.65). After this we show in the figures (4.66) and (4.67) the best fit that adapt to our data.

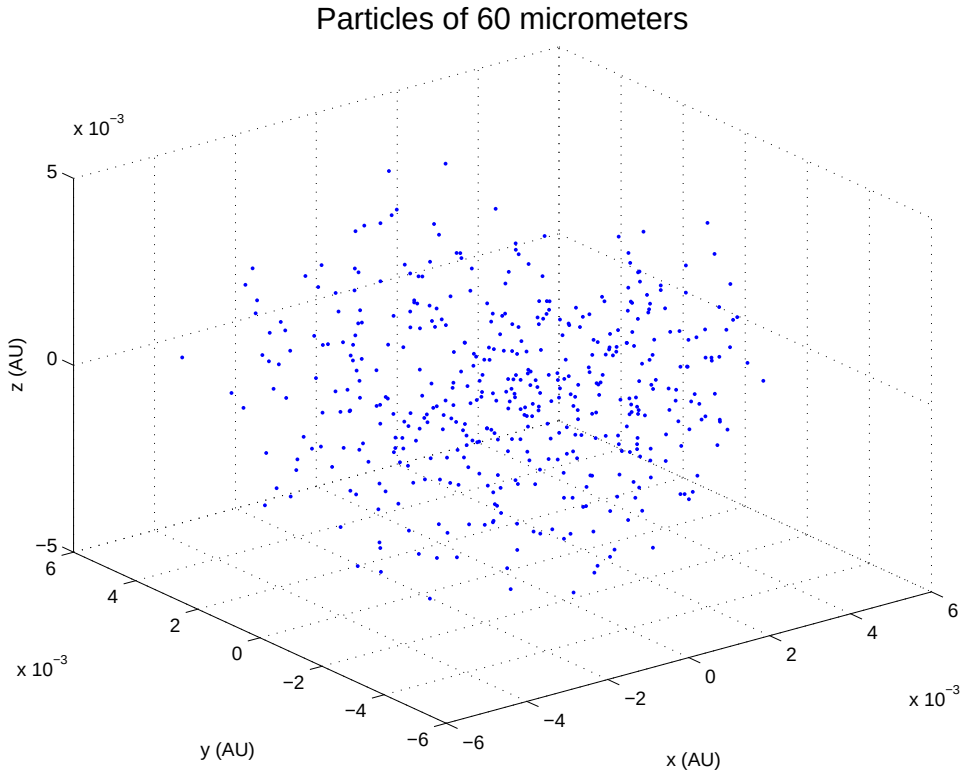

Figure 4.62: Coordinates distribution of particles of $6 \cdot 10^{-3}$ *cm* of radius.

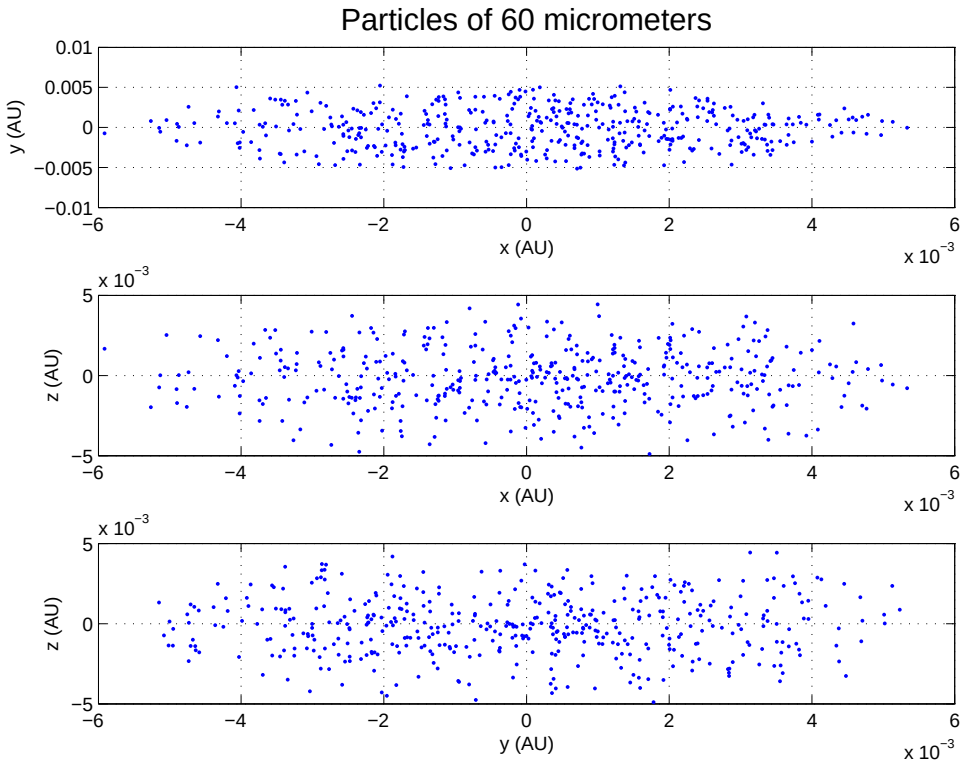

Figure 4.63: Coordinates distribution of particles of $6 \cdot 10^{-3}$ *cm* of radius.

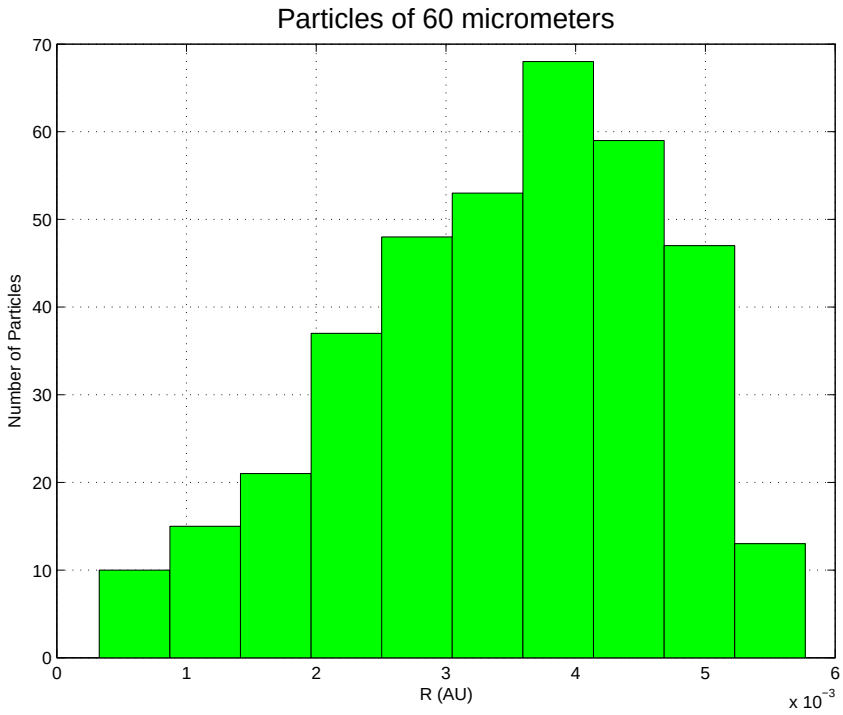

Figure 4.64: Distance distribution of particles of $6 \cdot 10^{-3}$ cm of radius.

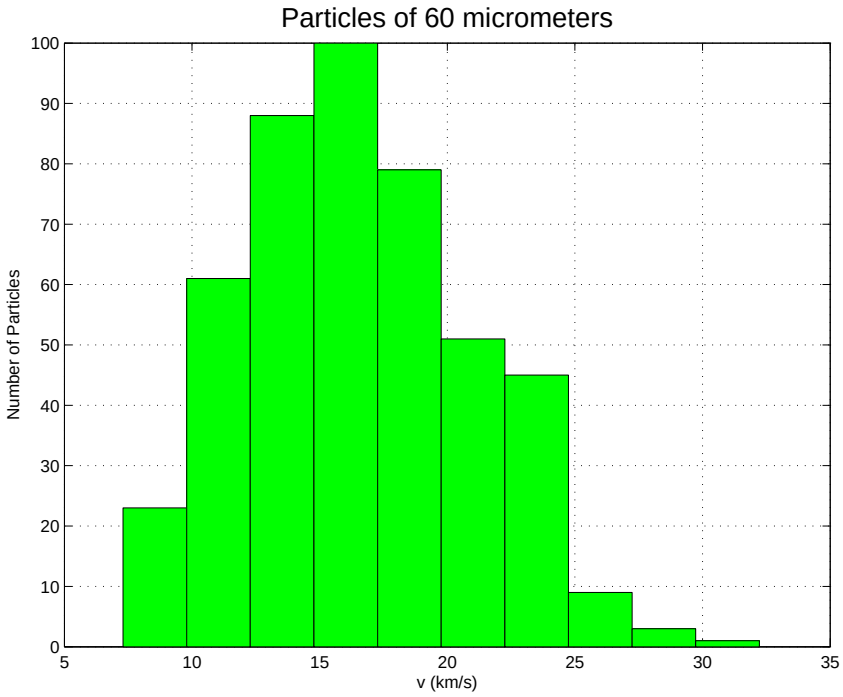

Figure 4.65: Velocity distribution of particles of $6 \cdot 10^{-3}$ cm od radius.

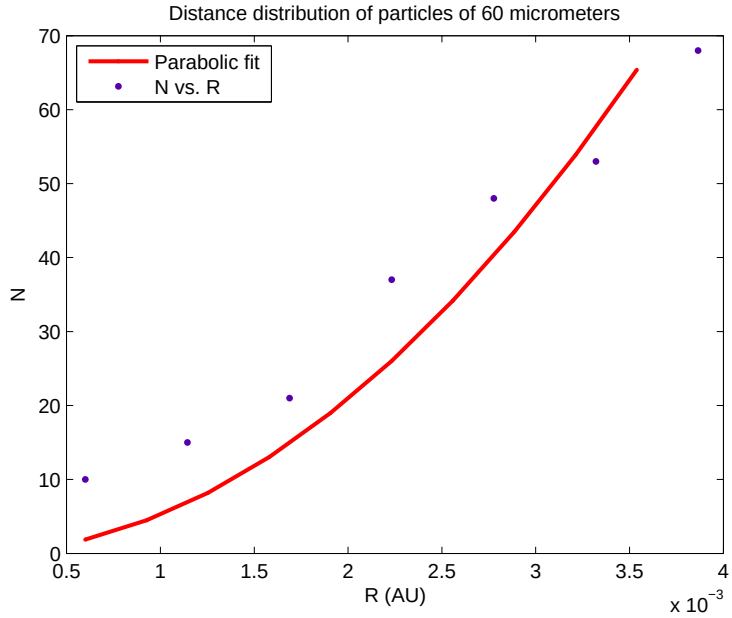

Figure 4.66: Quadratic distance distribution of particles of $6 \cdot 10^{-3}$ cm od radius.

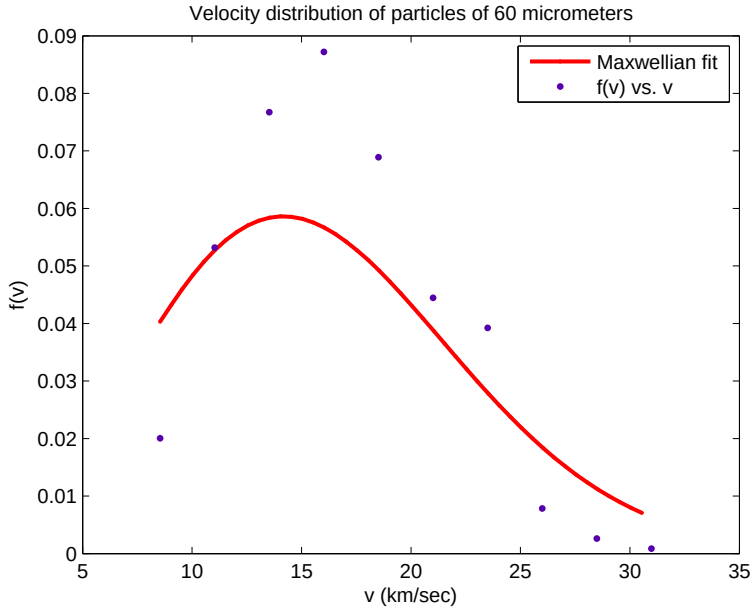

Figure 4.67: Gaussian velocity distribution of particles of $6 \cdot 10^{-3}$ cm od radius.

The best fit for the minimum distance distribution is a polynomial fit of degree 2

$$f(r) = p_1 r^2 \,. \tag{4.41}$$

The best fit for velocity distribution is a maxwellian expression

$$f(v) = \sqrt{\frac{2}{\pi}} a^{-\frac{3}{2}} v^2 \exp\left(-\frac{v^2}{2a}\right) \,. \tag{4.42}$$

Residuals

We show in the figure (4.38) the residuals for the minimum distance distribution and in the figure (4.39) the residuals for the velocity distribution.

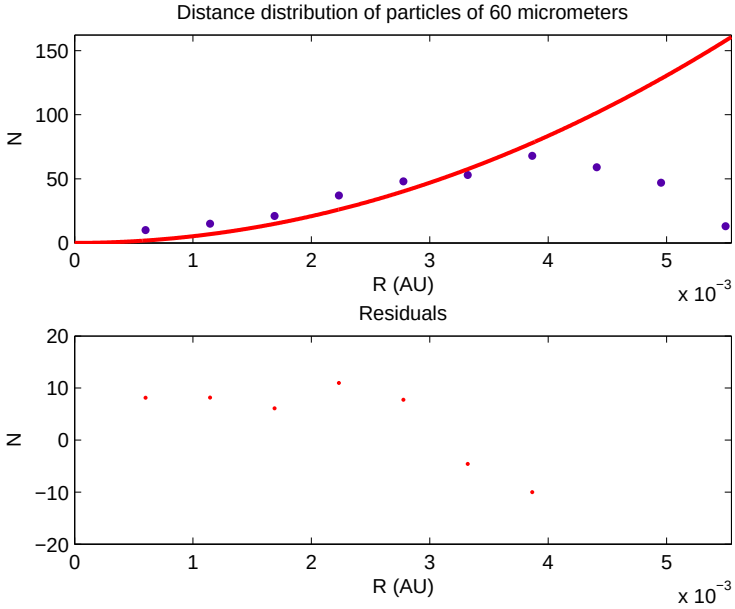

Figure 4.68: Residuals of distance distribution of particles with $6 \cdot 10^{-3}$ *cm* of radius.

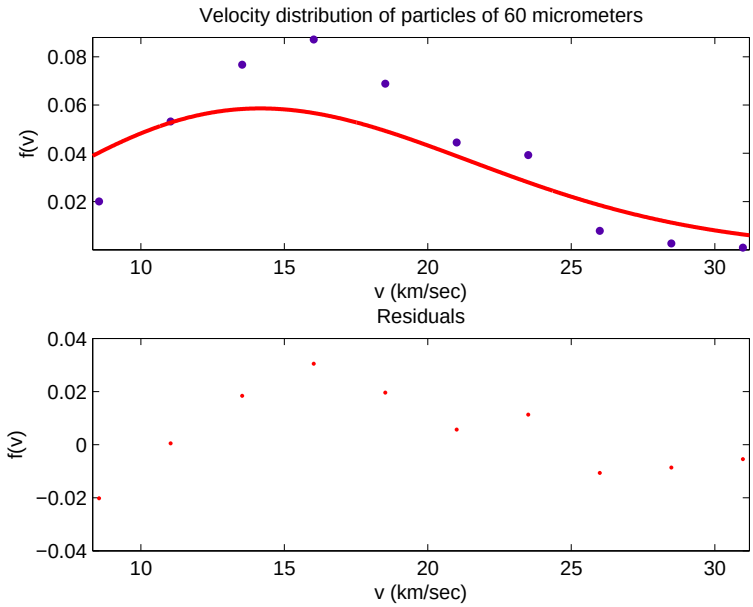

Figure 4.69: Residuals of velocity distribution of particles with $6 \cdot 10^{-3}$ cm of radius.

Goodness of fit statistics

For dust particles with $6 \cdot 10^{-3}$ cm of radius we report the value in the table (4.25) for the minimum distance distribution and in the table (4.26) for velocity distribution.

Goodness of fit	Value
SSE	89.73
R-square	0.8222
Adjusted R-square	0.8222
RMSE	3.867

Table 4.25: Goodness of fit for minimum distance distribution of dust particles with $6 \cdot 10^{-3}$ cm of radius.

Goodness of fit	Value
SSE	0.002438
R-square	0.7281
Adjusted R-square	0.7281
RMSE	0.01646

Table 4.26: Goodness of fit for velocity distribution of dust particles with $6 \cdot 10^{-3}$ cm of radius.

Confidence and prediction bounds

The bounds are defined with a level of certainty that it is possible to specify. The level of certainty is fixed at 95%. Below we report the confidence bound in table 4.27 for minimum distance distribution and in table 4.28 for velocity distribution. The predictions bounds are in figure (4.70) for minimum distance distribution and in figure (4.71) for velocity distribution.

Coefficients of fit	Coefficient values	Confidence bound at 95%
p_1	$5.221 \cdot 10^6$	$3.986 \cdot 10^6 - 6.456 \cdot 10^6$

Table 4.27: Goodness of fit for minimum distance distribution of dust particles with $6 \cdot 10^{-3}$ cm of radius.

Coefficients of fit	Coefficient values	Confidence bound at 95%
a	100.3	$63.27 - 137.3$

Table 4.28: Goodness of fit for velocity distribution of dust particles with $6 \cdot 10^{-6}$ cm of radius.

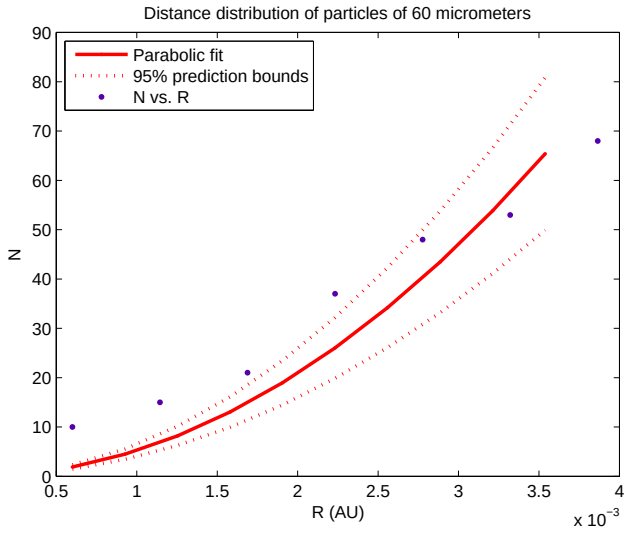

Figure 4.70: Bound of distance distribution of particles with $6 \cdot 10^{-3}$ cm of radius.

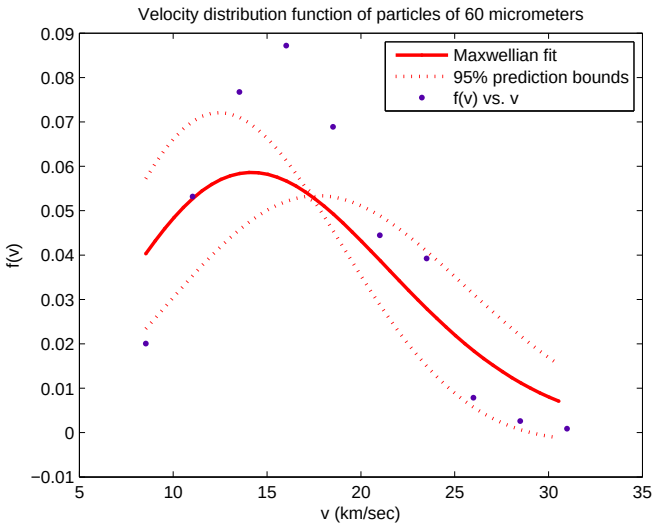

Figure 4.71: Bound of velocity distribution of particles with $6 \cdot 10^{-3}$ cm of radius.

4.3.8 Particles of $7 \cdot 10^{-3}$ cm of radius

Here we consider 1000 particles with $7 \cdot 10^{-3}$ cm of radius. In the figures below we show the three-dimensional coordinates distribution (figure 4.72) the bi-dimensional coordinates distribution (figure 4.73), the histogram that represent the distance distribution of dust particles (figure 4.74), that is the minimum distance particle-Mercury in a ten times the radius of the sphere of influence, and velocity distribution of dust particles (figure 4.75). After this we show in the figures (4.76) and (4.77) the best fit that adapt to our data.

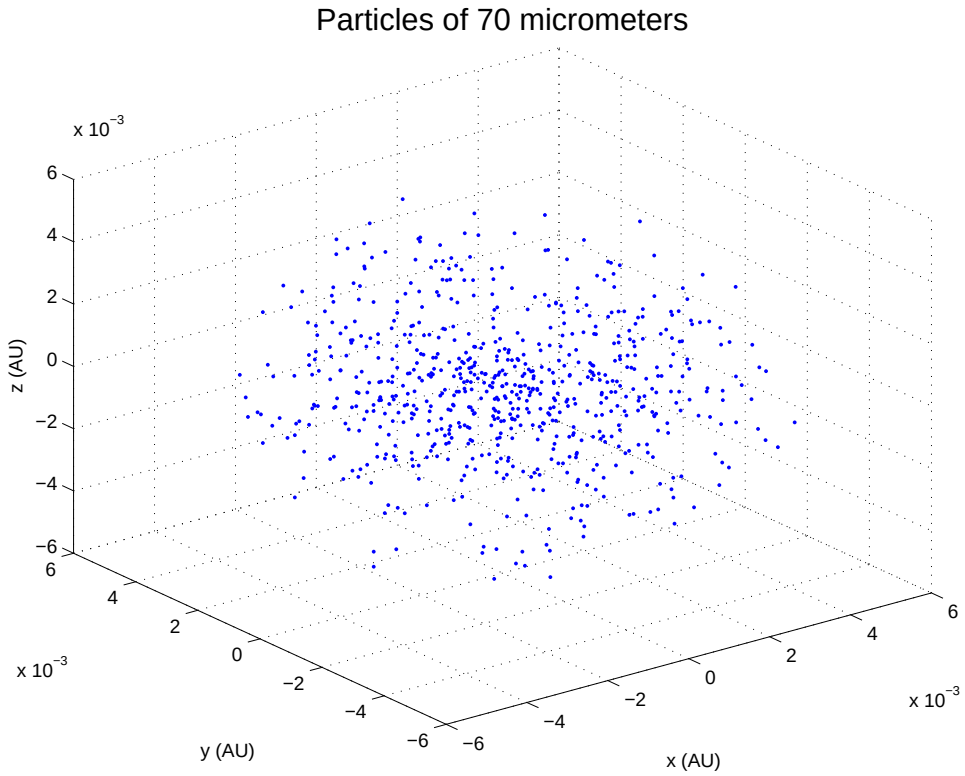

Figure 4.72: Coordinates distribution of particles of $7 \cdot 10^{-3}$ cm of radius.

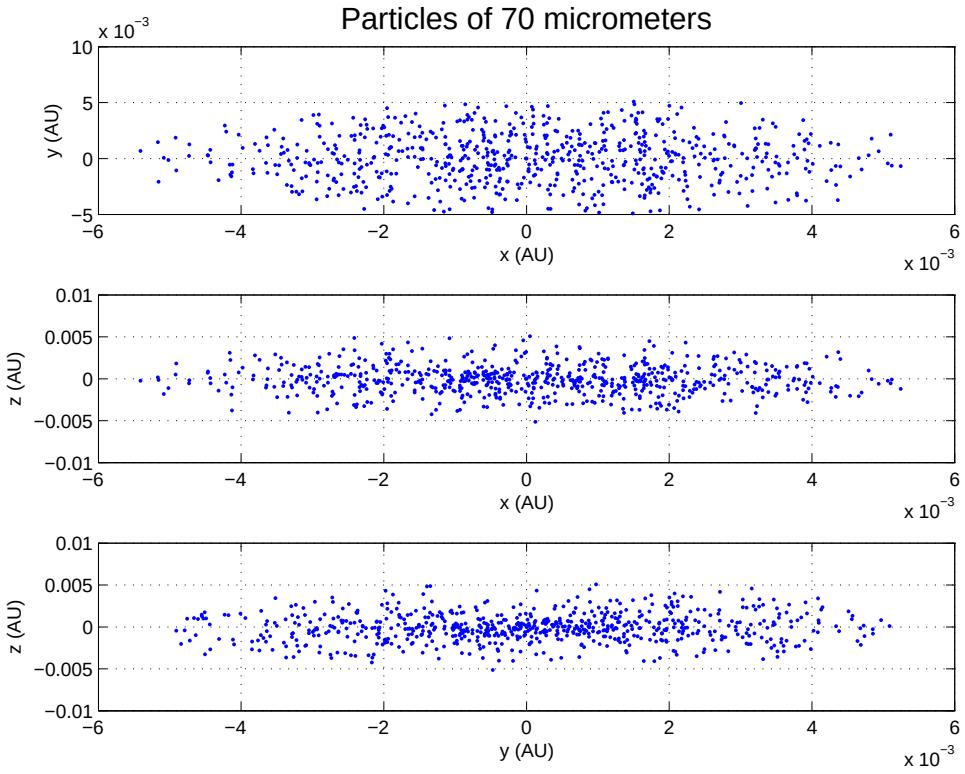

Figure 4.73: Coordinates distribution of particles of $7 \cdot 10^{-3}$ cm of radius.

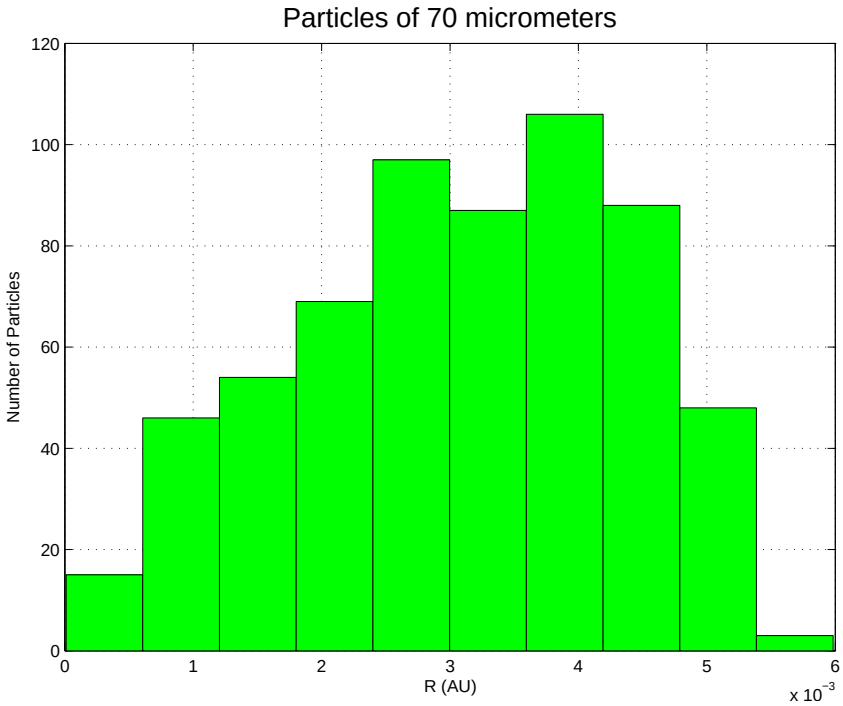

Figure 4.74: Distance distribution of particles of $7 \cdot 10^{-3}$ cm of radius.

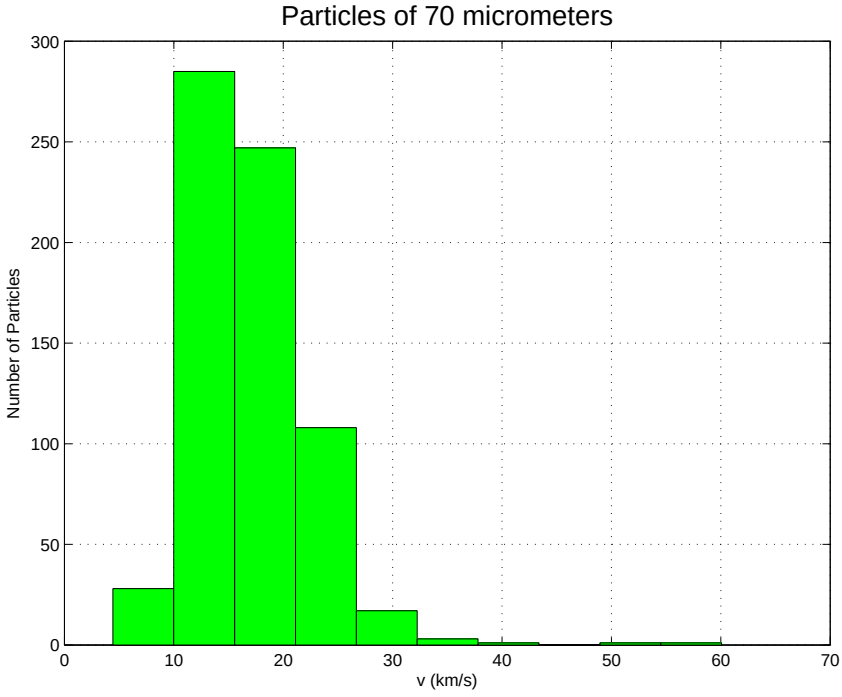

Figure 4.75: Velocity distribution of particles of $7 \cdot 10^{-3}$ cm od radius.

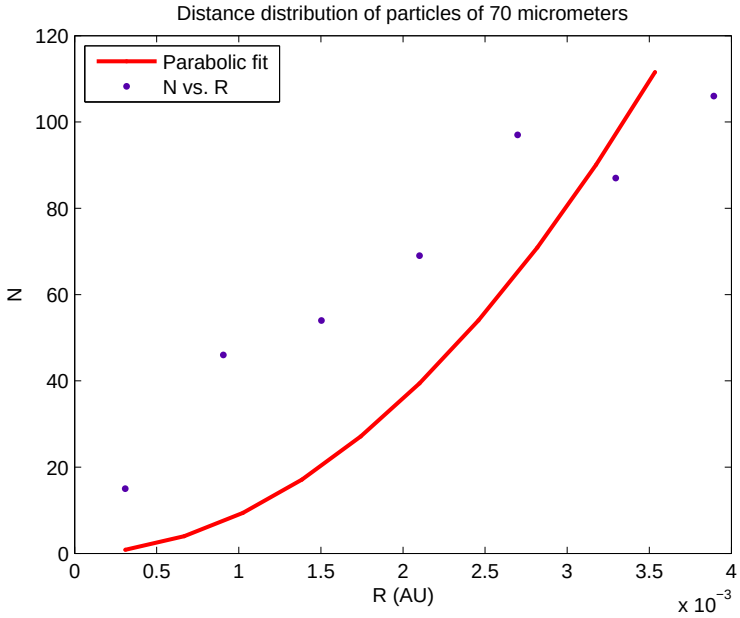

Figure 4.76: Quadratic distance distribution of particles of $7 \cdot 10^{-3}$ cm od radius.

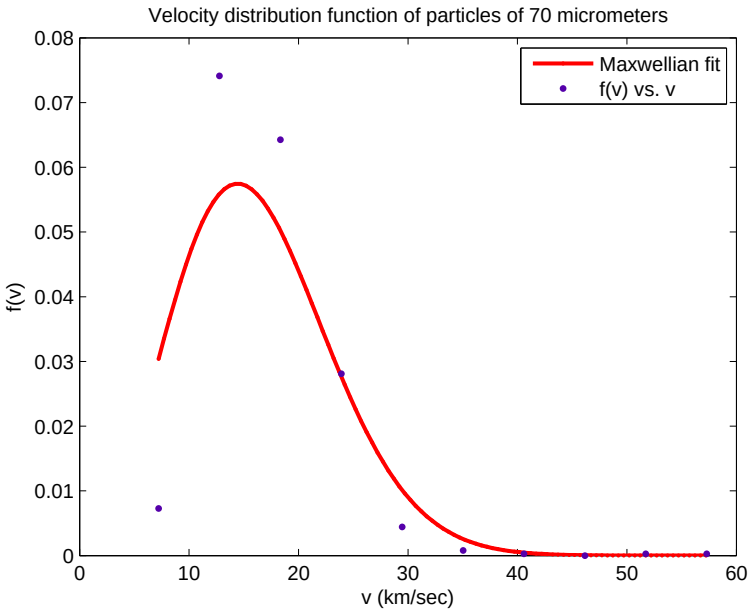

Figure 4.77: Gaussian velocity distribution of particles of $7 \cdot 10^{-3}$ cm od radius.

The best fit for the minimum distance distribution is a polynomial fit of degree 2

$$f(r) = p_1 r^2 \,. \tag{4.43}$$

The best fit for velocity distribution is a maxwellian expression

$$f(v) = \sqrt{\frac{2}{\pi}} a^{-\frac{3}{2}} v^2 \exp\left(-\frac{v^2}{2a}\right) \,. \tag{4.44}$$

Residuals

We show in the figure (4.78) the residuals for the minimum distance distribution and in the figure (4.79) the residuals for the velocity distribution.

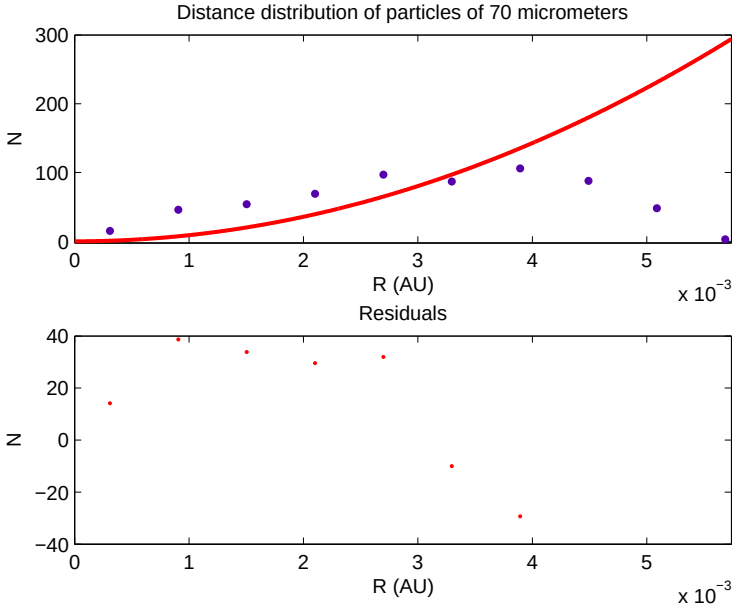

Figure 4.78: Residuals of distance distribution of particles with $7 \cdot 10^{-3}$ *cm* of radius.

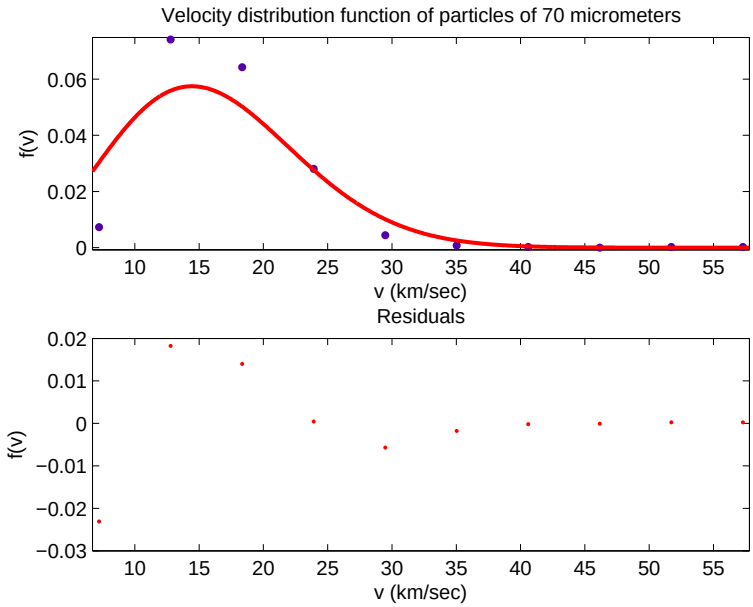

Figure 4.79: Residuals of velocity distribution of particles with $7 \cdot 10^{-3}$ cm of radius.

Goodness of fit statistics

For dust particles with $7 \cdot 10^{-3}$ cm of radius we report the value in the table (4.29) for the minimum distance distribution and in the table (4.30) for velocity distribution.

Goodness of fit	Value
SSE	731.2
R-square	0.2566
Adjusted R-square	0.2566
RMSE	11.04

Table 4.29: Goodness of fit for minimum distance distribution of dust particles with $7 \cdot 10^{-3}$ cm of radius.

Goodness of fit	Value
SSE	0.001098
R-square	0.8486
Adjusted R-square	0.8486
RMSE	0.01105

Table 4.30: Goodness of fit for velocity distribution of dust particles with $7 \cdot 10^{-3}$ cm of radius.

Confidence and prediction bounds

The bounds are defined with a level of certainty that it is possible to specify. The level of certainty is fixed at 95%. Below we report the confidence bound in table 4.31 for minimum distance distribution and in table 4.32 for velocity distribution. The predictions bounds are in figure (4.80) for minimum distance distribution and in figure (4.81) for velocity distribution.

Coefficients of fit	**Coefficient values**	**Confidence bound at 95%**
p_1	$8.928 \cdot 10^6$	$4.832 \cdot 10^6 - 1.302 \cdot 10^7$

Table 4.31: Goodness of fit for minimum distance distribution of dust particles with $7 \cdot 10^{-3}$ cm of radius.

Coefficients of fit	**Coefficient values**	**Confidence bound at 95%**
a	104.3	67.89 – 140.8

Table 4.32: Goodness of fit for velocity distribution of dust particles with $7 \cdot 10^{-3}$ cm of radius.

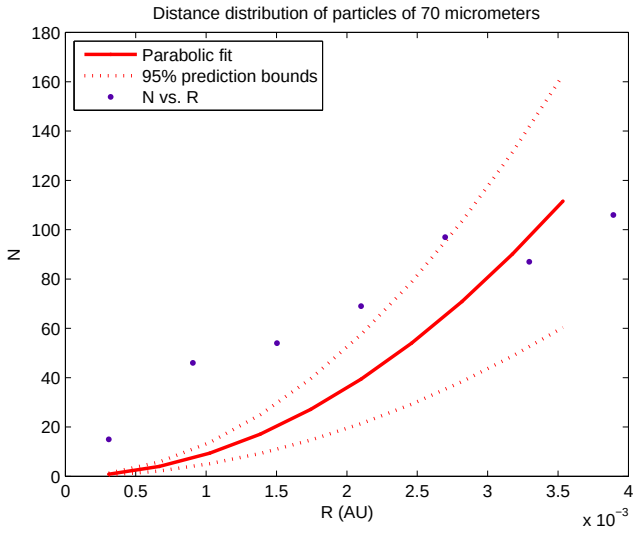

Figure 4.80: Bound of distance distribution of particles with $7 \cdot 10^{-3}$ cm of radius.

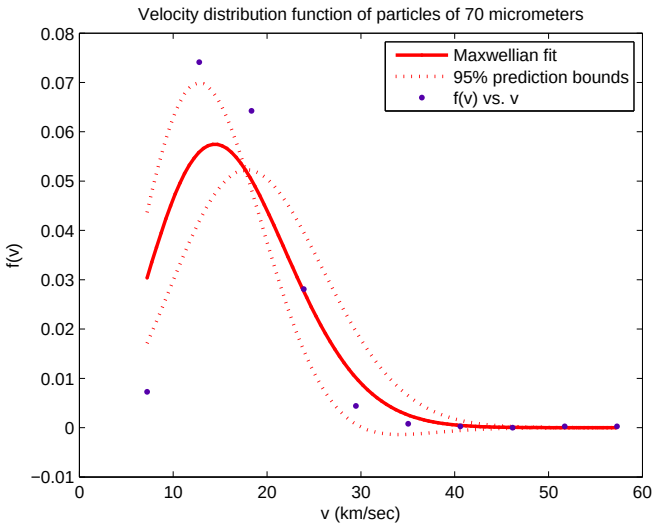

Figure 4.81: Bound of velocity distribution of particles with $7 \cdot 10^{-3}$ cm of radius.

4.3.9 Particles of $8 \cdot 10^{-3}$ cm of radius

Here we consider 1000 particles with $8 \cdot 10^{-3}$ cm of radius. In the figures below we show the three-dimensional coordinates distribution (figure 4.82) the bi-dimensional coordinates distribution (figure 4.83), the histogram that represent the distance distribution of dust particles (figure 4.84), that is the minimum distance particle-Mercury in a ten times the radius of the sphere of influence, and velocity distribution of dust particles (figure 4.85). After this we show in the figures (4.86) and (4.87) the best fit that adapt to our data.

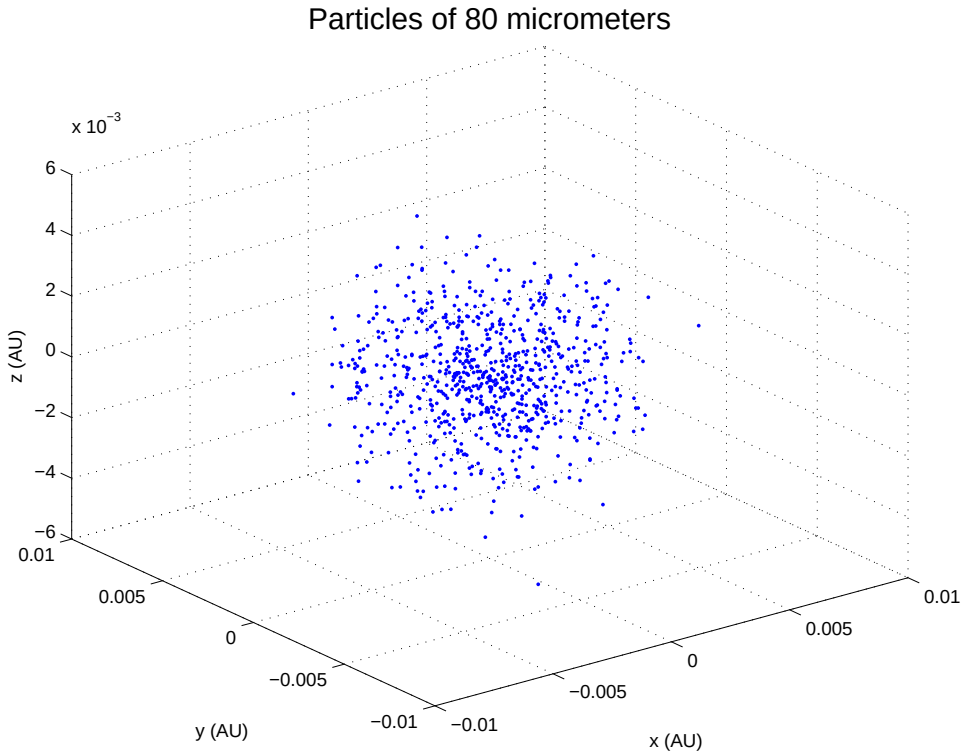

Figure 4.82: Coordinates distribution of particles of $8 \cdot 10^{-3}$ cm of radius.

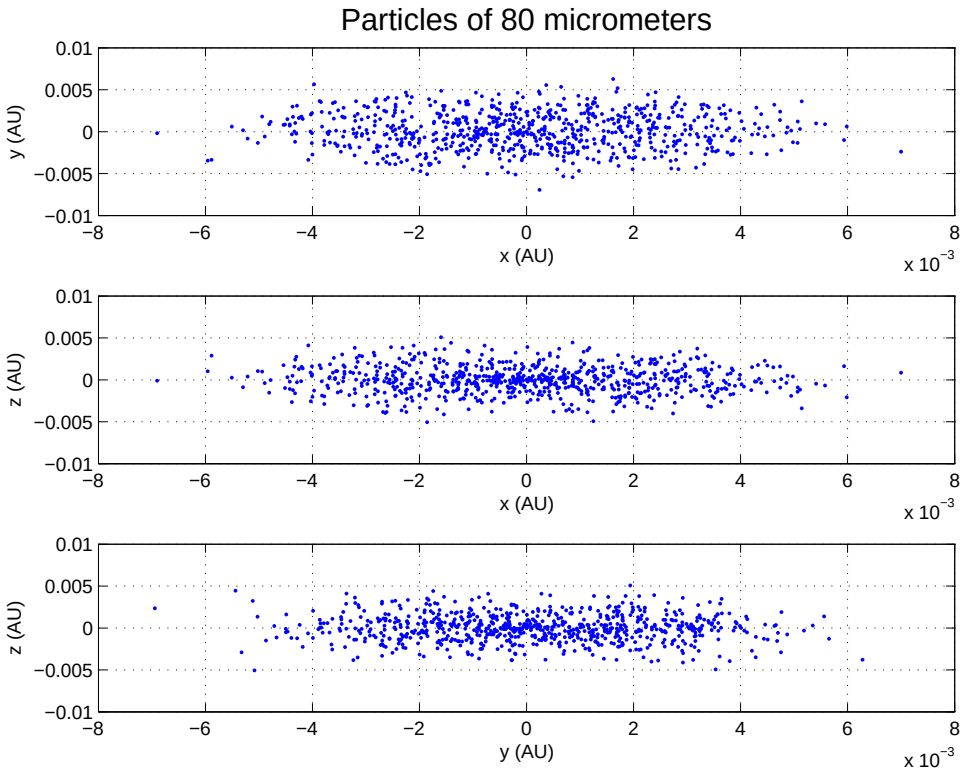

Figure 4.83: Coordinates distribution of particles of $8 \cdot 10^{-3}$ cm of radius.

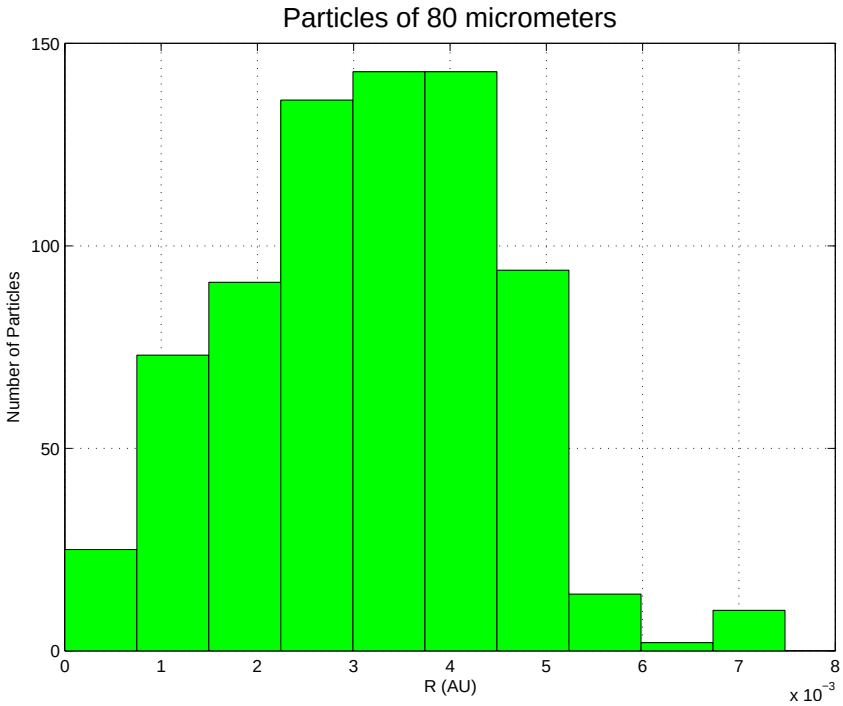

Figure 4.84: Distance distribution of particles of $8 \cdot 10^{-3}$ cm of radius.

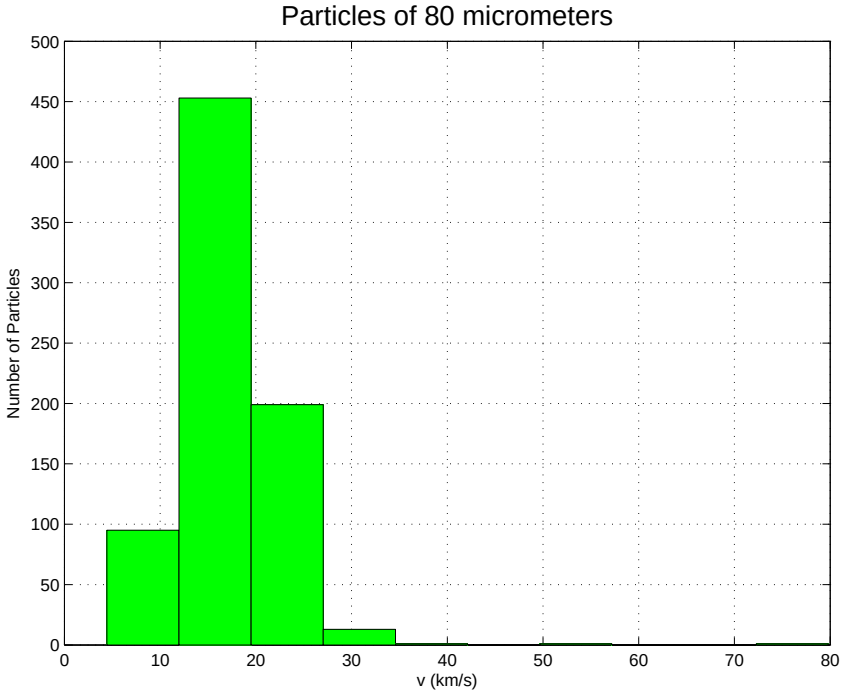

Figure 4.85: Velocity distribution of particles of $8 \cdot 10^{-3}$ cm od radius.

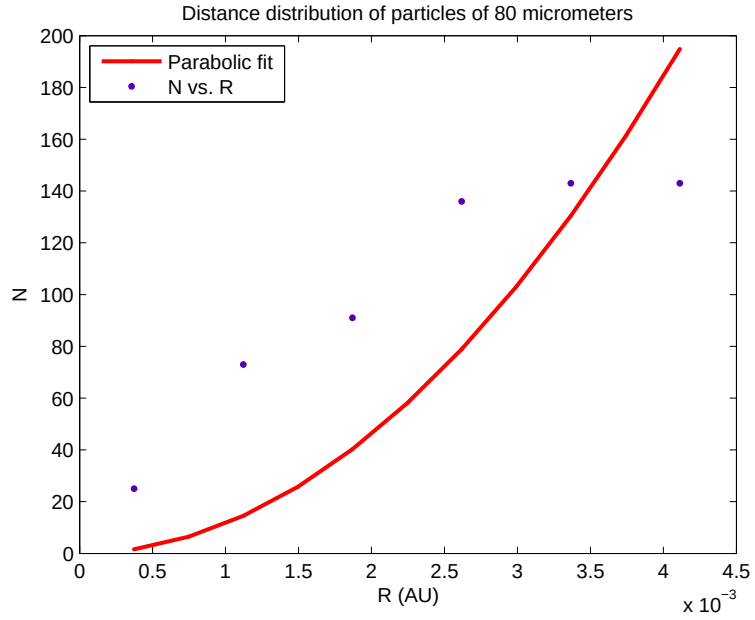

Figure 4.86: Quadratic distance distribution of particles of $8 \cdot 10^{-3}$ cm od radius.

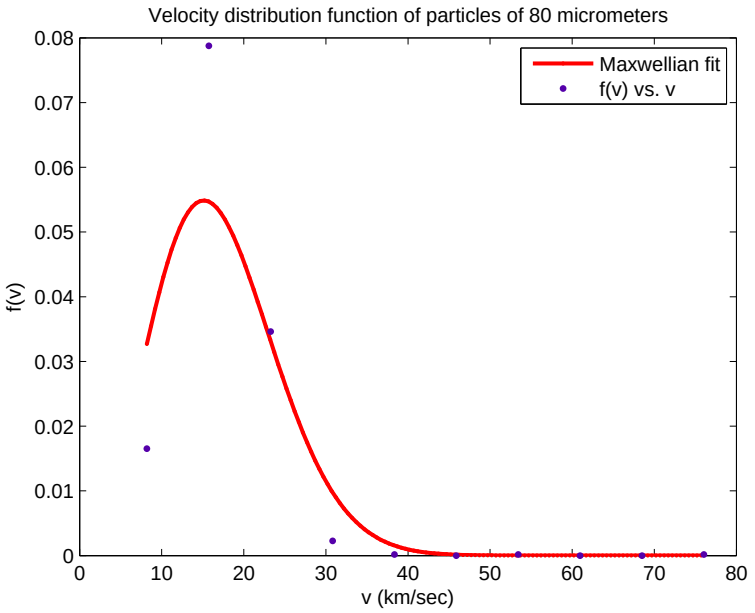

Figure 4.87: Gaussian velocity distribution of particles of $8 \cdot 10^{-3}$ cm od radius.

The best fit for the minimum distance distribution is a polynomial fit of degree 2

$$f(r) = p_1 r^2 \,. \tag{4.45}$$

The best fit for velocity distribution is a maxwellian expression

$$f(v) = \sqrt{\frac{2}{\pi}} a^{-\frac{3}{2}} v^2 \exp\left(-\frac{v^2}{2a}\right) \,. \tag{4.46}$$

Residuals

We show in the figure (4.88) the residuals for the minimum distance distribution and in the figure (4.89) the residuals for the velocity distribution.

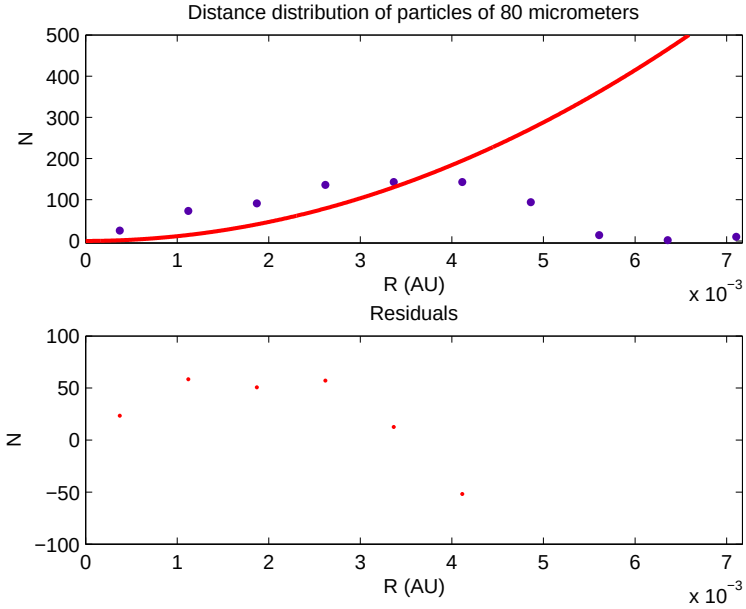

Figure 4.88: Residuals of distance distribution of particles with $8 \cdot 10^{-3}$ *cm* of radius.

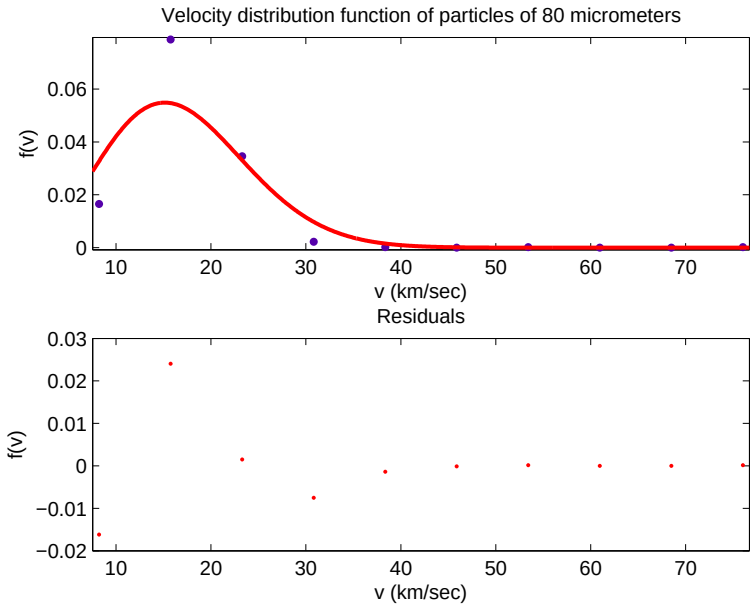

Figure 4.89: Residuals of velocity distribution of particles with $8 \cdot 10^{-3}$ cm of radius.

Goodness of fit statistics

For dust particles with $8 \cdot 10^{-3}$ cm of radius we report the value in the table (4.37) for the minimum distance distribution and in the table (4.34) for velocity distribution.

Goodness of fit	Value
SSE	1297
R-square	0.1485
Adjusted R-square	0.1485
RMSE	16.11

Table 4.33: Goodness of fit for minimum distance distribution of dust particles with $8 \cdot 10^{-3}$ cm of radius.

Goodness of fit	Value
SSE	0.0009012
R-square	0.8477
Adjusted R-square	0.8477
RMSE	0.01001

Table 4.34: Goodness of fit for velocity distribution of dust particles with $8 \cdot 10^{-3}$ cm of radius.

Confidence and prediction bounds

The bounds are defined with a level of certainty that it is possible to specify. The level of certainty is fixed at 95%. Below we report the confidence bound in table 4.35 for minimum distance distribution and in table 4.36 for velocity distribution. The predictions bounds are in figure (4.90) for minimum distance distribution and in figure (4.91) for velocity distribution.

Coefficients of fit	Coefficient values	Confidence bound at 95%
p_1	$1.152 \cdot 10^7$	$4.981 \cdot 10^6 - 1.805 \cdot 10^7$

Table 4.35: Goodness of fit for minimum distance distribution of dust particles with $8 \cdot 10^{-3}$ cm of radius.

Coefficients of fit	Coefficient values	Confidence bound at 95%
a	114.4	71.43 – 157.5

Table 4.36: Goodness of fit for velocity distribution of dust particles with $8 \cdot 10^{-3}$ cm of radius.

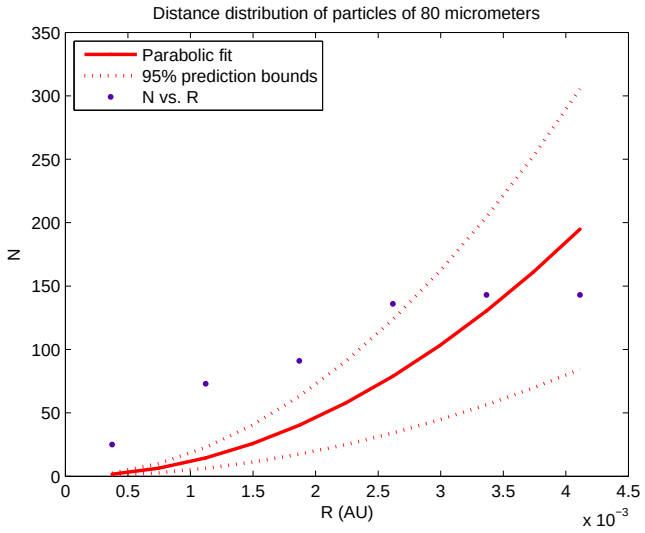

Figure 4.90: Bound of distance distribution of particles with $8 \cdot 10^{-3}$ cm of radius.

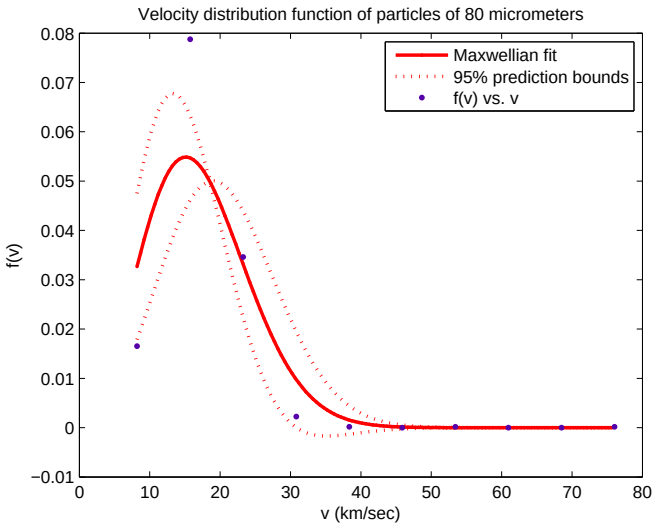

Figure 4.91: Bound of velocity distribution of particles with $8 \cdot 10^{-3}$ cm of radius.

4.3.10 Particles of $9 \cdot 10^{-3}$ cm of radius

Here we consider 1000 particles with $9 \cdot 10^{-3}$ cm of radius. In the figures below we show the three-dimensional coordinates distribution (figure 4.92) the bi-dimensional coordinates distribution (figure 4.93), the histogram that represent the distance distribution of dust particles (figure 4.94), that is the minimum distance particle-Mercury in a ten times the radius of the sphere of influence, and velocity distribution of dust particles (figure 4.95). After this we show in the figures (4.96) and (4.97) the best fit that adapt to our data.

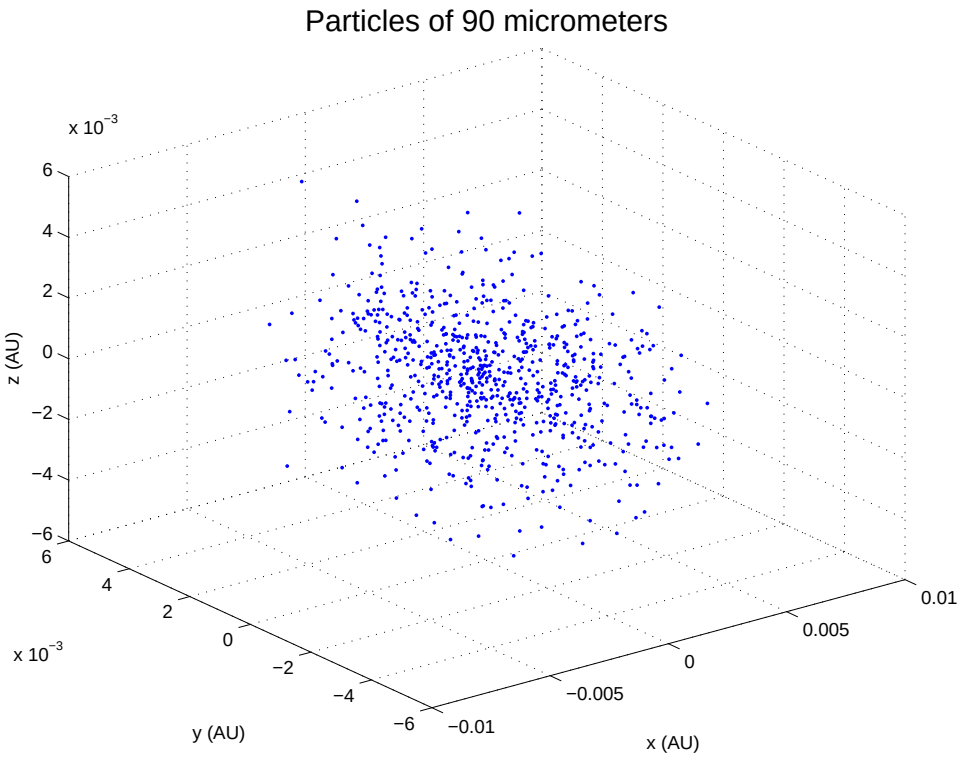

Figure 4.92: Coordinates distribution of particles of $9 \cdot 10^{-3}$ cm of radius.

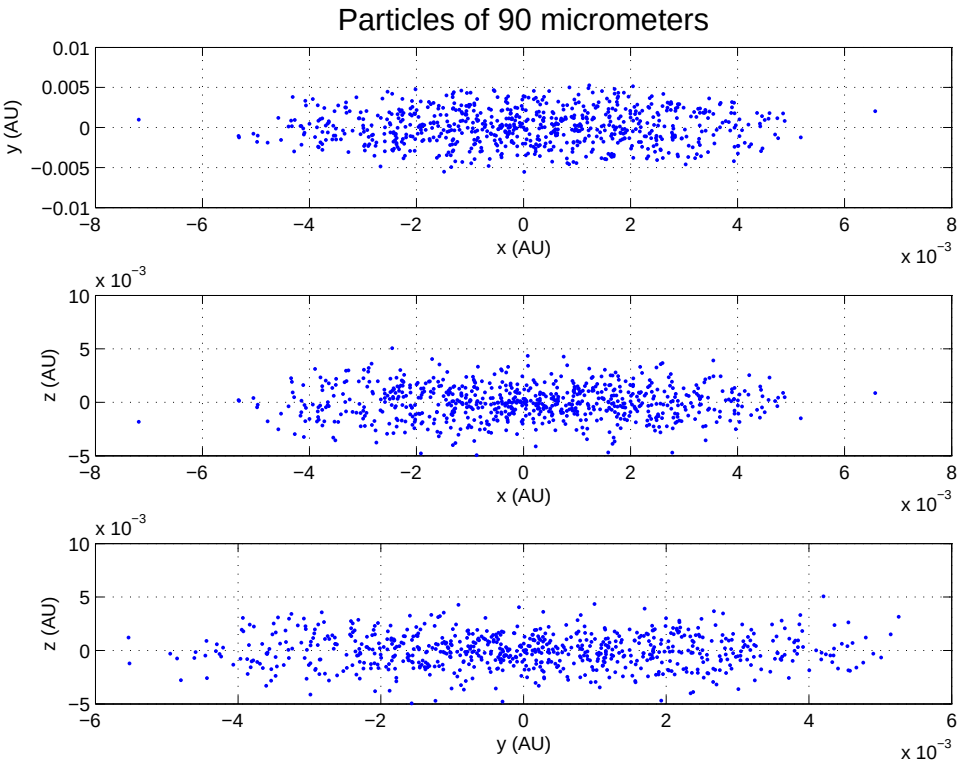

Figure 4.93: Coordinates distribution of particles of $9 \cdot 10^{-3}$ cm of radius.

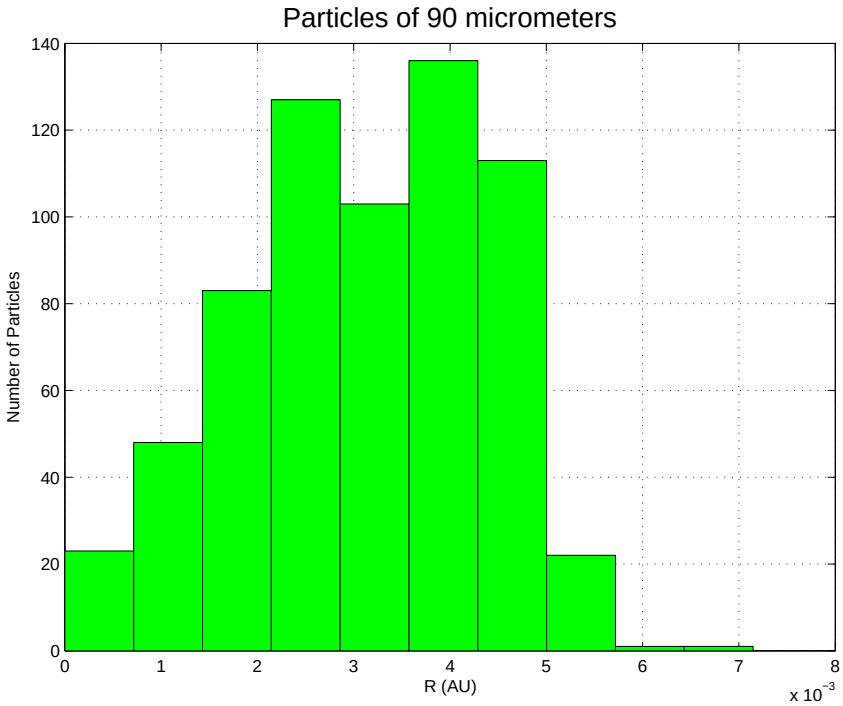

Figure 4.94: Distance distribution of particles of $9 \cdot 10^{-3}$ cm of radius.

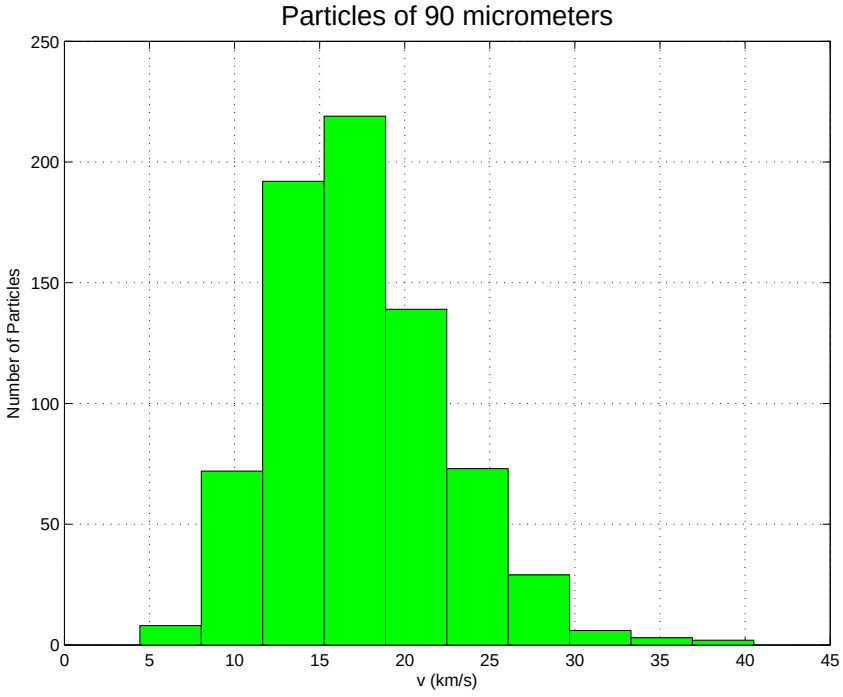

Figure 4.95: Velocity distribution of particles of $9 \cdot 10^{-3}$ cm od radius.

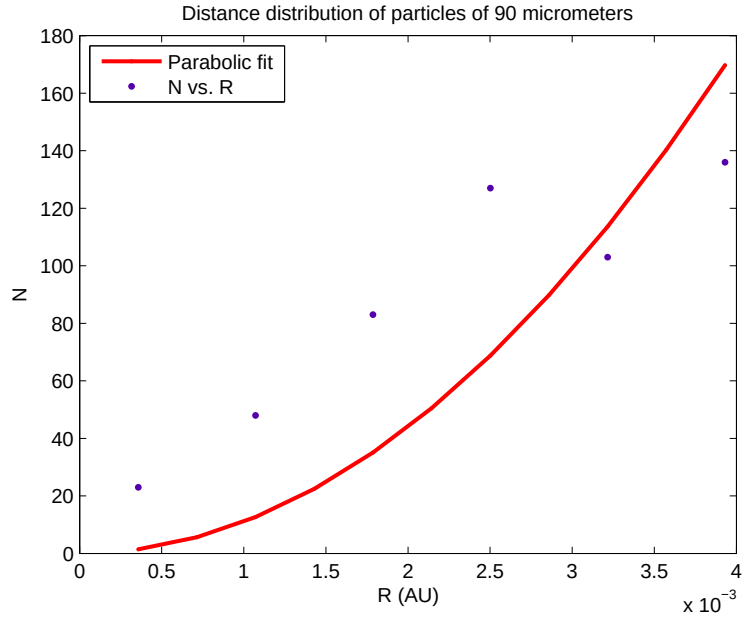

Figure 4.96: Quadratic distance distribution of particles of $9 \cdot 10^{-3}$ cm od radius.

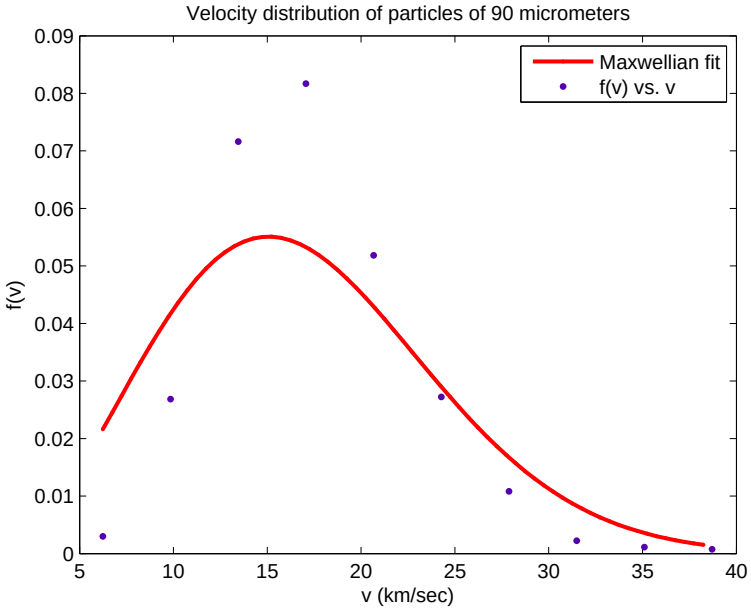

Figure 4.97: Gaussian velocity distribution of particles of $9 \cdot 10^{-3}$ cm od radius.

The best fit for the minimum distance distribution is a polynomial fit of degree 2

$$f(r) = p_1 r^2 \,. \tag{4.47}$$

The best fit for velocity distribution is a maxwellian expression

$$f(v) = \sqrt{\frac{2}{\pi}} a^{-\frac{3}{2}} v^2 \exp\left(-\frac{v^2}{2a}\right) \,. \tag{4.48}$$

Residuals

We show in the figure (4.98) the residuals for the minimum distance distribution and in the figure (4.99) the residuals for the velocity distribution.

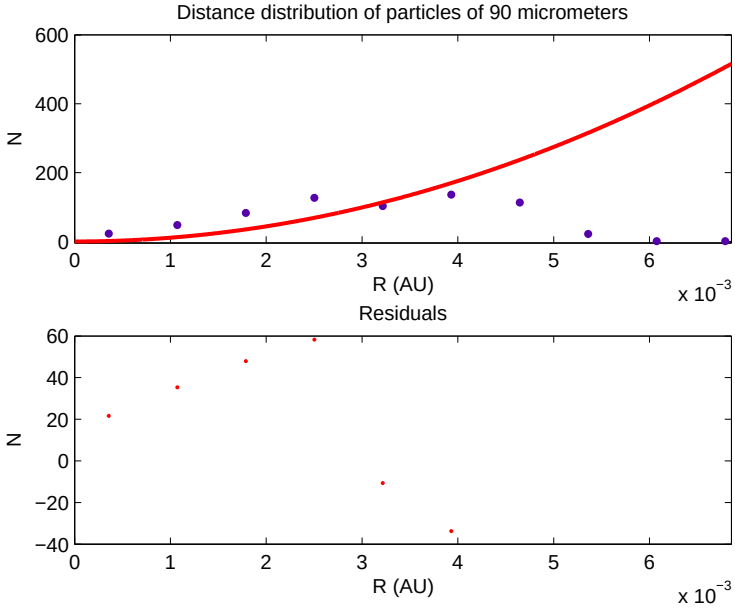

Figure 4.98: Residuals of distance distribution of particles with $9 \cdot 10^{-3}$ *cm* of radius.

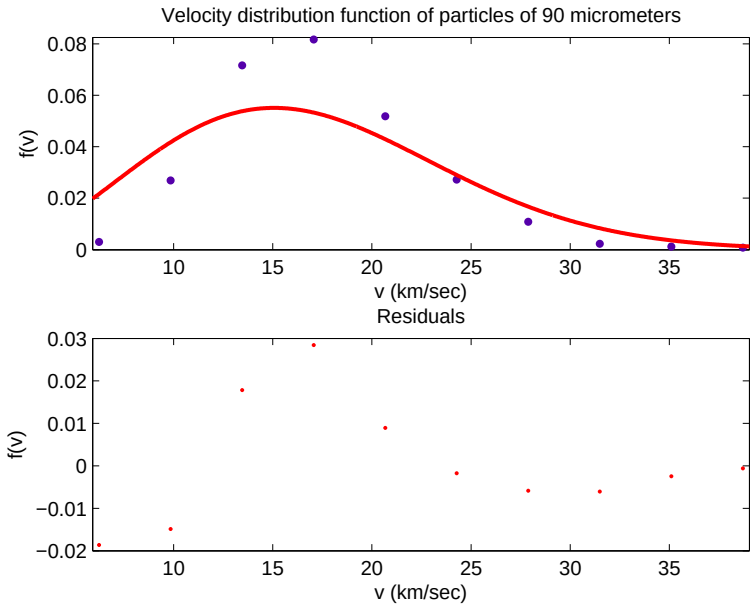

Figure 4.99: Residuals of velocity distribution of particles with $9 \cdot 10^{-3}$ cm of radius.

Goodness of fit statistics

For dust particles with $9 \cdot 10^{-3}$ cm of radius we report the value in the table (**??**) for the minimum distance distribution and in the table (4.38) for velocity distribution.

Goodness of fit	Value
SSE	940
R-square	0.2825
Adjusted R-square	0.2825
RMSE	13.71

Table 4.37: Goodness of fit for minimum distance distribution of dust particles with $8 \cdot 10^{-3}$ cm of radius.

Goodness of fit	Value
SSE	0.001855
R-square	0.7794
Adjusted R-square	0.7794
RMSE	0.01435

Table 4.38: Goodness of fit for velocity distribution of dust particles with $9 \cdot 10^{-3}$ cm of radius.

Confidence and prediction bounds

The bounds are defined with a level of certainty that it is possible to specify. The level of certainty is fixed at 95%. Below we report the confidence bound in table 4.39 for minimum distance distribution and in table 4.40 for velocity distribution. The predictions bounds are in figure (4.100) for minimum distance distribution and in figure (4.101) for velocity distribution.

Coefficients of fit	Coefficient values	Confidence bound at 95%
p_1	$1.099 \cdot 10^7$	$5.097 \cdot 10^6 - 1.688 \cdot 10^7$

Table 4.39: Goodness of fit for minimum distance distribution of dust particles with $9 \cdot 10^{-3}$ cm of radius.

Coefficients of fit	Coefficient values	Confidence bound at 95%
a	113.5	$71 - 156$

Table 4.40: Goodness of fit for velocity distribution of dust particles with $9 \cdot 10^{-3}$ cm of radius.

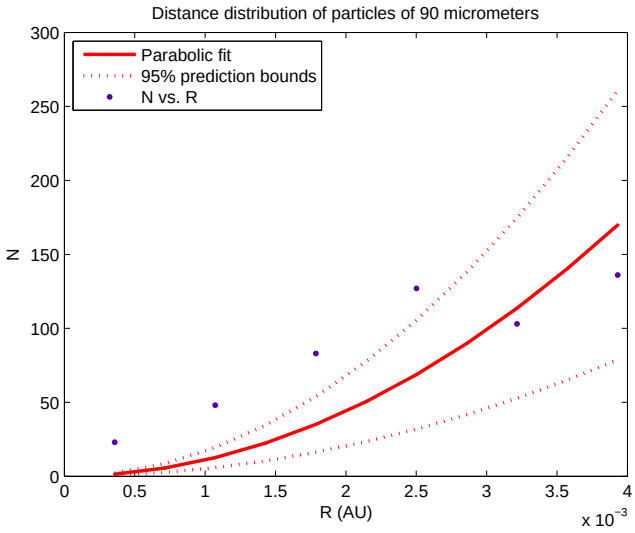

Figure 4.100: Bound of distance distribution of particles with $9 \cdot 10^{-3}$ cm of radius.

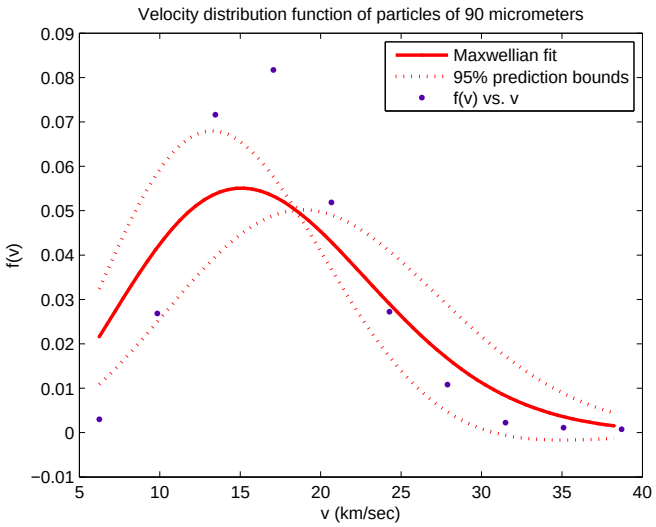

Figure 4.101: Bound of velocity distribution of particles with $9 \cdot 10^{-3}$ cm of radius.

4.3.11 Particles of 10^{-2} cm of radius

Here we consider 1000 particles with 10^{-2} cm of radius. In the figures below we show the three-dimensional coordinates distribution (figure 4.102) the bi-dimensional coordinates distribution (figure 4.103), the histogram that represent the distance distribution of dust particles (figure 4.104), that is the minimum distance particle-Mercury in a ten times the radius of the sphere of influence, and velocity distribution of dust particles (figure 4.105). After this we show in the figures (4.106) and (4.107) the best fit that adapt to our data.

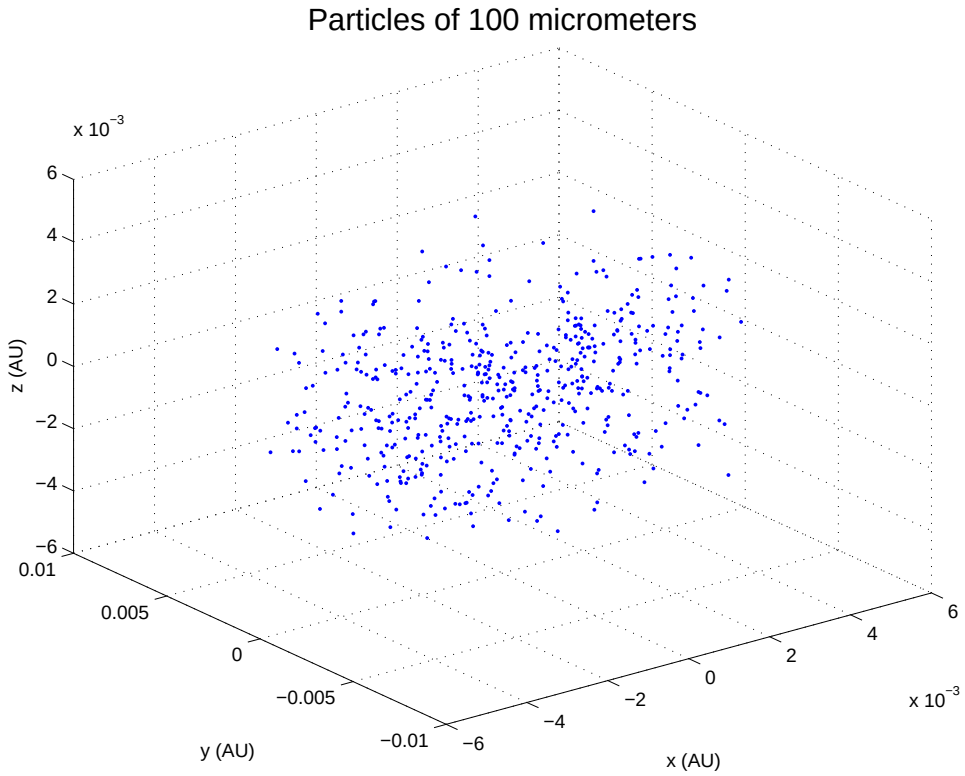

Figure 4.102: Coordinates distribution of particles of 10^{-2} cm of radius.

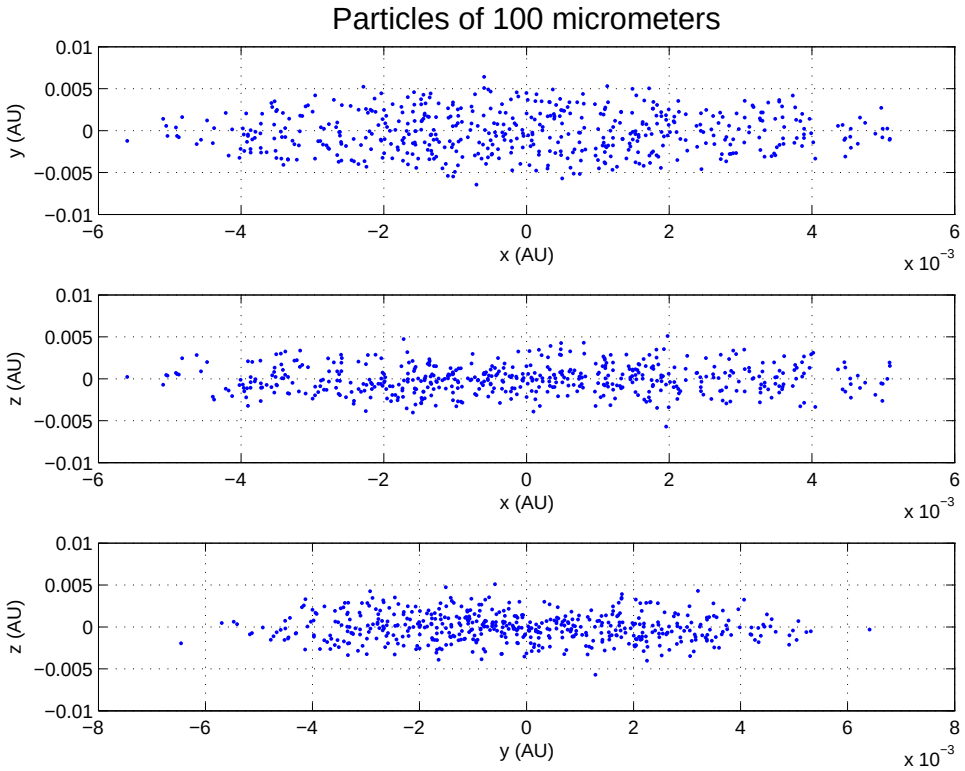

Figure 4.103: Coordinates distribution of particles of 10^{-2} cm of radius.

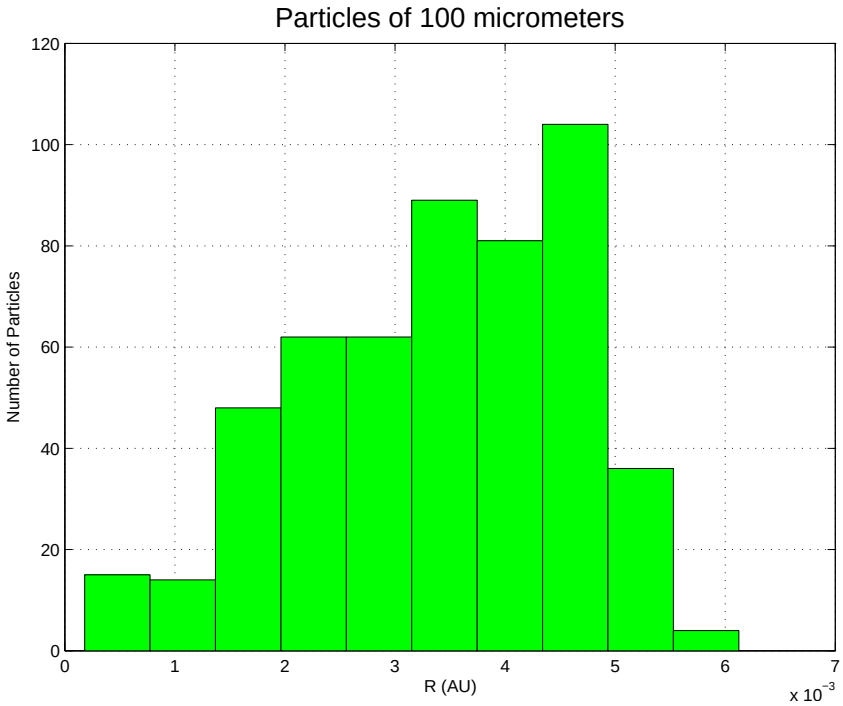

Figure 4.104: Distance distribution of particles of 10^{-2} cm of radius.

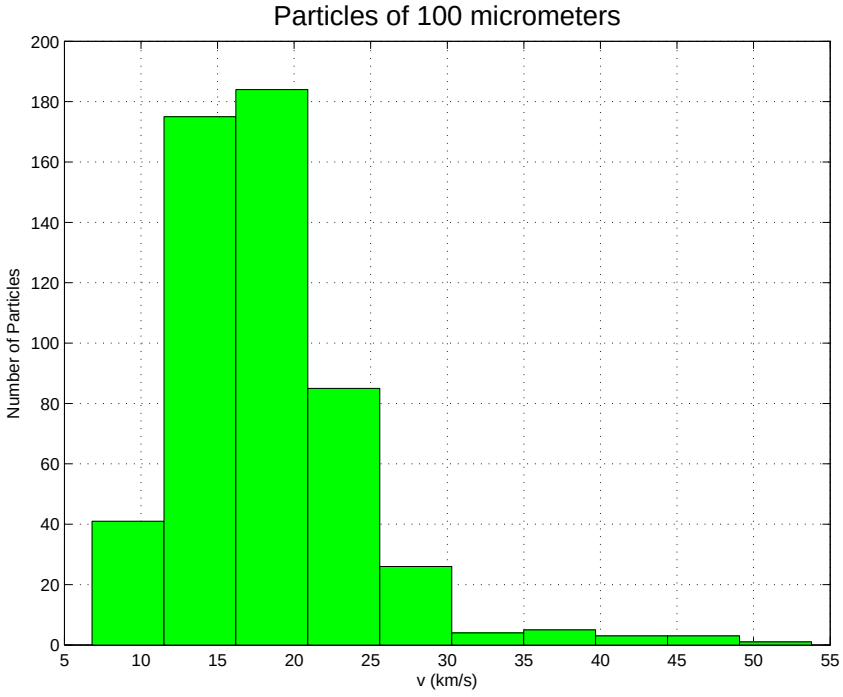

Figure 4.105: Velocity distribution of particles of 10^{-2} cm od radius.

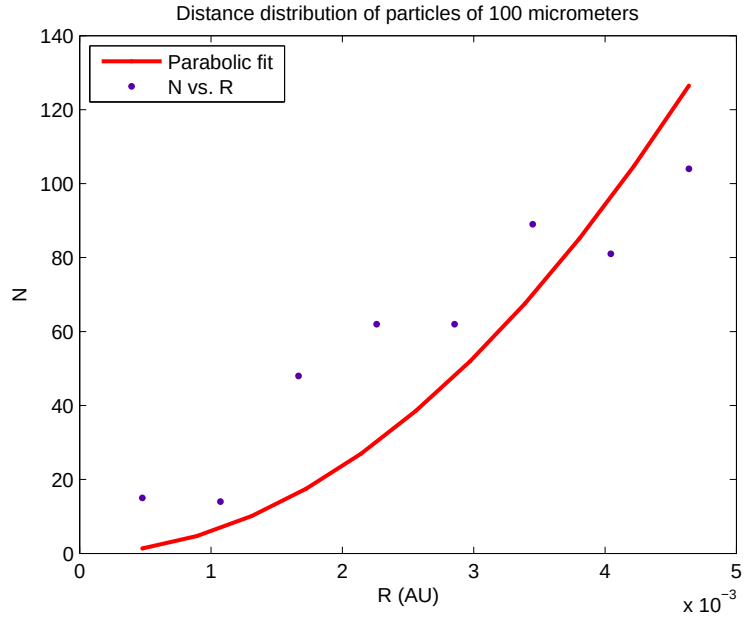

Figure 4.106: Quadratic distance distribution of particles of 10^{-2} cm od radius.

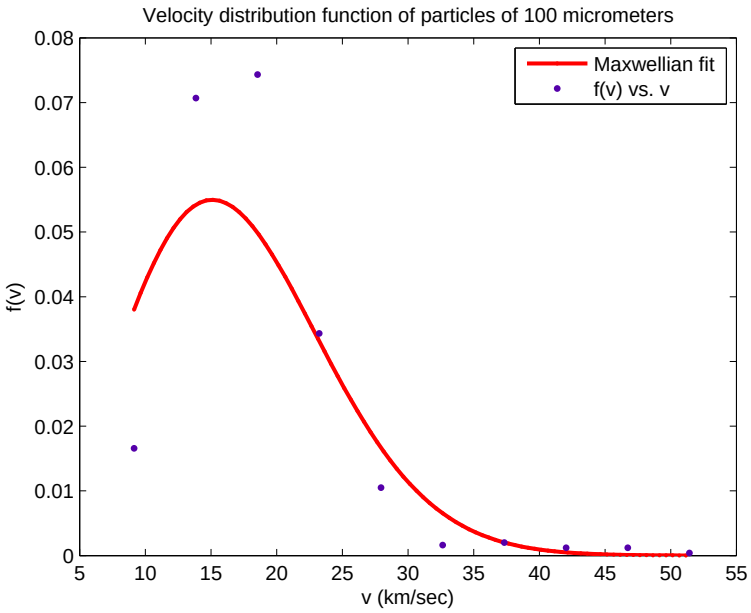

Figure 4.107: Velocity distribution of particles of 10^{-2} cm od radius.

The best fit for the minimum distance distribution is a polynomial fit of degree 2

$$f(r) = p_1 r^2 \,. \tag{4.49}$$

The best fit for velocity distribution is a maxwellian expression

$$f(v) = \sqrt{\frac{2}{\pi}} a^{-\frac{3}{2}} v^2 \exp\left(-\frac{v^2}{2a}\right) \,. \tag{4.50}$$

Residuals

We show in the figure (4.108) the residuals for the minimum distance distribution and in the figure (4.109) the residuals for the velocity distribution.

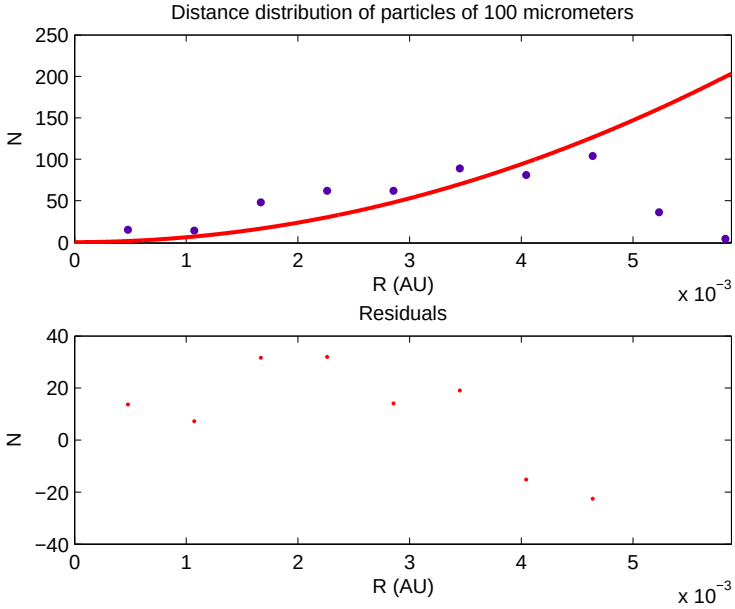

Figure 4.108: Residuals of distance distribution of particles with 10^{-2} *cm* of radius.

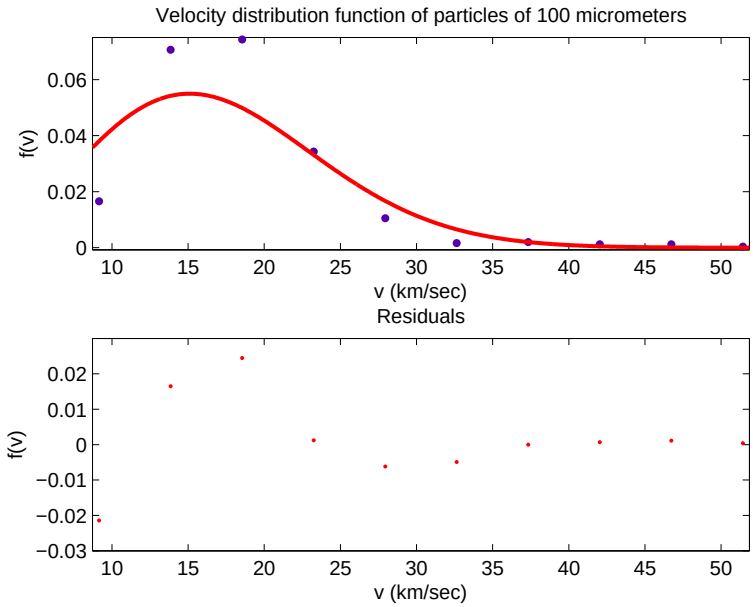

Figure 4.109: Residuals of velocity distribution of particles with 10^{-2} cm of radius.

Goodness of fit statistics

For dust particles with 10^{-2} cm of radius we report the value in the table (4.41) for the minimum distance distribution and in the table (4.42) for velocity distribution.

Goodness of fit	**Value**
SSE	475.2
R-square	0.6187
Adjusted R-square	0.6187
RMSE	8.24

Table 4.41: Goodness of fit for minimum distance distribution of dust particles with 10^{-2} cm of radius.

Goodness of fit	**Value**
SSE	0.001396
R-square	0.8155
Adjusted R-square	0.8155
RMSE	0.01245

Table 4.42: Goodness of fit for velocity distribution of dust particles with 10^{-2} cm of radius.

Confidence and prediction bounds

The bounds are defined with a level of certainty that it is possible to specify. The level of certainty is fixed at 95%. Below we report the confidence bound in table 4.43 for minimum distance distribution and in table 4.44 for velocity distribution. The predictions bounds are in figure (4.110) for minimum distance distribution and in figure (4.111) for velocity distribution.

Coefficients of fit	Coefficient values	Confidence bound at 95%
p_1	$5.88 \cdot 10^6$	$3.963 \cdot 10^6 - 7.796 \cdot 10^6$

Table 4.43: Goodness of fit for minimum distance distribution of dust particles with 10^{-2} cm of radius.

Coefficients of fit	Coefficient values	Confidence bound at 95%
a	114	$70.78 - 157.3$

Table 4.44: Goodness of fit for velocity distribution of dust particles with 10^{-2} cm of radius.

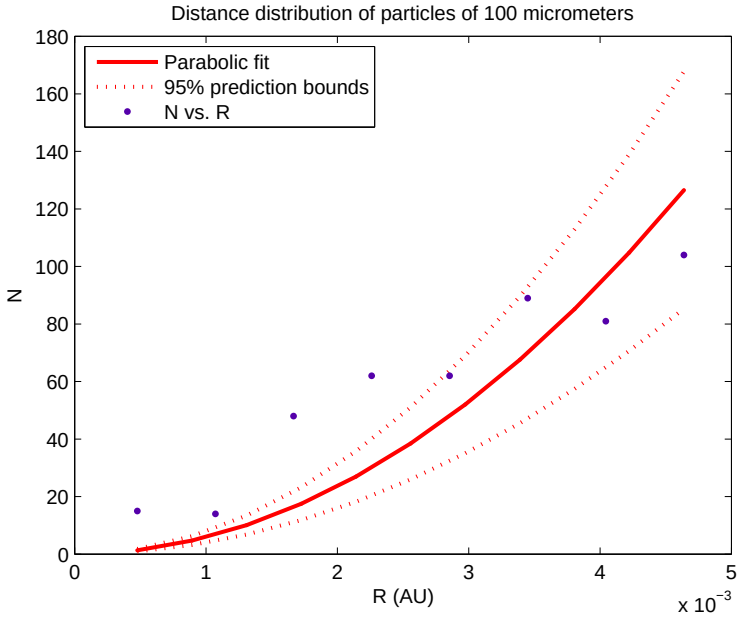

Figure 4.110: Bound of distance distribution of particles with 10^{-2} cm of radius.

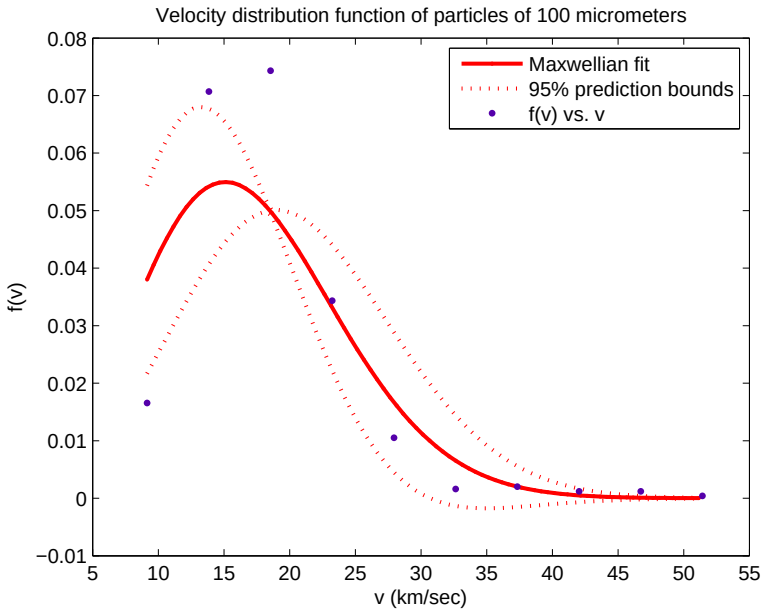

Figure 4.111: Bound of velocity distribution of particles with 10^{-2} cm of radius.

4.4 Calibration of flux

To calibrate our flux we need to know the number of particles in the Main Belt. At the beginning we have tried to search for information in the literature, but we do not find articles that give the number of dust particles coming from the Main Belt for different size of radius. We have found a relation, valid for the IRAS dust band, that gives the number of particles as a function of the radius and the size of the bodies of the specific family of the Main Belt ([49, Mann et al., 1996]).

In order to estimate this number we have run the model for the Earth, assuming that the perturbations due to Mars are negligible, and we have compared our results with the observed terrestrial flux reported in literature. In particular we have considered, as reference values, the estimate of Love and Brownlee ([45, Love et al., 1993]).

We have utilized the same input file that we have used for Mercury so it is possible to obtain the number of grains that fall dawn in a ten times the sphere of influence of the Earth and, using the same approach previously reported, we obtain the number of dust particles impacting the Earth. Comparing our flux with that reported by Love and Brownlee ([45, Love et al., 1993]) it is possible to get the number of dust particles coming from the Main Belt for each radius. It is important to note that Love and Brownlee used an average meteoroid speed of 16.9 km/sec. In our model for the Earth, we obtain a mean velocity of 18.6 km/sec. We have reproduced the equations and the plots of Love and Brownlee for different input velocities, and we have realized that they are very sensitive to this parameter. In the figure (4.112) it is possible to note the difference between the flux given by Love and Brownlee and the flux with the input mean velocity of 18.6 km/sec.

It is important to note that Love and Brownlee have determined the mass flux and size distribution of micrometeoroids in the submillimiter size range, in particular in the mass range 10^{-9} to 10^{-4} grams, by measuring hypervelocity impact craters found on the space-facing end of the gravity-gradient-stabilized Long Duration Exposure Facility (LDEF) satellite. They found that the total mass accreted by the Earth per year across the size range sampled in their work is $(40 \pm 20) \cdot 10^6 \, \frac{kg}{year}$. The major source of uncertainty lies in the value of the encounter velocity. A potentially larger error could exist if the velocity exponent in the Christiansen formula, that the authors use to derive the flux, is incorrect [45, Love et al., 1993].

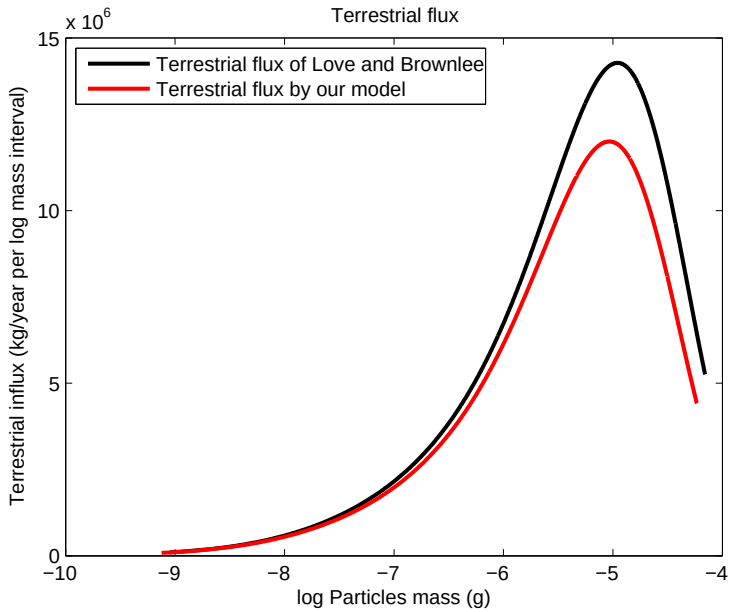

Figure 4.112: The black line represents the terrestrial flux of Love and Brownlee with an average meteoroid speed of 16.9 km/sec. The red line represents the terrestrial flux by our model with an average meteoroid speed of 18.6 km/sec.

After this, we can calibrate the flux given by our model and to obtain the flux on Mercury and we obtain the values reported in the table (4.45).

Radius of particle (μm)	**Particle mass (g)**	**Estimated flux (g/year r)**	**Estimated flux (N/year r)**
5	$1.309 \cdot 10^{-9}$	$4.551 \cdot 10^{9}$	$3.477 \cdot 10^{18}$
10	$1.047 \cdot 10^{-8}$	$7.478 \cdot 10^{9}$	$7.141 \cdot 10^{17}$
20	$8.378 \cdot 10^{-8}$	$1.531 \cdot 10^{10}$	$1.827 \cdot 10^{17}$
30	$2.827 \cdot 10^{-7}$	$1.027 \cdot 10^{11}$	$3.631 \cdot 10^{17}$
40	$6.702 \cdot 10^{-7}$	$2.169 \cdot 10^{11}$	$3.236 \cdot 10^{17}$
50	$1.309 \cdot 10^{-6}$	$3.637 \cdot 10^{11}$	$2.778 \cdot 10^{17}$
60	$2.262 \cdot 10^{-6}$	$3.670 \cdot 10^{11}$	$1.623 \cdot 10^{17}$
70	$3.592 \cdot 10^{-6}$	$5.467 \cdot 10^{11}$	$1.522 \cdot 10^{17}$
80	$5.362 \cdot 10^{-6}$	$5.130 \cdot 10^{11}$	$9.568 \cdot 10^{16}$
90	$7.634 \cdot 10^{-6}$	$3.243 \cdot 10^{11}$	$4.248 \cdot 10^{16}$
100	$1.047 \cdot 10^{-5}$	$6.882 \cdot 10^{11}$	$6.572 \cdot 10^{16}$

Table 4.45: Estimated flux at Mercury for each particle's dimension.

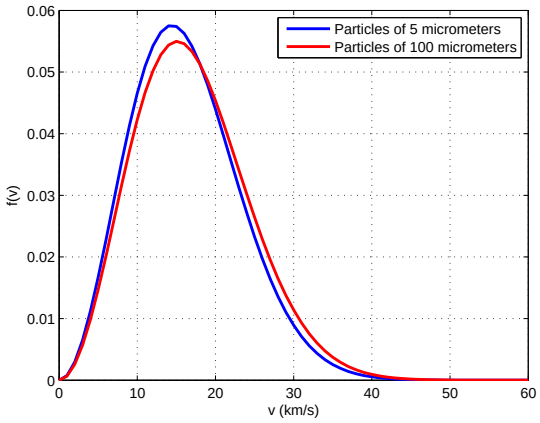

Figure 4.113: Velocity distribution function of particles with radius of 5 μm and 100 μm.

4.5 Impact velocity

The Cintala's model of vaporization originated by meteoroid impacts, considers particles with radius in the range $10^{-8} - 10^{-3}$ m, corresponding to a mass range of $10^{-18} - 10^{-2}$ g. Following Cintala ([7, Cintala, 1992]), the differential flux can be written as

$$\Phi(v, m) = f(v) \cdot h(m)\,, \tag{4.51}$$

where $f(v)$ is the velocity distribution of dust particles (km/s) and $h(m)$ is the mass distribution function of the impacting particles ($gcm^{-2}s^{-1}$).

The velocity distribution function is given by the following equation

$$f(v) = kr^{1.5}\left[\frac{v}{\sqrt{r(v^2 - v_{Me}^2) + v_{Ee}^2}}\right]^3 e^{\left(-\gamma\sqrt{r(v^2-v_{Me}^2)+v_{Ee}^2}\right)}\,, \tag{4.52}$$

where $k = 3.81$, $\gamma = 0.247$ are constant, $r = 0.387$ AU is the mean distance of Mercury from the Sun, v is the impact velocity of dust particles on Mercury, $v_{Ee} = 11.1$ km/s is the escape velocity for the Earth at 100 km altitude, $v_{Me} = 4.25$ km/s is the escape velocity at the surface of Mercury.

Equation (4.52) would provide the velocity distribution at the distance r AU- in the specific case at Mercury- if the spatial density of dust particles is equal to that at 1 AU. If we consider that the density of particles varies as $r^{-1.3}$ ([38, Leinert et al., 1981]), we will have

$$f(v) = kr^{0.2}\left[\frac{v}{\sqrt{r(v^2 - v_{Me}^2) + v_{Ee}^2}}\right]^3 e^{\left(-\gamma\sqrt{r(v^2-v_{Me}^2)+v_{Ee}^2}\right)}\,, \tag{4.53}$$

In our model we derive the histograms for the encounter velocity distribution for each particle size. The distributions of impact velocities are shown as histograms in figure (4.5) and (4.105) for particles of dimension of 5 μm and 100 μm, respectively.

In the figures (4.5), (4.105) and (4.114) it is possible to note that there is no substantial difference between them, so we can conclude that the dimension of dust particles does not affect the velocity distribution.

Since we consider particles with radius in a range $5 \cdot 10^{-6} - 10^{-4}$ m, we can compare directly our velocity distribution with the Cintala's one based on a size of $10^{-8} - 10^{-2}$ m. As we said before, we do not consider particles with radius smaller than 10^{-6} m because solar radiation pressure is dominant on solar gravity enough to drive dust particles out of the Solar System ([5, Burns et al., 1979], [73, Sykes

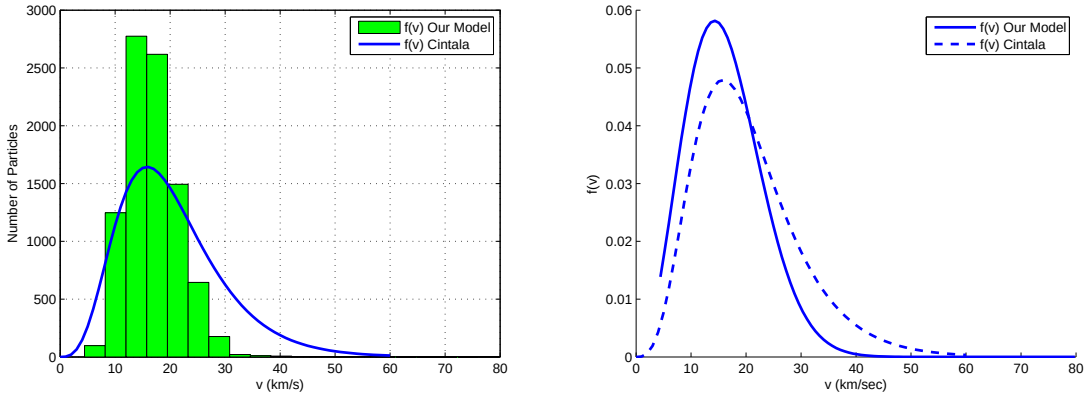

Figure 4.114: Comparison of velocity distribution function of particles given by our model and Cintala's model.

et al., 2004]), but in our work we compute the flux in the range $5 \cdot 10^{-6} - 10^{-4}$ m because the reference article for the calibration of our model consider particles with mass dimension in the range 10^{-9} to 10^{-5} grams.

4.6 Micrometeoroid flux on Mercury

The impact flux is dependent on two factors, that is, the velocity distribution of dust particles that impact the planet, as mentioned before, and the mass distribution function.

The Cintala's mass distribution is

$$h(r) = -\frac{1}{mF_1} \exp\left(\sum_{i=0}^{11} c_i \ln(m)^i\right) \cdot \left[\sum_{i=1}^{11} i \cdot c_i \ln(m)^{i-1}\right], \tag{4.54}$$

where m is the projectile mass, $F_1 = 0.364$, c_i are constants reported in the Cintala's article ([7, Cintala, 1992], [8, Cremonese et al., 2005]).

As written before, following Cintala, the differential flux $\phi(v, \mu)$ can be written as

$$\phi(v, \mu) = f(v)h(\mu)\,, \tag{4.55}$$

where $f(v)$ is the velocity distribution of the impactors and $h(\mu)$ is a function describing the mass distribution of impacting objects and that can be derived by (4.54).

The main difference between our model and Cintala's one is in the flux computation. While Cintala obtains the flux as the product of two functions (see equation (4.55)), in our model, performing numerical simulations, we obtain the flux directly per every particle's size. This is a great advantage because we don't have necessarely to use the mass distribution function.

4.7 Model comparison of micrometeoroid flux on Mercury

In this section we compare our results with Cintala's one. We have computed Cintala's fluxes for each particles dimension and we have compared them with our computations.

Radius of particle (μm)	**Cintala's flux** $\left(\frac{N}{year \cdot r}\right)$	**Our flux** $\left(\frac{N}{year \cdot r}\right)$	$\frac{\textbf{Cintala's flux}}{\textbf{Our flux}}$
5	$3.115 \cdot 10^{19}$	$3.477 \cdot 10^{18}$	8.967
10	$8.245 \cdot 10^{18}$	$7.141 \cdot 10^{17}$	11.550
20	$1.676 \cdot 10^{18}$	$1.827 \cdot 10^{17}$	9.172
30	$5.424 \cdot 10^{17}$	$3.631 \cdot 10^{17}$	1.494
40	$2.199 \cdot 10^{17}$	$3.236 \cdot 10^{17}$	0.680
50	$1.030 \cdot 10^{17}$	$2.778 \cdot 10^{17}$	0.371
60	$5.343 \cdot 10^{16}$	$1.623 \cdot 10^{17}$	0.329
70	$2.992 \cdot 10^{16}$	$1.522 \cdot 10^{17}$	0.197
80	$1.780 \cdot 10^{16}$	$9.568 \cdot 10^{16}$	0.186
90	$1.112 \cdot 10^{16}$	$4.248 \cdot 10^{16}$	0.262
100	$7.230 \cdot 10^{15}$	$6.572 \cdot 10^{16}$	0.110

Table 4.46: Comparison between Cintala and our flux. The flux is expressed in $\frac{N}{year \cdot r}$.

Radius of particle (μm)	**Cintala's flux** $\left(\frac{g}{cm^2 \cdot s \cdot r}\right)$	**Our flux** $\left(\frac{g}{cm^2 \cdot s \cdot r}\right)$	$\frac{\textbf{Cintala's flux}}{\textbf{Our flux}}$
5	$1.729 \cdot 10^{-15}$	$1.928 \cdot 10^{-16}$	8.967
10	$3.658 \cdot 10^{-15}$	$3.168 \cdot 10^{-16}$	11.550
20	$5.949 \cdot 10^{-15}$	$6.486 \cdot 10^{-16}$	9.172
30	$6.498 \cdot 10^{-15}$	$4.350 \cdot 10^{-15}$	1.494
40	$6.245 \cdot 10^{-15}$	$9.188 \cdot 10^{-15}$	0.680
50	$5.714 \cdot 10^{-15}$	$1.541 \cdot 10^{-14}$	0.371
60	$5.120 \cdot 10^{-15}$	$1.555 \cdot 10^{-14}$	0.329
70	$4.554 \cdot 10^{-15}$	$2.316 \cdot 10^{-14}$	0.197
80	$4.044 \cdot 10^{-15}$	$2.173 \cdot 10^{-14}$	0.186
90	$3.596 \cdot 10^{-15}$	$1.374 \cdot 10^{-14}$	0.262
100	$3.208 \cdot 10^{-15}$	$2.916 \cdot 10^{-14}$	0.110

Table 4.47: Comparison between Cintala and our flux. The flux is expressed in $\left(\frac{g}{cm^2 \cdot s \cdot r}\right)$.

The total flux in the range $5 - 100$ μm obtained by Cintala is

Range (μm)	$\frac{\textbf{N}}{\textbf{year}}$	$\frac{\textbf{g}}{\textbf{cm}^2 \cdot \textbf{s}}$
5-100	$4.073 \cdot 10^{16}$	$1.402 \cdot 10^{-16}$

Table 4.48: Cintala's flux in the range $5 - 100$ μm.

To calculate our flux we have decided to follow two ways and then to compare them.

In the first case we have decided to use the flux curve given by Love and Brownlee, that we have used to calibrate our data, shifting it to Mercury. We have compared the outputs of the numerical simulations per each particle's size on the Earth and on Mercury obtaining the ratio between the fluxes. Then we have computed the weighted mean, depending on the particle's number that arrive near the planet. In this way we have obtained the coefficient allowing us to shift the Love and Brownlee curve to Mercury.

The coefficient that we find is 36.5. In this way it is possible to shift the Love and Brownlee curve, to integrate the function and to obtain the flux on Mercury that is $2.317 \cdot 10^{-14}$ $\frac{g}{cm^2 \cdot sec}$ in the range $5 - 100$ μm.

Radius of particle (μm)	$\frac{\text{Mercury Flux}}{\text{Earth Flux}}$ from simulations	Number of particles	Weighted ratio
5	39.1	996	$3.89 \cdot 10^4$
10	19.4	739	$1.43 \cdot 10^4$
20	8.4	753	$6.32 \cdot 10^3$
30	30.8	804	$2.47 \cdot 10^4$
40	42.6	654	$2.79 \cdot 10^4$
50	52.2	722	$3.77 \cdot 10^4$
60	42.0	461	$1.93 \cdot 10^4$
70	53.3	692	$3.69 \cdot 10^4$
80	45.2	764	$3.45 \cdot 10^4$
90	27.2	744	$2.02 \cdot 10^4$
100	57.5	528	$3.03 \cdot 10^4$

Table 4.49: The table reports the ratio between the Mercury and the Earth fluxes and the related weighted ratio.

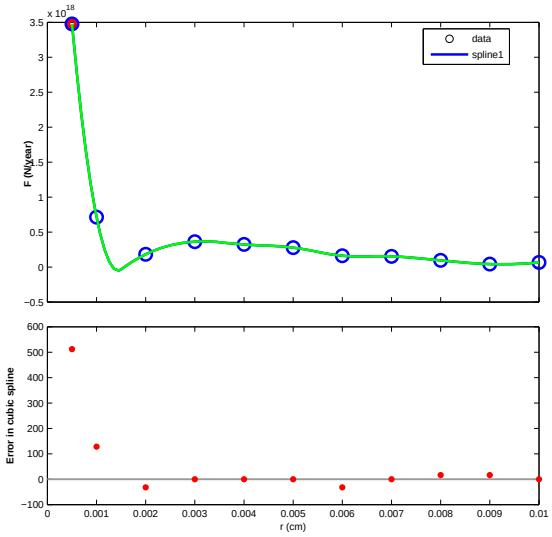

Figure 4.115: The flux on Mercury obtained by our numerical simulations (blue points) and the spline curve with the associated error.

In the second case we have used a spline curve (see figure 4.115) calculating the integral.

In this way we obtain a flux given in the following table.

Range (μm)	$\frac{\text{N}}{\text{year}}$	$\frac{\text{g}}{\text{cm}^2 \cdot \text{s}}$
5-100	$2.662 \cdot 10^{15}$	$5.718 \cdot 10^{-14}$

Table 4.50: The flux obtained by our model in the range $5 - 100$ μm.

It is possible to note that the number of impacts given by Cintala, measured in $\frac{N}{year}$, is 15.3 times higher than our estimate, but the flux given in $\frac{g}{cm^2 \cdot sec}$, is 407.8 times lower.

We can conclude that we have a number of impacts smaller than Cintala, but a mass contribution higher than Cintala.

It means that our numerical simulations yield a number of impacts higher than Cintala for larger particles.

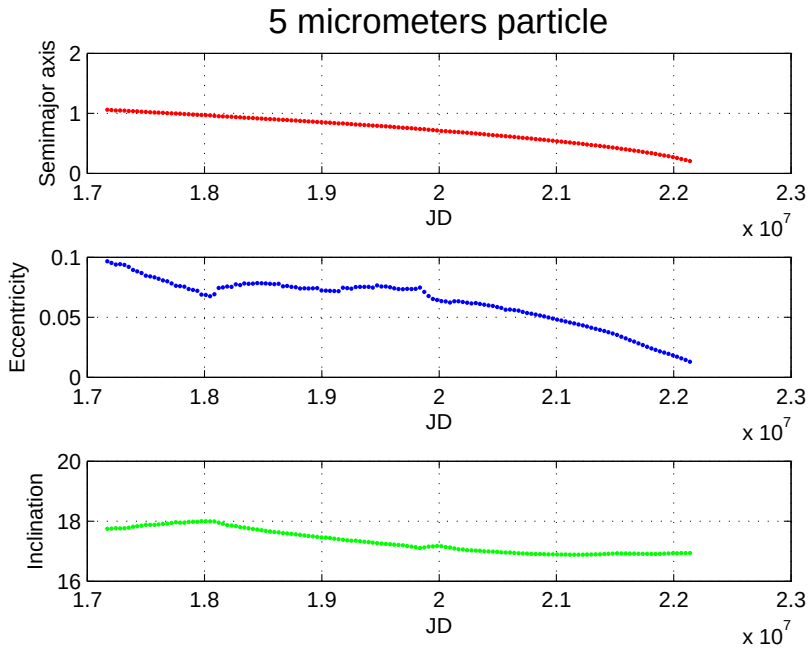

Figure 4.116: Semimajor axis, eccentricity and inclination for a particle of 5 μm of radius.

4.8 Lifetime and resonances

The lifetime of the dust particles depends on their radius and mass. In our numerical simulations we have seen that the lifetime increases with the radius of the micrometeoroids. We have also to take into account, for particles with the size higher than 10 μm, the resonances with the Earth.

The figures 4.116, 4.117, 4.118, 4.119, 4.120, 4.121, 4.122, 4.123, 4.124, 4.125 and 4.126 show that the resonance effects begin to influence weakly the particles of 10 μm, then they increase their influence up to particles of 100 μm.

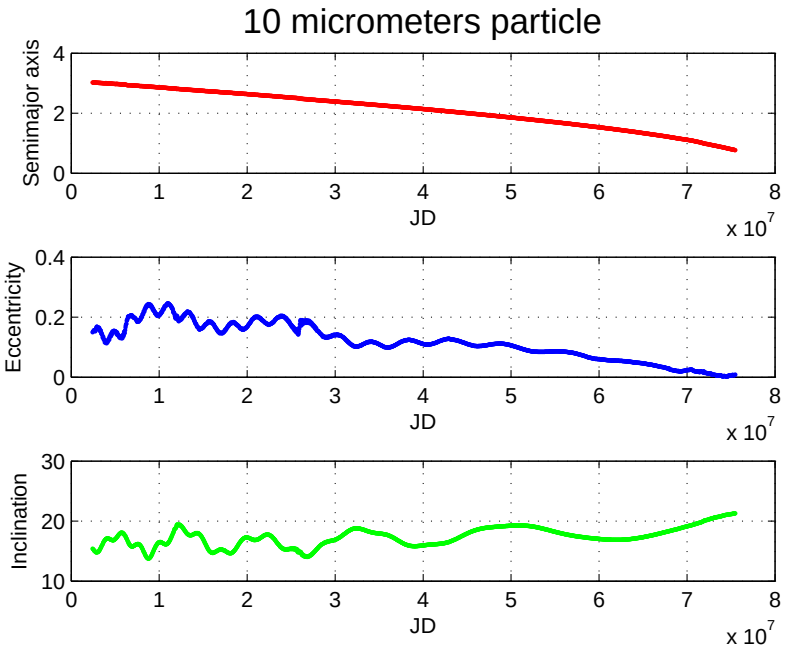

Figure 4.117: Semimajor axis, eccentricity and inclination for a particle of 10 μm of radius.

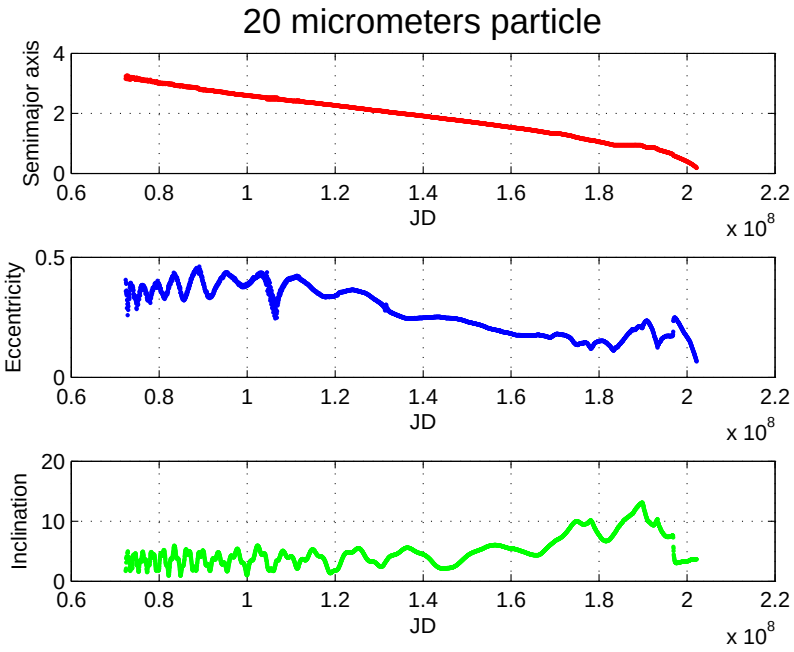

Figure 4.118: Semimajor axis, eccentricity and inclination for a particle of 20 μm of radius.

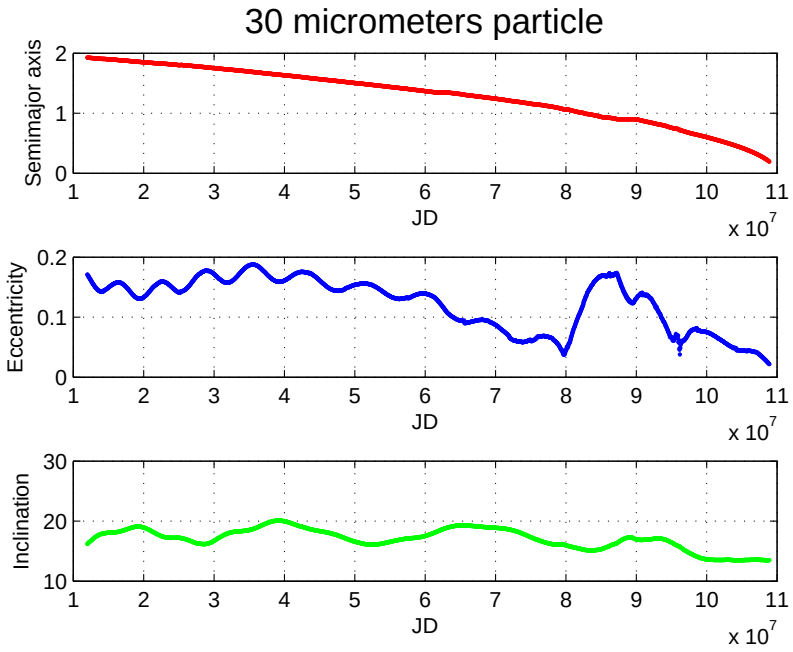

Figure 4.119: Semimajor axis, eccentricity and inclination for a particle of 30 μm of radius.

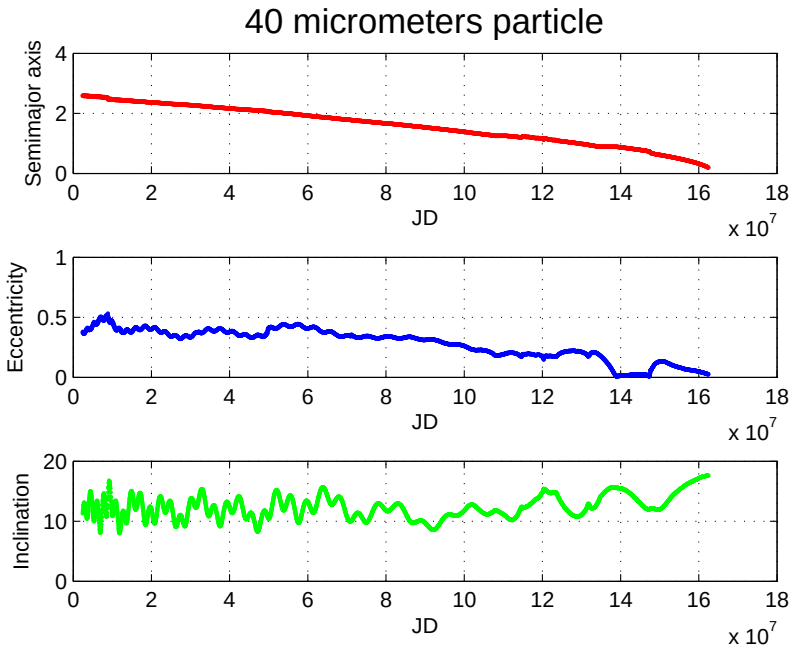

Figure 4.120: Semimajor axis, eccentricity and inclination for a particle of 40 μm of radius.

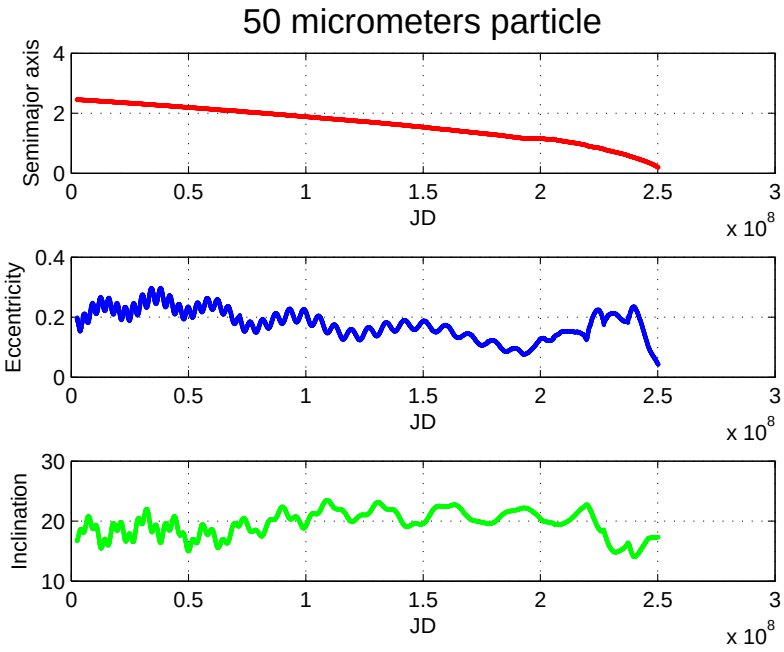

Figure 4.121: Semimajor axis, eccentricity and inclination for a particle of 50 μm of radius.

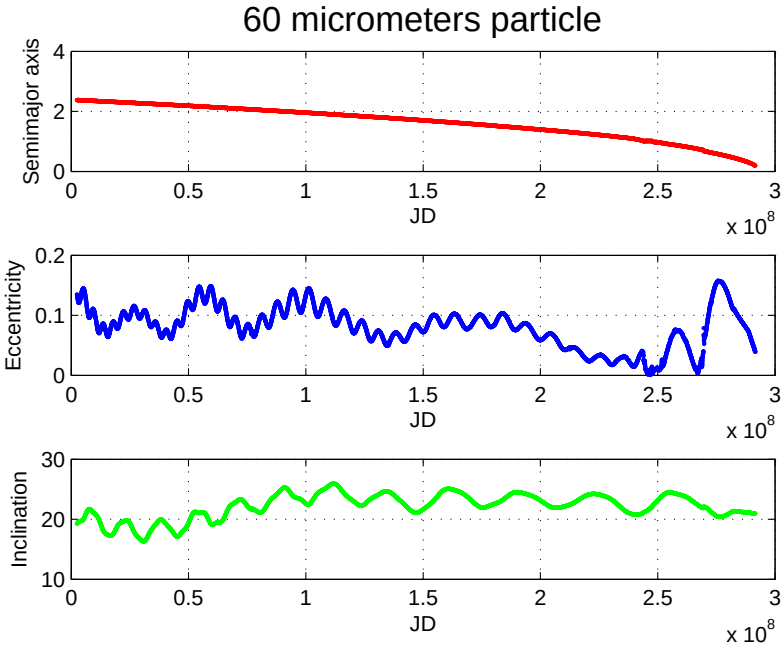

Figure 4.122: Semimajor axis, eccentricity and inclination for a particle of 60 μm of radius.

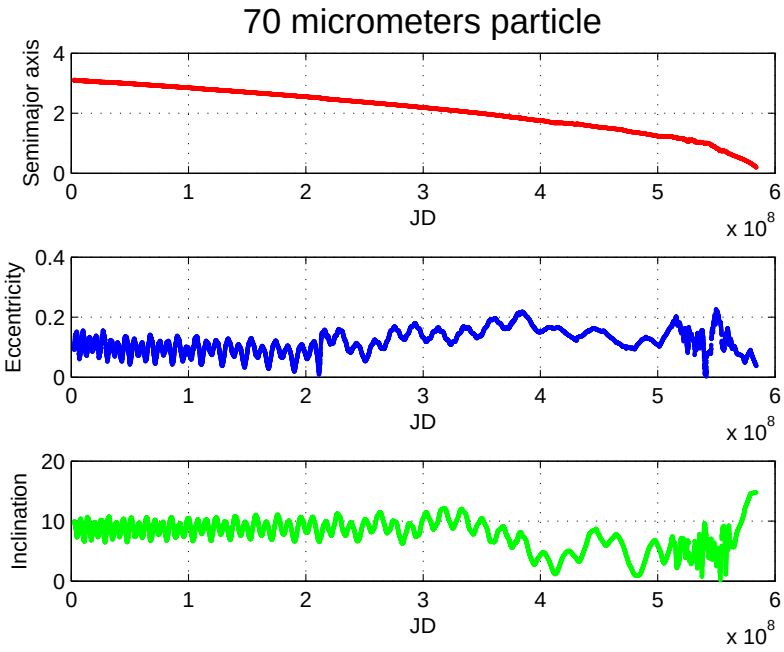

Figure 4.123: Semimajor axis, eccentricity and inclination for a particle of 70 μm of radius.

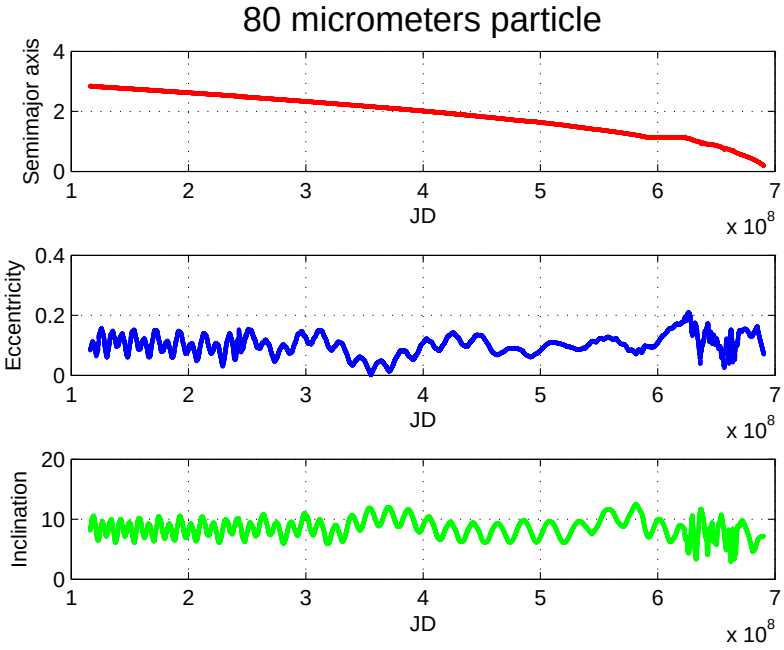

Figure 4.124: Semimajor axis, eccentricity and inclination for a particle of 80 μm of radius.

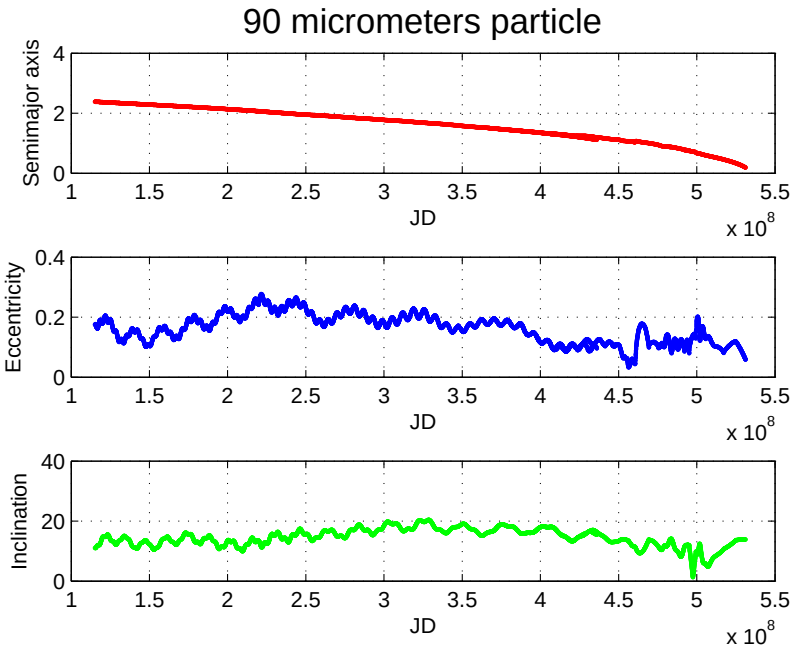

Figure 4.125: Semimajor axis, eccentricity and inclination for a particle of 90 μm of radius.

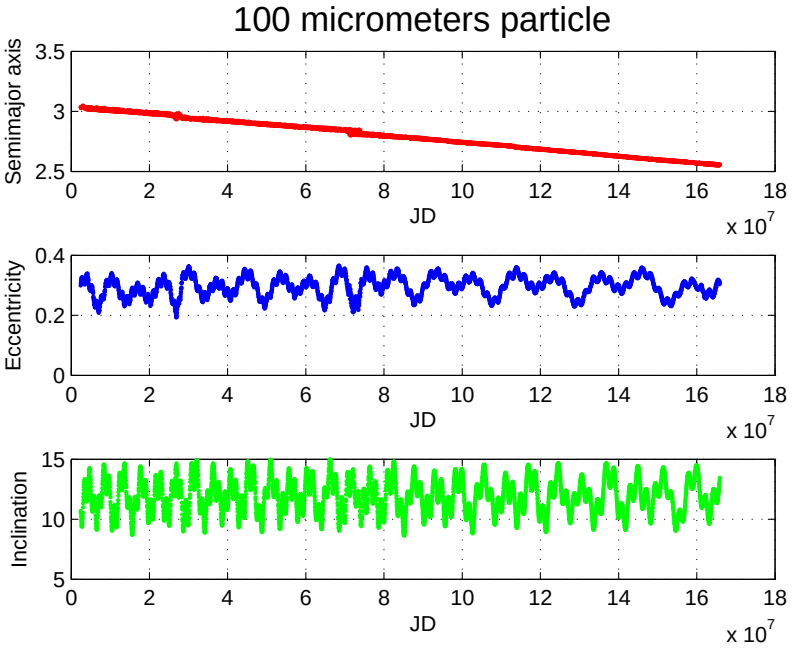

Figure 4.126: Semimajor axis, eccentricity and inclination for a particle of 100 μm of radius.

Chapter 5

Comets

5.1 Comets

The comets are solid, but fragile bodies with dimensions of around 1 to 10 km (called nucleus) revolving around the Sun, generally in elliptical orbits, with a period varying from a few years to hundreds and thousands of years. The material, gas and dust, coming out from the nucleus due to solar heating forms a spherical shell called coma. The various physical processes operating on the material in the coma due to the solar radiation and the solar wind give rise to all the observed effect including the plasma tail and the dust tail. Because of small sizes of comet nuclei, they are difficult to observe from the Earth.

Whether asteroidal dust is produced continuosly or stochastically, cometary dust is not produced in the same way. Asteroid particles are dynamically distinct from cometary particles in that they have smaller initial orbital eccentricities. After being generated in the asteroid belt, this dust evolves toward the Sun under the Poynting-Robertson drag. As it passes the orbit of Earth, some of it forms a circumsolar ring due to dust orbits resonant with that of Earth. The ring is just outside Earth orbit, at 1.03 AU, as the exterior resonances are more stable.

Comets are much fewer in number than asteroids, and material tracing their current orbits would produce a relatively lumpy cloud. Whether a cometary component could be smooth depends on the outcome of the race between differential precession of the ejected cometary particle orbits, collisional lifetimes, and orbital decay timescales.

Collisions govern the lifetimes of particles having large size ranges as well as larger particles up to the size of asteroids, whereas sublimation and breakup determine the lifetime of comets in the inner Solar System, < 5 AU. Transport of these larger meteoroids through the Solar System made easier by stochastic gravitational interactions with planets, by the systematically inward (toward the Sun) drift caused by the Pointing-Robertson effect, and by the Yarkovsky effect (a thermal radiation force) acting in directions that depend on the orientation of the spin axis, spin rate, and thermal properties of the object. However, since the collisional lifetime is shorter than the transport time, meteoroids only slowly diffuse away from their place of origin while at the same time they are ground down by collisions [5, Burns et al., 1979].

When a comet is discovered, it is identified by virtue of its fuzzy appearance, with perhaps a tail, arising from the loss of gas and dust. This dust represents the smallest-sized particle emissions from a comet (generally tens of μm and smaller, although significant coma surface area is argued to reside in very large particles ([17, Fulle, 2004])). These are entrained in the gas outflow and accelerated to speed up to $\sim 1\ km/s$ for the smallest particles. After decoupling from the gas, they are generally lost to the solar radiation field. The sensitivity of a particle to solar radiation pressure is described by the parameter, β, the ratio of radiation force to gravitational force felt by the particle [5, Burns et al., 1979]. Most of the particles observed in a comets tail at visible wavelengths are micrometer-sized and have $\beta > 1$. These particles are not gravitationally bound to the Sun and escape the Solar System, not contributing to the

interplanetary dust complex. Particles having lower β can also escape from the Solar System when they are released from an orbiting object like a comet, because of the contribution of the comets motion. For emission at perihelion, the value of β for escape is a function of orbital eccentricity of the parent body

$$\beta_p \geq \frac{1-e}{2}\,. \tag{5.1}$$

Thus, for a parabolic comet, all emitted particles would be lost. The Solar System loses particles tens of μm and smaller from long-period comets, while retaining particles on the order of several μm from short-period Jupiter-family comets (Figure 5.1). Almost all dust particles tens of μm and smaller are released from these latter comets into Jupiter-crossing orbits even comets whose orbits are completely interior to that of Jupiters (Figure 5.2). Subsequent perturbations on the orbits of these particles by Jupiter results in their loss while the distribution of many bear little resemblance to the elements of their parent comets [24, Gustafson et al., 1987]. Making the assumption that such scattered particles have randomized nodes (required to match the azimuthal symmetry of the cloud), Liou et al. (1996) was able to model a contribution to the cloud by single-sized particles from Encke, taking into account the radiation pressure, the Poynting-Robertson and the corpuscular drag, and the perturbations by Jupiter, which when combined with a model contribution from asteroid dust made good matches to selected scans of the zodiacal cloud by IRAS [42, Liou et al., 1995]. Cometary particles may undergo considerable orbital evolution with time, increasing the difficulty of distinguishing them from asteroidal particles. Liou and Zook (1996) determined that some cometary particles (from Tempel 2 like comets) could be injected into mean-motion resonances with Jupiter and trapped for thousands of years, after which their orbital eccentricities would be quite small. They would approach Earth with the low velocities expected for asteroid particles. This would help to explain the overlap in morphologies and compositions among collected cometary and asteroidal interplanetary dust particles, identified by their model atmospheric entry speeds [43, Liou and Zook, 1996].

The physical properties of the particles vary from one comet to another, from one region within a comet to another, and from one region within the interplanetary cloud to another. They can be characterized, through appropriate simulations (with realistic assumptions about the composition, the structure and the size of the particles) by studying how they scatter light, how the scattering depends upon the geometry and the wavelength of the observations, and how they re-emit the absorbed thermal energy.

The composition is revealed by in situ observations, by remote infrared spectroscopy, and by laboratory analysis of samples of interplanetary dust particles collected in the Earth atmosphere. Cometary dust is an unequilibrated, heterogeneous mixture of high- and low temperature condensates [25, Hanner and Bradley, 2004]. Major constituents are amorphous and crystalline silicate minerals (e.g. forsterite, enstatite) and organic refractory materials. The similarity between these properties and those of anhydrous chondritic interplanetary dust particles (fine-grained and complex mixtures of numerous mineral and amorphous components) strongly suggests that comets are the source of such fragile and highly porous particles. Interplanetary dust particles actually mostly belong to the chondritic class, with either anhydrous (pyroxene, olivine) or hydrated (layer silicate) constituents, somehow matching the abundances of CI chondrites [3, Brownlee, 1996]. Relatively high abundances in silicates may be the result of high melting point favoring atmospheric entry. It should be added that, as compared to the interplanetary dust particles (collected in the ecliptic at 1 AU, after they have suffered space weathering and atmospheric entry), the samples collected by the Stardust mission in the coma of comet 81P/Wild 2 are to provide an un-biased sample. The existence in cometary dust of crystalline olivine particles, formed in a hot (41000 K) environment, poses the problem of the trapping of minerals produced at high temperatures in comets [4, Brucato et al., 1999]. A recent 10 μm spectroscopic survey of Herbig Ae star discs has suggested that crystalline silicates are produced or reprocessed [74, Van Boekel et al., 2005]. In the proto-planetary disc of our Solar System, the olivine particles could have been generated in the hot region near the proto-Sun, and transported to the cold region of formation of comets. Some comets actually show a silicate emission feature near 10 μm, while other ones do not have such a feature. In addition,

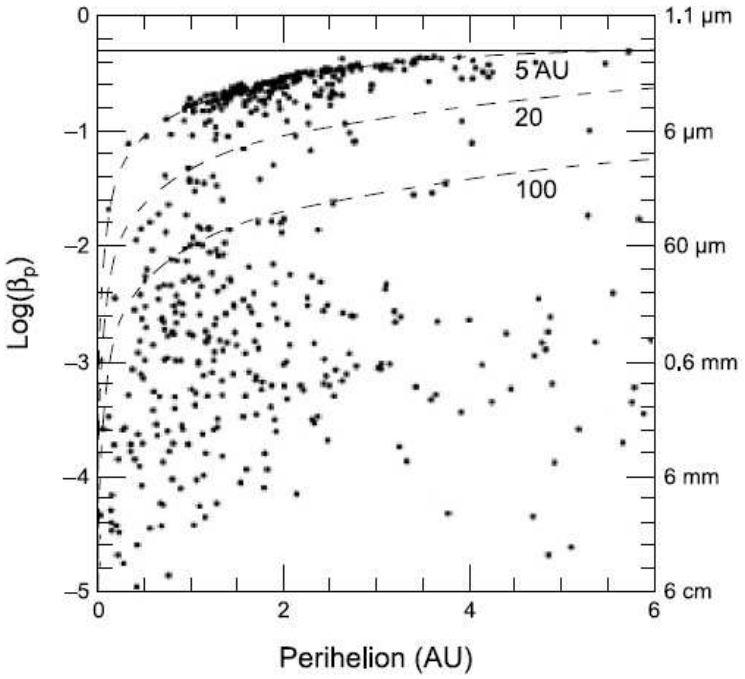

Figure 5.1: Maximum β (minimum radius, assuming a density of 1 $\frac{g}{cm^3}$) of particles from known comets on escape trajectories from the Solar System, assuming perihelion emission and zero ejection velocity. Aphelion distances of source comets are dashed lines. For circular orbits, $\beta_p = 0.5$. Particles are assumed to have zero albedo. From Sykes et al., *Inteplanetary Dust Complex and Comets* (2004).

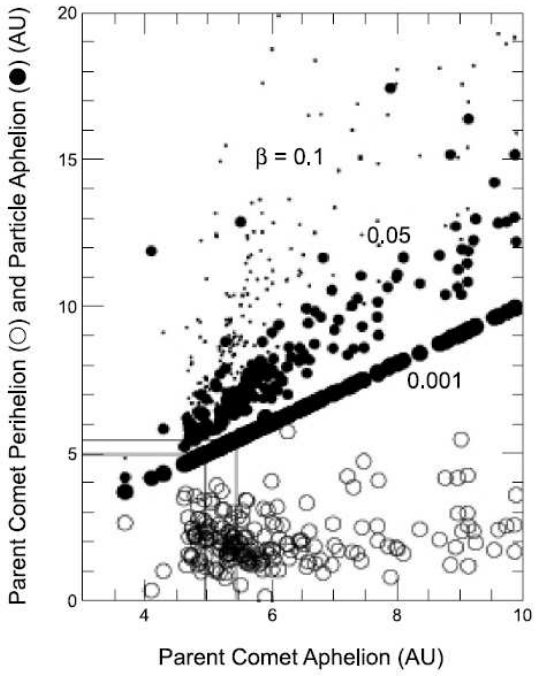

Figure 5.2: Perihelion and aphelion distances of parent comets (open circles) and the aphelia of emitted particles of different β (filled circles). Jupiters perihelion and aphelion distances are indicated by solid lines. From Sykes et al., *Inteplanetary Dust Complex and Comets* (2004).

comets exhibiting this emission feature may show a double peak, implying the existence of crystalline silicates, or a single broad peak, suggesting the existence of amorphous silicate. Cometary dust particles are likely to have low densities, about $100\,\frac{kg}{m^3}$ for comet 1P/Halley [16, Fulle et al., 2000], and to consist of easily fragmenting aggregates [12, Desvoivres et al., 2000]. Together with the D/H enrichment noticed in an interplanetary dust particles and with laboratory experiments on ballistic agglomeration, such results are in excellent agreement with the hypothesis that cometary dust particles could be "birdnest", i.e. porous aggregates of partly photo-chemically processed submicronic interstellar elongated dust grains, with possibly silicates cores and organics mantles.

5.1.1 Size distributions

Dust ejected by comets spans a broad size range, from sub-micrometer to millimetre or larger. From measurements of Giotto spacecraft at comet Halley, most of the mass is concentrated in large particles, while submicron and micron-sized particles dominate the extinction and scattering properties of comets in the visual to near infrared wavelength range. The sizes certainly vary from comet to comet, as well as within the coma, because of dynamical effects, evaporation and fragmentation. Size distributions are mostly derived from space probes data and dust tail and coma analysis based on ground-based observations, obtained during a cometary coma flyby or a cruise through the interplanetary dust cloud. They are usually described with a^s power laws, where a is the effective radius of the particle, and s the power law index.

Comets and asteroids are considered to be the two major sources of Solar System interplanetary dust particles. Interplanetary dust particle abundances are established from zodiacal light measurements, from meteoroid impacts onto spacecraft dust sensors [48, Mann and Grn, 1995], and from the samples collected by high altitude aircraft in the stratosphere [75, Zolensky et al., 1994]. Dust particles coming from comets generally have much higher Earth approaching and atmospheric entry velocities than do asteroidal grains, but the number of Earth-crossing comets per year are considerably less than near-Earth asteroids [78, Weissman, 2006]. The total cometary impact rate on the Earth, based on observed comets and crudely correcting for observational incompleteness, is $1.4 \cdot 10^{-7}$ per year, or one impact every 7.2 Myr. About 48% of this total is due to Jupiter-family comets, 14% due to Halley-type comets, and 38% due to long-period comets, though half of the long-period comets arrive in brief cometary showers of 2-3 Myr duration [78, Weissman, 2006]. If one combines the impact rate estimates for long period comets, Jupiter family comets and Encke type comets, then the total impact rate is $1.1 \cdot 10^{-7}$ per years, or one impact every 9.1 Myr. If comet showers are included, these numbers increase to $1.4 \cdot 10^{-7}$ per year, or one impact every 7.2 Myr. These are only a few per cent of the rates of NEAs.

Also the orbital integration of Jupiter-family comets, asteroidal and cometary dust particles, under the gravitational influence of the planets, the Poynting-Robertson drag, the radiation pressure and the solar wind drag, supports that written previously [26, Ipatov and Mather, 2005], [27, Ipatov and Mather, 2006]. These integrations demonstrated that, varying the ratio β between the radiation pressure force and the gravitational force, the collision probabilities of cometary dust particles are lower than the asteroidal dust particles, except dust particles coming from comets 10P/Tempel 2 that are closer to those particles coming from asteroids [26, Ipatov and Mather, 2005].

5.1.2 Orbits of comets

In this section we differentiate principally between two types of comets: those having orbital period of the order of tens of years, *short-period* comets, and the *long-period* comets whose orbital period are much longer. Short-period comets are of particular interest because they, together with asteroids, are believed to be the sources of smaller interplanetary objects, such as meteorites and interplanetary dust.

Short-period comets have orbits well within the Solar System with aphelia inside of Jupiter's orbits or somewhat beyond, ranging from 4 AU to about the orbit of Pluto. They are believed to have a lifetime

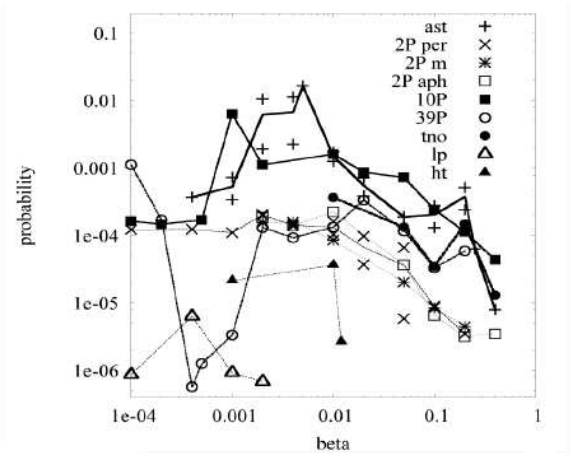

Figure 5.3: The probability P of collisions of dust particles with the Earth versus β for particles launched from asteroids (ast), trans-Neptunian object (tno), Comet 2P/Encke at perihelion (2P per), Comet 2P/Encke at aphelion (2P m), Comet 10P/Tempel 2 (10P), Comet 39P/Oterma (39P), long period comets (lp) at $e = 0.995$ and $q = 0.9$ AU, and Halley-type comets (ht) at $e = 0.975$ and $q = 0.5$ AU. From Ipatov and Mather, *Migration of dust particles to the terrestrial planets* (2005).

of the order of thousands of years or much shorter because, after some hundreds of perihelion passages, their volatile substance will have largely evaporated and the remaining less-volatile matrix fragmented by excessive internal stress produced during evaporation into objects smaller than can be observed by telescopes. In this manner they are a major source of minor interplanetary objects. Even if they could maintain their material for longer periods, short-period comets tend to be rather short-lived objects for an additional reason: having aphelia close to Jupiter's orbit they suffer strong Jovian perturbations with survival times ranging from a few years to a few million years. It is believed that Jovian perturbations eventually send these objects into hyperbolic orbits provided that they have not already disintegrated because of thermal stresses and explosive processes caused by the rapid evaporation during perihelion passage.

5.2 Sungrazing comets

The Kreutz sungrazing group of comets with perihelion distances q less than about 2 solar radii, have periods P apparently in the range 300-900 years and closely similar to orbital planets. They are clearly related to one another, but their origin has been an enigma since Kreutz first called attention to the group in the last century.

Sungrazing comets maybe can originate from the decay of a single massive comet which first passed close to the Sun. This general picture leads to possible periods for the progenitor ranging between 360-380 years and 700-800 years.

Fragmentation of a single giant comet, then, may explain the number and orbital similarities of the Kreutz sungrazer group, but it does not immediately explain the orbit of the progenitor.

The sungrazer have relatively short period and do not pass close to any of the major planets. Their orbits are remarkably stable, and changes in the perihelion distance due to stellar or planetary perturbations, or even non-gravitational forces, are usually believed to be negligible. The new-comet flux from the Oort cloud, comprising comets with $q < 0.01\ AU$ yet massive enough to explain the whole sungrazer family, is so small that the inferred recent injection of a large comet from the Oort cloud is itself unlikely.

These previous investigations have not involved long-term integrations of sungrazing orbits, so effects due to slowly acting secular perturbations have not been apparent.

This suggests that the progenitor may have undergone hundreds of revolutions at small perihelion distance, a figure which could be significantly reduced only by invoking strong systematic non-gravitational forces.

5.2.1 SOHO's comets

Since the turn on of the Large Angle Spectrometric Coronagraph (LASCO) on the Solar and Heliospheric Observatory (SOHO) satellite, on December 30 1995, it has discovered over 1100 new comets, of which over 900 belong to the Kreutz sungrazing group.

All the observed comets have clearly been very small, and the data suggest that few survived perihelion passage in any coherent fashion. The brightness distributions of the Kreutz comets detected with SOHO/LASCO indicate an increasing number of comets with decreasing size and the size distribution of nuclei is probably described with a power law [71, Sprague et al., 2007].

Mann [50, Mann et al., 2000] tried to estimate the dust supply from the sungrazers assuming a spherical comet of 20 m radius fragmented into 10 μm spherical particles and distributed in a sphere of 10 solar radii. They found a number density of $10-17\ cm^3$, which is below typical densities of $10-14\ cm^3$ for particles of this size range. They assumed this large size of dust grains, since for size distributions that are similar to that in the interplanetary dust cloud, the majority of mass would be contained in fragments of this size. Analysis of the dust tails of sungrazing comets shows that the sungrazers emit small particles of sizes 0.1 μm and that the dust in the sungrazing comets has a narrow size distribution [67, Sekanina, 2000]. When making this rough estimate for 0.1 μm spherical particles, the number density amounts to $10-12\ cm^3$, which is comparable to typical dust densities in this size range. Moreover, the dust that is produced by sungrazers will quickly leave the solar corona. The Kreutz comets are in highly elliptic or hyperbolic orbits, their speed is approximately 230 $\frac{km}{s}$ at 7 solar radii and can be described as bodies with initial speeds of zero at infinity that fall into the Sun. Dust grains released from the sungrazers are in similar orbits.

Mann et al. [50, Mann et al., 2000] concluded that the dust supply from the frequently observed sungrazing comets is negligible, but they did not have a complete dynamical model of small particles released by these objects that may supply a large amount of dust. Considering that we do not have the size distribution released by the sungrazers, we cannot obtain a good estimate of the dust supply in the inner Solar System. The dust supply from larger comets near the Sun can produce dust density enhancements that are comparable to the dust densities in the solar environment [50, Mann et al., 2000].

The dust density may be raised many fold over a time span of weeks. Such relatively lower probability events are important for providing volatiles to the inner solar system.

5.3 Conclusion

In the future work we will operate some simulations with dust particles originating from comets in order to know which is the contribution of this dust source at the flux on Mercury. However, following the literature, we believe that the contribution of this kind of dust particles at the flux on Mercury is lower than that originating from dust particles coming from the Main Belt.

Chapter 6

Model comparison and BepiColombo mission

6.1 Interplanetary flux model by Grün et al.

The following characteristics of the interplanetary meteoroid population are assumed to be constant:

- the effective meteoroid density is $\varrho = 2.5 \frac{g}{cm^3}$;
- at 1 AU the relative effective speed between different meteoroids as well as the impact speed on the Moon is $v_0 = 20\ km/sec$;
- the flux on the Earth as well as the mutual impact flux is isotropic.

Grün et al. determined meteoroid densities by a number of methods and they conclude that only 20 to 40% of the meteoritic particles are of low densities ($\varrho \leq 1\ \frac{g}{cm^3}$) whereas the majority of meteoroids have densities $\varrho = 2$ to $3\ \frac{g}{cm^3}$. They use an effective density of $\varrho = 2.5\ \frac{g}{cm^3}$.

Meteoroid speeds have been derived from meteor observations and satellite measurements.

The directionality of the meteoroid flux is obtained from meteor data and satellite measurements and they approximate this distribution by an isotropic distribution and neglect the directional enhancements [20, Grün et al., 1985].

Mass (g)	**Grün Model Flux** ($m^{-2}sec^{-1}$)	**Our Model Flux** ($m^{-2}sec^{-1}$)
10^{-18}	$2.6 \cdot 10^{-1}$	-
10^{-17}	$3.8 \cdot 10^{-2}$	-
10^{-16}	$5.9 \cdot 10^{-3}$	-
10^{-15}	$1.1 \cdot 10^{-3}$	-
10^{-14}	$2.5 \cdot 10^{-4}$	-
10^{-13}	$8.3 \cdot 10^{-5}$	-
10^{-12}	$3.4 \cdot 10^{-5}$	-
10^{-11}	$1.5 \cdot 10^{-5}$	-
10^{-10}	$6.4 \cdot 10^{-6}$	-
10^{-9}	$3.0 \cdot 10^{-6}$	$5.5 \cdot 10^{-6}$
10^{-8}	$1.2 \cdot 10^{-6}$	$2.3 \cdot 10^{-6}$
10^{-7}	$3.0 \cdot 10^{-7}$	$6.0 \cdot 10^{-6}$
10^{-6}	$4.7 \cdot 10^{-8}$	$1.9 \cdot 10^{-7}$
10^{-5}	$4.6 \cdot 10^{-9}$	$7.1 \cdot 10^{-8}$
10^{-4}	$3.3 \cdot 10^{-10}$	-
10^{-3}	$1.9 \cdot 10^{-11}$	-
10^{-2}	$9.7 \cdot 10^{-13}$	-
10^{-1}	$4.7 \cdot 10^{-14}$	-
10	$2.2 \cdot 10^{-15}$	-
10^{1}	$1.0 \cdot 10^{-16}$	-
10^{2}	$4.7 \cdot 10^{-18}$	-

Table 6.1: Interplanetary flux model at 1 AU by Grün et al. and results from simulations of our model at the Earth. From Grün et al., "Collisional Balance of the Meteoritic Complex", 1985.

6.2 BepiColombo mission

BepiColombo is an interdisciplinary mission to explore the planet Mercury through a partnership between ESA and Japan's Aerospace Exploration Agency (JAXA). From their dedicated orbits two spacecraft, the Mercury Planetary Orbiter (MPO) and the Mercury Magnetospheric Orbiter (MMO), will be studying the planet and its environment. They will be launched together on a single Ariane 5. The launch is foreseen for 2014 with arrival in the 2020. Solar electric propulsion will be used for the journey to Mercury. The MMO provided by JAXA focuses on investigating the wave and particle environment of the planet from an eccentric orbit. The MPO, a three-axis-stabilized and nadir-pointing spacecraft in a low-eccentricity polar orbit, is dedicated to the characterization of Mercury. It will provide high accuracy measurements of the planet's interior structure, a characterization of Mercury's exosphere and a full coverage of the planet surface at high resolution, whereby surface morphology will be correlated to surface composition. Major effort was put into optimizing the scientific return by defining the payload complement such that individual measurements can be interrelated and complement each other. The MPO payload comprises 11 instruments/instrument packages; the MMO payload consists of 5 instruments/instrument packages. Together, the scientific payload of both spacecraft will provide the detailed information necessary to understand Mercury and its magnetospheric environment and to find clues to the origin and evolution of a planet close to its parent star.

The main issues to be addressed are:

- Origin and evolution of a planet close to its parent star.
- Mercury's figure, interior structure, and composition.
- Interior dynamics and origin of its magnetic field.
- Exogenic and endogenic surface modifications, cratering, tectonics, volcanism.

- Composition, origin and dynamics of Mercury's exosphere and polar deposits.
- Structure and dynamics of Mercury's magnetosphere.
- Test of Einstein's theory of general relativity.

The complexity of these fundamental scientific objectives poses high requirements on the payload of the mission. None of the objectives concerning Mercury can be reached through measurements of any single instrument. However, the combination of the measurements of the various instruments aboard the MPO and the MMO will provide answers to key questions related to these topics. The results expected from the BepiColombo mission will resolve many outstanding questions related to the origin and evolution of Mercury as the innermost member of the group of the terrestrial planets [65, Schulz and Benkhoff, 2005].

	Mercury Planetary Orbiter (MPO)	**Mercury Magnetospheric Orbiter (MMO)**
Stabilization	3-axis stabilised	15-rpm spin-stabilised
Orientation	Nadir	Spin axis at 90 to Sun
Spacecraft Mass	500 kg	250 kg
Payload Mass	60 kg	40 kg
Power	450 W	300 W
TM band	X/Ka-band	X-band
Deployment	400 1508 km	400 11 824 km
Operational lifetime	$>$ 1 year	$>$ 1 year
Data volume	1550 Gb/year	160 Gb/year
Equivalent average data rate	50 kb/s	5 kb/s
Antenna	1.0 m X/Ka-band high-gain steerable antenna	0.8 m X-band phased array high-gain antenna
Thrusters	Ion thrusters from on-going commercial development	
Other equipment	high temperature resistant thermal protection, solar arrays	

Table 6.2: Spacecraft.

6.2.1 ESA study of micrometeoroids flux on BepiColombo

The meteoroid fluxes can be important for spacecraft being stabilized on three axis. Most impacts from meteoroids will occur on forward facing surfaces. The number of impacts, N, increases linearly with exposed area and with exposure time:

$$N = F \cdot A \cdot T\,, \tag{6.1}$$

where F is the number of impacts per unit area, A is the total exposed area and T is the exposure time. The fluence is the flux integrated over time. Once N has been determined, the probability of exactly n impacts occurring in the corresponding time interval is given by Poisson statistics:

$$P_n = \frac{N^n}{n!} \exp^{-N}\,. \tag{6.2}$$

The probability for no impacts, P_0 is thus given by

$$P_0 = \exp^{-N}\,. \tag{6.3}$$

For values of $N \ll 1$ the probability, Q, for at least one impact ($Q = 1 - P_0$) is equal to N

$$Q = 1 - \exp^{-N} \approx 1 - (1 - N) = N\,. \tag{6.4}$$

6.2.2 ESA Model

The METEM model is used to calculate the meteoroid fluences on the BepiColombo mission during the interplanetary cruise and for 88 days (one Mercury year) around Mercury. The METEM meteoroid fluxes include the contributions from 5 different populations. The model can be applied to distances between 0.1 10 AU from the Sun. At 1 AU from the Sun Fluxes from METEM are similar to those obtained from the standard meteoroid reference model for Earth orbits [20, Grün et al., 1985]. The total average meteoroid fluence (sporadic + stream average), N, is the number of particles with mass m per m^2 impacting a randomly-oriented flat plate under a viewing angle of 2π during the mission duration.

The METEM meteoroid flux model gives a yearly average. Relative to a spacecraft with fixed orientation w.r.t. the flight direction the meteoroid flux has a directional dependence. The flux on a specific spacecraft oriented surface and velocity vector can be calculated numerically [70, Sørensen and Evans, 2004].

6.2.3 Meteoroid fluences

In this work it is assumed a density of 2.0 $\frac{g}{cm^3}$ and a spherical shape has been used to convert particle masses and diameters.

Table 6.3 give meteoroid fluences as obtained from the METEM model. The table gives the number of impacts, $N/m^2/mission$ (one Mercury year, 88 Earth days, in orbit around the planet) from one side to a randomly oriented plate for a range of minimum particle sizes.

Mass (g)	**Diameter** (cm)	**Fluence** ($/m^2/88\ days$)
10^{-15}	$9.85 \cdot 10^{-6}$	$3.54 \cdot 10^{4}$
10^{-14}	$2.12 \cdot 10^{-5}$	$1.09 \cdot 10^{4}$
10^{-13}	$4.57 \cdot 10^{-5}$	$4.37 \cdot 10^{3}$
10^{-12}	$9.85 \cdot 10^{-5}$	$2.38 \cdot 10^{3}$
10^{-11}	$2.12 \cdot 10^{-4}$	$1.40 \cdot 10^{3}$
10^{-10}	$4.57 \cdot 10^{-4}$	$8.75 \cdot 10^{2}$
10^{-9}	$9.85 \cdot 10^{-4}$	$3.27 \cdot 10^{2}$
10^{-8}	$2.12 \cdot 10^{-3}$	$7.97 \cdot 10^{1}$
10^{-7}	$4.57 \cdot 10^{-3}$	$1.62 \cdot 10^{1}$
10^{-6}	$9.85 \cdot 10^{-3}$	2.38
10^{-5}	$2.12 \cdot 10^{-2}$	$1.99 \cdot 10^{-1}$
10^{-4}	$4.57 \cdot 10^{-2}$	$7.82 \cdot 10^{-3}$
10^{-3}	$9.85 \cdot 10^{-2}$	$2.06 \cdot 10^{-4}$
10^{-2}	$2.12 \cdot 10^{-1}$	$5.58 \cdot 10^{-6}$
10^{-1}	$4.57 \cdot 10^{-1}$	$1.57 \cdot 10^{-7}$
1	$9.85 \cdot 10^{-1}$	$4.71 \cdot 10^{-9}$

Table 6.3: Cumulative number of meteoroid impacts, N, per m^2 from 1 side to a randomly oriented surface for a range of minimum particle sizes as obtained by the METEM model. The results are for a spacecraft at Mercury and a duration of 88 Earth days. A density of $\varrho = 2.0\ \frac{g}{cm^3}$ and spherical shape were used to convert masses to diameters. From "Mercury Environmental Specification (Part II) BepiColombo Definition Study ", Sørensen and Evans, 2004.

The meteoroids impacting BepiColombo will show a distribution of velocities ranging from below 10 $\frac{km}{s}$ up to values larger than 100 $\frac{km}{s}$. Smaller particles have higher average impact velocities than larger particles. For meteoroids with masses around 1 g the average impact velocity during the cruise phase is in the range $20 - 25\ \frac{km}{s}$. For the assessment of impact effects a constant velocity of 25 $\frac{km}{s}$ shall be used for both of the two cruise trajectories considered. When the spacecraft will be in orbit around Mercury a constant velocity of 30 $\frac{km}{s}$ shall be used. An average impact angle of 45° from the surface normal shall be used.

The impact angle distribution can be assumed as isotropic or obtained from the METEM model [70, Sørensen and Evans, 2004].

6.2.4 Model uncertainties

The uncertainties in the meteoroid models mainly result from uncertainties in the particle densities and masses. Near Earth fluxes for meteoroids larger than 10^{-6} g are well defined, but the associated masses are quite uncertain. The mass density of the meteoroids spans a wide range, from about 0.15 $\frac{g}{cm^3}$ to values as large as 8 $\frac{g}{cm^3}$, it imply an uncertainty in the flux of a factor 0.1 to 10. For meteoroids smaller than 10^{-6} g the flux uncertainties are estimated to be a factor of 0.33 to 3. The uncertainties in the meteoroid fluences at heliocentric distances different from 1 AU are larger and they cannot be quantified [70, Sørensen and Evans, 2004].

6.2.5 Comparison with our model

In our work we assumed a density of 2.5 $\frac{g}{cm^3}$ and a spherical shape were used to convert particle masses and diameters.

Diameter of particle (cm)	**Particle mass (g)**	**Estimated flux** ($N/m^2/88\ days$)
$1 \cdot 10^{-3}$	$1.31 \cdot 10^{-9}$	$1.12 \cdot 10^{4}$
$2 \cdot 10^{-3}$	$1.05 \cdot 10^{-8}$	$2.30 \cdot 10^{3}$
$4 \cdot 10^{-3}$	$8.38 \cdot 10^{-8}$	$5.89 \cdot 10^{2}$
$6 \cdot 10^{-3}$	$2.83 \cdot 10^{-7}$	$1.17 \cdot 10^{3}$
$8 \cdot 10^{-3}$	$6.70 \cdot 10^{-7}$	$1.04 \cdot 10^{3}$
10^{-2}	$1.31 \cdot 10^{-6}$	$8.95 \cdot 10^{2}$
$1.2 \cdot 10^{-2}$	$2.26 \cdot 10^{-6}$	$5.23 \cdot 10^{2}$
$1.4 \cdot 10^{-2}$	$3.59 \cdot 10^{-6}$	$4.90 \cdot 10^{2}$
$1.6 \cdot 10^{-2}$	$5.36 \cdot 10^{-6}$	$3.08 \cdot 10^{2}$
$1.8 \cdot 10^{-2}$	$7.63 \cdot 10^{-6}$	$1.37 \cdot 10^{2}$
$2 \cdot 10^{-2}$	$1.05 \cdot 10^{-5}$	$2.12 \cdot 10^{2}$

Table 6.4: Estimated flux at Mercury for each particle's dimension following our model.

Chapter 7

Conclusions and future work

7.1 Conclusions

Mercury has an extended and tenuous exosphere containing H, He, O, Na, K, and Ca. The exosphere of Mercury is the result of a dynamical balance between different sources and sink mechanisms acting on the planetary surface. A good way to understand the exosphere of the planet is to include the different processes involved both in its formation and in its depletion. Among these processes, there is the meteoroid impact vaporization, i.e., the vapor production derived from the infall of small and medium-sized objects present in the Solar System.

Recent papers attribute to impacting particles smaller than 1 cm the major contribution to exospheric gases.

On the basis of existing models ([31, Killen et al., 2001], [37, Leblanc et al., 2003], [57, Morgan et al., 1988]), the fraction of sodium atoms released by this mechanism is estimated to be in the range from about 10% to 100% (in the case of no release of regolith erosion products). According to a different hypothesis, the composition of the Hermean exosphere reflects the chemical composition of meteorites impacting Mercury, possibly mixed with solar wind products.

However, fluxes and impact velocities for different sizes are based on old extrapolations of the same quantities at the Earth. In fact, the literature faced the topic of micrometeoroid flux at the Earth and at Mercury, but on the latter, the estimate of the flux is made by means of an extrapolation of results obtained on our Planet.

The work performed in this research proposes to develop a dynamical evolution model of dust particles smaller than 0.1 mm, coming from the Main Belt, until they reach Mercury in order to obtain the micrometeoroid flux directly without any extrapolation. The results obtained by means of this model take issue with those given by Cintala in his article, that is the reference author in this field ([7, Cintala, 1992]).

In particular, the main results are that the Cintala flux, expressed in terms of mass ($\frac{g}{cm^2 \cdot s}$) is 407.8 times lower.

This comparison yields that our model estimate a number of impacts smaller than Cintala, but a mass contribution much higher.

The reason of this result is due to the fact that our numerical simulations give a number of impacts higher than Cintala for larger particles. This explains the major mass contribution.

7.2 Future work

In the near future we will go on the simulations for dust particles larger than 0.1 mm in order to understand where the Poynting-Robertson effect starts to be less important than the gravitational effect.

Then we will operate some simulations with dust particles originating from comets in order to know which is the contribution of this dust source at the flux on Mercury.

A recent work ([52, Marchi et al., 2005]) showed that the flux of large meteoroids has two asymmetries in longitude, on the Mercury's surface, and in true anomaly of its orbit around the Sun, and they depends from the particle size.

Since in our model we have considered an isotropic flux, in the future we will look for possible asymmetry in the flux and, consequently, in the impact rate on the surface of the planet, taking into account the spin-orbit resonance of Mercury.

Finally, starting from the results given by the model we will calculate the new contribution of micrometeoroid impacts to the exosphere of the planet.

Appendix A

Spin-Orbit resonance

Consider the motion of a small satellite whose spin axis is normal to the plane of its fixed elliptical orbit. Let the long axis of the satellite make an angle ϑ with a reference axis that is fixed in inertial space, which in this two-body, keplerian system we can take to be the major axis of the satellite's orbit. The long axis of the satellite makes an angle ψ with the satellite-planet centre line. Hence

$$\psi = f - \vartheta \,, \tag{A.1}$$

where f is the true anomaly. In the absence of tidal torques, the equation of motion for ϑ is

$$C\ddot{\vartheta} - \frac{3}{2}(B-A)\frac{Gm_p}{r^3}\sin 2\psi = 0 \,, \tag{A.2}$$

where $A = \sum \delta m(y^2+z^2)$, $B = \sum \delta m(z^2+x^2)$ and $C = \sum \delta m(x^2+y^2)$ are the moments of inertia with respect to the coordinates axes (with $m_s = \sum \delta m$, satellite's mass), m_p is the mass of the planet and r is the distance between planet and satellite.

Because r and ψ vary with f, which is a nonlinear function of time, this equation is nonintegrable. However, in those cases in which the spin rate $\dot{\vartheta}$ is commensurate with the mean motion n, we can derive an equation of motion that, although an approximation, is both useful and integrable [61, Murray and Dermott, 1999] .

Because we are interested in those cases for which $\dot{\vartheta}$ is a rational multiple of the mean motion, we introduce a new variable

$$\gamma = \vartheta - pM \,, \tag{A.3}$$

where p is a rational and M is the mean anomaly. Given than n is a constant, $\ddot{\vartheta} = \ddot{\gamma}$ and the equation of motion for γ is

$$\ddot{\gamma} + \frac{3}{2}n^2\left(\frac{B-A}{C}\right)\left(\frac{a}{r}\right)^3 \sin(2\gamma + 2pM - 2f) = 0 \,. \tag{A.4}$$

This equation can be expanded in a Fourier-like Poisson series in terms of e and M using standard expressions for $(\frac{a}{r})^3$, $\sin f$, and $\cos f$.

Including all terms of $\mathfrak{O}(e^2)$, we have

$$\sin f = \left(1 - \frac{7}{8}e^2\right)\sin M + e\sin 2M + \frac{9}{8}e^2 \sin 3M \,, \tag{A.5}$$

$$\cos f = \left(1 - \frac{9}{8}e^2\right)\cos M + e(\cos 2M - 1) + \frac{9}{8}e^2 \cos 3M \,, \tag{A.6}$$

and

$$\left(\frac{a}{r}\right)^3 = 1 + 3e\cos M + \frac{3}{2}e^2(1+3\cos 2M)\,. \tag{A.7}$$

We can write

$$\begin{aligned}\sin(2\gamma + 2pM - 2f) &= \sin 2\gamma(\cos 2pM\cos 2f + \sin 2pM\sin 2f)\\ &+ \cos 2\gamma(\sin 2pM\cos 2f - \cos 2pM\sin 2f)\,.\end{aligned} \tag{A.8}$$

Hence

$$\left(\frac{a}{r}\right)^3 \sin(2\gamma + 2pM - 2f) = [S_1 + S_2]\sin 2\gamma + [S_3 + S_4]\cos 2\gamma\,, \tag{A.9}$$

where

$$S_1 = \left(\frac{a}{r}\right)^3 \cos 2pM\cos 2f\,, \qquad S_2 = \left(\frac{a}{r}\right)^3 \sin 2pM\sin 2f\,, \tag{A.10}$$

$$S_3 = \left(\frac{a}{r}\right)^3 \sin 2pM\cos 2f\,, \qquad S_4 = \left(\frac{a}{r}\right)^3 \cos 2pM\sin 2f\,. \tag{A.11}$$

To $\mathfrak{O}(e^2)$, the S_i are given by

$$\begin{aligned}S_1 &= \frac{1}{2}[\cos 2(1-p)M + \cos 2(1+p)M]\\ &+ \frac{1}{4}e[7\cos(3+2p)M + 7\cos(3-2p)M - \cos(1+2p)M - \cos(1-2p)M]\\ &+ \frac{1}{4}e^2[-5\cos 2(1+p)M - 5\cos 2(1-p)M + 17\cos 2(2+p)M + 17\cos 2(2-p)M]\,,\end{aligned} \tag{A.12}$$

$$\begin{aligned}S_2 &= \frac{1}{2}[\cos 2(1-p)M - \cos 2(1+p)M]\\ &+ \frac{1}{4}e[-7\cos(3+2p)M + 7\cos(3-2p)M - \cos(1-2p)M + \cos(1+2p)M]\\ &+ \frac{1}{4}e^2[5\cos 2(1+p)M - 5\cos 2(1-p)M - 17\cos 2(2+p)M + 17\cos 2(2-p)M]\,,\end{aligned} \tag{A.13}$$

$$\begin{aligned}S_3 &= \frac{1}{2}[\sin 2(1+p)M - \sin 2(1-p)M]\\ &+ \frac{1}{4}e[7\sin(3+2p)M - 7\sin(3-2p)M + \sin(1-2p)M - \sin(1+2p)M]\\ &+ \frac{1}{4}e^2[-5\sin 2(1+p)M + 5\sin 2(1-p)M + 17\sin 2(2+p)M - 17\sin 2(2-p)M]\,,\end{aligned} \tag{A.14}$$

$$\begin{aligned}S_4 &= \frac{1}{2}[\sin 2(1+p)M + \sin 2(1-p)M]\\ &+ \frac{1}{4}e[7\sin(3+2p)M + 7\sin(3-2p)M - \sin(1-2p)M - \sin(1+2p)M]\\ &+ \frac{1}{4}e^2[-5\sin 2(1+p)M - 5\sin 2(1-p)M + 17\sin 2(2+p)M + 17\sin 2(2-p)M]\,.\end{aligned} \tag{A.15}$$

Therefore, the equation of motion for γ (A.4) can be written as

$$\ddot{\gamma} + \frac{3}{2}\frac{B-A}{C}n^2([S_1+S_2]\sin 2\gamma + [S_3-S_4]\cos 2\gamma) = 0\,. \tag{A.16}$$

Note that S_1 and S_2 only contain cosines, whereas S_3 and S_4 only contains sines. The equation is exact, but the S_i are infinite series in e and M and thus the equation is still nonintegrable. To progress, we must resort to approximations [61, Murray and Dermott, 1999] .

If the spin rate of the satellite is close to a spin-orbit resonance, then $\dot{\vartheta} \approx pn$ and γ is slowly varying, that is, $\dot{\gamma} \ll n$ and we can produce an approximate equation of motion by averaging all terms in equation (A.16) over one orbital period while holding γ fixed. We then obtain

$$\ddot{\gamma} + \frac{3}{2}\frac{B-A}{C}n^2([\langle S_1\rangle + \langle S_2\rangle]\sin 2\gamma + [\langle S_3\rangle - \langle S_4\rangle]\cos 2\gamma) = 0\,, \tag{A.17}$$

where

$$\langle S_i\rangle = \frac{1}{2\pi}\int_0^{2\pi} S_i dM\,, \qquad i = 1,2,3,4 \tag{A.18}$$

and it is now understood that γ refers to the averaged value.

The S_i have to be evaluated for a particular value of the rational p corresponding to the particular spin-orbit resonance under consideration. Because cosines and sines with arguments that are integer multiples of M average out to zero over one orbital period, the only terms in S_i that make a nonzero contribution to the equation of motion are those cosine terms with zero arguments.

For example, in the synchronous case for which $p = 1$, only those cosine terms with arguments containing $p - 1$ as a factor contribute to the equation of motion. If we carry out the same procedure for other values of p, then inspection of the same equations (or the equivalent set that contains terms of higher order in e) shows that only values of p that are an integer multiple of $\frac{1}{2}$ can contribute to the averaged equation of motion. In those cases, we can write

$$\ddot{\gamma} + \frac{3}{2}\frac{B-A}{C}n^2 H(p,e)\sin 2\gamma = 0\,. \tag{A.19}$$

By introducing an approximation, we have reduced the full equation of motion (A.2), to the pendulum equation, which we can write as

$$\ddot{\gamma} = -[signH(p,e)]\frac{1}{2}\omega_0^2 \sin 2\gamma\,, \tag{A.20}$$

where

$$\omega_0 = n\left[3\frac{B-A}{C}|H(p,e)|\right]\,, \tag{A.21}$$

is the libration frequency. In the presence of tidal torque acting to brake the spin of the satellite, a term representing the mean tidal torque averaged over one orbital period, $\langle N_s\rangle$, can be added to the averaged equation of motion to give

$$\ddot{\gamma} = -[signH(p,e)]\frac{1}{2}\omega_0^2 \sin 2\gamma + \frac{\langle N_s\rangle}{C}\,. \tag{A.22}$$

If

$$\frac{\langle N_s\rangle}{C} < \frac{1}{2}\omega_0^2\,, \tag{A.23}$$

then the sign of $\ddot{\gamma}$ must reverse periodically and thus it is possible for the satellite to be trapped in a spin-orbit resonance for which $\langle\dot{\vartheta}\rangle = pn$.

If equation (A.23), the *strength criterion*, is satisfied, then the mean torque due to the resonant interaction between the planet and the quadrupole moment of the satellite compensates for the mean

tidal torque acting to change the spin period of the satellite, $\langle\ddot{\gamma}\rangle = 0$, and γ librates about an equilibrium value γ_0 given by

$$\gamma_0 = \frac{1}{2}\sin^{-1}\left[\frac{2\langle N_s\rangle}{-[signH(p,e)]\omega_0^2 C}\right]. \tag{A.24}$$

The equilibrium orientation of the satellite and the sign of γ_0 are determined by the sign of $H(p,e)$. For small displacements of γ from γ_0, the sign of $\ddot{\gamma}$ must be such as to return γ to the equilibrium displacement, γ_0. If the mean tidal torque is weak in comparison with the resonant torque, that is, if

$$\frac{\langle N_s\rangle}{C} \ll \frac{1}{2}\omega_0^2\,, \tag{A.25}$$

then, if $H(p,e) > 0$, $\gamma_0 \approx 0$ or π and the long axis of the satellite points towards the planet on passage of the satellite through pericentre. Conversely, if $H(p,e) < 0$, $\gamma_0 \approx \frac{\pi}{2}$ or $\frac{3}{2}\pi$ and the long axis of the satellite points in a direction perpendicular to the planet-satellite line on passage of the satellite through pericentre [61, Murray and Dermott, 1999].

A.1 Mercury

We now consider the rotation of Mercury and give a simple, physical interpretation of the averaged equation of motion. The case of Mercury is particularly interesting because it was only after radar observations revealed that the planet is trapped in a 3:2 spin-orbit resonance with the Sun [19, Goldreich and Peale, 1968], [61, Murray and Dermott, 1999].

The spin period of the planet is 58.65 days, while its orbital period is $87.97 = 1.5 \times 58.65$ days. Thus, the planet rotates on its axis three times while it orbits the Sun twice and on successive passages of Mercury through perihelion, opposite faces of the planet are presented to the Sun. The physical meaning of the angle γ is that it describes the orientation of the long axis of the satellite on passage of the satellite through pericentre, that is, it is a stroboscopic angle that is evaluated when $M = 0$. The rotational and orbital motions of Mercury in an inertial reference frame are shown in figure (A.1).

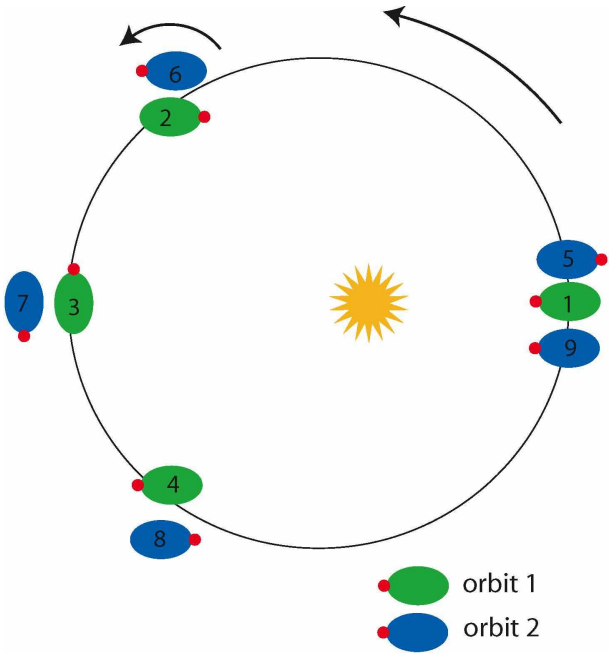

Figure A.1: In two revolutions of Mercury around the Sun, the planet rotates three times on its axis.

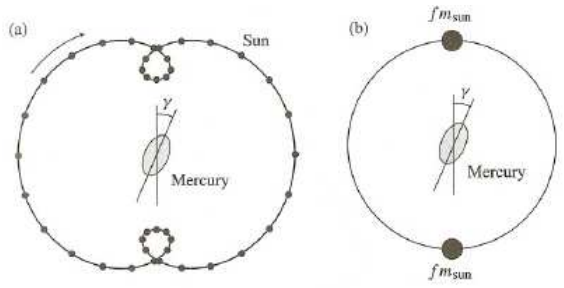

Figure A.2: (a) The motion of the Sun in a reference frame centred on Mercury and rotating with the planet's mean, resonant spin rate, $\frac{3}{2}n$, where n is Mercury's mean motion. (b) The gravitational interaction between the quadrupole moment of Mercury and the Sun can be modelled by spreading the mass of the Sun around the closed path with a local line density proportional to the time spent in that part of the path or by two point masses, fm_{Sun} where $f = \frac{1}{2}H(\frac{3}{2}, e)$. From Murray and Dermott, "Solar System Dynamics"(1999).

Figure A.2 shows the motion of the Sun in a reference frame centred on Mercury and rotating with the planet's mean, resonant spin rate, $\frac{3}{2}n$, where n is Mercury's mean motion. The points on the looped path indicate the position of the Sun at equal intervals of time. The path of the Sun in this rotating reference frame is closed only because the spin-orbit resonance exists and it is this crucial fact that validates our use of the averaging method [61, Murray and Dermott, 1999].

The average gravitational interaction between the quadrupole moment of the planet and the Sun can be modelled by spreading the mass of the Sun along this closed path in such a way that the local line density is proportional to the time spent by the Sun in that part of the path. The line density is inversely proportional to the spacing of the points shown in figure A.2.

The angle γ can now be interpreted as the deviation of the long axis of the planet from the planet-perihelion direction in the rotating frame A.2. From the symmetry of this figure, we further deduce that the gravitational interaction could be modelled by replacing the mass distribution of the Sun with a circular distribution of uniform line density that does not contribute to the torque plus two point masses, fm_{sun}, positioned as shown in figure A.2, where

$$f = \frac{1}{2}H(p, e) \approx \frac{7}{4}e\,, \tag{A.26}$$

and m_{sun} is the mass of the Sun [61, Murray and Dermott, 1999].

Bibliography

[1] Bate, R. R., Mueller, D. D. and White, J. E., 1971: *Fundamentals of Astrodynamics*, Dover Publications, Inc., New York

[2] Brownlee, D. E., 1978: *Microparticle Studies by Sampling Techniques*, Cosmic Dust, Edited by J. A. M. McDonnell

[3] Brownlee, D. E., 1996: *The Elemental Composition of Interplanetary Dust*, Physics, Chemistry, and Dynamics of Interplanetary Dust, ASP Conference Series, vol. **104**

[4] Brucato, J. R. et al., 1999: *Mid-infrared spectral evolution of thermally annealed amorphous pyroxene*, Astronomy and Astrophysics, **348**, pp. 1012-1019

[5] Burns, J. A. et al., 1979: *Radiation Forces on Small Particles in the Solar System*, Icarus **40**, pp. 1-48

[6] Ceplecha, Z., 1992: *Influx of interplanetary bodies onto Earth*, Astronomy and Astrophysics, **263**, pp. 361-366

[7] Cintala, M. J., 1992: *Impact-Induced Thermal Effects in the Lunar and Mercurian Regoliths*, Journal of Geophysical Research, Vol. **97**, No. E1, pp. 947-973

[8] Cremonese, G. et al., 2005: *Release of neutral sodium atoms from the surface of Mercury induced by meteoroid impacts*, Icarus, **177**, pp. 122-128

[9] Cremonese, G. et al., 1997: *Orbital evolution of meteoroids from short period comets*, Astronomy and Astrophysics, **324**, pp. 770-777

[10] De Elia, G. C. and Brunini, A., 2007: *Collisional and dynamical evolution of the main belt and NEA population*, Astronomy and Astrophysics, **466**, pp. 1159-1177

[11] Dermott, S., F. et al., 1996: *Sources of Interplanetary Dust*, Physics, Chemistry and Dynamics of Interplanetary Dust, ASP Conference Series, vol. **104**

[12] Desvoivres, E. et al., 2000: *Modeling the Dynamics of Cometary Fragments: Application to Comet C/1996 B2 Hyakutake*, Icarus **144**, pp. 172181

[13] Dohnanyi, J. S., 1966: *Model Distribution of Photographic Meteors*, Bellcom TR-66-340-1, Bellcomm, Inc.

[14] Erickson, J. E., 1968 : Velocity distribution of sporadic meteors, Journal of Geophysical Research, **73**, pp. 3721-3726

[15] Fechtig, H., 1982: *Cometary dust in the solar system*, Comets, University of Arizona Press, Tucson, pp.370-382

[16] Fulle, M. et al., 2000: *In situ measurements from within the coma of 1P/Halley: First-order approximation with a dust dynamical model*, The Astronomical Journal, **119**, pp. 1968-1977

[17] Fulle, M., 2004: *Motion of cometary dust*, Comets II, University of Arizona Press, Tucson, p.565-575

[18] Galligan, D. P. and Baggaley, W. J., 2001: *Probing the structure of the interplanetary dust cloud using the AMOR meteoroid orbit radar*, Proceedings of the Meteoroids 2001 Conference, 6-10 August 2001, Kiruna, Sweden, pp. 569-574

[19] Goldreich, P. and Peale, S. J., 1968: *The dynamics of planetary rotations*, Annual Review of Astronomy and Astrophysics, vol. **6**, p.287

[20] Grün, E. et al., 1985: *Collisional Balance of the Meteoritic Complex*, Icarus, **62**, pp. 244-272

[21] Grün, E. et al., 1994: *Interstellar dust in the heliosphere*, Astronomy and Astrophysics, **286**, pp. 915-924

[22] Grün, E. at al., 1997: *South-North and Radial Traverses through the Interplanetary Dust Cloud*, Icarus **129**, pp. 270-288

[23] Gustafson, B. Å. S. et al., 1987: *Interplanetary Dust Dynamics, II. Poynting-Robertson Drag and Planetary Perturbations on Cometary Dust*, Icarus **72**, pp. 568-581

[24] Gustafson, B. Å. S. et al., 1987: *Interplanetary Dust Dynamics, III. Dust Released from P/Encke: Distribution with Respect to the Zodiacal Cloud*, Icarus **72**, pp. 582-592

[25] Hanner, M. S. and Bradley, J. P., 2004: *Composition and mineralogy of cometary dust*, Comets II, University of Arizona Press, Tucson, pp.555-564

[26] Ipatov, S. I. and Mather, J. C., 2005: *Migration of dust particles to the terrestrial planets*, Proceedings "Dust in Planetary Systems", Kauai, Hawaii

[27] Ipatov, S. I. and Mather, J. C., 2006: *Migration of small bodies and dust to near-Earth space*, Advances in Space Research, **37**, pp. 126-137

[28] Ishiguro, M. et al., 2002: *First detection of an optical dust trail along the orbit of 22P/KOPFF*, The Astrophysical Journal, **572**, pp. L117-L120

[29] Ishimoto, H., 2000: *modeling the number density distribution of interplanetary dust on the ecliptic plane within 5 AU of the Sun*, Astronomy and Astrophysics, **362**, pp. 1158-1173

[30] Kessler, D. J., 1981: *Derivation of the Collision Probability Between Orbiting Objects: the lifetimes of Jupiter's Outer Moons*, Icarus, **48**, pp. 39-48

[31] Killen, R. M. et al., 2001: *Evidence for space weather at Mercury*, Journal Geophys. Res. Planets, **106**, pp. 2050920526

[32] Kimura, H. et al., 1998: *influence of dust shape and material composition on the solar F-corona*, Planetary and Space Science, volume **46**, Isuue 8, pp. 911-919

[33] Krivov, A. et al., 1998: *Dynamics of Dust near the Sun*, Icarus **134**, pp. 311-327

[34] Krüger, H. et al., 2006: *Five years of Ulysses dust data: 2000-2004*, Planetary and Space Science, **54**, pp. 932-956

[35] Lamy, L., 1974: *Interaction of Interplanetary Dust Grains with the Solar Radiation Field*, Astronomy and Astrophysics, **35**, pp. 197-207

[36] Lamy, L., 1974: *The Dynamics of Circum-solar Dust Grains*, Astronomy and Astrophysics, **33**, pp. 191-194

[37] Leblanc, F. and Johnson, R. E., 2003: *Mercurys sodium exosphere*, Icarus, **164**, pp. 261281

[38] Leinert, C. et al., 1981: *The Zodiacal Light from 1.0 to 0.3 A.U. as Observed by the Helios Space Probes*, Astronomy and Astrophysics, **103**, pp. 177-188

[39] Leinert, C. et Grün, E., 1990: *Interplanetary Dust*, Physics and Chemistry in Space - Space and Solar Physics, vol. **20**, Physics of the Inner Heliosphere I, Editors: R. Schwenn, E. Maesch

[40] Leinert, C. et al., 1998: *The 1997 reference of diffuse night sky brightness*, Astronomy and Astrophysics Supplement Series, **127**, pp. 1-99

[41] Levasseur-Regourd, A. C. et al., 2007: *Physical properties of cometary and interplanetary dust*, Planetary and Space Science, **55**, pp. 1010-1020

[42] Liou, J. C. et al., 1995: *The contribution of cometary dust to the zodiacal cloud*, Planetary and Space Science, Vol. **43**, No. 6, pp. 717-722

[43] Liou, J. C. and Zook, H. A., 1996: *Comets as a Source of Low Eccentricity and Low Inclination Interplanetary Dust Particles*, Icarus **123**, pp. 491-502

[44] Liou, J. C. et al., 1996: *Kuiper Belt Dust Grains as a Source of Interplanetary Dust Particles*, Icarus, **124**, pp. 429-440

[45] Love, S. G. and Brownlee, D. E., 1993: *A Direct Measurement of the Terrestrial Mass Accreation Rate of Cosmic Dust*, Science, Vol. 262

[46] Mann, I., 1992: *The solar F-corona: calculations of the optical and infrared brightness of circumsolar dust*, Astronomy and Astrophysics, **261**, pp. 329-335

[47] Mann, I. et al., 1994: *Fractal aggregate analogues for near solar dust properties*, Astronomy and Astrophysics, **291**, pp. 1011-1018

[48] Mann, I. and Grün, E., 1995: *Dust particles beyond the asteroid belt- A study based on recent results of the Ulysses dust experiment*, Planetary and Space Science, Vol. **43**, No. 6, pp. 827-832

[49] Mann, I. et al., 1996: *The Contribution of Asteroid Dust to the Interplanetary Dust Cloud: The Impact of ULYSSES Results on the Understanding of Dust Production in the Asteroid Belt and of the Formation of the IRAS Dust Bands*, Icarus **120**, pp.399-407

[50] Mann, I., et al., 2000: *Dust Cloud near the Sun*, Icarus, **146**, pp. 568-582

[51] Mann, I., Kimura, H. et al., 2004 : *Dust near the Sun*, Space Sciences Reviews **110**, pp. 269-305

[52] Marchi, S. et al., 2005 : *Flux of meteoroid impacts on Mercury*, Astronomy and Astrophysics, **431**, pp. 1123-1127

[53] Marsden, B. G., 1967: *The Sungrazing Comet Group*, The Astronomical Journal, Volume **72**, Number 9

[54] Marzari, F. and Vanzani, V., 1994: *Dynamical evolution of interplanetary dust particles*, Astronomy and Astrophysics, **283**, pp. 275-286

[55] Marzari, F. et al., 1996: *Collision Rates and Impact Velocities in the Trojan Asteroid Swarms*, Icarus, **119**, pp. 192-201

[56] Montenbruck O. and Gill E., 2000: *Satellite Orbits, Models, Methods, Applications*, Springer

[57] Morgan, T. H. et al., 1988: *Impact-Driven Supply of Sodium and potassium to the Atmosphere of mercury*, Icarus **75**, pp. 156-170

[58] Mukai, T. and Yamamoto, T., 1979: *A Model of the Circumsolar Dust Cloud*, Publ. Astron. Soc. Japan, **31**, pp. 585-595

[59] Mukai, T. and Schwehm, G., 1981: *Interaction of Grains with the Solar Energetic Particles*, Astronomy and Astrophysics, **95**, pp. 373-382

[60] Mukai, T. and Yamamoto, T., 1982: *Solar Wind Pressure on Interplanetary Dust*, Astronomy and Astrophysics, **107**, pp. 97-100

[61] Murray, C. D. and Dermott, S. F., 1999: *Solar System Dynamics*, Cambridge University Press

[62] Öpik, E. J., 1951: *Collision Probabilities with the Planets and the Distribution of Interplanetary Matter*, Proceedings of the Royal Irish Acedemy, vol **54**, sect. A

[63] Peterson, A. W., 1963: *Thermal radiation from interplanetary dust*, American Astronomical Society

[64] Peterson, C., 1976: *A Source Mechanism for Meteorites Controlled by the Yarkovsky Effect*, Icarus, **29**, pp. 91-111

[65] Schulz, R. and Benkhoff, J., 2005: *BepiColombo: Payload and mission updates*, Advances in Space Research 38, pp. 572577

[66] Southworth, R. B. and Sekanina, Z., 1973: *Physical and Dynamical Studies of Meteors*, NASA Contractor Report

[67] Sekanina, Z., 2000: *Solar and heliospheric observatory sungrazing comets with prominent tails: evidence on dust-production peculiarities*, The Astrophysical journal, **545**, pp. L69-L72

[68] Shoemaker, E. M., 1983: *Asteroid and comet bombardement of the Earth*, Ann. Rev. Earth Planet. Sci., **11**, pp. 461-494

[69] Shoemaker, E. M. et al., 1990: *Asteroid and comet flux in the neighborhood of the Earth*, Global Catastrophes in Earth History, Geological Society of America

[70] Sørensen, J. and Evans, H, 2004: *Mercury Environmental Specification (Part II) BepiColombo Definition Study*, Space Environment and Effects Analysis Section, ESA/ESTEC/TOS-EMA, 9 February 2004

[71] Sprague, A. et al., 2007: *Mercurys Surface Composition and Character as Measured by Ground-Based Observations*, Space Science Reviews

[72] Swamy Krishna, K. S., 1995: *Impact of comets on solar system objects*, Bull. Astr. Soc. India, **23**, pp. 411-418

[73] Sykes, M. V. et al., 2004: *The Interplanetary Dust Complex and Comets*, Comets II, University of Arizona Press, Tucson, pp. 677-693

[74] Van Boekel, R. et al., 2005: *A 10 μm spectroscopic survey of Herbig Ae star disks: Grain growth and crystallization*, Astronomy and Astrophysics, **437**, pp. 189-208

[75] Zolensky, M. E. et al., 1994: *Collection and curation of interplanetary dust particles recovered from the stratosphere*, Lunar and Planetary Inst., Workshop on the Analysis of Interplanetary Dust Particles, pp. 56-57

[76] Zook, H. A., 1975: *The State of Meteoritic Material on the Moon*, Proc. Lunar Sci. Conf., 6th, pp. 1653-1672

[77] Wehry, A. and Mann, I., 1999: *Identification of β-meteoroids from measurements of the dust detector onboard the Ulysses spacecraft*, Astronomy and Astrophysics, **341**, pp. 296-303

[78] Weissman, P. R., 2006: *The cometary impactor flux at the Earth*, Near Earth Object, our Celestial Neighbors: Opportunity and Risk, Proceedings IAU Symposium No. 236

Acknowledgements

I heartly wish to express my gratitude to Professor Bernacca for helping me out through a difficult situation by giving me a choice when I was feeling like at a dead end.

My gratefulness also goes to Dr. Cremonese for believing in me, stiring up my cultural interests even further and supporting me with his wise advice and guidance throughout all these years of Ph.d.

Last but not least, I want to thank Professor Marzari who has been the "invisible hand" throughout this subject of research, by giving me precious guidelines both on programming language and theoretical levels.